Experimental study and simulation of cyclic softening of tempered martensite ferritic steels

Pierre-François Giroux

▶ **To cite this version:**

Pierre-François Giroux. Experimental study and simulation of cyclic softening of tempered martensite ferritic steels. Materials. École Nationale Supérieure des Mines de Paris, 2011. English. NNT : 2011ENMP0087 . pastel-00710628

HAL Id: pastel-00710628
https://pastel.hal.science/pastel-00710628

Submitted on 21 Jun 2012

HAL is a multi-disciplinary open access archive for the deposit and dissemination of scientific research documents, whether they are published or not. The documents may come from teaching and research institutions in France or abroad, or from public or private research centers.

L'archive ouverte pluridisciplinaire **HAL**, est destinée au dépôt et à la diffusion de documents scientifiques de niveau recherche, publiés ou non, émanant des établissements d'enseignement et de recherche français ou étrangers, des laboratoires publics ou privés.

ParisTech
INSTITUT DES SCIENCES ET TECHNOLOGIES
PARIS INSTITUTE OF TECHNOLOGY

MINES ParisTech

École doctorale n°432 : Sciences des Métiers de l'Ingénieur

Doctorat ParisTech

T H È S E

pour obtenir le grade de docteur délivré par

l'École Nationale Supérieure des Mines de Paris

Spécialité « Sciences et Génie des Matériaux »

présentée et soutenue publiquement par

Pierre-François GIROUX

le 22 décembre 2011

Étude expérimentale et modélisation de l'adoucissement cyclique des aciers ferritiques-martensitiques revenus

Experimental study and simulation of cyclic softening of tempered martensite ferritic steels

Directrice de thèse : **Anne-Françoise GOURGUES-LORENZON**
Co-encadrement de la thèse : **Maxime SAUZAY**
France DALLE
Thilo MORGENEYER

Jury

M. Alain MOLINARI, Professeur, Université Paul Verlaine Metz, France	Président
M. Gunther EGGELER, Professeur, Ruhr-University Bochum, Allemagne	Rapporteur
M. Antonín DLOUHÝ, Professeur, Institute of Physics of Materials Brno, République Tchèque	Rapporteur
M. Félix LATOURTE, Ingénieur de Recherche, EdF R&D Les Renardières, France	Examinateur
M. Emmanuel CINI, Ingénieur de Recherche, Vallourec Research Aulnoye, France	Examinateur
Mme Anne-Françoise GOURGUES-LORENZON, Professeur, MINES ParisTech, France	Examinateur
M. Maxime SAUZAY, Chercheur-Ingénieur, CEA Saclay, France	Examinateur
Mme France DALLE, Chercheur-Ingénieur, CEA Saclay, France	Invité
M. Thilo MORGENEYER, Chargé de Recherche, MINES ParisTech, France	Invité

T H È S E

MINES ParisTech
Centre des Matériaux - UMR CNRS 7633
B.P. 87 - 91003 Évry Cedex, France

Résumé

Inscrit au sein d'un grand projet aboutissant à la mise en œuvre des réacteurs nucléaires de génération IV, ce travail de thèse porte sur l'étude des aciers martensitiques revenus à 9 % de chrome. Actuellement utilisés pour des applications à haute température, notamment dans les centrales thermiques, ils présentent en fatigue et en fatigue-fluage un phénomène d'adoucissement mécanique et des évolutions microstructurales particulièrement prononcées, en particulier disparition de nombreux joints de sous-grains et baisse de la densité de dislocations. Les objectifs principaux de cette thèse sont (i) d'établir expérimentalement une corrélation entre l'adoucissement mécanique des aciers à 9 % de chrome constaté en fatigue à 550 ℃ et l'évolution de leur microstructure au cours de ce type de sollicitation et (ii) de modéliser les mécanismes physiques de déformation afin de prédire les évolutions de la microstructure et du comportement mécanique de ces aciers sous chargement cyclique.

Une étude des propriétés mécaniques en traction monotone et sous sollicitations cycliques à 550 ℃ a été conduite sur un acier de Grade 92 (9Cr-0,5Mo-1,8W-V-Nb) en faisant varier vitesse et amplitude de déformation. L'expertise des éprouvettes de traction suggère que le faible adoucissement du matériau est principalement lié à l'effet de la striction et à une augmentation de la taille moyenne des sous-grains de plus de 15 % par rapport à l'état initial. L'étude de l'évolution de la contrainte macroscopique durant les essais cycliques montre que l'adoucissement du matériau est dû à la diminution de l'écrouissage cinématique. Les observations effectuées au MET montrent une augmentation de la taille moyenne des sous-grains comprise entre 60 et 100 % et une diminution de la densité de dislocations de plus de 50 % dans le matériau après les essais de fatigue, par rapport à l'état initial.

Un modèle auto-cohérent à champ moyen fondé sur l'élastoviscoplasticité cristalline et les densités de dislocations continues, prédisant le comportement mécanique macroscopique du matériau et l'évolution microstructurale au cours de la déformation est proposé. En se fondant sur les mécanismes choisis à partir des observations microstructurales, le modèle nécessite l'ajustement de seulement deux paramètres du glissement viscoplastique (énergie et volume d'activation effectifs) induits par les obstacles variés (petits précipités, solution solide...). Les valeurs de l'ensemble des autres paramètres sont fixées grâce à des mesures expérimentales ou des calculs issus de la littérature. Le modèle prédit convenablement l'adoucissement macroscopique ainsi que l'évolution microstructurale au cours de la déformation. L'étude paramétrique montre que les prédictions sont stables dès lors que les paramètres du modèle varient dans des intervalles physiquement acceptables d'après les données de la littérature. La prise en compte d'une distribution initiale de taille de sous-grains et d'une distribution initiale de densités de dislocations permet d'améliorer les prédictions du comportement mécanique macroscopique et de l'évolution de la microstructure. Enfin, des essais de torsion cyclique sont simulés et le modèle est appliqué à un acier EUROFER 97 afin de prédire les évolutions microstructurales au cours d'un essai cyclique à température ambiante.

Mots-clés: Adoucissement cyclique à haute température ; Aciers martensitiques revenus ; Évolution microstructurale ; Modélisation polycristalline ; Densités de dislocations continues.

Abstract

The present work focuses on the high temperature mechanical behaviour of 9%Cr tempered martensite steels, considered as potential candidates for structural components in the next Generation IV nuclear power plants. Already used for energy production in fossil power plants, they are sensitive to softening during high-temperature cycling and creep-fatigue. This phenomenon is coupled to a pronounced microstructural degradation: mainly vanishing of subgrain boundaries and decrease in dislocation density. This study aims at (i) linking the macroscopic cyclic softening of 9%Cr steels and their microstructural evolution during cycling and (ii) proposing a physically-based modelling of deformation mechanisms in order to predict the macroscopic mechanical behaviour of these steels during cycling.

Mechanical study includes uniaxial tensile and cyclic test at 550 ℃ performed on a Grade 92 steel (9Cr-0,5Mo-1,8W-V-Nb). The effect of both strain amplitude and rate on mechanical behaviour is studied. Examination of tensile specimens suggests that the physical mechanism responsible for slight measured softening is mainly the necking phenomenon and the evolution of mean subgrain size, which increases by more than 15 % compared to the as-received state. The evolution of the macroscopic stress during cycling shows that cyclic softening is due to the decrease in kinematic stress. TEM observations highlights that the mean subgrain size increases by 60 to 100 % while the dislocation density decreases by more than 50 % during cycling, compared to the as-received state.

A self-consistent homogenization model based on crystalline elastoviscoplasticity and dislocation densities, predicting the mechanical behaviour of the material and its microstructural evolution during deformation is proposed. This model takes some of the main physical deformation mechanisms into account and only the two parameters of crystalline viscoplasticity should be ajusted (the effective activation energy and volume) linked to the various small obstacles present in the material (microprecipitates, solid solution...). The value of the other parameters are either experimentally measured or deduced from computation results available in literature. The model correctly predicts the macroscopic softening behaviour and as well as the microstructural evolution during cycling. The parametrical study shows that the predictions are rather stable with respect to the variation of the physically-based parameter values. Predictions are improved by taking the initial subgrain size distribution and the initial dislocation density distribution into account. Finally, torsion tests are simulated and the presented model is used to predict the microstructural evolution of EUROFER 97 steel during cycling at room temperature.

Keywords: High-temperature cyclic softening; Tempered martensite steels; Polycrystalline model; Microstructural evolution.

Remerciements

Je pense que je n'étonnerai personne en écrivant qu'il serait trop simpliste de résumer le doctorat au seul aspect scientifique. Durant ces trois années, j'ai eu la chance de rencontrer nombre de personnes qui ont participé, chacun à leur manière, à l'aboutissement de ce projet. Donc, avant de commencer à vous raconter mon histoire sur les aciers à 9 % de chrome, je tiens à remercier toutes ces personnalités croisées au cours de cette aventure.

J'adresse tout d'abord mes remerciements à mes encadrants pour la confiance et l'autonomie qu'ils m'ont accordées. Je souhaite donc remercier Maxime Sauzay qui, en plus de sa disponibilité et de son enthousiasme, a su m'initier au monde de la modélisation polycristalline. Un grand merci à Anne-Françoise Gourgues-Lorenzon qui a su diriger cette thèse tout en m'accordant la liberté de mener mes travaux selon mes initiatives. Je souhaite aussi remercier France Dalle de m'avoir permis de débuter cette aventure, ainsi que pour son soutien durant ces trois ans. Enfin merci à Thilo Morgeneyer pour son apport scientifique lors de nos réunions de travail.

J'aimerais également remercier l'ensemble des membres du jury pour l'intérêt qu'ils ont porté à mes travaux : merci aux Professeurs Gunther Eggeler et Antonín Dlouhý d'avoir accepté de relire le présent manuscrit ; au Professeur Alain Molinari de m'avoir fait l'honneur de présider ce jury, ainsi qu'à Félix Latourte d'avoir accepté d'y participer. Enfin, merci à Emmanuel Cini pour les échanges scientifiques enrichissants, à la fois en tant que partenaire industriel de ce projet et membre du jury.

Je tiens à remercier Luc Paradis, chef du Service de Recherche Métallurgiques Appliquées du CEA, Laurence Portier, chef du Laboratoire d'étude du Comportement Mécanique des Matériaux et Esteban Busso, directeur du Centre des Matériaux MINES ParisTech, de m'avoir accueilli au sein de leur laboratoire afin que puisse se dérouler au mieux l'ensemble de ces travaux.

Je souhaite remercier les collègues du SRMA qui m'ont aidé à mettre en place les essais mécaniques et à utiliser les moyens de caractérisation indispensables à l'analyse expérimentale menée au cours de cette thèse. Je remercie donc Christel Caës qui, outre sa disponibilité et sa gentillesse, a mis en place les essais de fatigue et de fatigue-fluage présentés dans ce manuscrit. De même, merci à Ivan Tournié d'avoir lancé les essais de fluage. Je souhaite également remercier Joël Malaplate et Thierry Van Den Berghe de m'avoir formé à l'utilisation du MET et aidé à effectuer de nombreux clichés. Merci à Benoit Arnal d'avoir pris les clichés durant cette dernière année. Enfin, merci à Benjamin Fournier pour les multiples échanges autour des aciers à 9 % de chrome.

Si ce travail de thèse a pu être mené à bien à l'issue de ces trois années, c'est aussi grâce à tous ceux qui, quotidiennement, apportent leur bonne humeur, leur écoute et leur amitié. Je tiens donc à remercier chaleureusement Camille et Antonin pour tous les moments que nous avons partagés autour de la machine à café ou d'un tableau blanc (un merci spécial à Antonin pour les longues discutions liées au fonctionnement de SiDoLo). Merci à Lionel, Christian et Aurélien d'avoir contribué à l'ambiance agréable de nos pauses-déjeuner. Merci également à Denis et Fret, coureurs de haut niveau, qui m'ont accompagné (ou plutôt trainé) lors de nos séances de course à pied, particulièrement salutaires. Je

souhaite remercier Nathalie pour ses qualités professionnelles, mais aussi et surtout pour les moments passés en compagnie de Khadija, Louis, Yang et Jérôme. Je remercie aussi Laurent, Thomas, Aurélie, Florine, Grégory et Lingtao qui m'ont accompagné au cours de ces trois années et avec qui j'ai partagé de très bon moments au Centre des Matériaux. Enfin, merci à tous les doctorants et stagiaires croisés durant cette période très enrichissante : Charlotte, Léa, Louise, Emma, Gwenaël, Daniel, Cyril, Marian, Rodrigo, Ronald, Claire... Un merci spécial à Clara pour l'écoute et la disponibilité dont elle a fait preuve durant ces trois ans.

Pour finir, j'adresse mes plus sincères remerciements à mes proches qui m'ont soutenu tout au long de cette aventure. Merci à Julien, Émilie, Benoit, Guillaume, Alexandre et tous les autres amis de lycée de m'avoir offert quelques soirées de détente en votre compagnie ; merci aux thésards de l'université de Strasbourg pour les virées lors de mes week-end dans l'Est de la France ; merci aux handballeurs de l'Entente avec qui j'ai passé un grand nombre de samedis soirs. Je souhaite sincèrement remercier mes parents pour leur soutien indéfectible tout au long de mes études. Enfin, merci à Chloé pour sa présence, son soutien et ses encouragements qui ont été une grande source de réconfort.

Contents

Abstract (in French) **3**

Abstract **5**

Acknowledgments (in French) **7**

About the manuscript (in French) **13**

About the manuscript **15**

Table of symbols and notations **17**

1 General introduction and presentation of the material under study (in French) **19**

1.1 General context of the study and problematic 20

1.2 Tempered martensite ferritic steels - Presentation of the material under study 21

1.2.1 Chemical composition and heat treatments 21

1.2.1.1 Chemical composition of the material under study 21

1.2.1.2 Heat treatments applied to the material under study 21

1.2.2 Microstructure of tempered martensite steels 22

1.2.2.1 The various scales of the microstructure 22

1.2.2.2 From austenitic microstructure to martensite microstructure 23

1.2.2.3 From martensite microstructure to tempered martensite microstructure 25

1.2.2.4 Dislocation density 26

1.2.2.5 Dislocations nature 27

1.2.2.6 Inclusions and cavities 28

1.2.2.7 Composition of the precipitates 29

1.2.2.8 Precipitates size 30

1.2.2.9 Localisation of the precipitates 30

2 Mechanical and microstructural stability of P92 steel under uniaxial tension at high temperature 33

Abstract (in French) . . . 35

2.1 Introduction . . . 37

2.2 Material and experimental procedure . . . 37

2.2.1 Material . . . 37

2.2.2 Tensile tests . . . 37

2.2.3 Metallographic investigation of the tensile specimens after the tests . . . 38

2.2.3.1 Damage evolution . . . 38

2.2.3.2 Macroscopic necking . . . 38

2.2.3.3 Microstructural evolution . . . 38

2.3 Results of tensile tests carried out up to fracture . . . 39

2.4 Damage assessment . . . 40

2.5 Necking: experimental results and modelling . . . 42

2.5.1 Interrupted tensile tests and onset of macroscopic necking . . . 42

2.5.2 Prediction of mechanical instability and of fracture elongation . . . 45

2.6 Microstructural evolution of the matrix during tensile deformation . . . 51

2.6.1 Experimental results: EBSD and TEM investigations . . . 51

2.6.2 Modelling of microstructural evolution during straining . . . 51

2.7 Conclusions . . . 57

3 Mechanical behaviour and microstructural evolution during cyclic and creep loading 59

Abstract (in French) . . . 61

3.1 Macroscopic cyclic loading, creep and creep-fatigue behaviour . . . 63

3.1.1 Cyclic loading tests . . . 63

3.1.1.1 Experimental conditions and specimen geometry . . . 63

3.1.1.2 Influence of strain amplitude at high strain rate on cyclic flow behaviour and fatigue lifetime . . . 64

3.1.1.3 Influence of strain rate on cyclic flow behaviour and fatigue lifetime . 65

3.1.2 Creep tests . . . 68

3.1.2.1 Experimental conditions and specimen geometry . . . 68

3.1.2.2 Creep curves and lifetime . . . 68

3.1.3 Cyclic test including tensile holding periods . . . 71

3.1.3.1 Experimental conditions and specimen geometry 72
3.1.3.2 Creep-fatigue mechanical behaviour 72
3.2 Macroscopic analysis of softening during cyclic loading 74
3.3 Observations of microstructural evolutions during cyclic loading tests 76
3.3.1 Evolution of the subgrain size distribution 77
3.3.1.1 Methodology 77
3.3.1.2 Evolution of subgrain size distribution during fatigue test 77
3.3.1.3 Effect of the strain on subgrain size evolution 79
3.3.2 Evolution of the dislocation density during high temperature cyclic loading . . 84
3.3.3 Discussion about deformation and annihilation mechanisms 85
3.4 Concluding remarks 87

4 Modelling of the cyclic behaviour and microstructure evolution during cycling 89
Abstract (in French) 91
4.1 Introduction to polycrystalline modelling 93
4.2 Crystalline constitutive equations 94
4.2.1 Description and hypotheses of the modelling 94
4.2.1.1 Dislocations types considered in the model 95
4.2.1.2 Low-angle boundaries structures 95
4.2.1.3 Crystallographic features at the block scale 97
4.2.2 Isotropic stress 98
4.2.3 Evolution of the kinematic stress 99
4.2.4 Crystal viscoplasticity flow rule 102
4.3 Modelling the microstructural evolutions 103
4.3.1 Modelling the evolution of dislocation density 103
4.3.1.1 Production of dislocations 104
4.3.1.2 Inter-annihilation of free dislocations 105
4.3.1.3 Annihilation of free dislocations with low-angle boundary dislocations 106
4.3.2 Modelling of low-angle boundaries misorientation evolution 106
4.3.3 Modelling the subgrain size evolution 108
4.4 Self-consistent homogenization scheme 108
4.4.1 Thermoelastic modelling proposed by Kröner 108
4.4.2 Molinari's model for viscoplastic material 109

4.5 Choice of the values of the model parameters . . . 110
4.5.1 Measured, calculated and fixed parameters . . . 110
4.5.2 Identification process . . . 112
4.6 Simulation of cyclic loading . . . 115
4.6.1 Validation of the model on the first macroscopic loop for both strain rates . . . 115
4.6.2 Prediction of cyclic softening for both strain rates . . . 115
4.6.2.1 Predicted macroscopic behaviour . . . 115
4.6.2.2 Predicted microstructural evolution . . . 116
4.6.3 Predictions of the macroscopic cyclic softening for different strain amplitudes . 120
4.6.4 Sensitivity of model predictions to the values of model parameters . . . 122
4.6.4.1 Influence of the critical annihilation distance for edge dislocations on model predictions . . . 123
4.6.4.2 Influence of the critical annihilation distance for screw dislocations on model predictions . . . 125
4.6.4.3 Influence of the initial mean low-angle boundary misorientation on model predictions . . . 127
4.6.4.4 Influence of the value of the critical misorientation on model predictions 129
4.6.4.5 Influence of the respective fractions of mobile edge / screw dislocation densities on model predictions . . . 131
4.6.4.6 Concluding remarks from the parametric study . . . 133
4.7 Concluding remarks . . . 133

5 Influence of the initial heterogeneity of microstructure, multiaxiality, temperature and material on the model predictions (in French) 135
5.1 Use of the measured initial distributions of subgrain sizes and dislocation densities . . 136
5.1.1 Initial subgrain size distribution . . . 136
5.1.2 Initial mobile dislocation density distribution . . . 142
5.2 Simulations of cyclic torsion . . . 148
5.3 Modelling of the cyclic behaviour of the EUROFER 97 steel at room temperature . . 149
5.4 Conclusions . . . 151

6 General conclusions and recommendations for further work 153
6.1 Conclusions . . . 154
6.2 Some recommendations for future work . . . 156

References 159

À propos du manuscrit

Le présent manuscrit est structuré en six chapitres. Le premier chapitre est une introduction générale au travail de thèse. Après une introduction des objectifs de ce travail, le matériau étudié, l'acier Grade 92, est présenté et une courte synthèse bibliographique concernant la microstructure des aciers martensitiques revenus est décrite.

Le chapitre 2 est consacré à l'étude du comportement mécanique de l'acier Grade 92 en traction monotone à 550 ℃. Trois phénomènes sont étudiés afin de comprendre les mécanismes à l'origine de l'adoucissement macroscopique mesuré : l'instabilité mécanique (striction), l'endommagement et l'évolution de la taille des sous-grains. Deux modèles analytiques prédisant l'apparition de l'instabilité mécanique et la croissance des sous-grains sont proposés.

Le chapitre 3 est dédié à l'étude du comportement mécanique de l'acier Grade 92 lors de sollicitations de type chargement cyclique continu et fluage à 550 ℃. L'étude se concente sur les mécanismes de déformation lors des essais sous chargement cyclique continu, avec notamment la décomposition de la contrainte macroscopique selon la méthode de Cottrell. Des observations MET visant à caractériser l'évolution de la microstructure sont finalement présentées et discutées.

Le chapitre 4 est dédié à la modélisation polycristalline du comportement mécanique de l'acier Grade 92 lors de sollicitations cycliques continues à 550 ℃. Le modèle est construit autour de deux axes majeurs : le changement d'échelle (du bloc de martensite revenu au polycristal) et la modélisation de l'évolution de la microstructure (taille de sous-grain et densité de dislocations). Les résultats des prédictions du comportement mécanique macroscopique et de l'évolution microstructurale sont ensuite présentés. Enfin, l'influence de la valeur des paramètres physiques du modèle sur les prédictions est étudiée et discutée.

Le chapitre 5 présente deux améliorations apportées au modèle décrit dans le chapitre 4 : la prise en compte de distributions initiales de taille de sous-grains et de densité de dislocations moyenne par bloc. Dans un second temps, le modèle est appliqué à des chargements cycliques de torsion et les prédictions obtenues sont étudiées qualitativement. Ce chapitre se clôt sur une présentation des simulations de sollicitation cyclique à température ambiante sur l'acier EUROFER 97 en collaboration avec M. F. Giordana (*Universidad Nacional de Rosario*, Argentina).

Enfin, les conclusions et perspectives de ce travail sont présentées dans le chapitre 6.

Ce manuscrit ne comporte pas de chapitre consacré à une revue bibliographique extensive des aciers martensitiques revenus et de leur comportement mécanique en général. Cependant, chaque composante de cette étude insère des éléments bibliographiques présentant les travaux et résultats disponibles dans la littérature.

About the manuscript

This present manuscript is divided into six chapters. The first one focuses on the general context of this study. After an introduction to the objectives of this work, a description of the material under study, a Grade 92 steel, and a short literature survey of the tempered martensite ferritic steel microstructure are presented.

Chapter 2 focuses on the mechanical behaviour of the Grade 92 steel during monotonic tensile tests at 550 ℃ at various strain rates. Three phenomena are studied in order to understand the physical mechanisms inducing the observed softening stage: mechanical instability (necking), damage and subgrain size evolution. Two analytical models predicting respectively the beginning of the mechanical instability and the subgrain growth are proposed.

Chapter 3 focuses on the experimental mechanical behaviour of the Grade 92 steel during continuous cyclic loading and creep at 550 ℃. Then, the study focuses on the physical mechanisms of deformation during continuous cycling deformation based on the partition of macroscopic stress proposed by Cottrell. Finally, TEM observations of the microstructure are presented in order to characterize quantitatively the microstructure evolution and the possibly involved physical mechanisms are discussed.

Chapter 4 focuses on the modelling of the mechanical behaviour of Grade 92 steel during continuous cycling at 550 ℃. The description of the hypotheses of the modelling is divided into two parts: polycrystalline homogeneisation (from the tempered martensite block to the macroscopic scale) and microstructural evolution modelling (subgrain size and dislocation density). Then, the predictions of the modelling of the macroscopic mechanical behaviour and microstructural evolution are presented. Finally, the influence of the values of the used parameters on the predictions is studied and discussed.

Chapter 5 focuses on two important improvements of the model presented in chapter 4 : an initial mean subgrain size distribution per block and an initial dislocation density distribution are taken into account instead of using averaged values. Then, predictions of the model under cyclic torsion are studied. Finally, some results about the predictions of the microstructural evolution of EUROFER 97 steel during cycling at room temperature are presented, in collaboration with M. F. Giordana (*Universidad Nacional de Rosario*, Argentina).

Finally, general conclusions and recommendations for further work are presented in chapter 6.

In this manuscript, no chapter presents a general literature survey of the tempered martensite steels and their mechanical behaviour under various loading conditions. However, each part of this study is presented with literature elements available published work and results.

Table of symbols and notations

Symbols

d	Total derivative
∂	Partial derivative
δ	Infinitesimal change in the value of a variable
Δ	Macroscopic change in the value of a variable
u	Scalar quantity
$\bar{u}$	Mean value
$\underline{u}$	First-order tensor
$\underline{\underline{u}}$	Second-order tensor
$\underline{\underline{\underline{u}}}$	Fourth-order tensor

Notations

b	Bürgers vector magnitude
d	Subgrain diameter
e	Thin foil thickness
l	Mean path of a dislocation
l_i	Length of a segment
m	Hart's viscoplastic parameter
n_i	Number of intersections between a segment and a dislocation
s	Standard deviation of a distribution
t_f	Failure time of creep test
x	Mean block kinematic shear stress
x_{max}	Mean block maximum kinematic shear stress

A_d	Area swept by a dislocation
A	Cross-section of a specimen
A_0	Initial cross-section of a specimen
$\underline{\underline{E}}^p$	Macroscopic plastic strain tensor
R	Isotropic part of the macroscopic stress
X	Kinematic part of the macroscopic stress
γ	Hart's strain hardening parameter
γ^p	Plastic slip
ϵ, ϵ_1	Axial engineering strain
ϵ_2, ϵ_3	Radial engineering strain
$\underline{\underline{\epsilon}}^e$	Elastic engineering strain tensor
$\underline{\underline{\epsilon}}^p$	Plastic engineering strain tensor
ε^{vp}	Principal component of visco-plastic strain tensor
$\dot{\varepsilon}^{vp}$	Principal component of visco-plastic strain rate tensor
$\dot{\varepsilon}_s$	Minimum (or secondary) creep rate
$\underline{\underline{\varepsilon}}^p$	Mean block plastic strain tensor
μ	Elastic shear modulus
ν	Elastic Poisson ratio
ρ	Total dislocation density
σ	Principal component of stress tensor
$\underline{\underline{\sigma}}$	Mean block stress tensor
τ	Mean block shear stress
Σ_v	Viscous part of the macroscopic stress
$\underline{\underline{\Sigma}}$	Macroscopic stress tensor

Chapitre 1

Introduction générale et présentation du matériau de l'étude

This first chapter focuses on the general context of this study. After an introduction to the objectives of this PhD work, a description of the material under study – Grade 92 steel (9%Cr-0.5%Mo-1.8%W-NbV) – and a short literature survey on tempered martensite-ferritic steel microstructures are presented, together with the properties of the material.

Ce premier chapitre présente le contexte général de l'étude de la déformation. Une introduction à la problématique de la thèse et une rapide présentation du matériau étudié, l'acier Grade 92 (9%Cr-0.5%Mo-1.8%W-NbV), sont proposées. Enfin, une description bibliographique succincte axée sur la microstructure de ces matériaux est présentée, et mise en regard des propriétés du matériau.

Contents

1.1 General context of the study and problematic 20
1.2 Tempered martensite ferritic steels - Presentation of the material under study 21
1.2.1 Chemical composition and heat treatments 21
1.2.2 Microstructure of tempered martensite steels 22

1.1 Contexte général de l'étude et problématique

Afin d'apporter une réponse à la demande croissante en énergie, les principaux acteurs de l'industrie nucléaire tel que le Commissariat à l'Énergie Atomique ont orienté des projets de recherche vers la réalisation d'un nouveau type de réacteur de fission à neutrons rapides, dit de Génération IV. Cette technologie, plus sûre en termes d'exploitation et moins risquée vis-à-vis des problèmes liés à la prolifération, a également pour objectif d'allonger la durée de vie de ces nouveaux réacteurs à la conception et d'améliorer leur rendement énergétique. Une des voies explorées pour parvenir à la réalisation de ce dernier objectif passe par l'augmentation de la température de fonctionnement (entre 450 et 600 ℃ contre 300 à 400 ℃ pour les réacteurs actuels) et par conséquent, nécessite le choix d'un fluide caloporteur autre que l'eau, tel que le sodium.

Cette accroissement de la température de fonctionnement et de la durée de vie des réacteurs induit inévitablement des répercussions sur le choix des matériaux de structure. C'est dans ce contexte que les aciers martensitiques revenus à 9 % de chrome ont été retenus comme candidats potentiels pour la conception de certains éléments de circuiterie tels que les générateurs de vapeur. En effet, ces aciers présentent une meilleure conductivité thermique et un coefficient de dilatation thermique plus faible que les aciers austénitiques de type AISI 316L, ce qui peut permettre de réduire les sollicitations mécaniques liées à la fatigue thermique. Outre ces propriétés, son coût de production moindre peut être un avantage.

Les structures à haute température subiront des sollicitations de type fluage mais peuvent être aussi soumises à des chargements cycliques, liés aux phases d'arrêt et redémarrage des réacteurs. En vue de leur dimensionnement au sein du réacteur, l'étude des aciers martensitiques revenus à 9 % de chrome se doit de considérer leurs propriétés mécaniques lors de chargement cyclique, en fluage et fatigue-fluage. Ces sollicitations en conditions de service peuvent être assimiliées à du fluage long-terme (avec un temps de maintien de l'ordre du mois), interrompu par des chargements cycliques à faible amplitude de déformation. Bien entendu, une telle succession de sollicitations est impossible à reproduire en laboratoire pour des raisons de temps d'occupation des machines d'essais, *a fortiori*, sur une période de 60 ans.

Le dimensionnement des structures se fonde donc sur une extrapolation des résultats des essais réalisés en laboratoire. Or, celle-ci reste risquée si elle tient uniquement compte des résultats mécaniques macroscopiques obtenus lors de ces essais, relativement éloignés des sollicitations en conditions de service. Il s'avère donc primordial, afin d'améliorer la fiabilité de ces extrapolations, de comprendre et de modéliser les mécanismes physiques de la déformation qui induisent les résultats macroscopiques observés en laboratoire. C'est dans cette optique que s'incrit le présent travail de thèse.

Les différentes nuances d'aciers martensitiques revenus ont été optimisées dans l'optique d'améliorer leurs propriétés en fluage. Sous chargement cyclique, ils sont sensibles au phénomène d'adoucissement, qui se caractérise par une perte de la résistance mécanique. L'étude de ce phénomène est motivée par l'objectif lié à l'augmentation des durées de vie des composants. En effet, les aciers martensitiques revenus possèdent une durée de vie plus courte en fatigue sous air que sous vide [Kim and Weertman, 1988] et en environnement sodium [Kannan et al., 2009]. Dans ces deux derniers types d'environnement, la phase d'adoucissement cyclique se trouve donc prolongée. De plus, celle-ci est d'autant plus prononcée que la température est élevée [Armas et al., 2004]. Enfin, des résultats récents ont montré que la tenue mécanique en fluage chutait lorsque le matériau était soumis à un précyclage en fatigue [Fournier et al., 2011a], soulignant ainsi l'effet néfaste de l'adoucissement cyclique pour les applications industrielles visées. L'étude de l'influence des facteurs expérimentaux sur ce phénomène se révèle donc nécessaire. Peu abordés dans la littérature, nous avons choisi de nous concentrer sur les effets de la vitesse de déformation lors des essais cycliques en traction/compression à haute tem-

pérature.

Notre premier objectif est donc d'étudier les propriétés mécaniques de ces aciers à haute température. Dans ce cadre, des essais de traction, de fatigue, de fluage et de fatigue-fluage ont été menés sur un acier de Grade 92 afin de mettre en évidence le comportement mécanique macroscopique de cet acier sous diverses sollicitations. Dans un second temps, des observations de la microstructure ont été effectuées sur le matériau après chargement monotone ou cyclique continu dans le but de quantifier les modifications de la microstructure et de proposer des mécanismes de déformation en accord avec les observations.

Le second objectif consiste en l'intégration de ces mécanismes physiques au sein d'un modèle prédictif du comportement mécanique et de l'évolution de la microstructure sous chargement monotone et/ou cyclique. Les prédictions de ce modèle sont ensuite comparées aux données expérimentales précédemment obtenues puis discutées.

Avant d'entamer cette étude, nous allons poursuivre cette introduction en présentant succinctement la famille des aciers martensitiques revenus à 9 % de chrome. Nous accorderons une importance particulière à la description de leur microstructure, point de départ de la compréhension des mécanismes de déformation.

1.2 Les aciers martensitiques revenus - Présentation du matériau de l'étude

1.2.1 Composition chimique et traitements thermiques

1.2.1.1 Composition chimique du matériau de l'étude

La famille des aciers à 9%Cr possède un historique relativement riche en termes d'évolution de composition. Cette richesse se traduit par des optimisations successives en divers éléments d'alliage, dans le but de répondre à des critères de performances mécaniques toujours plus élevés essentiellement dans le domaine du fluage. Dans le présent travail de recherche, nous nous sommes particulièrement intéressés à un tube en acier de Grade 92 fourni par Vallourec & Mannesmann Tubes France, dont la composition chimique est reportée dans le Tableau 1.1.

C	N	Cr	Mo	W	Mn	V	Si	Ni	Al	Nb	P	S	B
0.12	0.046	8.68	0.37	1.59	0.54	0.19	0.23	0.26	0.02	0.06	0.014	0.004	0.002

Tab. 1.1. Composition chimique en pourcentage massique de l'acier de Grade 92 étudié.

Nous allons maintenant présenter les traitements thermiques appliqués à l'acier. Ces derniers influencent grandement sa microstructure et donc son comportement mécanique sous sollicitation.

1.2.1.2 Traitements thermiques appliqués au matériau de l'étude

Généralement, les traitements thermiques appliqués aux aciers 9%Cr se résument en une austénitisation, une trempe et un revenu, les paramètres de traitement pouvant différer d'un produit à l'autre en termes de durée ou de température. Dans le cas du tube en acier de Grade 92 étudié, l'étape d'austénitisation a été effectuée à 1060 ℃ pendant 30 minutes, suivie par une trempe à l'air et enfin par un revenu à 770 ℃ pendant 60 minutes.

Les traitements thermiques appliqués lors de l'étape d'élaboration permettent de former la microstructure de l'acier et conditionnent ainsi ses propriétés mécaniques macroscopiques. Ainsi, toute modification des paramètres inhérents aux traitements thermiques induit une transformation de la microstructure du matériau final, et *in fine*, une variation de ses propriétés mécaniques. Les effets de chaque traitement thermique appliqué aux aciers 9%Cr-1%Mo-NbV (composition typique de l'acier de Grade 91, proche du Grade 92) ont été largement étudiés, et sont résumés ci-dessous [Brachet, 1991, Bhadeshia, 2001] :

Austénitisation : en termes de transformations de phase, le domaine austénitique monophasé se situe approximativement entre 900 et 1275 ℃ pour la nuance 9%Cr-1%Mo optimisée en niobium et vanadium. La taille de grain austénitique est déterminée au cours de cette étape. Celle-ci augmente avec la température d'austénitisation, comme le montre la courbe de la Fig. 1.1. Aussi, elle est largement influencée par la présence de précipités au sein de la matrice austénitique qui vont permettre d'épingler les joints de grains et par conséquent, de limiter la croissance des grains austénitiques. Brachet [Brachet, 1991] et Ennis et Czyrska-Filemonowicz [Ennis and Czyrska-Filemonowicz, 2003] ont pu observer une mise en solution des précipités de type $M_{23}C_6$ pour une température supérieure à 1000 ℃. En revanche, les précipités de type carbonitrure de niobium MX restent stables jusqu'à 1100 ℃, entrainant la formation de grains austénitiques de taille fine au cours de l'austénitisation à 1060 ℃.

Trempe : cette étape consiste à transformer la totalité de l'austénite en martensite. Cette transformation de phase est extrêmement rapide et se produit sans diffusion, induisant l'apparition de fortes contraintes internes au sein de la microstructure. De ce fait, l'acier trempé renferme un grand nombre de défauts (forte densité de dislocations par exemple) et présente une dureté particulièrement élevée. En outre, Eggeler et al. [Eggeler et al., 1987] rapporte qu'à ce stade du traitement thermique, les carbures du type $M_{23}C_6$ n'ont pas encore précipité, phénomène justifié par le caractère non diffusif de la transformation martensitique.

Revenu : dans l'industrie, les températures de revenu de ces aciers se situent entre 600 et 800 ℃. A ces températures, Brachet a pu constater une généralisation de la précipitation des carbures $M_{23}C_6$ aux interfaces (anciens joints de grains austénitiques et joints de lattes) et un adoucissement important de l'acier [Brachet, 1991]. Ces phénomènes sont directement liés à la diminution du nombre de défauts dans le matériau. D'une part, nous assistons à une diminution des défauts dits ponctuels, à savoir les atomes interstitiels (notamment carbone) qui diffusent dans la martensite pour précipiter aux interfaces sous la forme de carbures $M_{23}C_6$. D'autre part, la restauration entraine une forte diminution de la densité de dislocations à l'intérieur des sous-grains et la formation de parois entre ces sous-grains [Guttmann, 1974].

1.2.2 Microstructure des aciers martensitiques revenus

1.2.2.1 Les différentes échelles de la microstructure

Il convient tout d'abord de décrire la microstructure typique des aciers martensitique revenus. Celle-ci comporte plusieurs échelles imbriquées, liées par des relations d'orientation cristallographique [Marder and Marder, 1969], résultat complexe de la succession des trois étapes composant le traitement thermique. Cette microstructure, shématisée sur la Fig. 1.2, peut être décrite comme suit :

Ancien grain austénitique : il s'agit de la plus grande échelle au sein de la microstructure. Sa

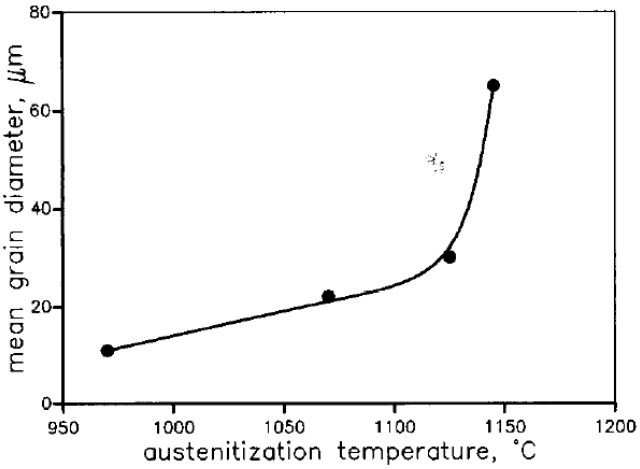

Fig. 1.1. Evolution de la taille des anciens grains austénitiques d'un acier de Grade 92 après 2 heures d'austénitisation à différentes températures [Ennis et al., 1997].

taille est typiquement comprise entre 10 et 60 µm [Ennis et al., 1997, Eggeler and Dlouhý, 2005]. Pour notre matériau d'étude, elle est comprise entre 20 et 30 µm.

Paquet : cette sous-structure est composée d'un ensemble de blocs ayant un plan $\{110\}_\alpha$ approximativement parallèles au plan $\{111\}_\gamma$ de l'austénite. Dans un paquet, les lattes sont approximativement parallèles les unes aux autres.

Bloc : avant revenu, il est défini par un ensemble de lattes de martensite faiblement désorientées les unes par rapport aux autres et allongées approximativement selon une direction $\langle 110\rangle_\gamma$ de l'austénite.

Latte : il s'agit de l'échelle la plus fine avant revenu. Après revenu, en toute rigueur, cette structure "disparaît" avec l'apparition des sous-grains.

Sous-grain : cette échelle apparaît après revenu, lors de la réorganisation de la microstructure martensitique. Comme nous le précisons plus loin dans ce chapitre, les sous-grains sont quasiment composés de ferrite et sont généralement faiblement désorientés entre eux. Une latte peut être considérée comme un alignement de sous-grains. Leur distribution de taille est d'allure lognormale [Polcik et al., 1999, Dronhofer et al., 2003] et leur taille moyenne est comprise entre 0,2 et 0,5 µm. Au sein du même bloc, ils sont désorientés de moins de 5 ° entre eux [Dronhofer et al., 2003, Tak et al., 2009].

Pour comprendre au mieux la structure complexe des aciers 9%Cr, il est nécessaire de rappeler la nature de la transformation de phase qui l'engendre.

1.2.2.2 La trempe de l'austénite à la martensite

À partir du domaine austénitique stable à haute température, l'application d'un refroidissement rapide par trempe de l'acier permet d'obtenir une nouvelle phase appelée *martensite*, de même composition que la phase mère, l'austénite. Cette transformation est très différente de la transformation perlitique et de la transformation bainitique car la rapidité du refroissement exclut toute possibilité de mise en place des mécanismes de diffusion.

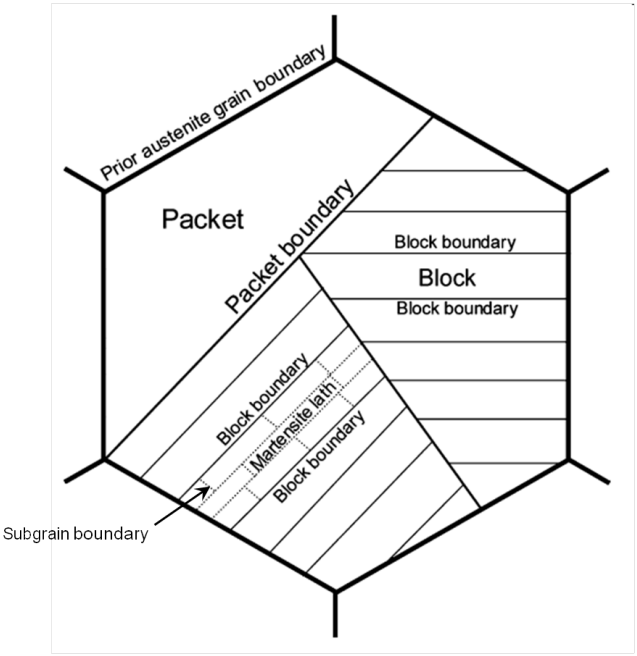

Fig. 1.2. Schéma de la microstruture d'un acier martensitique représentant les multiples échelles imbriquées. Modifié d'après une figure de [Kitahara et al., 2006].

La transformation martensitique rend impossible la diffusion des atomes de carbone lors du changement de phase. Ils ne peuvent donc pas se répartir entre les deux phases présentes sur le diagramme d'équilibre, à savoir la ferrite et la cémentite. D'un point de vue cristallographique, ils vont devoir demeurer en place lors du passage de la phase austénitique de structure cubique à faces centrées (c.f.c.) à la phase martensitique de structure cubique centrée (c.c.). La structure c.f.c. accepte une grande quantité d'atomes de carbone dans les sites octaédriques et tétraédriques. Ce n'est pas le cas de la structure c.c. : l'absence de diffusion va dès lors engendrer une sursaturation en carbone au sein de cette dernière. Plus précisément, les atomes de carbone vont occuper préférentiellement les sites octaédriques de la structure c.c. selon l'axe Oz de la maille, induisant une déformation tétragonale selon l'axe [001]. En toute rigueur, il faudrait alors parler de structure quadratique, et non cubique centrée. Cependant, la structure de la martensite reste très proche d'une structure cubique centrée pour une teneur en carbone inférieure à 0,2 % en masse. Dans le cadre de notre étude, nous pourrons donc considérer la martensite comme une structure cubique centrée avec les symétries associées.

La passage de la phase "mère" austénitique à la la phase "fille" martensitique s'effectue par un mouvement coopératif des atomes à vitesse élevée (de l'ordre de la vitesse du son, soit environ 10^3 m/s). Le mécanisme cristallographique qui permet cette transformation est du type cisaillement, permettant l'observation de relations d'orientations entre la phase austénitique et la phase martensitique. Celles-ci sont particulièrement bien décrites dans la littérature [Bhadeshia, 2001, Fournier, 2007], et il conviendra de retenir que les aciers à 9%Cr ne sont pas texturés si nous considérons deux anciens grains auténitiques différents.

Après la trempe, la structure martensitique de l'acier lui confère un caractère fragile et une dureté élevée (supérieure à 500 HV [Eggeler et al., 1987]). Ce phénomène est principalement dû aux fortes contraintes internes nées de la transformation martensitique. En effet, la cinétique de changement de phase particulièrement élevée induit une croissance rapide des lattes, provocant une rencontre violente entre ces dernières durant leur croissance. Celles-ci doivent dès lors absorber cette quantité d'énergie non négligeable sous forme de déformation : de nombreux défauts cristallographiques sont créés au

sein même de la latte, en particulier des dislocations.

1.2.2.3 De la martensite à la martensite revenue

Le traitement de revenu permet alors d'agir sur la microstructure de l'acier de manière à diminuer les contraintes internes. En effet, le maintien en température du matériau (entre 600 et 800 ℃) pendant un temps donné permet la mise en place de mécanismes microstructuraux thermiquement activés, tels que la *diffusion* et la *restauration* [Guttmann, 1974, Ennis et al., 1997]. Nous assistons donc à un réarrangement de la microstructure qui, selon les lois de la thermodynamique, tend à minimiser l'énergie du système.

L'activation des mécanismes de diffusion est à l'origine de l'apparition de plusieurs types de précipités, notamment $M_{23}C_6$, et ceci rapidement après le début de l'étape de revenu [Eggeler et al., 1987]. En termes de localisation, la germination des carbures se produit principalement aux interfaces, c'est-à-dire aux différents types de joints qui composent la microstructure (joints d'anciens grains austénitiques, de paquets, de blocs et de lattes). Ce phénomène s'explique aisément en considérant les lois thermodynamiques de germination et de ségrégation de phase [Béranger et al., 1994]. Nous verrons plus précisément dans la partie 1.2.2.7 les différentes caractéristiques de ces précipités, telles que leur composition, leur structure et leur taille.

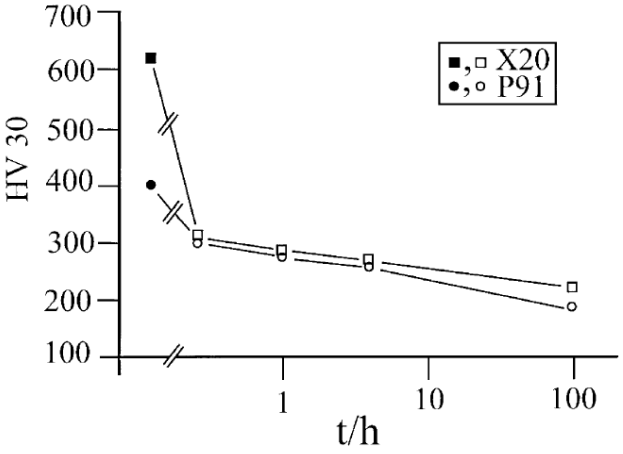

Fig. 1.3. Évolution de la dureté de deux aciers ferrito-martensitiques avec 9 % (P91) et 12 % (X20) de chrome pendant une étape de revenu à 750 ℃ après austénitisation et trempe. Les symboles pleins représentent un état martensitique (après austénitisation et trempe) et les symboles évidés un état ferritique (après revenu) [Pešička et al., 2003].

La restauration est le second phénomène important se produisant lors de l'étape de revenu. Ce phénomène se traduit par une diminution du nombre de défauts dans le matériau, induisant une réduction des contraintes internes en minimisant l'énergie du système. Nous assistons donc à un réarrangement de la configuration de la structure, sans émergence d'une nouvelle phase dans la matrice. Il est utile de remarquer que l'étape de revenu entraine une diminution de la dureté, particulièrement tôt lors de la transformation, comme le montre la Fig. 1.3 [Pešička et al., 2003]. L'activation thermique de la montée, rendue possible par la diffusion de lacunes, permet aux dislocations d'interagir entre elles et nous pouvons alors évoquer deux phénomènes remarquables :

- l'*annihilation*, si l'interaction se produit entre deux dislocations suffisament proches de même ligne de direction L mais de vecteurs de Burgers $\vec{b}$ opposés.

- le *réarrangement*, qui se traduit par une mise en ordre des dislocations. Ce phénomène réduit l'énergie du système en organisant les dislocations de manière à minimiser le champ de contrainte engendré par chacune d'entre elles. Ce mécanisme conduit à la formation de sous-joints faiblement désorientés constitués de réseaux réguliers de dislocations (voir Fig. 1.4).

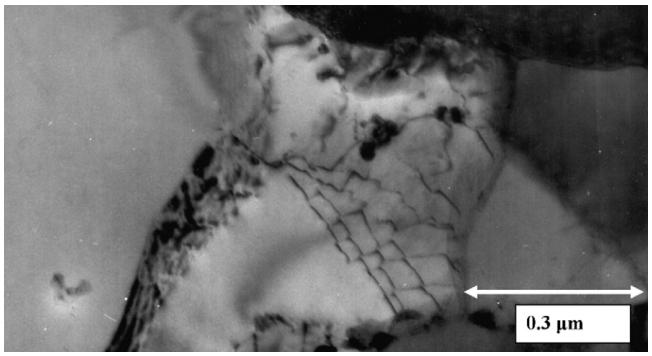

Fig. 1.4. Image MET montrant le mécanisme de "knitting-out" d'un sous-joint de faible désorientation (acier Grade 91 soumis à un essai de fatigue-fluage à 600 ℃ [Sauzay et al., 2008].

Ce deuxième point permet d'expliquer l'existence des sous-grains, échelle la plus fine de la microstructure du matériau considéré. En effet, le réarrangement des dislocations au sein de la latte les amène à s'espacer régulièrement les unes des autres pour former des parois de dislocations. Celles-ci se caractérisent par une désorientation de part et d'autre du réseau, partageant ainsi les lattes en sous-grains. Ce phénomène est nommé *polygonisation* [François et al., 1995a].

En termes de microstructure, la division en sous-grains des lattes de martensite lors de l'étape de revenu ne nous permet plus de parler de structure martensitique. En effet, comme le souligne Hald, ces sous-grains sont composés de ferrite [Hald, 2008] et sont aussi appelés "micrograins" [Dronhofer et al., 2003, Pešička et al., 2004, Tak et al., 2009]. Comme la microstructure est proche de celle de la martensite en lattes, nous lui préférerons donc l'appellation de *martensite revenue*.

Cette courte description de la structure martensitique revenue des aciers 9%Cr nous amène donc à entrevoir la complexité des mécanismes induit lors de la déformation à haute température. En se basant sur le mouvement des dislocations comme moteur de la déformation viscoplastique, il apparaît clairement que l'étude des mécanismes de déformation doit se baser sur les diverses interactions de ces dernières avec les éléments de la microstructure.

1.2.2.4 Densité de dislocations

Les dislocations apparaissent comme le point central de l'étude des mécanismes de déformation. Dans cette optique, leur quantification et leur localisation au sein de la structure sont essentielles. Pour commencer, nous avons donc réuni dans le Tableau 1.2 plusieurs valeurs de densité de dislocations relevées dans la littérature pour cette famille d'aciers, à l'état de réception.

Si la température d'austénitisation n'a aucun impact significatif sur la densité de dislocations, la température de revenu va influencer notablement le processus de restauration. En effet, en passant d'une température de 715 à 835 ℃, la densité de dislocations chute d'un facteur proche de 5. La maîtrise des conditions de revenu est donc particulièrement importante pour le contrôle de l'adoucissement du matériau.

Traitements thermiques	Densité de dislocations (10^{14} m^{-2})	Références
1070℃ (2h) - 715℃ (2h)	$9,0 \pm 1,0$	
1070℃ (2h) - 775℃ (2h)	$7,0 \pm 0,9$	[Ennis et al., 1997]
1070℃ (2h) - 835℃ (2h)	$2,3 \pm 0,6$	
970℃ (2h) - 775℃ (2h)	$8,7 \pm 1,2$	[Ennis et al., 2000]
1070℃ (2h) - 775℃ (2h)	$7,9 \pm 0,8$	[Ennis and Czyrska-Filemonowicz, 2003]

Tab. 1.2. Densités de dislocations mesurées au MET par la technique d'intersection des segments, dans l'acier de Grade 92.

1.2.2.5 Nature des dislocations

La nature des dislocations est un paramètre important dans l'étude des mécanismes de déformation. Il existe en effet schématiquement deux grands types de dislocations : les dislocations *coin* et les dislocations *vis*. Par définition, une dislocation coin se caractérise par un vecteur de Burgers $\vec{b}$ orthogonal à sa ligne $\overrightarrow{L}$ alors que la dislocation vis se caractérise par un vecteur de Burgers parallèle à sa ligne. Au sein de la microstructure, il est fréquent de rencontrer des dislocations dites *mixtes*, c'est-à-dire dont le vecteur de Burgers forme un angle compris entre 0 et 90 ° avec la ligne de la dislocation.

Outre leur nature, les dislocations présentes au sein d'un acier martensitique revenu se divisent en deux grandes familles [Pešička et al., 2004] :

- *Les dislocations mobiles* ("free dislocations" [Eggeler, 1989]) qui, par définition, se déplacent lors de la déformation viscoplastique. C'est lors de ce mouvement qu'elles vont interagir avec des éléments présents dans la microstructure (autres dislocations composant la forêt, atomes ou amas d'atomes en solution solide, précipités, sous-joints de grains...).
- *Les dislocations composant les sous-joints* dont nous avons évoqué l'existence dans la partie 1.2.2.3. Réarrangées, elles forment les sous-joints de faible désorientation [Read and Shockley, 1950]. Ces sous-joints sont composé en générale de deux familles de dislocations [Guttmann, 1974] de caractère vis [Guétaz et al., 2003]. Nous verrons qu'elles jouent un rôle important dans la croissance de la taille des sous-grains, observée lors de sollicitations en fatigue, fluage et fatigue-fluage.

En termes de population, il est donc possible de répartir la densité de dislocations totale entre la densité de dislocations mobiles et la densité de dislocations composant les sous-joints de grains. Globalement, la microstructure martensitique revenue de l'acier de Grade 92 se caractérise par une forte densité de dislocations, de l'ordre de 10^{14} m^{-2} après le revenu : [Pešička et al., 2004] pour le X20, [Sauzay et al., 2005] pour le Grade 91, [Giordana et al., 2011] pour l'EUROFER 97.

Si nous nous intéressons maintenant à la nature des dislocations, chacune de ces deux populations peut alors être définie comme un ensemble de dislocations de type coin, de type vis et de type mixte. L'observation des dislocations au sein des aciers nous rapporte l'existence de boucles, phénomène dû à l'ancrage sur deux obstacles (atomes ou clusters d'atomes en solution solide, précipités, joints de grains...) de la dislocation qui continue à glisser entre ces deux derniers sous l'effet de la contrainte appliquée (Fig. 1.5). Nous pouvons dès lors comprendre aisément que le caractère de la dislocation varie le long de sa ligne de direction, démontrant ainsi qu'il n'existe pas de dislocations purement coin ou purement vis.

Lors de leur mouvement, les dislocations mobiles vont interagir avec différents éléments présents dans la matrice, notamment avec les précipités et les atomes en solution solide. Comme la forêt

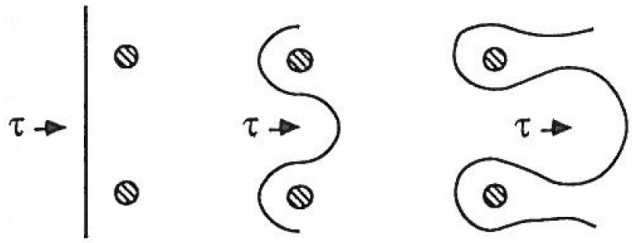

Fig. 1.5. Schéma représentant l'évolution du caractère d'une dislocation lorsqu'elle interagit avec des précipités sous l'effet d'un cisaillement τ [François et al., 1995a].

de dislocations, les précipités, et plus rarement les inclusions et les cavités présentes dans les aciers 9%Cr, se comportent comme des obstacles au mouvement des dislocations. Ils ont donc une influence remarquable sur le comportement mécanique de l'acier et nous présentons maintenant brièvement ces trois types d'obstacles en s'attachant essentiellement au cas de l'acier de Grade 92 à l'état revenu.

1.2.2.6 Inclusions et cavités

A la différence des précipités, les inclusions sont des particules étrangères s'insérant dans le matériau lors de son élaboration. Leur composition chimique est donc indépendante de celle du métal. Peu d'études sont consacrées à leur influence sur la déformation du fait de leur faible fraction volumique dans le matériau (moins de 5×10^{-4} d'après Zhang [Zhang et al., 1991]). Néanmoins, les inclusions se révèlent être redoutables vis-à-vis de la résistance du matériau à la rupture. De plus, ces particules ont un caractère incohérent vis-à-vis de la matrice. Leur aptitude à la décohésion entraîne la formation de cavités de taille non négligeable pour des valeurs importantes de déformation, comme le montre la Fig. 1.6.

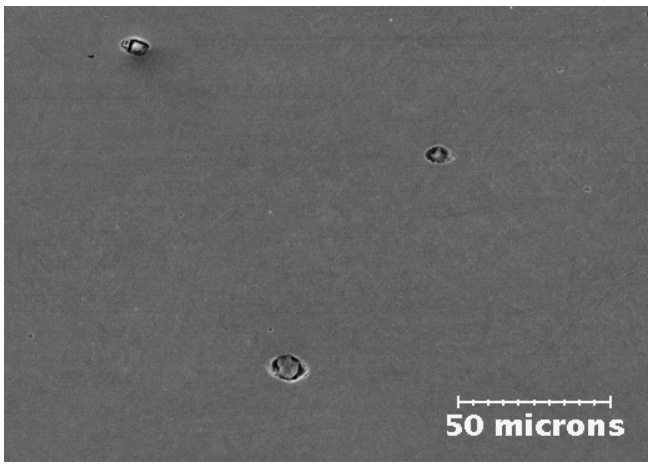

Fig. 1.6. Exemple de décohésion inclusionnaire dans l'acier de Grade 92 étudié [Giroux et al., 2009].

La présence d'inclusions et de cavités dégrade notablement les propriétés mécaniques de l'acier. Cependant, nous n'aborderons pas leur influence sur la déformation dans cette étude. Il apparaît en effet que leurs interactions avec les dislocations mobiles sont limitées du fait de leur très faible fraction volumique et des faibles niveaux de déformation testés.

1.2.2.7 Nature des précipités

La nature des précipités est particulièrement influencée par deux paramètres : la teneur en éléments d'addition présents dans l'alliage et les traitements thermiques appliqués [Brachet, 1991, Götz and Blum, 2003]. Dans le cas des aciers de Grades 91 et 92 à l'état revenu, il existe principalement trois types de précipités. Ces derniers sont listés dans le Tableau 1.3.

Aciers	Précipités	Formules	Remarques
P91	$M_{23}C_6$	$(Cr,Fe,Mo)_{23}C_6$	Précipitent pendant l'étape de revenu
	MX primaires	(Nb,V)(N,C)	Non dissous pendant l'étape d'austénitisation
	MX	(V,Nb)(N,C)	Précipitent pendant l'étape de revenu
P92	$M_{23}C_6$	$(Cr,Fe,Mo,W)_{23}C_6$	Précipitent pendant l'étape de revenu
	MX primaires	(Nb,V)(N,C)	Non dissous pendant l'étape d'austénitisation
	MX	(V,Nb)(N,C)	Précipitent pendant l'étape de revenu

Tab. 1.3. Principaux précipités dans les aciers de Grade 91 et 92 [Hald, 2008].

Ces trois types de précipités sont les plus courants au sein de la matrice, puisqu'ils représentent au moins 96 % de la population totale : en volume, les précipités du type $M_{23}C_6$ sont de loin les plus communs (85 à 90 %), suivis par les V(N,C) (10 à 13%) et enfin par les Nb(C,N) (1 à 2%) [Gieseke et al., 1993]. Ennis [Ennis et al., 1997] insiste sur le fait que les précipités de type MX apparaissent dans un ordre défini. Les précipités Nb(C,N) de forme sphéroïdale ne sont pas dissous pendant l'étape d'auténitisation et certains d'entre eux peuvent servir de sites de germination à des précipités V(N,C) en forme de lamelles lors du revenu. Dans ce cas, nous pouvons observer des précipités de formes et de compositions complexes, couramment nommés "V-wings" [Ennis et al., 1997], comme le montre la Fig. 1.7.

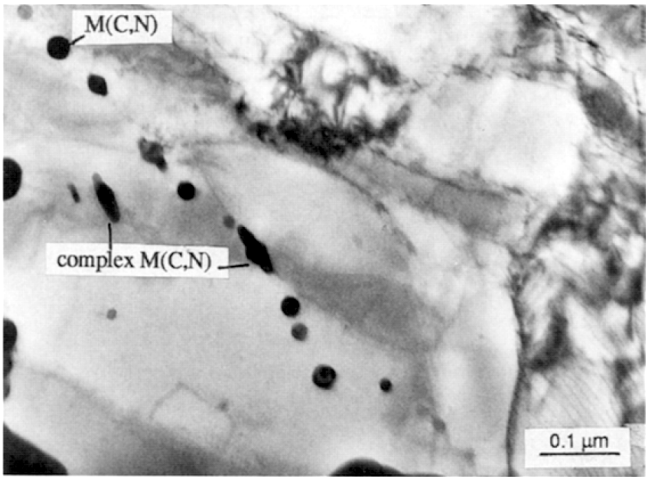

Fig. 1.7. Observation en microscopie électronique en transmission d'un acier de Grade 92 (normalisé à 970 ℃ et revenu à 775 ℃) montrant des précipités sphériques M(C,N) riches en Nb et des précipités complexes de M(C,N) [Ennis et al., 1997].

Le reste des précipités, présents en faible quantité dans la matrice, sont de composition chimique et stœchiométrie variées : M_2X, M_3C, M_7C_3... Leur présence dépend essentiellement des caractéristiques des traitements thermiques appliqués et de la composition chimique des aciers étudiés. Enfin, d'autres phases telles que les phases de Laves et les phases-Z peuvent apparaitre dans ces aciers [Panait, 2010].

1.2.2.8 Taille des précipités

Tout comme leur composition chimique, la taille des précipités est directement influencée par les traitements thermiques appliqués. Plusieurs valeurs pour diverses nuances d'aciers 9%Cr ont été relevées dans la littérature et il est intéressant de retenir les points suivants :

- Les précipités de type MX ont un diamètre moyen compris entre 5 et 60 nm suivant le traitement thermique. Pour le Grade 92 avec un traitement thermique proche de celui de la présente étude, le diamètre moyen des MX se situe entre 15 et 20 nm [Ennis et al., 1997,Hättestrand and Andrén, 2001,Park et al., 2001,Gustafson and Hättestrand, 2002,Ennis and Czyrska-Filemonowicz, 2003]. Ces précipités résistent à la coalescence puisque leur diamètre moyen augmente de quelques nanomètres lorsque la température de revenu augmente de 715 à 835℃. Ils sont incohérents avec la matrice dès que leur taille dépasse 10 nm, ce qui est le cas du matériau de l'étude.
- Les précipités de type $M_{23}C_6$ ont un diamètre moyen compris entre 50 et 350 nm suivant le traitement thermique [Eggeler et al., 1987, Eggeler, 1989, Park et al., 2001, Götz and Blum, 2003]. Pour le Grade 92 avec un traitement thermique proche de celui de la présente étude, le diamètre moyen des $M_{23}C_6$ se situe entre 70 et 100 nm [Ennis et al., 1997, Hättestrand and Andrén, 2001, Gustafson and Hättestrand, 2002, Ennis and Czyrska-Filemonowicz, 2003]. Ce type de précipité résiste moins bien à la coalescence que les MX puisque leur diamètre moyen augmente de 72 à 89 nm lorsque la température de revenu augmente de 715 à 775℃.
- Les distributions de taille de précipités sont d'allure log-normale [Eggeler, 1989, Cerri et al., 1998, Götz and Blum, 2003]
- Les précipités $M_{23}C_6$ ayant germé sur ou à proximité des joints d'anciens grains austénitiques ont un diamètre moyen deux fois plus important que ceux ayant germé sur les sous-joints [Eggeler, 1989].

Ce dernier point nous mène directement à l'étude de la localisation des précipités dans la matrice.

1.2.2.9 Localisation des précipités

La localisation des précipités est intimement liée à l'étape du traitement thermique durant laquelle ils sont formés. Ainsi, les observations microstructurales publiées dans la littérature conduisent généralement aux deux conclusions suivantes :

- Les précipités de type $M_{23}C_6$ se situent sur les anciens joints de grains auténitiques pour les plus volumineux, et les joints de paquets, blocs, lattes et sous-joints pour les autres [Eggeler, 1989, Eggeler and Dlouhý, 2005].
- Les précipités de type MX, de taille plus faible que les précipités $M_{23}C_6$, sont dispersés au sein même des sous-grains et sur l'ensemble des anciens joints de grains auténitiques, de paquets, de blocs, de lattes et de sous-grains [Abe et al., 2007].

La localisation des précipités de types $M_{23}C_6$ et MX est clairement schématisée sur la Fig. 1.8.

Cette courte description de la microstructure des aciers martensitiques revenus nous a permis d'entrevoir très succinctement les principaux éléments sur lesquels repose une grande majorité des

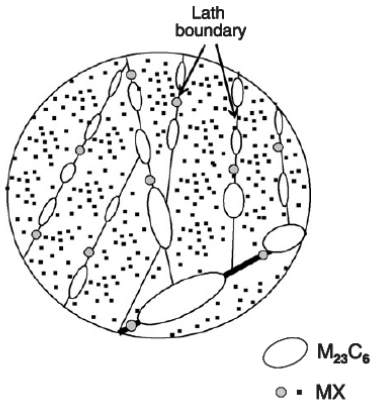

Fig. 1.8. Schéma de la distribution spatiale des précipités $M_{23}C_6$ et MX au sein de la microstructure pour ce qui est des joints de paquets, de blocs et de lattes [Abe et al., 2007].

modifications observées après exposition du matériau à haute température, avec ou sans sollicitation mécanique. Dans le chapitre suivant, nous allons étudier le comportement mécanique de l'acier de Grade 92 au cours d'essais de traction uniaxiale puis observer les évolutions de la microstructure induites par ce type de sollicitation monotone à haute témpérature.

Chapter 2

Mechanical and microstructural stability of P92 steel under uniaxial tension at high temperature

This second chapter focuses on the mechanical behaviour of Grade 92 steel during monotonic tensile tests at 550 ℃. Three phenomena are studied in order to understand the physical mechanisms inducing the weak softening stage observed: mechanical instability (necking), damage and subgrain size evolution. Two analytical models predicting respectively the beginning of the mechanical instability and the subgrain growth are proposed. This chapter was published in Materials Science and Engineering A - Structural Materials Properties Microstructure and Processing [Giroux et al., 2010].

Ce second chapitre est consacré à l'étude du comportement mécanique de l'acier Grade 92 en traction monotone à 550 ℃. Trois phénomènes sont étudiés afin de comprendre et quantifier les mécanismes à l'origine du léger adoucissement macroscopique mesuré : l'instabilité mécanique liée à la striction, l'endommagement ductile et l'évolution de la taille des sous-grains. Deux modèles analytiques prédisant respectivement l'apparition de l'instabilité mécanique et la croissance des sous-grains sont proposés. Ce chapitre a fait l'objet d'une publication dans le journal Materials Science and Engineering A - Structural Materials Properties Microstructure and Processing [Giroux et al., 2010].

Contents

Abstract (in French) **35**
2.1 Introduction **37**
2.2 Material and experimental procedure **37**
2.2.1 Material 37
2.2.2 Tensile tests 37
2.2.3 Metallographic investigation of the tensile specimens after the tests 38
2.3 Results of tensile tests carried out up to fracture **39**
2.4 Damage assessment **40**
2.5 Necking: experimental results and modelling **42**
2.5.1 Interrupted tensile tests and onset of macroscopic necking 42
2.5.2 Prediction of mechanical instability and of fracture elongation 45
2.6 Microstructural evolution of the matrix during tensile deformation **51**
2.6.1 Experimental results: EBSD and TEM investigations 51
2.6.2 Modelling of microstructural evolution during straining 51

2.7 Conclusions 57

Résumé

Ce chapitre présente les résultats de l'étude des propriétés mécaniques en traction monotone à 550 ℃ sous air sur l'acier Grade 92. Ces tests ont été effectués sur des éprouvettes cylindriques de 30 mm de longueur utile et 4 mm de diamètre, prélevées à mi-épaisseur dans le sens longitudinal d'un tube de 219 mm de diamètre extérieur et de 20 mm d'épaisseur. Les vitesses étudiées varient de $2{,}5 \times 10^{-3}$ s^{-1} à $2{,}5 \times 10^{-6}$ s^{-1} et sont controlées par le déplacement de la traverse. La température est mesurée avec une précision de ±3 ℃ grâce à deux thermocouples attachés à la partie utile de l'éprouvette .

Les courbes conventionnelles contrainte-déformation en traction monotone de l'acier Grade 92 à 550 ℃ se décomposent en trois partie. La première étape correspond à un faible écrouissage. Elle est suivie d'une longue et stable décroissance de la contrainte, d'autant plus importante que la vitesse de déformation diminue. Enfin la dernière étape correspond à un changement de la pente d'adoucissement, conduisant à la rupture de l'éprouvette.

Trois phénomènes ont été étudiés dans le but de comprendre l'adoucissement mécanique de ce type d'acier : l'endommagement, la striction (instabilité mécanique) et l'évolution de la microstructure.

Des observations MEB ont été effectuées sur le matériau de réception et sur une éprouvette loin de la zone de rupture, après un essai de traction à 550 ℃ avec une vitesse de déformation de $2{,}5 \times 10^{-4}$ s^{-1}. Dans les deux échantillons, la taille maximale des cavités observées n'excède pas 5 µm. Ce résultat suggère que l'endommagement a une influence négligeable sur l'adoucissement du matériau.

Afin d'étudier l'influence de la striction sur le comportement mécanique, 7 essais de traction conduits à 550 ℃ avec une vitesse de déformation de $2{,}5 \times 10^{-4}$ s^{-1} ont été interrompus pour différentes valeurs de déformation axiale. Une étude profilométrique de ces éprouvettes non rompues a démontrée que la striction macroscopique apparaît à la fin de la longue et stable étape de décroissance de la contrainte. L'utilisation du critère établi par Hart [Hart, 1967] permet de prédir l'apparition de l'instabilité mécanique pour des valeurs de déformation correspondant à la fin de la première étape d'écrouissage. Ainsi, si la striction macroscopique est détectée après l'étape d'adoucissement linéaire de la contrainte, des instabilités mécaniques apparaissent probablement plus tôt au cours de la déformation homogène.

Les observations effectuées à l'EBSD n'ont pas permis de mesurer de modifications significatives de la microstructure au cours de la déformation uniaxiale. En revanche, les mesures effectuées sur les observations MET ont mis en évidence une augmentation de la taille moyenne des sous-grains de près de 21 % entre le matériau à l'état de réception et l'échantillon prélevé sur l'éprouvette loin de la zone de rupture, après un essai de traction à 550 ℃ et une vitesse de déformation de $2{,}5 \times 10^{-4}$ s^{-1}. Cette croissance de la taille des sous-grains contribue à l'adoucissement mesuré du matériau. Un modèle analytique, fondé sur la disparition des sous-joints au cours de la déformation [Sauzay, 2009] est proposé dans ce chapitre. La prédiction de la croissance des sous-grains est cependant surestimée et nécessite une meilleure prise en compte de la nature des sous-joints et de l'activation des systèmes de glissement au sein des blocs de martensite revenue. Ces améliorations sont discutées au chapitre 4.

2.1 Introduction

9-12%Cr creep resistant ferritic-martensitic steels possess high strength and high thermal conductivity, low thermal expansion, good corrosion resistance and good mechanical properties after irradiation [Yi et al., 2006, Greeff et al., 2000, Shamardin et al., 1999, Toloczko et al., 2003, Henry et al., 2003]. These characteristics permit to consider them as candidate materials for high temperature structural components of Generation IV nuclear power plants. However, 9-12%Cr steels are sensitive to softening during low-cycle fatigue, creep and creep-fatigue at high temperature [Shankar et al., 2006, Park et al., 2001, Polcik et al., 1999]. Several studies [Eggeler et al., 1987, Sawada et al., 1999, Cerri et al., 1998] showed that this softening behaviour is due to an increase in size of the microstructure, as revealed by transmission electron microscopy (TEM) or electron backscatter diffraction (EBSD) measurements. Although such mechanisms are difficult to observe in-situ during fatigue, creep and creep-fatigue tests, Sauzay [Sauzay, 2009] proposed a model based on destruction of the low-angle boundaries in order to predict coarsening of the matrix microstructure. During tensile tests at high temperature, a softening behaviour is also observed, characterized by low maximum homogeneous elongation compared to the fracture elongation [Milička and Dobeš, 2006].

In the following, the softening behaviour of an ASME Grade 92 (9%Cr-0.5%Mo-1.8%W) steel during uniaxial tension at high temperature is studied. Tensile tests were carried out at 550 ℃, a typical operating temperature of future components of nuclear power plants, in order to analyse the influence of three potential origins of the softening behaviour: damage development, mechanical instability (necking) and microstructural evolution. For each studied phenomenon, simple analytical models adapted from fatigue, creep and creep-fatigue studies are proposed in order to predict the material behaviour during uniaxial tension at high temperature.

2.2 Material and experimental procedure

2.2.1 Material

Tensile tests were conducted on P92 specimens taken out of a pipe of 219 mm in outer diameter and 20 mm in thickness. Its chemical composition is given in Table 2.1. The as-received material was austenized at 1060 ℃ for 30 minutes, quenched and tempered at 770 ℃ for 60 minutes.

C	N	Cr	Mo	W	Mn	V	Si	Ni	Al	Nb	P	S	B
0.12	0.046	8.68	0.37	1.59	0.54	0.19	0.23	0.26	0.02	0.06	0.014	0.004	0.002

Tab. 2.1. Chemical composition of P92 steel (in wt%).

2.2.2 Tensile tests

All tensile tests were performed in laboratory air at 550 ℃ with an INSTRON 4507 vertical tensile testing machine. Tests were conducted on smooth cylindrical specimens with 30 mm in gauge length and 4 mm in gauge diameter, machined from the mid-thickness of the pipe along its longitudinal axis. High temperature tensile tests were carried out under load line displacement control at four different initial strain rates, from 2.5×10^{-3} s^{-1} to 2.5×10^{-6} s^{-1}. The temperature along the gauge part of the specimen was controlled within ±3 ℃ by two thermocouples attached to the gauge part.

In order to study the initiation of macroscopic mechanical instabilities during straining, seven

tensile tests, carried out at 2.5×10^{-4} s^{-1}, were interrupted before fracture after various amounts of strain.

2.2.3 Metallographic investigation of the tensile specimens after the tests

2.2.3.1 Damage evolution

A JEOL 5400 scanning electron microscope (SEM) was used to investigate cavitation, both for the as-received material and for the specimen fractured at 2.5×10^{-4} s^{-1}. Observations were carried out on the homogeneously deformed part of the specimen, far from the necking area. The observed sample was cut at mid-thickness of the tensile specimen, parallel to the loading axis. It was then mechanically polished down to 3 µm diamond paste followed by colloidal silica polishing during 4 hours. Typical magnification used is about 300, allowing cavities larger than about 0.5 µm to be detected. The fracture surface of the specimen fractured at 2.5×10^{-4} s^{-1} was also observed by SEM in order to study the fracture mode and inclusions from which voids nucleated.

2.2.3.2 Macroscopic necking

A LASERMIKE 183B-100 laser profilometer bench (optical resolution of 0.3 µm) was used to study the development of macroscopic necking along the gauge part of each specimen after tensile tests interrupted before fracture.

2.2.3.3 Microstructural evolution

The microstructure of the tempered martensite matrix of 9%Cr steels is composed of several elements at various scales: former austenite grains, packets, blocks, laths, and subgrains [Marder and Marder, 1969]. We focused on the observation of subgrain evolution during deformation, because of the expected influence of this phenomenon on material softening during fatigue, creep and creep-fatigue tests.

Prior austenite grains were distinguished on the as-received material with an OLYMPUS IX70 optical microscope after a Villela etching – 5 cm^3 of hydrochloric acid, 100 cm^3 of ethanol and 1 g of picric acid (see Fig. 2.1).

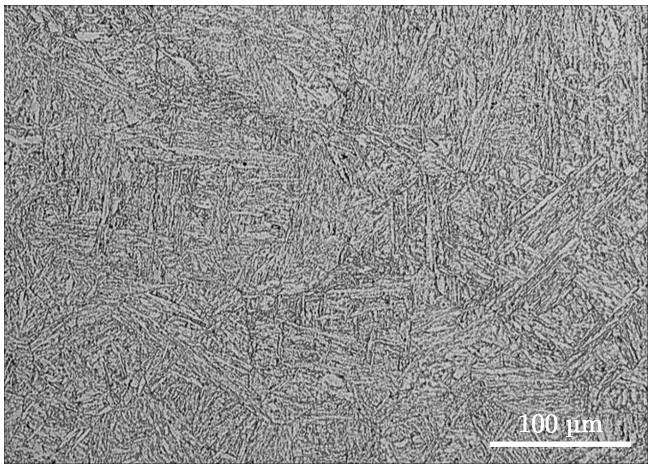

Fig. 2.1. Optical micrograph of P92 steel in the as-received condition. Villela etching.

EBSD measurements were carried out in order to study the microstructural evolution of the homogeneously deformed part of the samples for two values of the strain rate, namely, 2.5×10^{-4} s^{-1} and 2.5×10^{-6} s^{-1}. To prepare specimens for EBSD measurements, the cross-section cut along the specimen axis were mechanically polished in three short steps with 9 µm, 6 µm and 1 µm diamond pastes. The fourth step consisted in colloidal silica polishing for 10 minutes.

EBSD measurements were performed on a Zeiss DSM 982 Gemini field emission gun (FEG) scanning electron microscope (SEM) with an accelerating voltage of 20 kV, an aperture of 120 µm, a working distance of 19 mm and a tilt angle of 70 °. For all investigations, a magnification of 500 and a scan step size of 0.15 µm (square grids) were chosen. This value yields a good compromise between observation of fine tempered martensite substructure (which requires high spatial resolution) versus investigation over large areas to get statistically representative data. To cleanup EBSD data by a grain dilation procedure, only misorientation angles higher than 2 ° and crystals larger than 5 pixels were considered.

Subgrains were observed with a PHILIPS EM430 Transmission Electron Microscope operated at 300 kV. Thin foils were taken from the as-received material and from the homogeneously deformed part of the specimen fractured at 2.5×10^{-4} s^{-1}, perpendicular to the tensile axis. Their preparation consisted in cutting and mechanically polishing a small slice of both as-received material and fractured specimen far from the necking region, down to a thickness of 200 µm. Three-millimeter-diameter discs were punched and electrolytically thinned with a solution composed of 90% ethanol and 10% perchloric acid.

To determine the average subgrain size, two typical TEM pictures with a magnification of 10,300 were selected from different observed regions on thin foils from both as-received and homogeneously deformed material. On each picture, the number of subgrains was manually counted in three chosen square areas of interest of about 15 µm^2 each. Subgrain boundaries were identified by a change in bright field contrast.

The average dislocation density, ρ, was determined within martensite subgrains from two TEM pictures with a mean linear intercept method using five randomly oriented segments per picture [Klaar et al., 1992]. The values of ρ were determined using Eq. 2.1.

$$\rho = \frac{2 \sum_{i=1}^{5} n_i}{e \sum_{i=1}^{5} l_i} \tag{2.1}$$

With e the thickness of the thin foil (which was assumed to be 150 nm), n_i the number of intersections between sampling segment i and a dislocation and l_i the length of segment i.

2.3 Results of tensile tests carried out up to fracture

The as-received P92 steel presents an average former austenite grains size of about $20 - 30$ µm (Fig. 2.1). A quasi-constant macrohardness of 224 ± 4 HV_{30} was found along the pipe thickness in sections both parallel and perpendicular to the pipe axis, suggesting that the plastic flow behaviour of the studied steel in as-received condition should be homogeneous. Engineering stress-strain curves of the steel at 550 ℃ for various initial strain rates from 2.5×10^{-3} s^{-1} to 2.5×10^{-6} s^{-1} are presented in Fig. 2.2 and 2.3. A short work hardening step (from O to A in Fig 2.3) is observed, followed by a long and stable softening stage (from A to B in Fig 2.3). The softening stage is characterised by a decrease in flow stress, more significant for lower strain rates. At point B, a higher softening induces

a change in slope and leads to fracture at point C. The results of these tensile tests are summarized in Table 2.2. The tensile test carried out up to fracture at 2.5×10^{-4} s^{-1} will be denoted as test 0 in the following.

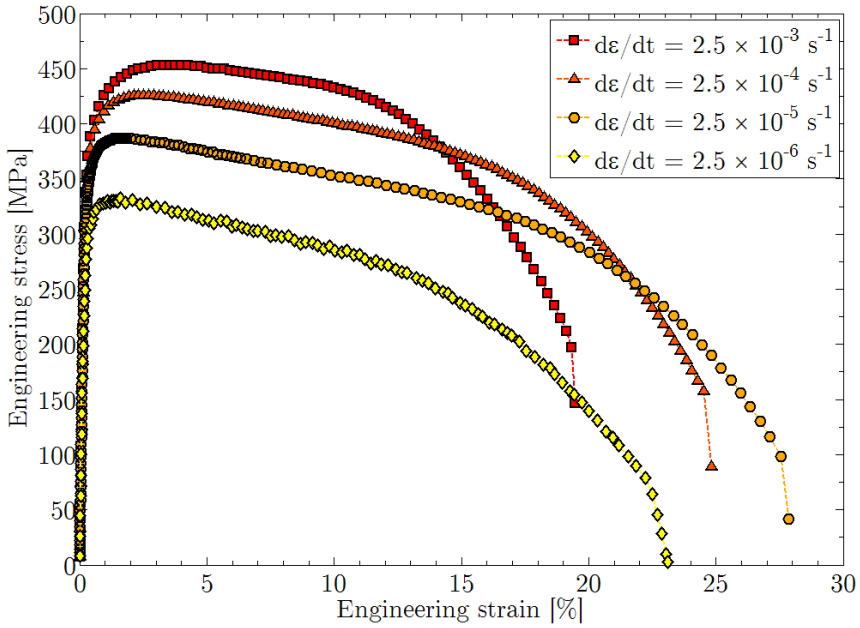

Fig. 2.2. Engineering stress-strain curves of the steel at 550 ℃. dε/dt is the applied elongation rate.

In order to understand the mechanisms responsible for the softening behaviour of the steel, the possible influence of three phenomena was investigated: damage development, mechanical instability (necking) and microstructural evolution.

Strain rate (s^{-1})	0.2% proof stress (MPa)	Tensile strength (MPa)	Elongation at point A (%)	Elongation at point B (%)	Softening slope (MPa)	Fracture elongation (%)	Reduction of area (%)
2.5×10^{-3}	388	454	3.2	10.1 ± 0.5	-370 ± 2	18.1	81 ± 1
2.5×10^{-4}	379	426	2.2	12.3 ± 0.5	-404 ± 2	25.0	85 ± 1
2.5×10^{-5}	358	390	1.6	13.8 ± 0.5	-442 ± 2	27.2	90 ± 1
2.5×10^{-6}	304	332	1.4	12.1 ± 0.5	-554 ± 2	23.1	93 ± 1

Tab. 2.2. Tensile results at 550 ℃.

2.4 Damage assessment

Fig. 2.4 shows a part of the fracture surface of the test 0 specimen, and suggests a ductile fracture mode. Inclusions have a size close to 5 µm and lead to the nucleation of voids which can reach a maximum diameter of about 25 µm on the fracture surface. Thus, damage was searched for as cavities in cross-section of the specimens. To this aim, SEM observations were carried out on the as-received material and on the homogeneously deformed part of the test 0 specimen (see Fig. 2.5).

The maximum void size observed on polished cross-sections for both as-received and homogeneously deformed part of the tension tested sample was about 5 µm, suggesting that the growth of cavities was insignificant during the uniaxial deformation, at least before initiation of macroscopic necking.

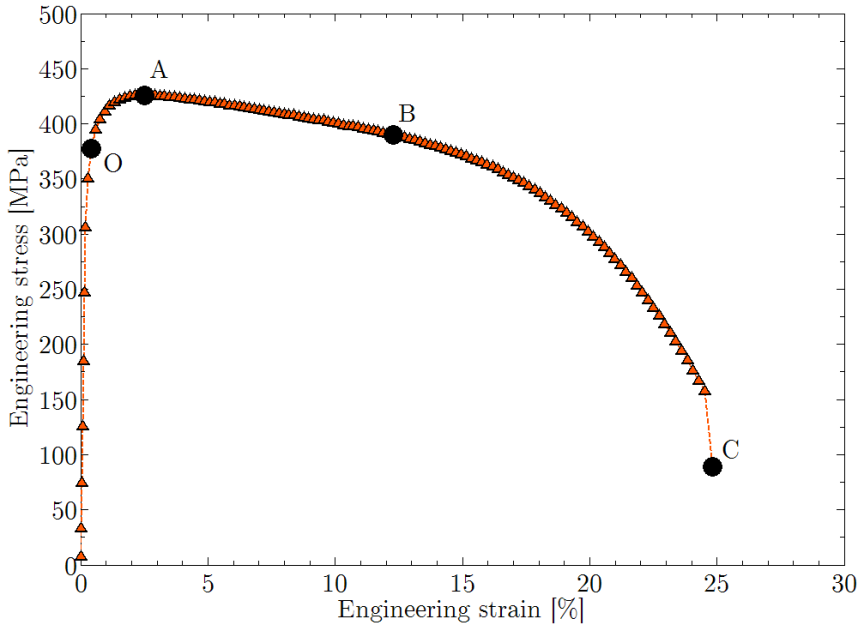

Fig. 2.3. Engineering stress-strain curve at 550 ℃ and 2.5×10^{-4} s^{-1} (test 0) with the 4 noticeable points described in part 2.3 (O, A, B and C).

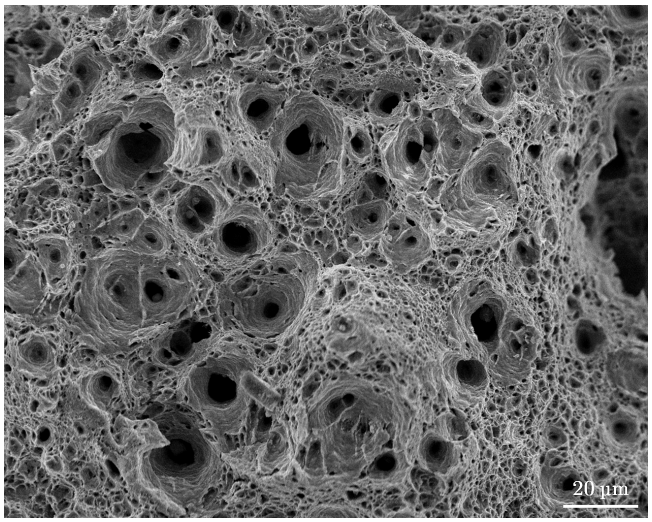

Fig. 2.4. Secondary electron SEM image of fractured test 0 specimen.

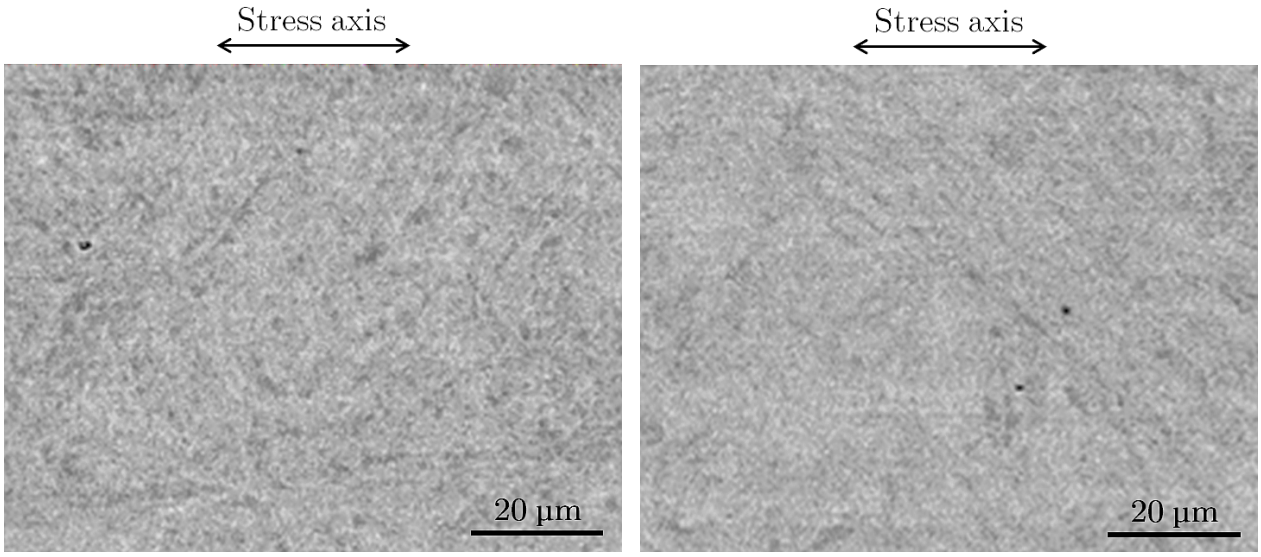

(a) (b)

Fig. 2.5. Backscattered electron SEM pictures taken from logitudinal cross-section of (a) the as-received steel and (b) the homogeneously deformed part of the test 0 specimen.

Even in the necked area, damage was only observed very close to the fracture surface. Senior et al. [Senior et al., 1986] observed ductile cavity nucleation at $M_{23}C_6$ carbides with a mean diameter of 34 nm in a commercial 9%Cr-1%Mo steel after room temperature tensile tests at 1.5×10^{-2} s^{-1}. The observations showed that void nucleation begins at $M_{23}C_6$ carbides for a plastic strain value of 0.25. For the test 0 specimen, the plastic strain reaches a maximum value lower than 0.1 (according to the corresponding average diameter) in the homogeneously deformed region. Consistently with Senior et al. [Senior et al., 1986], damage development is negligible in the homogeneously deformed part of the test 0 specimen and cannot be the cause of the observed softening behaviour.

2.5 Necking: experimental results and modelling

2.5.1 Interrupted tensile tests and onset of macroscopic necking

To study the beginning of macroscopic necking, seven different tests were interrupted at various values of elongation. The corresponding engineering stress-strain curves are presented in Fig. 2.6.

Although the seven curves are not superimposed with the curve corresponding to the reference test 0, experimental reproducibility remains acceptable. Only tests 6 and 7 significantly differ from test 0. If both tests had been carried out until fracture, test 6 would have shown a lower fracture elongation than test 0, and test 7 a higher one.

Following Fig. 2.7, macroscopic necking is observed for specimens 5, 6 and 7 whilst specimens 1, 2, 3 and 4 seem to be homogeneously deformed. To confirm this result, laser profilometry measurements along the gauge length of the seven specimens (Fig. 2.8) showed that necking appears clearly for specimens 5, 6, 7, and much less clearly for specimen 4. Interrupted tests were, accordingly, classified using the various stages identified in Fig. 2.3: tests on specimens 1, 2, 3 (and probably 4) were interrupted between O and B while tests on specimens 5, 6 and 7 were interrupted between B and C.

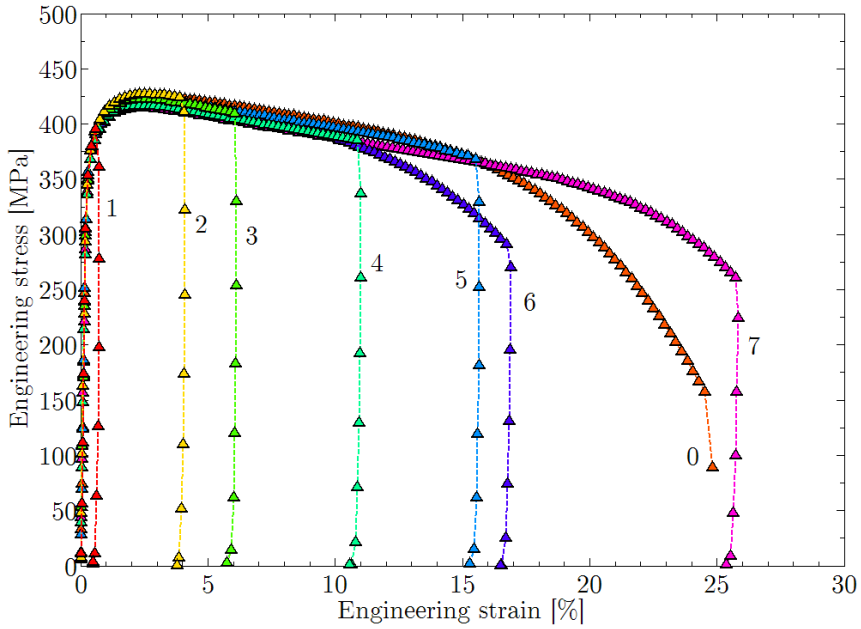

Fig. 2.6. Engineering stress-strain curves: test 0 (curve 0) and seven tensile tests (1-7) interrupted after various amounts of strain.

Fig. 2.7. The seven specimens after interrupted tensile tests.

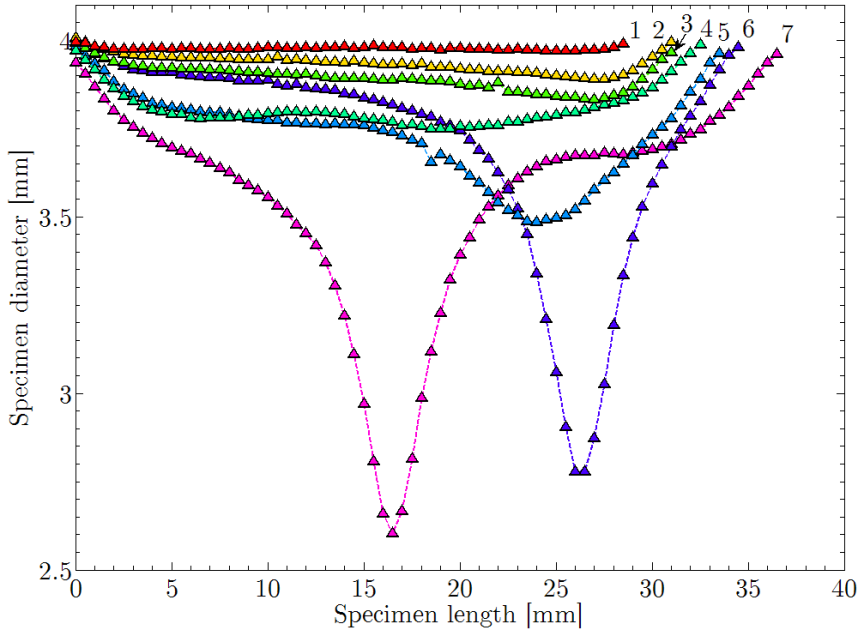

Fig. 2.8. Average diameters along the gauge length for the seven interrupted specimens, determined by laser profilometry. The accuracy of measurements is about 0.5 µm.

The hypothesis of volume conservation during plastic deformation (which is consistent with the absence of significant damage development mentioned above) is another way to confirm the onset of macroscopic necking. Under uniaxial tension, assuming an isotropic yield behaviour (to support this, at least, circular sections were observed to remain circular), neglecting elastic strains and considering the small perturbations hypothesis, the trace of the strain tensor is equal to zero if deformation is homogeneous and this hypothesis leads to a linear relationship between axial (ϵ_1) and radial (ϵ_2, ϵ_3) strains, as shown in Eq. 2.2:

$$\mathrm{Tr}\,\underline{\underline{\epsilon}}^p = 0 \quad \overset{\mathrm{Tr}\,\underline{\underline{\epsilon}}^e \ll \mathrm{Tr}\,\underline{\underline{\epsilon}}^p}{\Longrightarrow} \quad \mathrm{Tr}\begin{bmatrix} \epsilon_1 & \cdot & \cdot \\ \cdot & \epsilon_2 & \cdot \\ \cdot & \cdot & \epsilon_3 \end{bmatrix} = 0 \quad \overset{\epsilon_2=\epsilon_3}{\Longrightarrow} \quad \epsilon_2 = -\frac{1}{2}\,\epsilon_1 \tag{2.2}$$

Eq. 2.2 is plotted as a dotted straight line in Fig. 2.9. The experimental value of the radial strain ε_2 is calculated using three measurements of the diameter carried out on the homogeneously deformed section far from the necking region of the seven specimens. Points close to the dotted lines (tests 1, 2, 3, 4) correspond to specimens homogeneously deformed along their gauge length. For points far from the dotted line (tests 5, 6, 7), strain can not be homogeneous, which means that these tests were interrupted after the onset of macroscopic necking. This result confirms that macroscopic necking begins for a longitudinal elongation between those reached for specimens 4 and 5, respectively, consistently with point B of Fig. 2.3. In the following, it will be assumed that macroscopic necking starts at point B.

Elongation at point B was derived from each tensile curve at various strain rates by using the tangent to the softening part of the curve. A difference of 3 ± 1 MPa was arbitrarily chosen between the curve and the tangent to determine the elongation at point B. This method is illustrated in Fig. 2.10 for test 0 tensile curve and the results are presented in Table 2.2. The accuracy of this measurement leads to a sensitivity of $\pm 0.5\%$ in elongation at point B. Owing that deformation is homogeneous up to point B, it is possible to build and analyse true stress-strain curves from point O to point B, presented

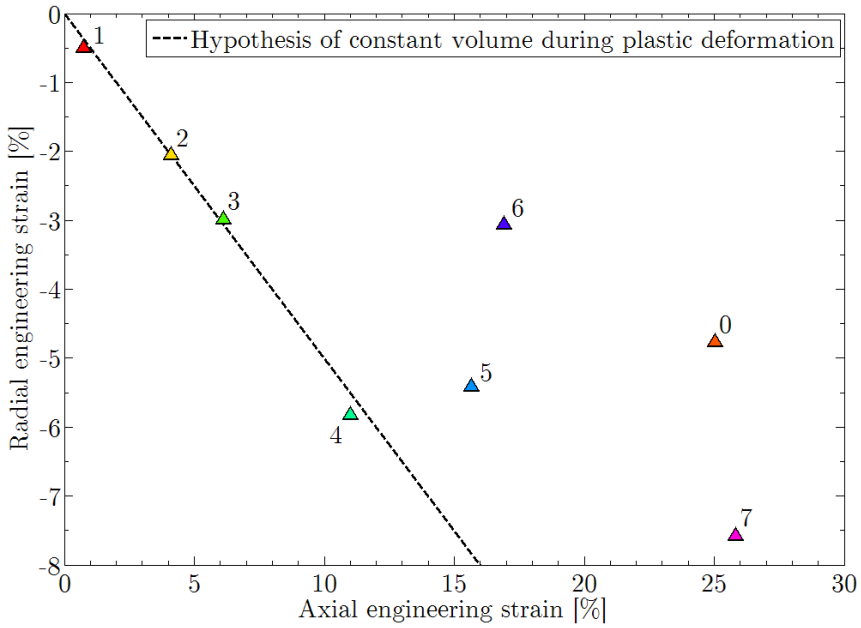

Fig. 2.9. Graph of the radial engineering strain versus axial engineering strain of the seven interrupted specimens and the fractured specimen. The dotted line corresponds to the linear relationship between radial and axial strain using the hypothesis of constant volume during homogeneous plastic deformation.

in Fig. 2.11.

Even when the true stress was taken into account, a softening behaviour of the steel was evidenced, especially for low strain rates. Consequently, at low strain rate, the existence of softening is not specifically due to a change in specimen geometry. Moreover, the softening slope decreases with decreasing the strain rate, suggesting a link between softening and strain rate. Indeed, the softening behaviour results from a competition between work hardening and recovery, which depends on the strain rate.

2.5.2 Prediction of mechanical instability and of fracture elongation

Interrupted tensile tests showed that macroscopic necking occurred for an elongation ranging between 10% and 14% (see Table 2.2). In this study, a criterion established by Hart [Hart, 1967] was used to predict the beginning of the mechanical instability in the specimen during homogeneous deformation, *i.e.*, elongation at point A. Hart's criterion is based on a relationship, which is not a constitutive equation, between the true stress σ, the true visco-plastic strain, ε^{vp} and the true viscoplastic strain rate, $\dot{\varepsilon}^{vp}$, allowing the material viscosity during high-temperature deformation to be taken into account. Elastic strains are neglected. In differential form, this relationship is given in Eq. 2.3:

$$\mathrm{d}\sigma = \frac{\partial \sigma}{\partial \varepsilon^{vp}}\left(\varepsilon^{vp}, \dot{\varepsilon}^{vp}\right)\mathrm{d}\varepsilon^{vp} + \frac{\partial \sigma}{\partial \dot{\varepsilon}^{vp}}\left(\varepsilon^{vp}, \dot{\varepsilon}^{vp}\right)\mathrm{d}\dot{\varepsilon}^{vp} \tag{2.3}$$

To use this relationship with the present results, a part of the true stress-strain curves were modelled with a term σ_1 depending on ε^{vp} and a term σ_2 depending on $\dot{\varepsilon}^{vp}$:

$$\sigma = \sigma_1\left(\varepsilon^{vp}\right) + \sigma_2\left(\dot{\varepsilon}^{vp}\right) \tag{2.4}$$

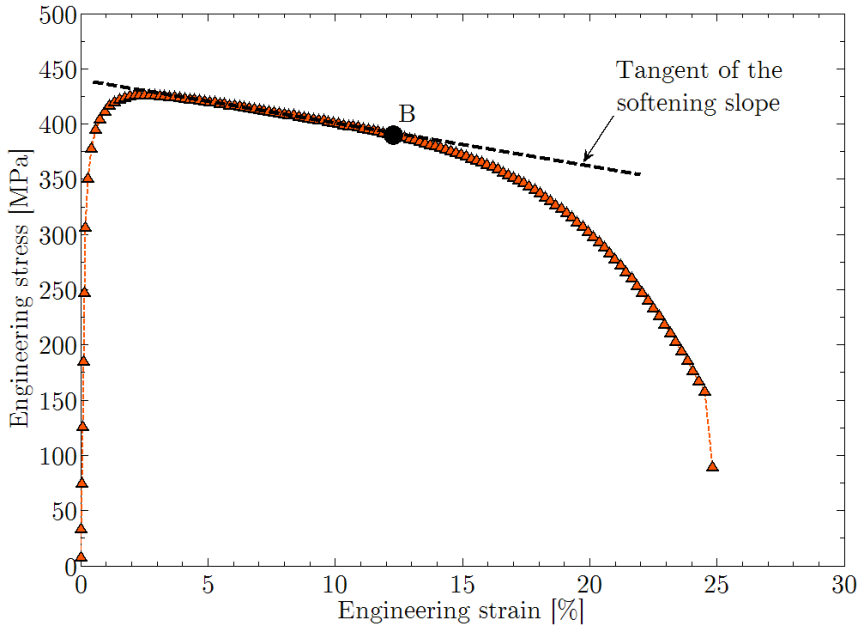

Fig. 2.10. Scheme of the test 0 engineering stain-stress curve illustrating the determination of the deformation at point B with the method of the tangent. A difference of 3 ± 1 MPa is chosen between the curve and the tangent to determine the elongation at point B.

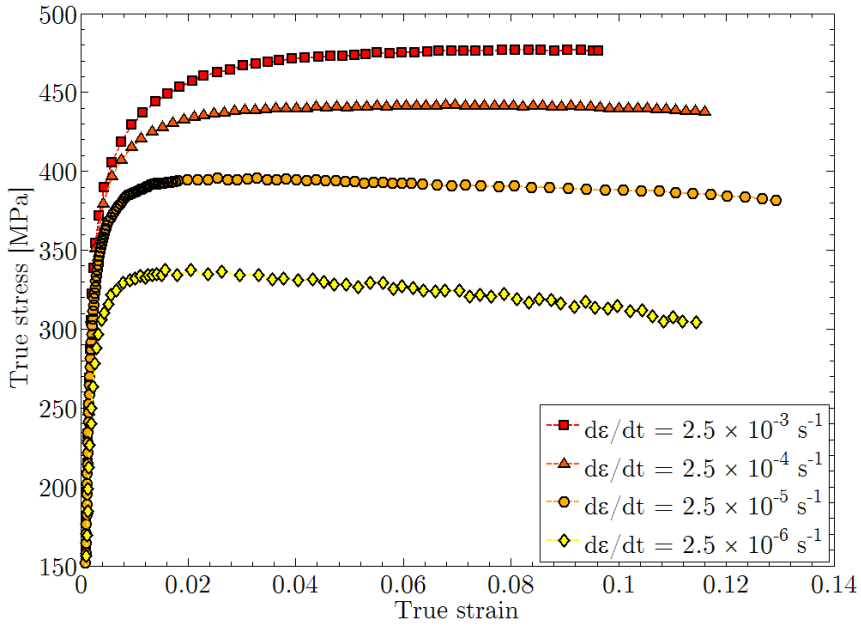

Fig. 2.11. Effect of the strain rate on the true stress-true strain curves derived from Fig. 2.2 (from point O to point B).

Term $\sigma_1(\varepsilon^{vp})$ was based on the empirical equation of Voce [Kishore and Sinha, 1996]:

$$\sigma_1 = \sigma_0 + Q\left[1 - \exp\left(-\beta\varepsilon^{vp}\right)\right] \tag{2.5}$$

Term $\sigma_2(\dot{\varepsilon}^{vp})$ was built with a classical expression corresponding to thermally activated viscoplastic flow [François et al., 1995a]:

$$\sigma_2 = \frac{1}{\alpha}\ln\left(\frac{\dot{\varepsilon}^{vp}}{\dot{\varepsilon}_0^{vp}}\right) \tag{2.6}$$

By combining Eqs. 2.4, 2.5 and 2.6, it was possible to model the true stress-strain curves with Eq. 2.7:

$$\sigma = \sigma_0 + Q\left[1 - \exp\left(-\beta\varepsilon^{vp}\right)\right] + \frac{1}{\alpha}\ln\left(\frac{\dot{\varepsilon}^{vp}}{\dot{\varepsilon}_0^{vp}}\right) \tag{2.7}$$

In order to improve the fit quality, the β coefficient was made dependent on $\dot{\varepsilon}^{vp}$ by Eq. 2.8:

$$\beta = \beta_1 \ln\left(\dot{\varepsilon}^{vp}\right) + \beta_2 \tag{2.8}$$

The six parameters values adjusted for predicting reasonably the true stress-strain curves for the different strain rates are reported in Table 2.3. The corresponding ajusted curves are presented in Fig 2.12.

Parameters	σ_0 (MPa)	Q (MPa)	β_1	β_2	α (MPa^{-1})	$\dot{\varepsilon}_0^{vp}$ (s^{-1})
Values	100	98	-42.92	-203.31	5.18×10^{-2}	1×10^{-9}

Tab. 2.3. Parameters values used for the fit of the true stress-strain curves (Eqs. 2.7 and 2.8).

The evolution of the mechanical instability during deformation was studied following the work of Hart. In the undeformed state, Hart considers that the specimen has a uniform cross-section A_0 except for a small part which has a cross-section of $A_0 - \delta A_0$ where δA_0 is small and corresponds to an imperfection of the specimen geometry. During deformation, the principal cross-section changes from A_0 to A and $A_0 - \delta A_0$ becomes $A - \delta A$. In this model, both sections (the necked area and the non-necked area) of the material are sustaining the same load, but may deform independently from each other, *i.e.* no constraint effect of the smallest section area by the largest one is taken into account. Hart computed the expression of δA from A, A_0 and δA_0:

$$\delta A = \delta A_0 \left(\frac{A_0}{A}\right)^{\frac{\gamma+m-1}{m}} \tag{2.9}$$

In Eq. 2.9, a term γ (Eq. 2.10) corresponding to strain hardening and a term m (Eq. 2.11) corresponding to visco-plasticity are defined:

$$\gamma = \frac{1}{\sigma}\frac{\partial\sigma}{\partial\varepsilon^{vp}} \tag{2.10}$$

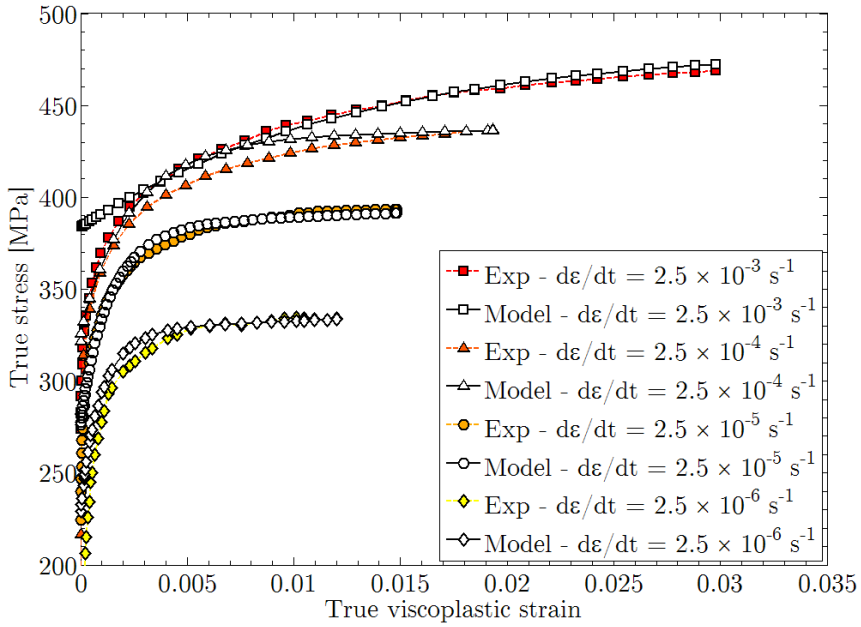

Fig. 2.12. Experimental (full symbols) and adjusted curves (open symbols) using Eq. 2.7, Eq. 2.8 and parameters values presented in Table 2.3.

$$m = \frac{\dot{\varepsilon}^{vp}}{\sigma}\frac{\partial \sigma}{\partial \dot{\varepsilon}^{vp}} \tag{2.11}$$

According to Eq. 2.9, the deformation is stable if $\gamma+m$ is higher than 1, then the offset δA decreases (in absolute value) and the section $A+\delta A$ becomes A, *i.e.* the initial geometrical defect is erased : both work hardening and viscosity tend to stabilize deformation along the gauge region. On the contrary, if $\gamma + m$ is lower than 1, then the offset δA increases (in absolute value), leading to further development of the mechanical instability and, eventually, to the onset of macroscopic necking. Hart proposes the following criterion to predict the initiation of the mechanical instability:

$$\gamma + m = 1 \tag{2.12}$$

Parameter δA_0 is determined by laser profilometry carried out on the specimens before the tensile tests. Considering d^+ (d^-) the maximun (minimum) value of the diameter measured for each specimen along the gauge part, δA_0 is defined as:

$$\delta A_0 = \frac{\pi}{4}\left[\left(d^+\right)^2 - \left(d^-\right)^2\right] \tag{2.13}$$

As elongation at the onset of macroscopic necking is much higher than 10^{-3}, elastic strains are neglected. In the homogeneously deformed part, the ratio $\frac{A_0}{A}$ and engineering strain ϵ are linked in the following way:

$$\frac{A_0}{A} = 1 + \epsilon \tag{2.14}$$

Calculating δA with Eq. 2.9, it is possible to plot the reduction of area $\frac{A-\delta A}{A_0}$ in the homogeneously deformed part during further deformation, as a function of axial elongation in the homogeneously deformed part of the specimens. This graph is presented in Fig. 2.13.

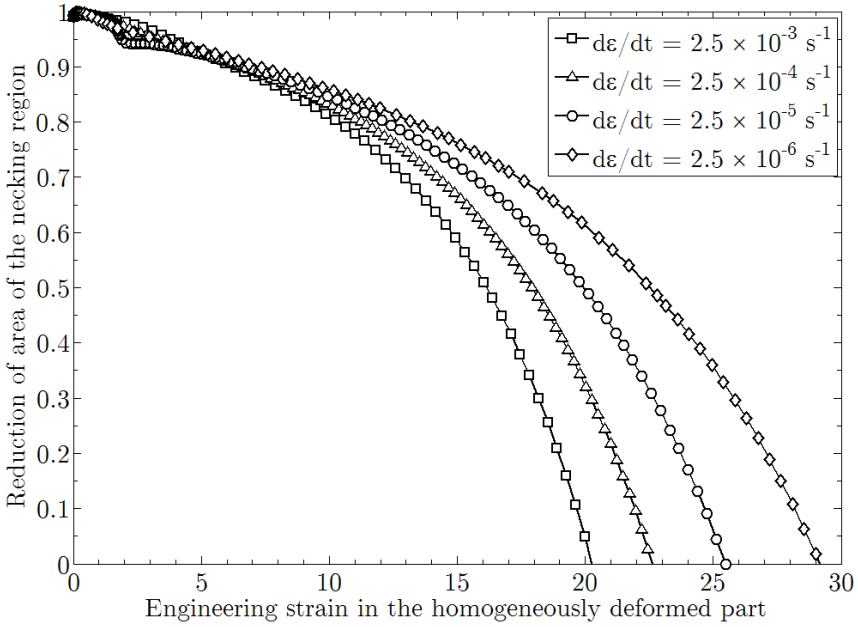

Fig. 2.13. Prediction of the reduction of area in the necking region during deformation versus the engineering strain in the homogeneously deformed part. For these curves, $A_0 = 1.1 \times 10^{-5}$ m^2 and $\delta A_0 = 1.2 \times 10^{-7}$ m^2.

In order to compare the results predicted with this model with experimental measurements, values of the section of the homogeneously deformed part determined by laser profilometry on the interrupted tests at 2.5×10^{-4} s^{-1} are reported on the graph in Fig. 2.14. To this aim, elongation of the necking region should be considered as negligeable. The model can thus predict the reduction in section during the deformation by considering that macroscopic necking is negligible. According to the previous results, only tests 1 to 4 are represented. For tests 5 to 7, the part affected by the macroscopic necking is too extended to consider its elongation negligible compared to that of the homogeneously deformed part. The model yields a good prediction of the reduction in section before the onset of macroscopic necking.

With the criterion presented in Eq. 2.12, the model predicts initiation of mechanical instability for an elongation close to the strain values at point A (Table 2.4), which satisfactorily corresponds with the Considère's criterion [Dumoulin et al., 2003]. The difference between values predicted by the model and experimental elongation at point B is explained this way: the model predicts initiation of a mechanical instability which has a slow development until point B. At point B, mechanical instability development accelerates and leads to macroscopic necking. Thus, macroscopic necking (and its "mechanical" softening effect) is only detected at point B but some mechanical instability has probably occurred as early as at point A.

This model established by Hart permits us to reasonably predict both initiation of the mechanical instability, corresponding to point A and evolution of section in the necking region of the specimen. However, it is impossible to take the length of the volume affected by macroscopic necking into account and to predict the whole elongation of the specimen. Material softening which affects the mechanical behaviour during deformation at high temperature could affect the curves as well. To study its contribution in more detail, observations of the microstructural evolution were carried out.

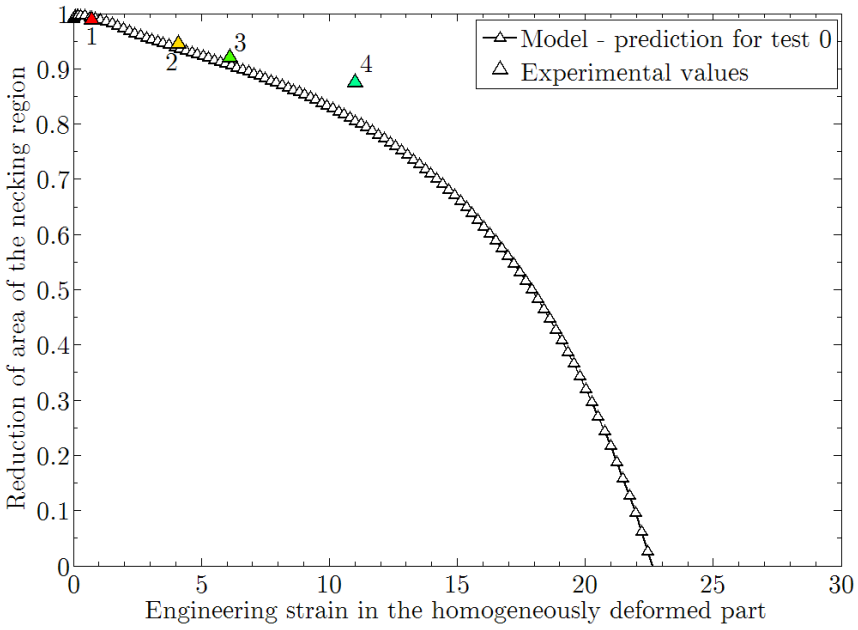

Fig. 2.14. Prediction of the reduction of the necking region during deformation at 2.5×10^{-4} s^{-1} compared with experimental results determined with tests 1 to 4. For this curve, $A_0 = 1.1 \times 10^{-5}$ m^2 and $\delta A_0 = 1.2 \times 10^{-7}$ m^2.

Strain rate (s^{-1})	Experimental value of elongation at point A (%)	Prediction of elongation at point A (%) using the present model
2.5×10^{-3}	3.2	3.6
2.5×10^{-4}	2.2	2.2
2.5×10^{-5}	1.6	1.6
2.5×10^{-6}	1.4	1.3

Tab. 2.4. Experimental measurements and predicted values of elongation at point A.

2.6 Microstructural evolution of the matrix during tensile deformation

2.6.1 Experimental results: EBSD and TEM investigations

TEM measurements of the average dislocation density within subgrains yielded a value of about 2×10^{14} m^{-2} for both samples taken from the as-received material and from the homogeneously deformed part of the test 0 specimen. This value is close to those reported in literature [Ennis et al., 2000, Ennis and Czyrska-Filemonowicz, 2003]. Thus, no obvious difference in dislocation density can be invoked to account for the observed softening. This result does not correspond to the observations carried out on creep specimens [Ennis and Czyrska-Filemonowicz, 2003, Eggeler et al., 1987, Pešička et al., 2003]. However, as tempered martensite is not a stable structure at high temperature, subgrain growth was also investigated as another possible cause of "metallurgical" softening.

First, EBSD investigations were carried out on the as-received material and on the homogeneously deformed part of test 0 specimen, longitudinally cut along the tensile axis.

Considering Inverse-Pole Figure (IPF) maps and the corresponding Image Quality (IQ) maps in Fig. 2.15, it is possible to observe blocks and groups of parallel martensite laths. Although it is difficult to give them a characteristic size because of their complicated shape, no obvious change in structure was evidenced at this scale of investigation. Some subgrains are visible on the IQ maps, but their small number prevents from establishing any reliable statistics. Tak et al. [Tak et al., 2009] showed that high resolution Orientation Imaging Microscopy with a step size of 10 nm permits to build an IQ map close to the contrast offered by TEM bright-field imaging. However, in the present study, only TEM images (Fig. 2.16) were used to estimate the size of subgrains for the as-received material and test 0 specimens.

Measurements carried out using TEM pictures provide an estimate of the average subgrain size equal to 0.37 µm for the as-received material and to 0.43 µm for the homogenously deformed part of test 0 specimen. Thus, during homogenous deformation, the mean subgrain size increases by 21% between the initial state and the deformed state. During creep tests, the mean subgrain size can increase up to more than twice the size of the subgrain in the initial state for P92 steel [Ennis et al., 1997] and up to 600% for a 12%Cr during fatigue tests at 650 ℃ [Dubey et al., 2005]. Subgrain growth is another possible cause of the softening stage during plastic deformation, which is linked to the Hall-Petch type relationship [Milititsky et al., 2008].

2.6.2 Modelling of microstructural evolution during straining

According to TEM observations and EBSD measurements, the following mechanism was suggested to account for subgrain growth of the material during plastic deformation. Subgrain boundaries inside a given block usually exhibit low misorientation angles θ (generally lower than 5 °) for tempered martensite ferritic steel with 10%Cr [Tak et al., 2009]. Read and Shockley [Read and Shockley, 1950] assumed that such low-angle boundaries can be considered as arrays of edge and screw-type dislocations. If a simple tilt low-angle boundary is considered (see Fig. 2.17), it is modelled as an array of parallel edge-type dislocations. In this case, the misorientation angle θ, the Burgers vector length b and the edge dislocation density Λ along the low-angle boundary are linked by Eq. 2.15:

$$\Lambda = \frac{\theta}{b} \tag{2.15}$$

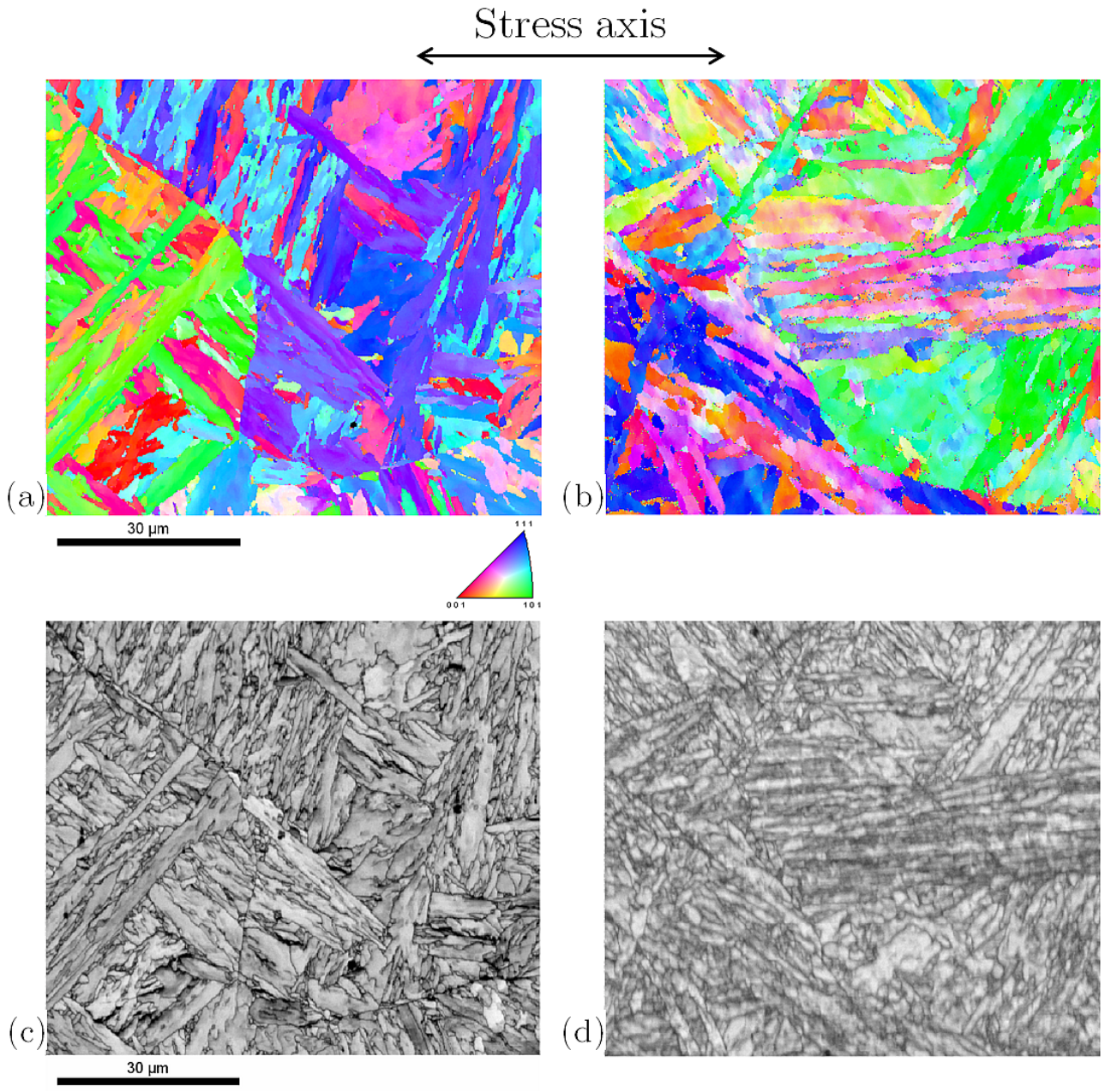

Fig. 2.15. Inverse pole figure maps of (a) as-received material and (b) homogeneously deformed part of test 0 specimen. The unit triangle is a colour key according to the crystallographic poles aligned with the sample surface normal direction. (c) and (d) Image Quality maps of the same region as (a) and (b), respectively. The tensile axis is horizontal and the scale bar stands for 30 µm in all maps.

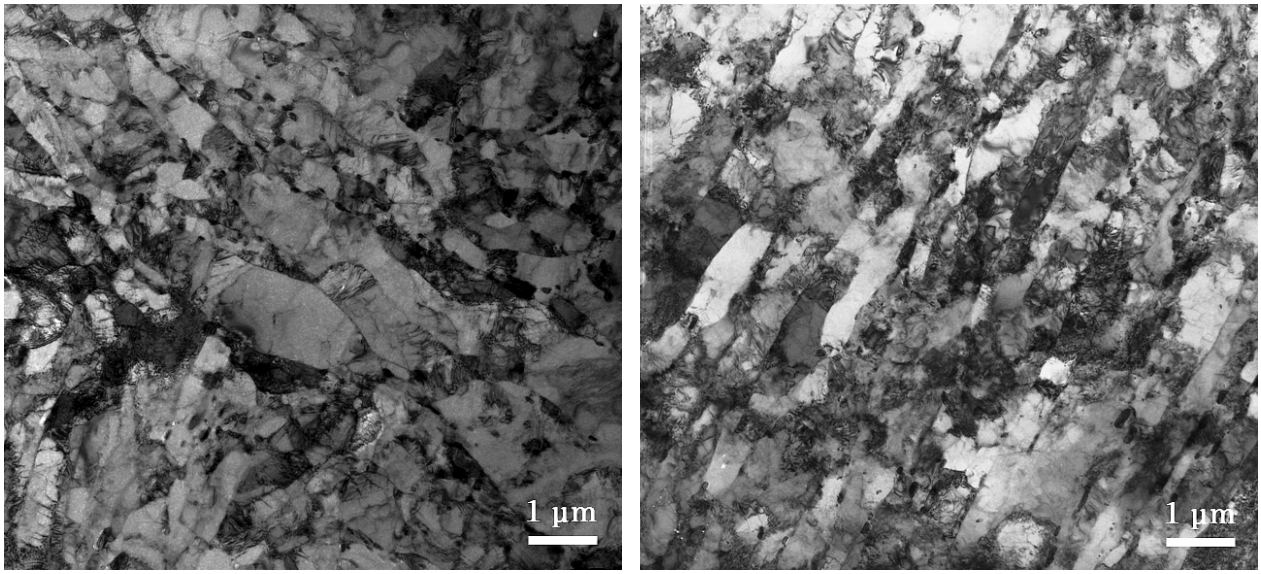

(a) (b)

Fig. 2.16. TEM pictures taken from (a) a sample from the as-received steel and (b) a sample taken far from the necking region, *i.e.* in the homogeneously deformed part of test 0 specimen. The direction of the tube axis is perpendicular to the plane of the picture.

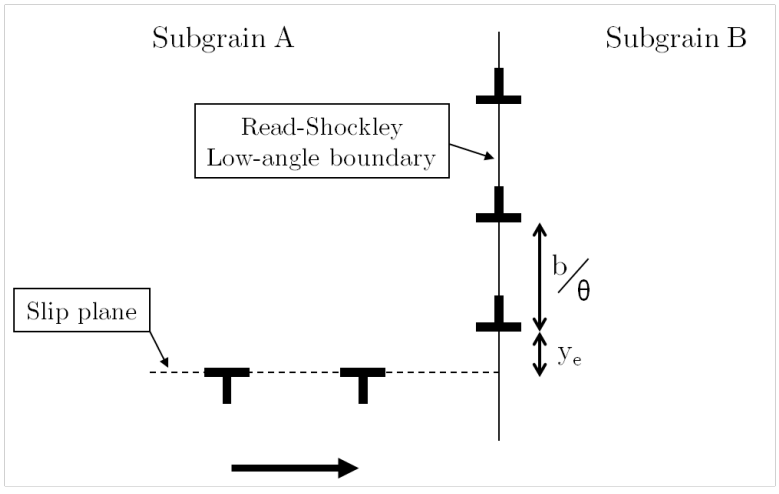

Fig. 2.17. Scheme of the interactions between mobile edge dislocations (moving along the dashed line) and parallel low-angle boundary edge dislocations (aligned along the continuous line) (symmetric tilt low-angle boundary).

Sauzay [Sauzay, 2009] proposed a model to predict the decrease in misorientation of the low-angle boundaries during high temperature deformation of tempered martensite ferritic steel. Mobile dislocations interact with low-angle boundaries during glide. Indeed, if appropriate slip systems are activated, mobile dislocations may move toward a low-angle boundary which contains parallel dislocations of opposite sign. Annihilation takes place between two edge (or screw) dislocations of opposite signs and parallel line vectors, if their distance is smaller than a critical value. These critical distances are denoted as y_e for edge dislocations and as y_s for screw dislocations. Considering Eq. 2.15, annihilation of dislocation of opposite signs induces a decrease in boundary dislocation density, Λ, and consequently in the misorientation angle θ of the boundary under interest. During deformation, accumulated strain may increase high enough to allow complete annihilation of many low-angle boundaries and thus an increase in subgrain size. The purpose of this section is to apply this model to the tensile deformation of the P92 specimens at 823 K. If the Burgers vectors of the mobile dislocations are parallel to those of boundary dislocations, misorientation angles θ_e (resp. θ_s) for low-angle boundaries consisting of edge (rep. screw) dislocations is given by Sauzay's model [Sauzay, 2009] as a function of the plastic strain ϵ^P, the Burgers vector length b, the Taylor factor M, the critical annihilation distance y_e (resp. y_s) and the initial misorientation θ_0 of low-angle boundaries:

$$\theta_e = \theta_0 \exp\left(\frac{y_e}{b}\frac{M}{5}\epsilon^P\right) \tag{2.16}$$

$$\theta_s = \theta_0 \exp\left(\frac{y_s}{b}\frac{M}{5}\epsilon^P\right) \tag{2.17}$$

For y_e, y_s and M parameters, the following values were used: $y_e \approx 1.6$ nm, $y_s \approx 50$ nm (due to lack of information, dislocation annihilation distances in copper at room temperature were used [Essmann and Differt, 1996]) and $M \approx 2.9$ (Taylor factor value for a textureless body centred cubic structure [Taylor, 1938]). Although martensitic steels are characterised by a microtexture, prior austenite grains are considered as textureless to simplify the model. Otherwise, finite element modelling is necessary to take the influence of texture on local stress and strain fields into account, which is outside the scope of this study.

Interactions between low-angle boundary dislocations and mobile parallel ones are limited by the number of slip systems activated in each subgrain. The crystal structure of the P92 tempered martensite matrix was supposed to be body-centred cubic. Two families of slip systems were considered: $\{110\}$ and $\{112\}$ planes and $\langle 111\rangle$ slip directions. Altogether, this means 24 slip systems. Indeed, the model considers activation of mobile dislocations in neighbouring subgrains A and B during deformation. As dislocations with Burgers vector $\vec{b}$ move in the direction opposite to that of parallel ones with a Burgers vector $-\vec{b}$, interactions between low-angle boundary dislocations and mobile parallel ones with a Burgers vector $\vec{b}$ or $-\vec{b}$ is possible during deformation, independently of the dislocation moving direction. Consequently, in this model one considers that two opposite slip systems are equivalent, leading to divide by 2 the total number of possible activated slip systems.

In a major part of subgrains, several slip systems are likely to be activated, due to the high macroscopic plastic strain. This is why the Taylor model is used in the present work: the plastic strain is supposed to be the same in each subgrain as well as in each block, packet and prior austenite grain. Taylor suggests that only five slip systems are generally activated in each subgrain to accommodate the macroscopic plastic strain. The number of ways to choose 5 slip systems among 24 is noted C_{24}^5,

corresponding to the following definition:

$$C_n^p = \frac{n\,!}{p\,!\,(n-p)\,!} \tag{2.18}$$

To allow annihilation between a mobile dislocation and a low-angle boundary dislocation, their Burgers vectors have to be opposite. This means that to avoid annihilation, it is necessary to choose 5 slip systems with none having dislocations parallel to the boundary ones. The number of ways to choose 5 different slip systems with no dislocation parallel to the considered low-angle boundary ones is noted C_{24-q}^5 where q is the number of slip systems with dislocation parallel to the ones of the subgrain boundary. Consequently, the probability of non-annihilation is $\frac{C_{24-q}^5}{C_{24}^5}$, and the probability $P(q)$ of annihilation is:

$$P(q) = 1 - \frac{C_{24-q}^5}{C_{24}^5} \tag{2.19}$$

For low-angle boundary dislocations of edge (resp. screw) type, q is equal to 1 (resp. 6). The probability P_e (resp. P_s) of annihilation for edge (resp. screw) type is equal to 0.21 (resp. 0.81).

To determine the misorientation angle of subgrain boundaries, it is assumed that:

- subgrain boundaries are either pure tilt or either pure twist *i.e.* that they are described using either one set of edge dislocations, or one set of screw dislocations.
- the fraction of pure tilt and pure twist boundaries are, respectively, the same as the edge (screw) mobile dislocation density.

Using Eqs. 2.16 and 2.17 and considering the proportion N_e (resp. N_s) of low-angle boundary dislocations of edge (resp. screw) type, it is possible to determine the cumulated frequency after deformation of:

- The low-angle boundaries (pure tilt and pure twist) which did not interact with mobile dislocations. Their final misorientation is equal to their initial one, and their cumulated frequency is equal to $N_e(1-P_e) + N_s(1-P_s)$.
- The pure tilt low-angle boundaries which interacted with mobile dislocations. Their final misorientation is equal to θ_e, and their cumulated frequency is equal to $N_e P_e$.
- The pure twist low-angle boundaries which interacted with mobile dislocations. Their final misorientation is equal to θ_s, and their cumulated frequency is equal to $N_s P_s$.

As accurate values of the model parameters could not be estimated, the proportions N_e and N_s were considered as equal ($N_e = N_s = 0.5$). Using the cumulated frequency of low boundary misorientation angles in a tempered martensite ferritic steel (X 20 CrMoV 12 1) measured by Tak et al. [Tak et al., 2009], the cumulated frequency of misorientation angles versus the misorientation angle was plotted in Fig. 2.18. The value of plastic strain $\epsilon^P = 9.6\%$, considered in the graph, corresponds to the strain in the homogeneous part of test 0 specimen, far from the necking region.

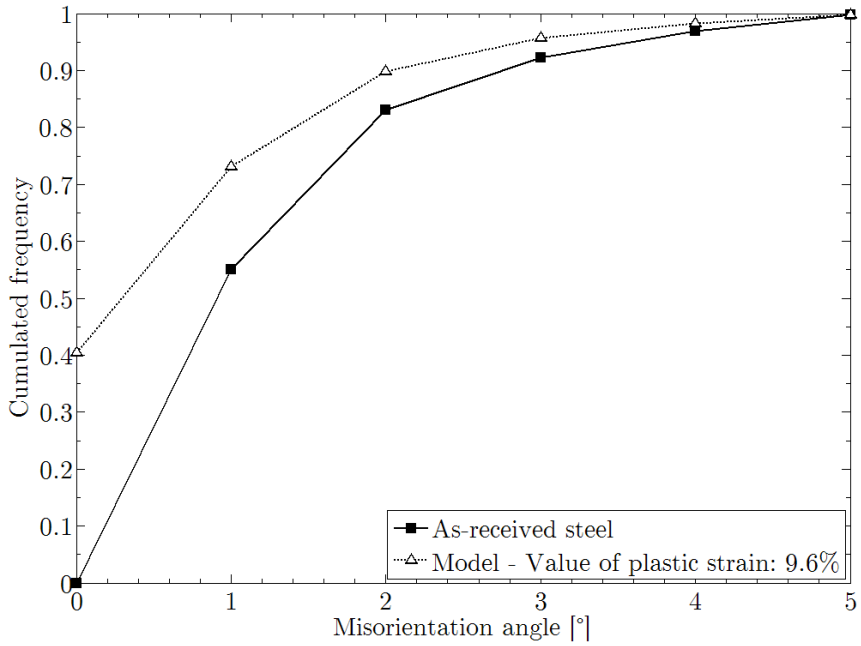

Fig. 2.18. Experimental cumulative frequency histogram of subgrain misorientation angles for a 12%Cr steel (X 20 CrMoV 12 1) [Tak et al., 2009] and predicted histogram in the homogeneously deformed part of the test 0 specimen for $\epsilon^P = 9.6\%$.

Sauzay's model is alse able to predict the decrease in average subboundary misorientation angle in the material during deformation. Using Fig. 2.18, the fraction of low-angle boundaries which vanish because of their misorientation angles becoming lower than a critical value can be assessed. Following dislocation dynamics computations of Holec and Dlouhý [Holec and Dlouhý, 2005], when the misorientation angle is lower than a critical value, interaction forces between low-angle boundary dislocations and the $M_{23}C_6$ precipitates are too weak and lead to the disappearance of the low-angle boundary. For tempered martensite ferritic steels, the critical misorientation angle was found to be about 0.4 ° [Holec and Dlouhý, 2005]. According to the model (Fig. 2.18), it corresponds to the disappearance of 55% of low-angle boundaries in the material after 9.6% of plastic deformation.

Then, considering the proportion of vanished low-angle boundaries, an estimation of subgrain growth was carried out. Subgrains were modelled as cubes with uniform initial edge length Φ_0 and low-angle boundaries correspond to the faces of these cubes. In a given unit volume homogeneously deformed in tension, the initial area S_0 per unit volume made of low-angle boundaries is computed by:

$$S_0 = \frac{1}{\Phi_0^3}\Phi_0^2\frac{6}{2} = \frac{3}{\Phi_0} \tag{2.20}$$

The first term $\frac{1}{\Phi_0^3}$ corresponds to the number of cubes in the considered unit volume, Φ_0^2 is the surface of one low-angle boundary and $\frac{6}{2}$ is the number of faces per cube (two neighbour cubes sharing the same face). The vanishing of a proportion κ of low-angle boundaries during deformation is supposed to be followed by boundary migration, so that after such migration, all subgrains remain cubic with a uniform edge length Φ. Then, annihilation of boundaries leads to a decrease in S_0. If the area per unit volume filled with low-angle boundaries after deformation is called S, the relationship between

S_0 and S is:

$$S = (1 - \kappa)\, S_0 \tag{2.21}$$

In the same way as in Eq. 2.20, S is defined as a function of the edge length Φ of the cube after deformation:

$$S = \frac{3}{\Phi} \tag{2.22}$$

Knowing that the proportion κ of vanished low-angle boundaries is equal to 55% (Fig. 2.18), this leads to the following relationship:

$$\Phi \approx 2.2\Phi_0 \tag{2.23}$$

The model predicts a growth of the microstructure equal to a factor of about 2.2. This result is higher than the growth factor equal to about 1.2 deduced from the TEM pictures in part 2.6.1. The difference between experimental and predicted results can be due to the following reasons:

- Experimental results, manually determined with about 100-120 subgrains from TEM pictures, were used to estimate an average subgrain size. This method induces a problem of statistical significance of the data set, and the growth factor should be probably different if it was determined from a whole subgrain size distribution.
- In the model, subgrain boundaries are either of pure tilt or of pure twist-type. This hypothesis is very strong, because most subgrain boundaries are composed with a mix of edge and screw dislocations [Guttmann, 1974]. In this case, interactions between mobile dislocations and low-angle boundaries (arrays of somewhat entangled dislocations) are more complex and induce a decrease in the probability of annihilation of all dislocations of the low-angle boundary and thus in the predicted growth factor. Consequently, pure low-angle twist boundaries will be considered as arrays of two families of screw dislocations [Guttmann, 1974].
- The activation of exactly five slip systems in each grain during the deformation, due to the Taylor's model, is probably overestimated for the tempered martensite ferritic steels. The activation of less slip systems may be enough to permit the deformation. Consequently, it would lead to a decrease of the probability of annihilation of the low-angle boundary dislocations.

Polycrystalline modelling is needed for predicting more accuratly the progressive activation of slip systems in the various blocks.

2.7 Conclusions

Tensile tests at various strain rates were carried out at 550 ℃ on a P92 steel. True stress-strain curves confirm the existence of a weak softening stage during deformation at low strain rate, a typical characteristic of 9%Cr steels deformed at high temperature. Considering the relatively low temperature

of 550 ℃ and the high strain rates of tensile tests (compared to creep), the diffusion processes are neglected. The softening mechanisms are based on the annihilation of subgrain boundaries and mobile dislocations. Nucleation, growth and coarsening of precipitates can be neglected because of the preliminar tempering and short test duration ($\leq$ 15 hours) at 550 ℃. Experimental results and model predictions lead to the following conclusions:

1. For strain rates up to 2.5×10^{-4} s^{-1}, both engineering and true stress-strain curves show a first softening stage well before the onset of macroscopic visible necking. This stage is characterised by constantly decreasing load and true stress, which depends on the applied elongation rate: the lower the elongation rate, the more pronounced the softening stage.

2. The Hart's criterion predicts the onset of mechanical instability for a low elongation close to the elongation at maximum load. In fact, diffuse necking occurs after a few percents of elongation. Macroscopic necking, in turn, induces a second softening stage with a stronger decreasing slope, leading to fracture.

3. This first softening stage is not due to cavity nucleation and growth in the specimen, which occurs only in the necking volume and shortly before fracture. TEM observations show that the subgrain size increases by about 21%, contributing to the material softening behaviour. This growth is overestimated by the low-angle boundary vanishing model in its present form. Improved modelling taking into account more accuratly low-angle boundary structure and activation of slip systems within tempered martensite blocks is needed. This will be carried out in chapter 4.

In the following chapter, we focus on the mechanical behaviour and microstructural evolution during cycling at 550 ℃. A more detailled study of the subgrain size distribution and dislocation density evolution, using fatigue test interrupted after a given number of cycles, is proposed. This chapter is dedicated to experimental results which permit us to propose a model coupling mechanical behaviour and microstructural evolution in chapter 4.

Chapter 3

Mechanical behaviour and microstructural evolution during cyclic and creep loading

This third chapter focuses on the mechanical behaviour of Grade 92 steel during continuous cyclic loading and creep at 550 ℃. Two creep tests performed at 600 ℃ and cyclic test including tensile holding periods at 550 ℃ are also presented. Then, the study focuses on the physical mechanisms of deformation during continuous cycling test. The macroscopic stress partition based on Cottrell's method is applied. Finally, TEM observations of the microstructure are presented in order to characterize microstructure evolution and possibly involved physical mechanisms are discussed.

Ce troisième chapitre est dédié à l'étude du comportement mécanique de l'acier Grade 92 lors de sollicitations de type chargement cyclique continu et fluage à 550 ℃. Deux essais de fluage à 600 ℃ et un essai de chargement cyclique avec temps de maintien en traction à 550 ℃ sont aussi présentés. Par la suite, l'étude se focalise sur les mécanismes de déformation lors des essais sous chargement cyclique continu. La décomposition de la contrainte macroscopique selon la méthode de Cottrell est appliquée. Enfin, des observations MET visant à caractériser l'évolution de la microstructure sont présentées et les mécanismes potentiellement impliqués sont discutés.

Contents

Abstract (in French) **61**
3.1 Macroscopic cyclic loading, creep and creep-fatigue behaviour **63**
3.1.1 Cyclic loading tests 63
3.1.2 Creep tests 68
3.1.3 Cyclic test including tensile holding periods 71
3.2 Macroscopic analysis of softening during cyclic loading **74**
3.3 Observations of microstructural evolutions during cyclic loading tests . . **76**
3.3.1 Evolution of the subgrain size distribution 77
3.3.2 Evolution of the dislocation density during high temperature cyclic loading . . 84
3.3.3 Discussion about deformation and annihilation mechanisms 85
3.4 Concluding remarks **87**

Résumé

Ce chapitre présente les résultats de l'étude des propriétés mécaniques en chargement cyclique continu et en fluage à 550 ℃ sous air sur l'acier Grade 92. Toutes les éprouvettes ont été prélevées à mi-épaisseur dans le sens longitudinal du tube. Les essais de fatigue ont été effectués sur des éprouvettes cylindriques de 16 mm de longueur utile et 8 mm de diamètre. Les essais de fluage ont été conduits sur des éprouvettes cylindriques de 30 mm de longueur utile et 8 mm de diamètre.

Dix essais ont été effectués pour des amplitudes de déformation totale variant de ±0,2 à ±0,5 %, avec une vitesse de déformation de 2×10^{-3} s^{-1}. Afin d'étudier l'influence de la vitesse de déformation sur le comportement mécanique et l'évolution de la microstructure, un essai a été effectué avec une amplitude de déformation de ±0,35 % et une vitesse de déformation de 1×10^{-5} s^{-1}. Enfin, pour mesurer l'évolution de la microstructure au cours du cyclage, trois essais de fatigue interrompus à 60, 300 et 1 000 cycles ont été menés avec une amplitude de déformation de ±0,35 % et une vitesse de déformation de 1×10^{-5} s^{-1}.

Les résultats de ces essais n'ont montré aucune différence significative entre les aciers Grade 91 et 92 en termes de durée de vie en fatigue. De même, les paramètres de Monkman-Grant, utilisant les résultats des essais de fluage de l'acier Grade 92, sont très proches de ceux établis dans la littérature pour l'acier Grade 91.

Les résultats des essais de fatigue ont montré que l'acier Grade 92 est sensible à l'adoucissement cyclique. Bien que plus prononcé pour les amplitudes de déformation élevées, ce phénomène est aussi observé pour les très faibles valeurs d'amplitude de déformation plastique (environ 10^{-4}). L'adoucissement est aussi influencé par la vitesse de déformation : plus celle-ci est faible, plus l'amplitude de déformation viscoplastique par cycle est élevée, plus la chute de la contrainte est rapide. Cependant, l'impact de la vitesse de déformation sur la durée de vie en fatigue est faible.

Dans le but d'étudier le phénomène d'adoucissement cyclique, une décomposition de la contrainte macroscopique mesurée selon la méthode de Cottrell [Cottrell, 1953] est proposée. Comme pour l'acier Grade 91, les résultats montrent que l'adoucissement cyclique de l'acier Grade 92 à 550 ℃ est principalement dû à la diminution de la composante cinématique au cours du cyclage. Cette observation indique une décroissance des interactions à longue portée entre les dislocations mobiles et la forêt de dislocations ou les sous-joints de faible désorientation.

Pour confirmer ces hypothèses, des observations MET ont été effectuées afin de mesurer l'évolution de la distribution de la taille des sous-grains et de la densité moyenne de dislocations au cours du cyclage. Les distributions de tailles des sous-grains, correctement décrites par des fonctions de densité de probabilité lognormale, montrent une croissance globale de la taille moyenne et une augmentation de la dispersion des mesures durant la déformation cyclique. La densité de dislocations dans les sous-grains diminue au cours de l'essai. Ces évolutions microstructurales sont d'autant plus prononcées que la vitesse de déformation est faible. À ce stade, les observations MET sont compatibles avec l'hypothèse de mécanismes de déformation liant la décroissance de la densité de dislocations et l'augmentation de la taille des sous-grains. Cette hypothèse est développée dans le chapitre 4.

3.1 Macroscopic cyclic loading, creep and creep-fatigue behaviour

This present section aims to describe the results of cyclic loading tests, creep tests and cyclic loading tests with holding periods, carried out on Grade 92 steel at 550 ℃. Creep tests performed at 600 ℃ are also presented.

3.1.1 Cyclic loading tests

Several grades of 9% and 12% chromium tempered martensitic steels (EUROFER 97 [Armas et al., 2002, Lindau et al., 2002, Marmy and Kruml, 2008], Grade 91 [Kim and Weertman, 1988, Choudhary et al., 1991, Kunz and Lukáš, 2001, Nagesha et al., 2002, Fournier et al., 2010], Grade 92 [Kannan et al., 2010, Fournier et al., 2011a], X20 and X22 [Earthman et al., 1989, Eggeler, 1989, Petersmeier et al., 1998, Kostka et al., 2007, Aghajani et al., 2009]) are known to be sensitive to softening during cyclic loading at high temperature. This softening stage is characterized by a continous decrease in flow stress amplitude, leading to an increase in viscoplastic strain amplitude per cycle if loading is deformation controlled. Tomkins showed that the crack propagation rate during fatigue test is proportional to the visco-plastic strain range [Tomkins, 1968]. The mechanical softening, which induces a decrease in resistance to crack propagation, is mainly due to microstructural instability, characterized by an increase in subgrain size and a decrease in dislocation density. This point is exposed in section 3.3. The influence of the strain localisation and fatigue damage during cycling on the mechanical behaviour is not studied in this PhD work. Formation of intense slip bands has been already observed during fatigue tests on Grade 91 steel at room temperature, but not yet for higher temperatures [Fournier et al., 2006b]. Although these sources of microstructural heterogeneities may occur at high temperature, the present study only focuses on the subgrain size and dislocation density evolution during cycling.

3.1.1.1 Experimental conditions and specimen geometry

Cyclic loading tests, conducted at CEA/SRMA laboratory, were performed in laboratory air at 550 ℃ using a MAYES ESM100 servo-mechanical machine with resistance furnace heating. They were carried out on smooth cylindrical specimens with 16 mm in gauge length, 8 mm in gauge diameter and a shoulder radius of 16 mm (see Fig. 3.1), machined from mid-thickness of the pipe along its longitudinal axis. The temperature along the gauge part of the specimen was controlled within ± 2 ℃ by thermocouple attached to the gauge part.

Cyclic loading tests were performed under total strain control, measured by a capacitive extensometer (10 mm in gauge length) directly attached on the gauge part of the specimen. The accuracy of elongation measurements is better than 0.5 µm, allowing cyclic loading tests with a total strain range as low as 0.1 % to be conducted. Ten cyclic loading tests were carried out at 2×10^{-3} s^{-1} for various values of the total strain amplitude from ± 0.50 % to ± 0.20 %. In order to estimate the experimental scatter, two cyclic tests were performed at 2×10^{-3} s^{-1} and 550 ℃ for every value of strain amplitude. Additionally, a test was performed at 1×10^{-5} s^{-1} for a total strain amplitude of ± 0.35 % to investigate the effect of strain rate on both macroscopic flow behaviour and microstructural evolution of the material. Considering the very low values of deformation which are expected to be involved for structural components in nuclear reactors, the softening mecanisms observed in 9%Cr tempered martensite steels should necessarily be studied and understood in order to predict the mechanical behaviour during service conditions.

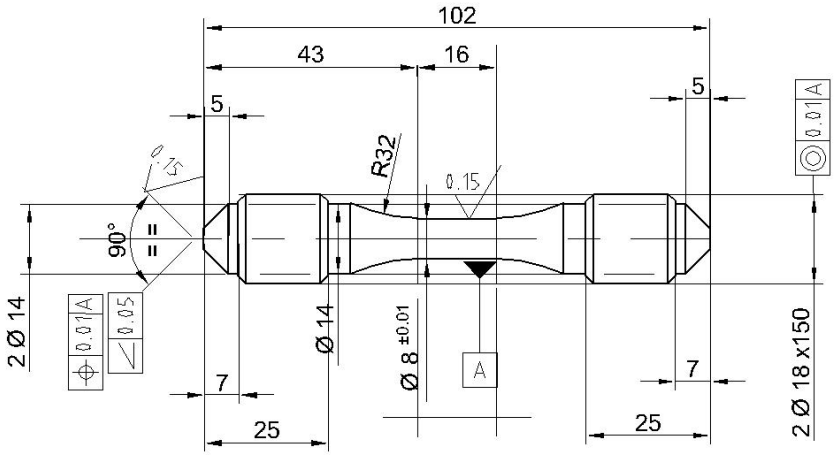

Fig. 3.1. Geometry of the smooth specimens used for cyclic loading tests (dimensions in mm).

3.1.1.2 Influence of strain amplitude at high strain rate on cyclic flow behaviour and fatigue lifetime

Mechanical results of cyclic loading tests on Grade 92 steel at 550 ℃ are reported in Table 3.1. The relationship between plastic strain range and fatigue lifetime* for Grade 91 and Grade 92 steels is presented in Fig. 3.2. For both steels, tests were performed at 2×10^{-3} s^{-1} in conditions described in part 3.1.1.1. The test carried out on Grade 92 steel at 1×10^{-5} s^{-1} is also presented in Table 3.2.

Strain rate (s^{-1})	ΔE (%)	ΔE^p (%)	N_{50} (cycles)	N_f (cycles)
2×10^{-3}	1.00	0.610	1,872	2,291
2×10^{-3}	1.00	0.618	2,225	2,392
2×10^{-3}	0.70	0.335	4,450	4,552
2×10^{-3}	0.70	0.334	5,193	6,689
2×10^{-3}	0.60	0.245	7,613	8,545
2×10^{-3}	0.60	0.242	8,482	9,786
2×10^{-3}	0.50	0.155	12,957	13,450
2×10^{-3}	0.50	0.158	15,374	15,961
2×10^{-3}	0.40	0.083	144,766	157,017
2×10^{-3}	0.40	0.089	169,793	170,829

Tab. 3.1. Cyclic loading tests results on Grade 92 steel at 550 ℃. ΔE is the macroscopic strain range (R= -1) and ΔE^p is its plastic part at N_{50}. N_{50} and N_f are respectively the number of fatigue cycles leading to a 50 % decrease in maximum stress and leading to fracture.

For the cyclic tests performed at 2×10^{-3} s^{-1}, no significant difference between Grade 91 and Grade 92 steels is observed in terms of lifetime. Indeed, the Manson-Coffin parameters of each adjusted curves for both steels do not differ significantly with respect to experimental scatter.

The influence of strain amplitude on the evolution of stress amplitude is presented in Fig. 3.3(a). A significant cyclic softening effect is observed and it is more pronounced for the higher values of strain amplitude. However, the comparison between tests is more relevant in terms of cumulated viscoplastic strain, as shown in Fig. 3.3(b). From this graph, the cyclic softening observed for each test is faster

*The fatigue lifetime N_{50} is defined as the number of cycles corresponding to a decrease of 50 % of the maximum stress measured during the test. This had been shown to be close to the final failure number of cycles (see Table 3.1).

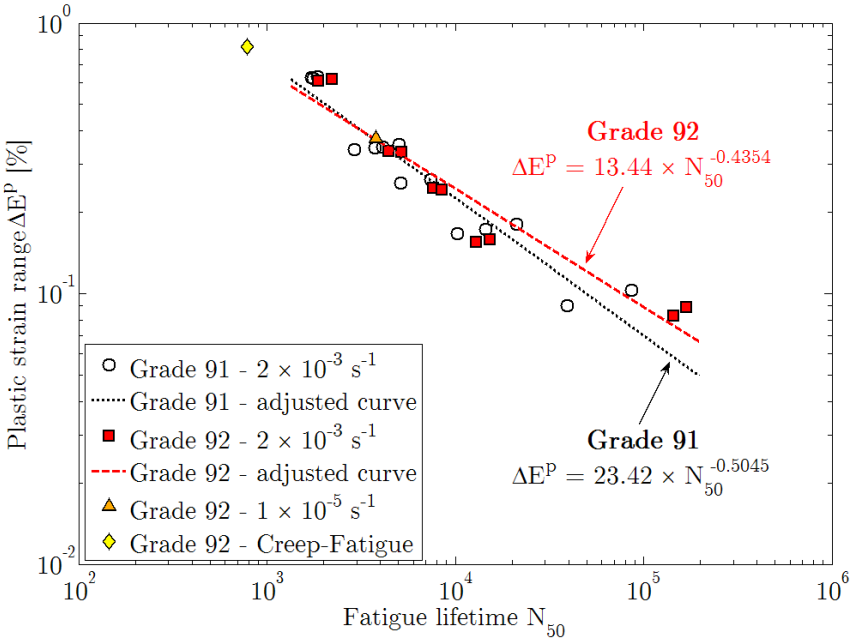

Fig. 3.2. Manson-Coffin curves for Grade 91 [Fournier et al., 2008] and Grade 92 steels at 550 ℃.

for the higher values of strain amplitude in terms of cumulative viscoplastic strain. Moreover, fatigue lifetime is also impacted by strain amplitude: the lower the strain amplitude, the higher the cumulated visco-plastic strain before fracture, in agreement with the Manson-Coffin law. These results mean that Grade 92 steel is more sensitive to softening for the higher values of strain amplitude.

Fig 3.3 shows that while the softening phenomenon is more pronounced for higher values of strain amplitude, it is still significant for the lower values of strain amplitude. Thus, for a total strain amplitude of 0.2 %, Grade 92 steel is characterized by a decrease in stress amplitude of about 50 MPa whereas the viscoplastic strain amplitude is very low at half-life and only about 4×10^{-4} at the first cycle (see Table 3.1).

To complete this study, results published in literature show that tempered martensite ferritic steel are sensitive to cyclic softening even at room temperature [Kunz and Lukáš, 2001, Armas et al., 2004, Giordana et al., 2011]. This softening behaviour is more pronounced at higher temperature [Armas et al., 2004].

From our knowledge, the influence of strain rate on the cyclic softening has not been as studied as the influence of amplitude, temperature and environment [Earthman et al., 1989, Petersmeier et al., 1998, Kunz and Lukáš, 2001, Nagesha et al., 2002, Armas et al., 2004, Shankar et al., 2006, Kannan et al., 2009, Kannan et al., 2010, Fournier et al., 2011a] but not on the effect of the strain rate. This is why we will focus from now on the effect of strain rate on the cyclic behaviour of the studied Grade 92 steel.

3.1.1.3 Influence of strain rate on cyclic flow behaviour and fatigue lifetime

For Grade 92 steel, the influence of strain rate on fatigue lifetime is studied based on the Manson-Coffin curves presented in Fig. 3.2 . Although only one cyclic test was carried out at 1×10^{-5} s^{-1}, it seems that the strain rate has no significant influence on fatigue lifetime. However, some other tests on Grade 92 steel at low strain rate and for lower strain amplitude are necessary to definitely conclude

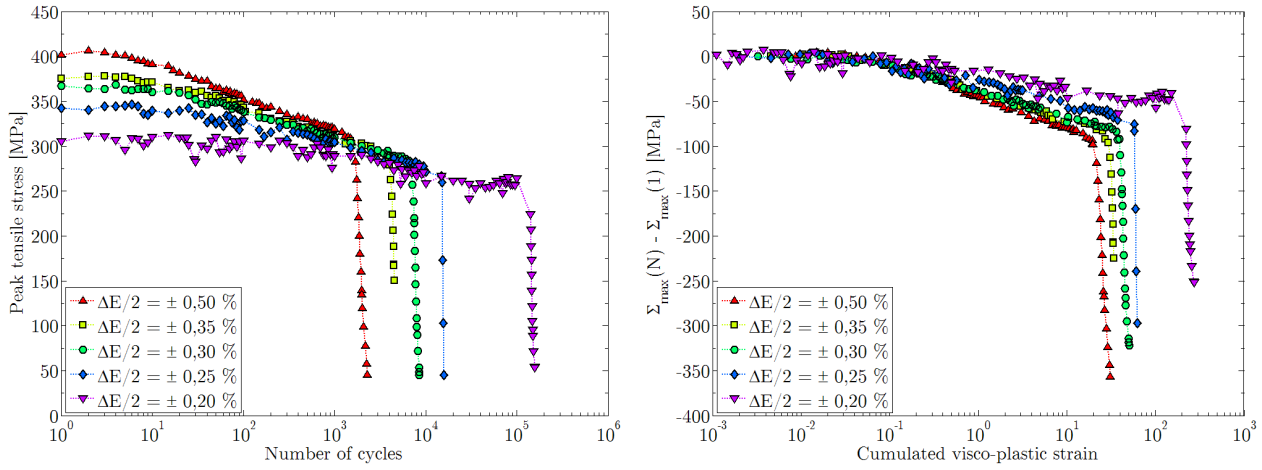

Fig. 3.3. Variation (a) of the peak tensile stress during cyclic loading tests for various applied amplitudes of the total strain at 550 ℃ and (b) of the difference between the peak tensile stress at the Nth cycle and that at the first cycle during cyclic loading tests at 2×10^{-3} s^{-1}.

about the effect of strain rate on the fatigue lifetime.

Strain rate (s^{-1})	ΔE (%)	ΔE^p (%)	N_{50}	N_f	N_{int}
2×10^{-3}	0.70	0.335	4,450	4,552	-
2×10^{-3}	0.70	0.334	5,193	6,689	-
1×10^{-5}	0.70	0.376	3,793	3,960	-
Interrupted tests					
1×10^{-5}	0.70	-	-	-	60
1×10^{-5}	0.70	-	-	-	300
1×10^{-5}	0.70	-	-	-	1,000

Tab. 3.2. Results of the cyclic loading tests on Grade 92 steel at 550 ℃ for two different values of the applied total strain rate. ΔE is the macroscopic strain range and ΔE^p is its plastic part at N_{50}. N_{50} and N_f are the number of fatigue cycles leading to a 50 % decrease in maximum stress and leading to fracture, respectively. N_{int} is the number of fatigue cycles corresponding to a voluntary interruption of the cyclic loading test.

Table 3.2 presents the cyclic loading tests results on Grade 92 steel at 550 ℃ and ± 0.35 % of strain amplitude for two different values of total strain rate. Hysteresis loops recorded at 1st, 10th, 100th and 1,000th cycles of pure fatigue test for both strain rates are presented in Fig. 3.4. Fig 3.5(a) shows the effect of strain rate on cyclic loading softening curves plotted in terms of number of cycles. For both strain rates, cyclic softening is significant. The difference between the stress levels for a given number of cycles is constant and thus considered to be mainly due to viscosity effects at high temperature. Fig 3.5(b) presents the softening curve as a function of the cumulated visco-pastic strain. In this graph, the stress drop is slightly more pronounced for the curve corresponding to the lower strain rate. As the total strain amplitude is constant during the tests, the lower the peak tensile stress, the higher the visco-plastic strain amplitude per cycle. Although the impact on fatigue lifetime is slight (see Tab 3.2), this result means that Grade 92 steel is more sensitive to softening for lower strain rate.

Three tests performed at 1×10^{-5} s^{-1} were interrupted after the 60th, 300th and 1,000th cycles respectively. These values were choosen in order to obtain three specimens at three different steps of the softening curve and thus to get insight into the metallurgical evolution of the specimen during

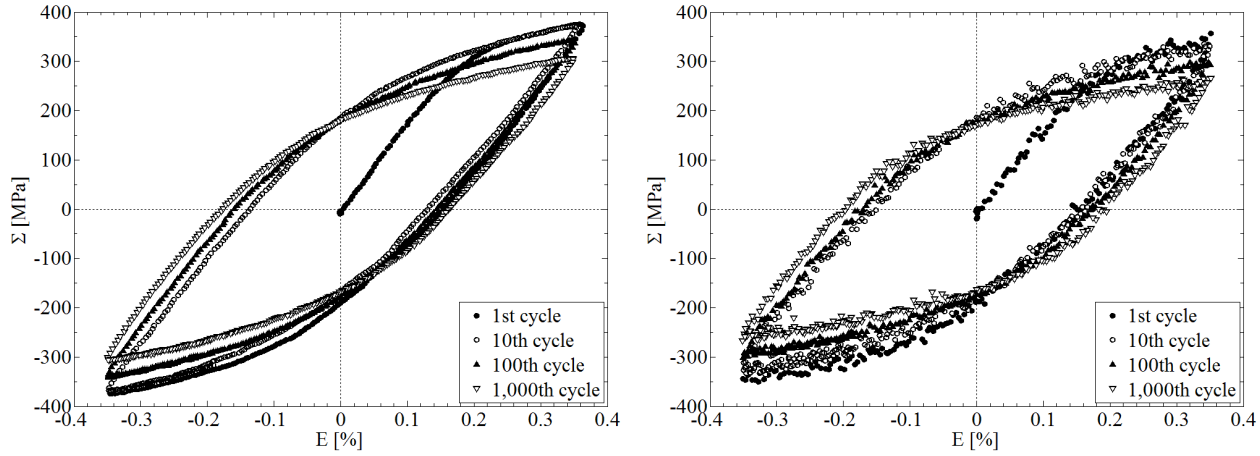

Fig. 3.4. Hysteresis loops recorded at 1^{st}, 10^{th}, 100^{th} and $1{,}000^{th}$ cycles of pure fatigue test for strain rate of (a) 2×10^{-3} s^{-1} and (a) 1×10^{-5} s^{-1}.

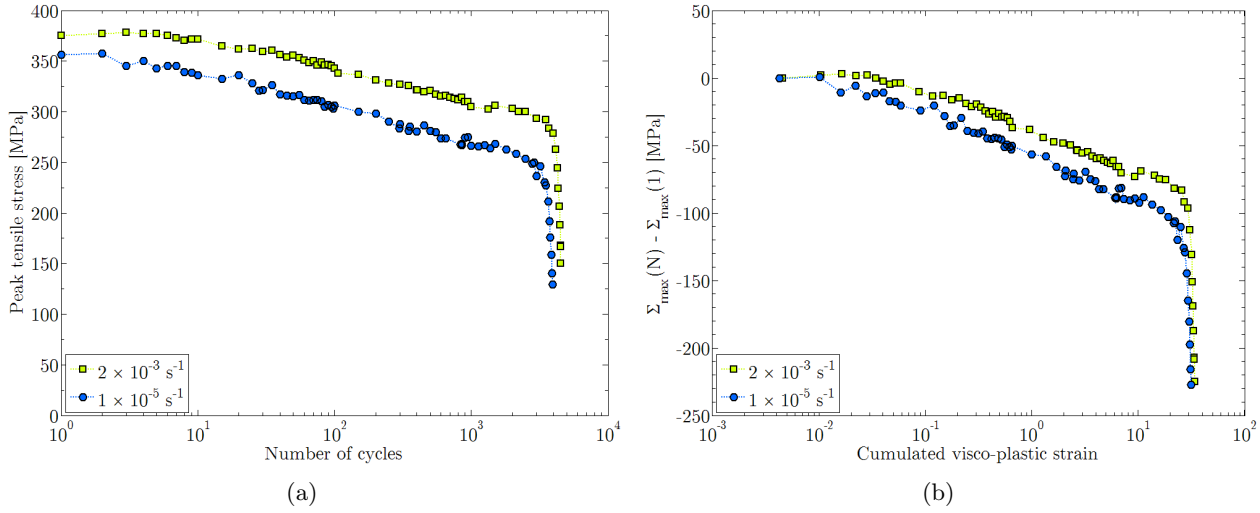

Fig. 3.5. (a) Variation of the peak tensile stress during cyclic loading tests at 2×10^{-3} s^{-1} and 1×10^{-5} s^{-1} for a strain amplitude of $\pm$ 0.35 % at 550 ℃ and (b) variation of the difference between the peak tensile stress at the N^{th} cycle and at the first cycle during cyclic loading tests at 2×10^{-3} s^{-1} and 1×10^{-5} s^{-1} for a strain amplitude of $\pm$ 0.35 % at 550 ℃ in terms of cumulated visco-plastic strain.

cyclic loadings.

3.1.2 Creep tests

Microstructural instability of tempered martensite steels has been observed during long-term exposure and creep test at high temperature [Eggeler et al., 1987, Eggeler, 1989, Abe, 2001, Abe et al., 2004, Abe, 2004, Vaillant et al., 2008, Zhang et al., 2011]. Indeed, microstructural evolution induces a decrease in creep resistance, an acceleration of the creep rate and consequently a decrease in lifetime [Lim et al., 2011]. As shown in chapter 2, necking is the main mechanism of failure provided strain rate is not too low.

Different modifications of the chemical composition and heat treatments were conducted on 9%Cr steel in order to impove the creep resistance. For example, the addition of tungsten induces a strong decrease of the minimum creep rate [Abe, 2001]. The 100,000 hours stress rupture strength of the Grade 92 was extrapolated to be 115 MPa at 600 ℃ [Ennis et al., 1997] whereas this value is about 90 MPa for Grade 91 at 600 ℃ [Haney et al., 2009]. Thus, Grade 92 steel is characterized by a higher creep resistance than Grade 91, as it is illustrated in Fig 3.6.

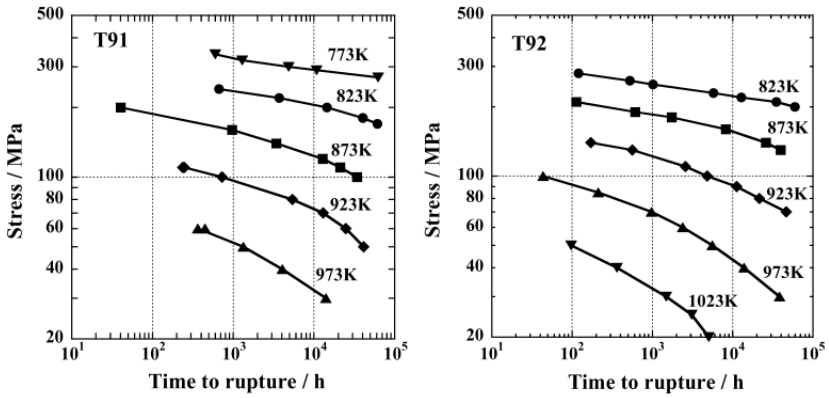

Fig. 3.6. Creep curves of Grade 91 and Grade 92 steels at various temperatures [Sawada et al., 2007].

3.1.2.1 Experimental conditions and specimen geometry

Creep tests, conducted at CEA/SRMA laboratory, were performed in air at 550 and 600 ℃ on smooth cylindrical specimens with 30 mm in gauge length, 8 mm in gauge diameter and a shoulder radius of 0.5 mm (see Fig. 3.7). The specimens were machined from mid-thickness of the pipe along its longitudinal axis. The temperature along the gauge part of the specimen was controlled within ± 3 ℃ using attached thermocouples. Axial strain during creep tests was measured by a capacitive extensometer directly attached on the gauge part of the specimen. Nine creep tests were carried out at 550 ℃ under constant load corresponding to various initial values of the applied stress from 145 to 235 MPa. Two additional tests were performed at 600 ℃ under initial applied stress of 145 and 160 MPa.

3.1.2.2 Creep curves and lifetime

Tables 3.3 and 3.4 presents the results of the creep tests conducted at 550 and 600 ℃ on Grade 92 steel specimens. Corresponding creep curves are plotted in Figs. 3.8 and 3.9. The creep curve obtained under 185 MPa at 550 ℃ is ahead the one obtained for 190 MPa, which is unexpected. Moreover, the

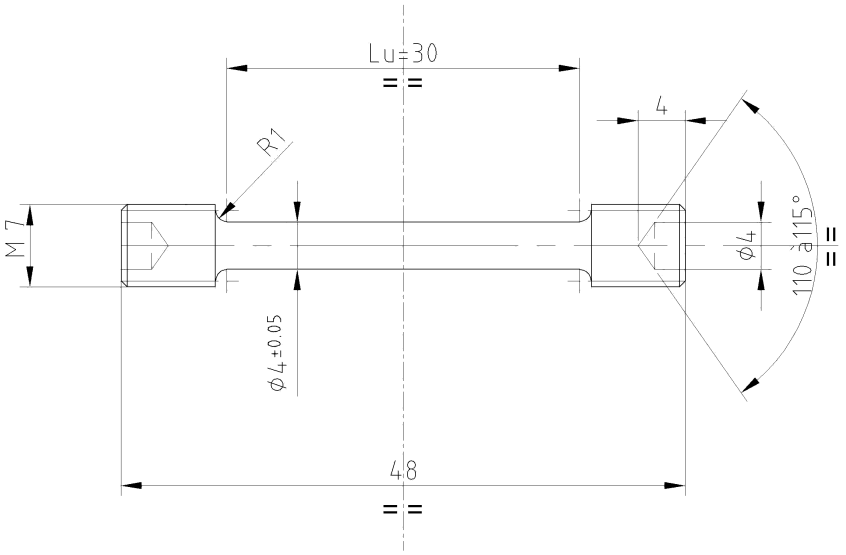

Fig. 3.7. Geometry of the smooth specimens used for creep tests (dimensions in mm).

secondary creep strain rate for the test at 185 MPa is higher than the corresponding one for the test at 190 MPa. Later during the tests, predicted strain rates are closer and closer between these two tests.

Temperature	Applied stress	Beginning of secondary creep stage	Beginning of tertiary creep stage	Time to rupture	Secondary creep strain rate
550 ℃	235 MPa	310 h	850 h	2,037 h	20.8×10^{-6} h^{-1}
550 ℃	220 MPa	1,500 h	4,100 h	6,337 h	6.27×10^{-6} h^{-1}
550 ℃	210 MPa	2,760 h	8,450 h	15,257 h	2.46×10^{-6} h^{-1}
Tests in progress					
550 ℃	200 MPa	4,000 h	17,800 h	$>$ 20,980 h	0.321×10^{-6} h^{-1}
550 ℃	190 MPa	10,330 h	$>$ 25,560 h	-	$< 0.176 \times 10^{-6}$ h^{-1}
550 ℃	185 MPa	13,000 h	$>$ 25,560 h	-	$< 0.194 \times 10^{-6}$ h^{-1}
550 ℃	175 MPa	9,400 h	$>$ 25,320 h	-	$< 0.140 \times 10^{-6}$ h^{-1}
550 ℃	160 MPa	10,300 h	$>$ 17,750 h	-	$< 0.142 \times 10^{-6}$ h^{-1}
550 ℃	145 MPa	12,500 h	$>$ 22,279 h	-	$< 0.031 \times 10^{-6}$ h^{-1}

Tab. 3.3. Results of creep tests conducted at 550 ℃ on smooth specimens of Grade 92 steel.

In Table 3.3, results corresponding to the fractured specimens show that the tertiary creep stage represents approximatly 30 to 60 % of the specimen lifetime.

The secondary creep strain rate for each applied stress is estimated based on a linear fit. As tertiary creep stage has not begun yet for the tests carried out under 145, 160, 175, 185 and 190 MPa, only the upper limit of the secondary creep strain rate is given for these tests. Considering this approximation, Fig. 3.10 presents the empirical relationship between time to rupture and secondary creep rate proposed by Monkman and Grant more than fifty years ago [Monkman and Grant, 1956]:

$$t_f \left(\dot{\varepsilon}_s\right)^m = C \tag{3.1}$$

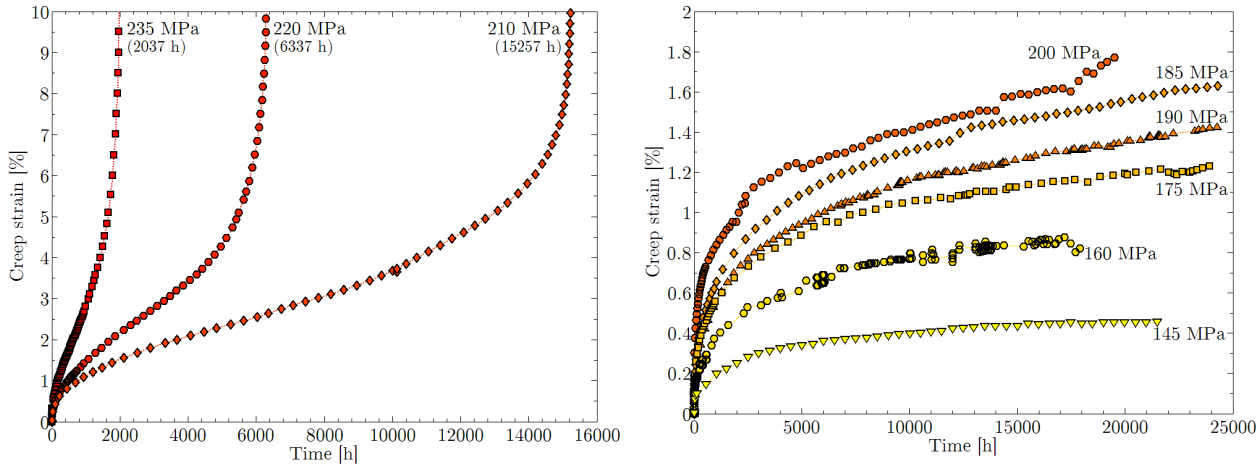

(a) (b)

Fig. 3.8. Creep curves of Grade 92 steel at 550 ℃ for different stresses: (a) fractured specimens and (b) tests in progress.

Temperature	Applied stress	Beginning of secondary creep stage	Beginning of tertiary creep stage	Time to rupture	Secondary creep strain rate
600 ℃	165 MPa	600 h	1,450 h	2,612 h	13.8×10^{-6} h^{-1}
600 ℃	145 MPa	1,300 h	6,810 h	13,995 h	1.58×10^{-6} h^{-1}

Tab. 3.4. Results of creep tests conducted at 600 ℃ on smooth specimens of Grade 92 steel.

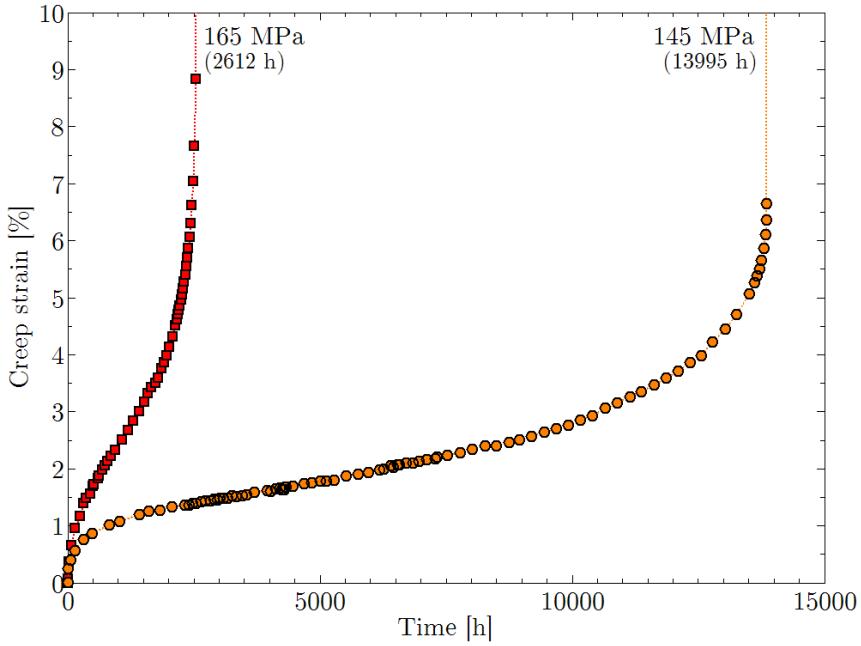

Fig. 3.9. Creep curves of Grade 92 steel at 600 ℃ under 165 and 145 MPa.

Eq. 3.1 can be written in logarithmic form:

$$\log\left(\dot{\varepsilon}_s\right) = m' \log\left(t_f\right) + C' \tag{3.2}$$

In both equations, m, m', C, and C' are constants. For the moment, the limited number of plots for Grade 92 steel creep tests at 550 and 600 ℃ in this study does not permit us to evaluate correctly the Monkman-Grant equation. In order to adjust the parameters, creep data from the present work are compared with the results of creep test performed on Grade 92 steel at 600 and 650 ℃ by Panait [Panait, 2010] and Ennis [Ennis et al., 1997, Ennis and Czyrska-Filemonowicz, 2003].

Fig. 3.10 shows that Monkman-Grant equation can be fitted on creep data with $m' = -1.2$ and $C' = -2.1$. These values are close to those established for Grade 91 steel [Haney et al., 2009]. In these conditions, it is possible to predict the time to rupture of specimens which are already in the tertiary creep stage. Thus, the time to rupture of the creep specimen at 200 MPa is predicted to be 62,100 hours. For tests carried out under lower stress values, the predictions based on the Monkman-Grant relationship must be handled carefully. Indeed, several studies [Povolo, 1985, Dlouhý et al., 2009] lead to the conclusion that the exponent m different from 1 compensates for stress dependencies of the rupture strain and the creep curve shape factor. In the low stress domain where the creep rupture strain significantly decreases, the extrapolation of the short term data may lead to large overestimation of the creep life.

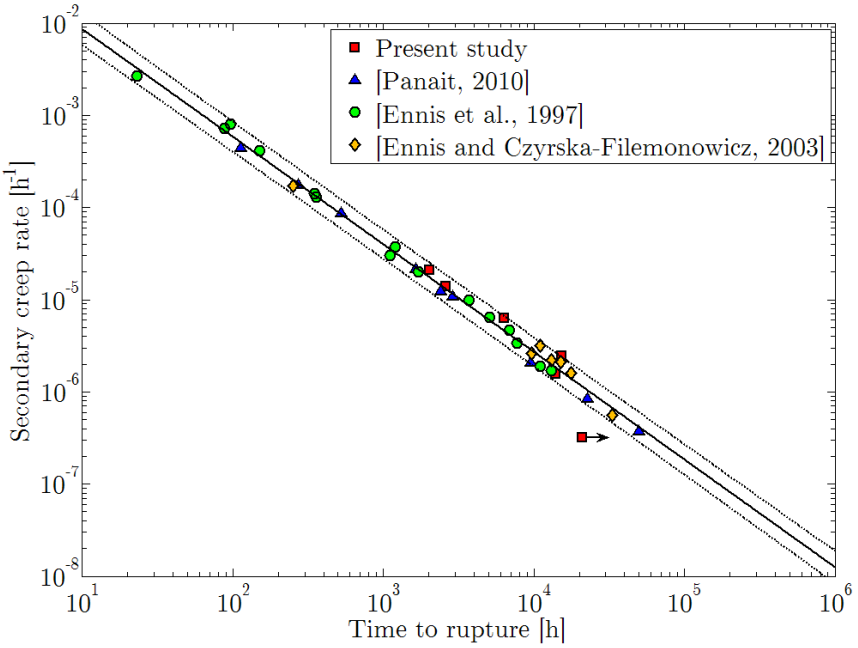

Fig. 3.10. Monkman-Grant equation plots for Grade 92 steel. Continuous straight line corresponds to Eq. 3.2 with $m' = -1.2$ and $C' = -2.1$. Dotted straight lines correspond to the 95 % confidence interval.

3.1.3 Cyclic test including tensile holding periods

In the present work, one cyclic loading test with tensile holding periods was conducted in order to study the interaction between cyclic and creep flow behaviour. This test results are compared with the results obtained during similar cyclic loading test but without holding time in terms of macroscopic mechanical behaviour.

3.1.3.1 Experimental conditions and specimen geometry

A cyclic test including tensile holding periods was conducted at CEA/SRMA laboratory using specimen geometry FFL4, shown in Fig. 3.1. It was carried out in the same conditions as the cyclic tests presented in subsection 3.1.1.1. The test was performed under total strain control. During tensile holding periods, the stress was held constant up to 0.5 % of creep strain or until 12 hours of creep time is reached. Tensile and compressive stress peaks where recorded for all cycles. Stress-strain hysteresis loops were recorded for selected cycles (about 830 points per loop).

This cyclic test including tensile holding periods was carried out at 2×10^{-3} s^{-1} for a total cyclic strain amplitude of $\pm$ 0.35 % and a tensile creep strain of 0.5 %. These experimental conditions were chosen in order to compare this test to a pure fatigue test performed in the same cyclic conditions.

3.1.3.2 Creep-fatigue mechanical behaviour

Cyclic deformation is known to induce a decrease in creep resistance of tempered martensite steels. Indeed, a significative increase in secondary creep strain rate has been observed for a specimen after cycling, compared to the as-received state [Dubey et al., 2005, Fournier et al., 2011a]. These results seem to be linked to the microstructural evolution observed during cyclic tests, as will be discussed in section 3.3.

The results of the present creep-fatigue test are presented in Table 3.5. In terms of number of cycles, creep holding periods induce a reduction of lifetime by more than 80 % compared to a pure fatigue test performed in the same cyclic conditions.

Strain rate (s^{-1})	ΔE_{fat} (%)	ΔE^p_{creep} (%)	ΔE^p (%)	$N_{50}(0.5\%)$	$N_f(0.5\%)$	$N_{50}(0.5\%)/N_{50}(0\%)$
2×10^{-3}	$\pm$ 0.35	0.5	0.82	787	832	0.18

Tab. 3.5. Cyclic loading test including tensile holding periods results on Grade 92 steel at 550 ℃ for a cyclic strain amplitude of $\pm$ 0.35 % and a tensile creep strain up to 0.5 %. $N_{50}(0.5\%)/N_{50}(0\%)$ correspond to the ratio of number of cycles N_{50} with and without holding periods at the maximum load.

The hysteresis loops presented in Fig. 3.11(a) show significative softening of the specimen during the test. They are characterized by an asymmetry between the peak stress in tension and in compression. This phenomenon is induced by the tensile holding periods: indeed, the total fatigue strain is equal to 0.3 % in tension whereas it is equal to 0.8 % in compression. During the test, for the 800^{th} cycle, damage influence is visible on the compressive part of the cycle as a decrease in the initial linear slope during unloading. The creep time recorded for each cycle is reported in Fig. 3.11(b). Its evolution is thought to be governed by two phenomena, which have opposite effects: the decrease in stress applied during the holding periods and the coarsening of the microstructure. The creep time evolution during the test follows three stages as found for Grade 91 steel [Fournier et al., 2011a]:

1. For the first twenty cycles, the fast decrease in dislocation density and subgrain growth due to cyclic loading (see section 3.3) leads to a significative softening and to a fast decrease in the peak tensile stress: the creep time increases from 380 s to about 2,000 s.
2. From the 20^{th} up to the 500^{th} cycle, the mean creep time value slightly decreases: subgrain growth and decrease in dislocations induce a decrease in creep resistance.
3. After the 500^{th} cycle, the softening behaviour leads to a gradual decrease in the peak tensile stress and to an increase in the mean creep time. At the end of the test, damage is a major factor which leads to fast increase in creep holding time.

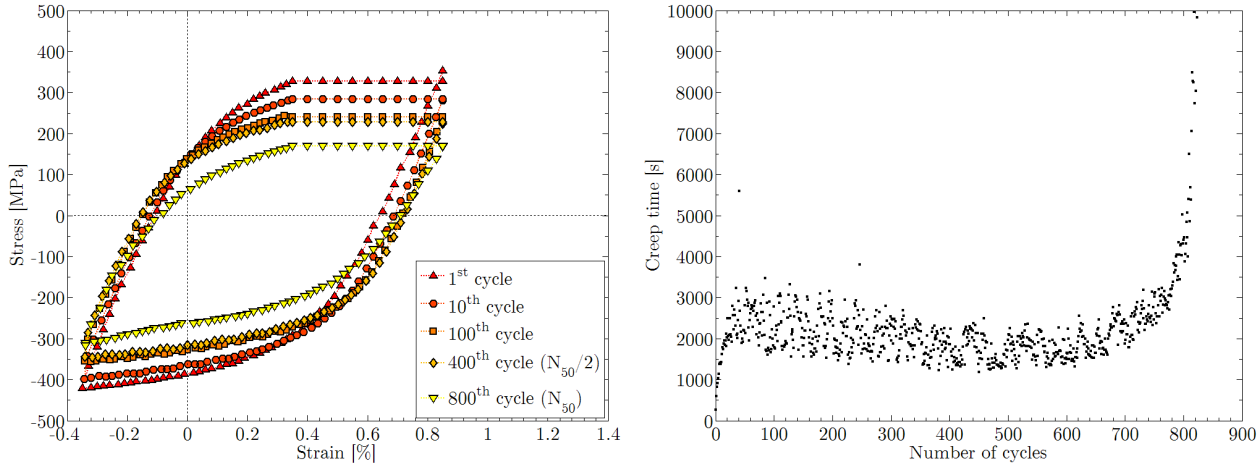

(a) (b)

Fig. 3.11. Mechanical behaviour of Grade 92 steel during the creep-fatigue test at 550 ℃: (a) hysteresis loops recorded at 1^{st}, 10^{th}, 100^{th}, 400^{th} (corresponding approximatively to $N_{50}/2$) and 800^{th} (corresponding approximatively to N_{50}) cycles and (b) evolution of creep time during each cycle.

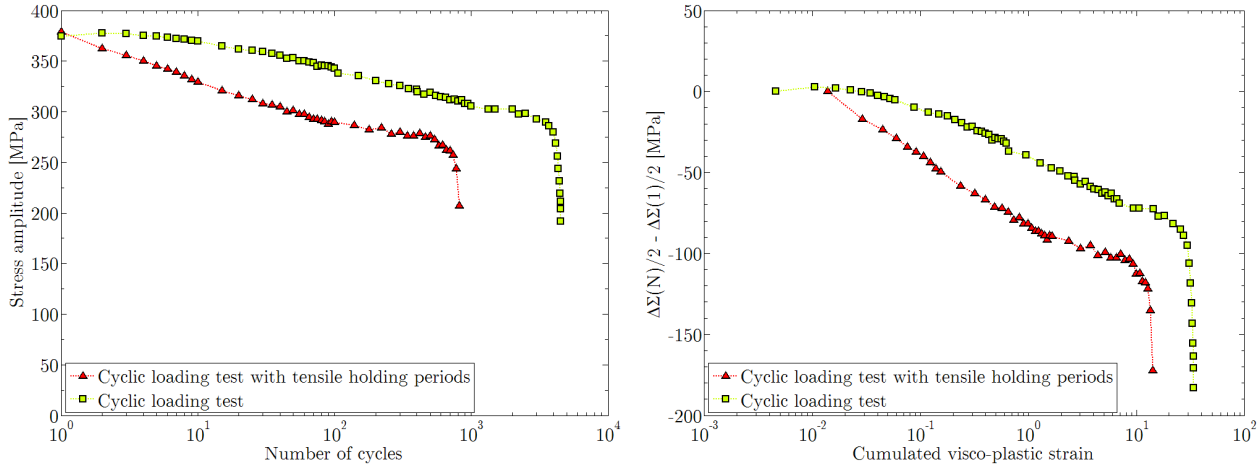

(a) (b)

Fig. 3.12. (a) Evolution of the peak tensile stress during cyclic tests at 2×10^{-3} s^{-1} at 550 ℃ for a strain amplitude of ± 0.35 % with and without tensile holding period (creep strain: 0.5 %) and (b) evolution of the difference between the peak tensile stress at the N^{th} cycle and at the first cycle during cyclic tests at 2×10^{-3} s^{-1} at 550 ℃ for a strain amplitude of ± 0.35 % with and without tensile holding period (creep strain: 0.5 %), as a function of cumulated visco-plastic strain.

Fig 3.12 presents the softening curves with and without tensile holding period. In terms of cumulated visco-plastic strain, the softening behaviour is more significant for creep-fatigue than for pure cyclic loading. Moreover, creep-fatigue induces a decrease in specimen lifetime. The fractured specimen has a lower cumulated visco-plastic strain than the specimen after pure cyclic loading. These results suggest that cyclic loading test with tensile holding period leads to a larger microstructural evolution than pure cyclic loading.

3.2 Macroscopic analysis of softening during cyclic loading

To improve the understanding of softening during cyclic loading tests, the evolution of the isotropic R, the kinematic X and the viscous Σ_v parts of the macroscopic stress was studied in detail. This partition is used to investigate the mechanisms responsible for the mechanical behaviour of crystalline materials under cyclic loading [Cottrell, 1953, Lemaitre and Chaboche, 1990, Fardoun et al., 1997, Feaugas and Gaudin, 2001, Polák et al., 2001a, Polák et al., 2001b, Sauzay et al., 2005, Fournier et al., 2006b, Fournier et al., 2006a, Blum and Eisenlohr, 2009].

The sum of the isotropic and viscous parts, called effective stress, corresponds to short-range interactions and is assimilated to the stress required to move a dislocation locally [Haddou et al., 2004]. Thus, this quantity depends mainly on solid solution, small precipitates and other short-range obstacles to mobile dislocations. The kinematic stress corresponds to long-range interactions, which are divided into two contributions to the internal stress [Feaugas and Haddou, 2003]:

- Intergranular stress induced by subgrain boundary effects (production of glissile dislocations in the neighbouring subgrain) and plastic strain incompatibilities between neighbouring subgrains due to crystallographic misorientations.
- Intragranular stress which corresponds to the heterogeneous distribution of dislocations in subgrains.

A procedure based on both Cottrell's method and statistical process control principles was developed by Fournier et al. for highly viscous materials [Fournier et al., 2006b]. This is used to automatically extract and study the evolution of the three components during one of the two cyclic loading tests at 550 ℃ with a strain amplitude of $\pm$ 0.35 % and a strain rate of 2×10^{-3} s^{-1} (Fig. 3.13).

Both in compression and in tension presented in Fig. 3.14, R and Σ_v are constant during the test: they do not decrease, except at the very end of the test, due to macroscopic cracks in the specimen. However, the evolution of X shows a gradual decrease: during the first cycles, X is about 70 MPa higher that R, whereas their respective values are equal at the end of the test. Thus, similarly to the case of Grade 91 steel [Fournier et al., 2006b], cyclic softening of Grade 92 steel during cyclic loading at 550 ℃ is mainly due to a decrease in kinematic hardening [Yaguchi and Takahashi, 2000] *i.e.* to a decrease in long-range interactions, probably induced by the decrease in dislocation density and the coarsening of laths and/or the vanishing of low-angle subgrain boundaries [Eggeler et al., 1987, Abe, 2004, Sauzay, 2009].

Concerning the cyclic test performed at 550 ℃ with a strain amplitude of $\pm$ 0.35 % and a strain rate of 1×10^{-5} s^{-1}, the significant noise which affects experimental data did not permit us to apply the same procedure to extract each stress contributions (see Fig. 3.4(b)). However, the curves presented in Fig. 3.5 show similar trends for both tests: a decrease in the value of X is also expected for test at lowest strain rate. In order to confirm these results, microstructural observations are presented in section 3.3.

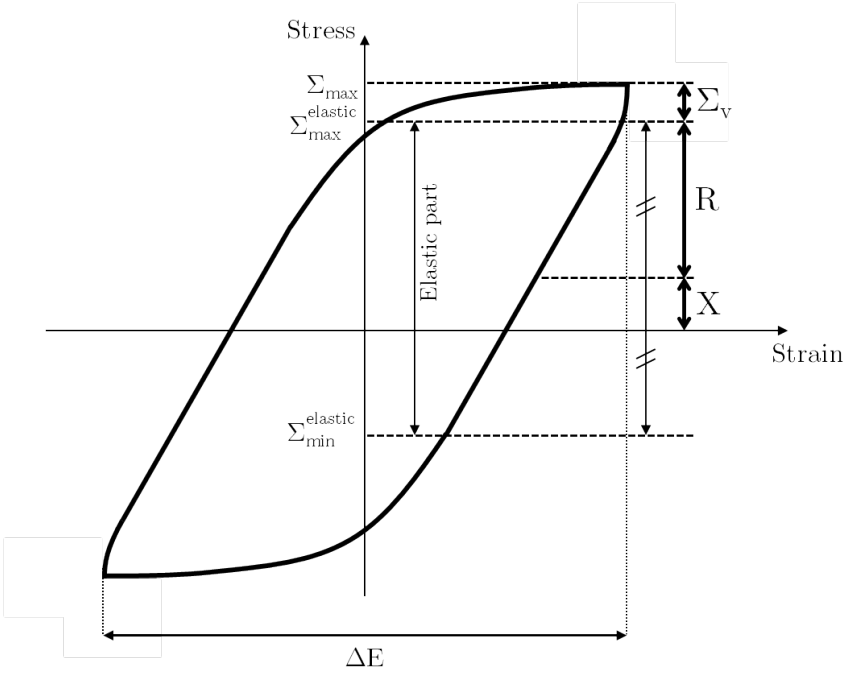

Fig. 3.13. Scheme of the stress partition applied to a schematic hysteresis loop.

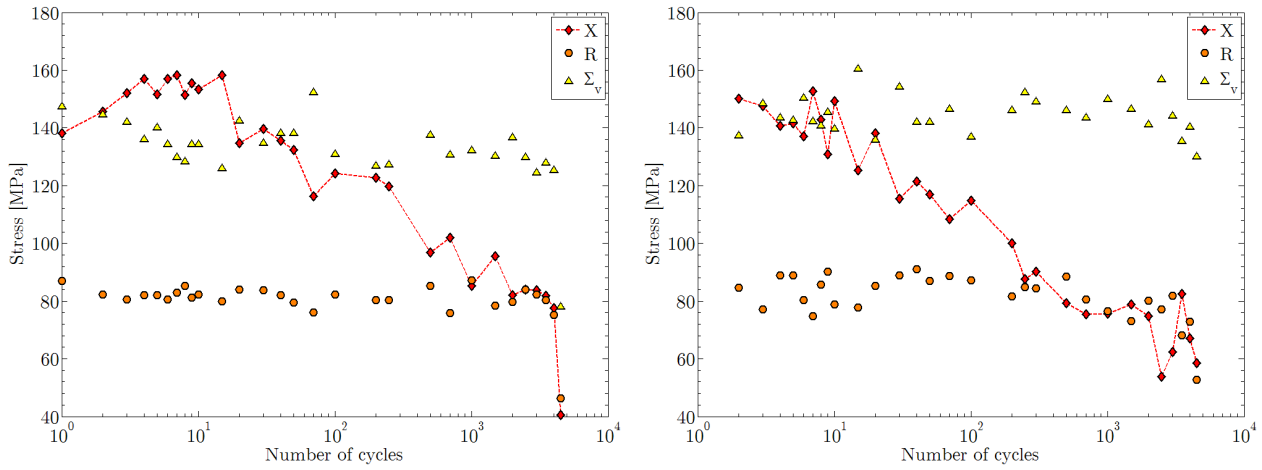

Fig. 3.14. Evolution of the kinematic (X), isotropic (R) and viscous (Σ_v) contributions to the total stress for a cyclic test at 550 ℃ with a strain amplitude of $\pm$ 0.35 % and a strain rate of 2×10^{-3} s^{-1} (a) in compression and (b) in tension.

3.3 Observations of microstructural evolutions during cyclic loading tests

The microstructure of 9% chromium tempered martensitic steels is presented in section 1.2. Various scales (former austenite grains, packets, blocks, laths and subgrains) are involved. The creep resistance of these materials is improved by the large number of obstacles which add pinning points and inhibit the dislocation motion (several kinds of boundaries, high dislocation density, small precipitates, solid solution strengthening by Mo and W solute atoms).

Due to the applied heat treatment, this microstructure is stable during thermal exposure up to about 550 ℃. For higher temperature, microstructural evolution is observed. At 600 ℃, thermal exposure leads to a slight increase in subgrain size [Ghassemi-Armaki et al., 2009, Stratil et al., 2011], a decrease in misorientation of low-angle boundaries [Dronhofer et al., 2003, Sanchez-Hanton and Thomson, 2007] and a decrease in dislocation density [Pešička et al., 2004, Panait et al., 2010a]. Growth of the $M_{23}C_6$ precipitates is observed up to 26,000 h [Hättestrand and Andrén, 2001] whereas the increase in size of MX precipitate is negligible [Gustafson and Hättestrand, 2002, Paul et al., 2008], even after creep test longer than 100,000 h [Panait et al., 2010b]. However, for higher temperature, precipitates coarsen faster and larger: at 750 ℃, MX precipitates size increase and the growth of $M_{23}C_6$ precipitates is larger [Sawada et al., 2001].

During high-temperature mechanical loading, microstructural evolution is faster and more pronounced than during stress-free thermal exposure [Orlová et al., 1998]. To summarize, several microstructural evolution mechanisms proposed in literature and observed at 550-600 ℃ are listed below [Nagesha et al., 2002, Shankar et al., 2006]:

1. Evolution from the initial thin lath and subgrain microstructure to larger equi-axed subgrains.
2. Decrease in dislocation density, initially high due to martensitic transformation (even after subsequent temper heat treatment).
3. Coarsening of precipitates if time exposure and temperature are high enough.

Some other mechanisms are observed at higher temperature or for tempered martensite-ferritic steels with a different chemical composition. Thus, during creep exposure over 600 ℃, Laves phase precipitates nucleate [Hättestrand et al., 1998]. Observations in tungsten-alloyed 9%Cr show that the presence of tungsten provide nucleation of a larger number of Laves phase particles [Hättestrand and Andrén, 2001, Korcakova et al., 2001] and reduces their coarsening during long-term creep exposure, with respect to steels containing only Mo, such as in Grade 91 steel, which probably leads to the improvement of creep resistance [Hald, 2008]. For 12%Cr steels, the modified Z-phase nucleates during long-term creep exposure apparently at the expense of MX precipitates [Sawada et al., 2006], leading to a creep strength degradation at long-term [Sawada et al., 2007]. Although the modified Z-phase is observed in 9%Cr steels after long-term creep tests at 600 ℃ [Sawada et al., 2006], it does not obviously induce a loss of creep resistance [Panait et al., 2010a].

Although Kim and Weertman observed coarsening of carbides during low-cycle fatigue including hold time at 593 ℃ in a modified 9Cr-1Mo-VNb steel [Kim and Weertman, 1988], this phenomenon does not seem to be significant during cycling at 550 ℃ [Fournier et al., 2009b]. Moreover, the addition of boron in Grade 92 steel contributes to reducing the coarsening rate of $M_{23}C_6$ precipitates [Hättestrand and Andrén, 1999, Abe et al., 2004, Abe, 2011] and stabilizing subgrain boundaries [Eggeler and Dlouhý, 2005]. Moreover, recent observations show that carbide coarsening is not significant (in Grade 91 steel) after short-time creep-fatigue tests at 550 ℃ [Fournier et al., 2011a]. Concerning the lost of solid

solution strengthening, Hald showed that a decrease in concentration of molybdenum and tungsten solute atoms due to Laves phase precipitation has a negligible influence on creep resistance in 9-12%Cr steels [Hald, 2008]. Consequently, the following study only focuses on the evolution of subgrain size and dislocation density, which appear to be the main microstructural changes in Grade 92 steel during cyclic tests at 550 ℃.

3.3.1 Evolution of the subgrain size distribution

3.3.1.1 Methodology

Subgrain and dislocation observations presented in this study were carried out using a PHILIPS EM430 Transmission Electron Microscope operated at 300 kV. One thin foil was taken out of each of five specimens after cyclic tests at ± 0.35 % and 550 ℃:

- As-received material
- Specimen of interrupted test after 60 cycles at 1×10^{-5} s^{-1}
- Specimen of interrupted test after 300 cycles at 1×10^{-5} s^{-1}
- Specimen of interrupted test after 1,000 cycles at 1×10^{-5} s^{-1}
- Fractured specimen at 1×10^{-5} s^{-1} (3,960 cycles)
- Fractured specimen at 2×10^{-3} s^{-1} (4,552 cycles)

For each specimen, thin foils were cut perpendicularly to the loading axes in the gauge length, far from any fracture surface. Their preparation is described in section 2.2.3.3.

To measure the subgrain size distributions, three TEM bright field pictures with a magnification of 5,550 were selected from different observed regions on various thin foils. Observations were performed on an area of interest of about 800 μm^2 for each sample. Subgrains were manually traced on a transparent medium. Then image processing using the Visilog software was applied. The measured subgrain areas were then convected to equivalent discs which permit us to calculate the equivalent diameter. Fig. 3.15 presents the different steps of image processing that were necessary to determine the distribution of subgrain size.

3.3.1.2 Evolution of subgrain size distribution during fatigue test

Fig. 3.16 presents three TEM pictures of Grade 92 steel. In each picture, subgrain boundaries are identified by a change in bright field contrast, due to small misorientations. The picture of as-received steel reveals a fine lath structure, composed by small subgrains (Fig. 3.16(a)). This microstructure is clearly modified after cyclic loading at 550 ℃: the fine subgrain structure changes into a larger microstructure, made of larger equi-axed subgrains. The influence of strain rate on the microstructural evolution is observed by comparing Fig. 3.16(b) with Fig. 3.16(c). TEM pictures show that the microstructural evolution is more pronounced in the fractured specimen after the cyclic test performed at the lowest strain rate. In Fig. 3.16(c), the subgrain size is larger and mobile dislocation density appears to be lower than in Fig. 3.16(b). No obvious difference is observed concerning the precipitate size.

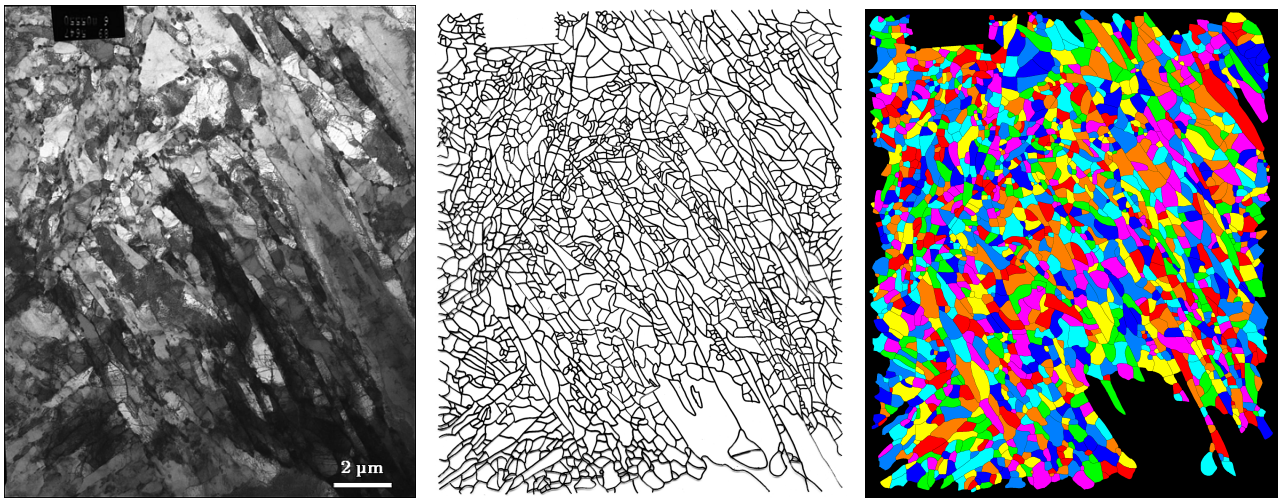

(a) (b) (c)

Fig. 3.15. The three steps required to measure the distribution of subgrain size. Grade 92 as-received steel: (a) bright field TEM picture (magnification of 5,550), (b) extraction of the boundaries and (c) individual subgrains identified by the image processing software.

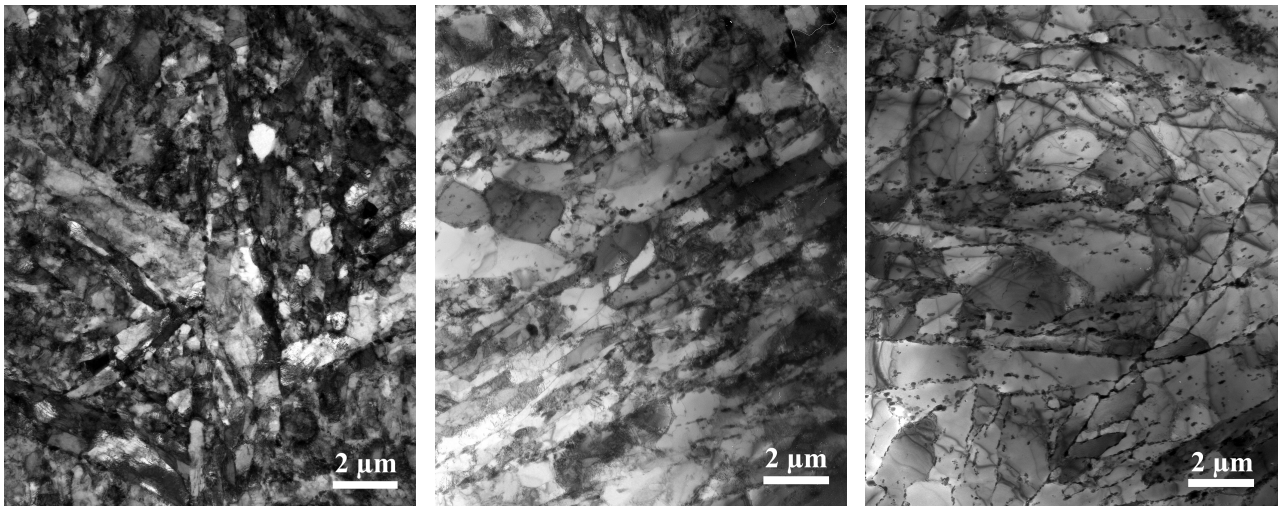

(a) (b) (c)

Fig. 3.16. TEM observations of the microstructure (magnification of 5,550) (a) in the as-received material, (b) in the specimen fractured after 4,552 cycles at 2×10^{-3} s^{-1} and 550 ℃ and (c) in the specimen fractured after 3,960 cycles at 1×10^{-5} s^{-1} and 550 ℃ (far away from the fractured surface).

Several authors describe the subgrain size distribution as approximately log-normal [Cerri et al., 1998, Polcik et al., 1999, Qin et al., 2003, Kostka et al., 2007]. Consequently, the Kolmogorov-Smirnov test and the Pearson's chi-square test were carried out on the three distributions (1, 2 and 3) and from their sum $(1+2+3)$ for each fatigue specimen. The results are presented in Table 3.6. With a probability error fixed to 5 %, the Kolmogorov-Smirnov test clearly shows that subgrain size distribution are drawn from a log-normal probability function, except for the as-received sample. The Pearson's chi-square test shows that the majority of the distributions do not correspond to a log-normal probability function. However, the ajusted log-normal probability functions are plotted in Fig 3.18 for the sum of the three distributions of each sample and describe well the subgrain size distribution.

1×10^{-5} s^{-1}	As-received steel		60 cycles		300 cycles		1,000 cycles		Fractured	
	K.-S.	χ^2	K.-S.	χ^2	K.-S.	χ^2	K.-S.	χ^2	K.-S.	χ^2
1	R	A	A	A	A	R	A	A	A	A
2	R	R	A	A	A	R	A	A	A	A
3	A	R	A	A	A	R	A	A	A	R
1+2+3	R	R	A	A	A	R	A	A	A	R

2×10^{-3} s^{-1}	Fractured	
	K.-S.	χ^2
1	A	A
2	A	A
3	A	R
1+2+3	A	R

Tab. 3.6. Results of Kolmogorov-Smirnov test (K.-S.) and Pearson's chi-square test (χ^2) with hypothesis H_0 "the sample is drawn from a log-normal distribution" for various subgrain size distributions of samples. A and R mean that H_0 is accepted or rejected with an error probability of 5 %, respectively.

For each sample, 1,000 to 5,000 subgrains were measured. Table 3.7 presents the mean subgrain equivalent diameter, d, for each sample. The mean value measured for the as-received steel corresponds to the mean value reported in literature for Grade 92 steel ($0.3 \leq \bar{d} \leq 0.5$ µm) [Ennis et al., 1997, Ennis and Czyrska-Filemonowicz, 2003, Ghassemi-Armaki et al., 2009]. In the specimens subjected to cyclic loading until failure, the growth of the mean subgrain size is observed. After cyclic test performed at 550 ℃, the mean subgrain size is multiplied by a factor 1.7 for a strain rate of 2×10^{-3} s^{-1} and 2.1 for a strain rate of 1×10^{-5} s^{-1}, respectively. It clearly shows the influence of strain rate under cyclic loading: the lower the strain rate, the larger the subgrain size after cycling. These growth factors are comparable to the observations carried out after cyclic loading performed at $\pm$ 0.3 % and 2×10^{-3} s^{-1} on a Grade 91 steel at 550℃ ($\times$1.9) [Fournier et al., 2009b].

3.3.1.3 Effect of the strain on subgrain size evolution

Fig. 3.17 presents the evolution of the mean subgrain size during cycling. The values measured on different specimens under cyclic loading at 1×10^{-5} s^{-1} show that the evolution rate of the subgrain width during testing is not constant. The subgrain growth is faster at the beginning of the test and decreases until fracture. This observation permits us to conclude that, during low-cycle fatigue test carried out with a constant total axial strain, the microstructural instability leads to a fast evolution of subgrain size although the value of the cumulated visco-plastic strain is low.

This microstructural evolution is linked to the evolution of stress during the test presented in Fig. 3.5(a). In similar manner as the subgrain growth evolution, the decrease of the stress amplitude

Strain rate	Sample	n	$\bar{d}$ (µm)	s (µm)	Median (µm)	$\bar{d}/\bar{d}_0$
-	As-received	4,956	0.37 ± 0.1	0.17	0.347	1.0
1×10^{-5} s^{-1}	Interrupted - 60 cycles	3,242	0.45 ± 0.03	0.23	0.406	1.22
1×10^{-5} s^{-1}	Interrupted - 300 cycles	2,073	0.52 ± 0.02	0.26	0.469	1.41
1×10^{-5} s^{-1}	Interrupted - 1,000 cycles	1,438	0.61 ± 0.05	0.33	0.542	1.65
1×10^{-5} s^{-1}	Fractured - 3,960 cycles	1,004	0.76 ± 0.08	0.39	0.680	2.05
2×10^{-3} s^{-1}	Fractured - 4,552 cycles	1,605	0.62 ± 0.12	0.31	0.557	1.67

Tab. 3.7. Results of the TEM observations performed on specimen samples after cyclic loading at 550 ℃. The number of counted subgrains is n (summarized over the three investigated region from each sample) and s is the standard deviation. $\bar{d}$ is the mean equivalent diameter of the n subgrains for each sample. The error corresponds to the interval in which the mean equivalent diameter values of each of the three distributions are included. $\bar{d}/\bar{d}_0$ is the ratio between the mean subgrain equivalent diameter of the considered sample and the mean subgrain equivalent diameter of the as-received steel.

is more pronounced at the beginning of the test than just before fracture.

The subgrain growth means a reduction of the number of subgrain boundaries. The fast decrease in the number of these obstacles, which already happen for low values of cumulated visco-plastic strain, should contribute to a drop of long-range obstacles to dislocation motion and to the observed evolution of the kinematic stress observed in Fig. 3.14 [Morrison and Moosbrugger, 1997, Moosbrugger et al., 2000, Haddou et al., 2001, Feaugas and Haddou, 2003]. The microstructural evolution, significant even for a low value of cumulated visco-plastic strain, is a real challenge for industrial applications. It means that during service condition in nuclear reactor, *i.e.* for low values of cumulated visco-plastic strain, this microstructural degradation could possibly happen and will lead to a decrease in the mechanical strength of the material.

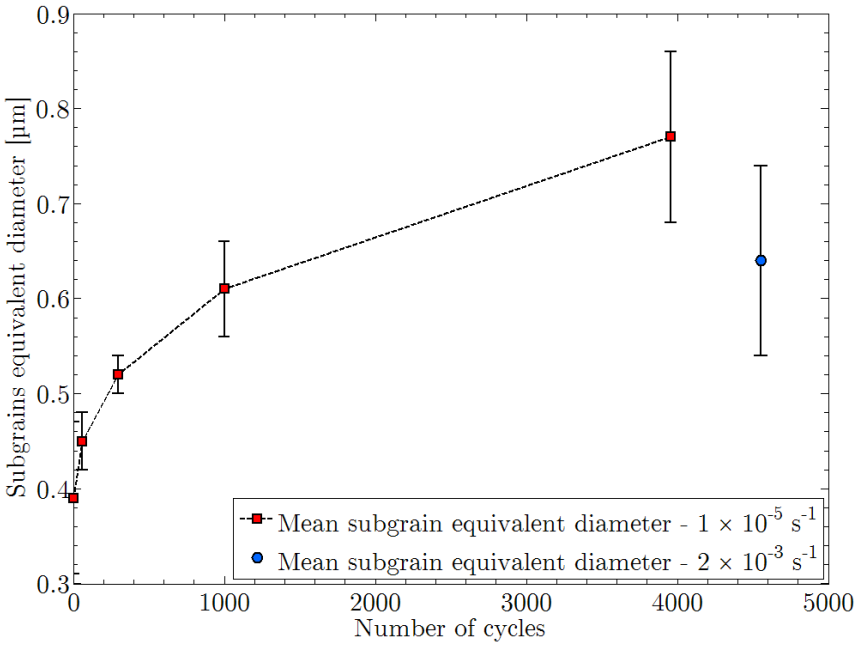

Fig. 3.17. Evolution of the mean subgrain equivalent diameter during cyclic loading tests performed at 550 ℃.

The evolution of the mean subgrain size gives us a global information about the microstructural degradation. In this study, we choose to focus on the evolution the subgrain size distribution during cyclic loading. The subgrain size distributions of the samples corresponding to the as-received material,

the three interrupted specimens and the fractured specimen after tests performed at 1×10^{-5} s^{-1} are plotted in Fig. 3.18. The number of bins is determined by the number of measured subgrain (it is equal to $\sqrt{n}$) and the distributions are normalized.

For the as-received material, the distribution is characterized by low scatter, meaning that a large majority of subgrains has a equivalent diameter close to the mean value, equal to 0.37 µm. The coefficient of variation $s/\bar{d}$ of the distributions and the difference between the maximum and minimum values of equivalent subgrain diameter increase with the number of cycles (see Fig. 3.19). These curves permits us to conclude that the scattering of the subgrain size distribution increases during the test. This indicates that the subgrain growth is more pronounced for larger subgrain than for smaller subgrains [Eggeler et al., 1987].

This result is confirmed by the plot of the cumulative distribution functions of subgrain equivalent diameter (Fig. 3.20). It shows that a large majority of subgrain increase in size during the test and it permits us to conclude that subgrain growth is rather homogeneous during cycling at 550 ℃ for a total strain amplitude of ± 0.35 %. This result is in accordance with the observations on Grade 91 steel: after cyclic loading with a strain amplitude higher than ± 0.15 % at 550 ℃, subgrain growth was homogeneous, whereas it was heterogeneous for a strain amplitude of ± 0.15 % [Fournier, 2007].

Over all the distributions, the maximum value of subgrain size was lower than $2.5 - 3$ µm. This value corresponds to the block size, defined in chapter 1. It permits us to conclude that the microstructural evolution during cycling is limited to the subgrains: block boundaries appear to be stable during cycling at high temperature [Fournier, 2007].

Subgrain equivalent diameter distributions after two cyclic tests performed at 550 ℃, for a total strain amplitude of ± 0.35 % and at different strain rates (2×10^{-3} s^{-1} and 1×10^{-5} s^{-1}) are presented in Fig. 3.21(a). According to the results presented in Table 3.7, experimental observations lead to the following conclusions:

- The mean subgrain size is higher for the test performed at 1×10^{-5} s^{-1} after 3,990 cycles than for the test performed at 2×10^{-3} s^{-1} after 4,552 cycles: the lower the strain rate, the higher the visco-plastic strain amplitude, the higher the subgrain coarsening (see Table 3.2).

- The spread of subgrain size distribution is higher for the lower strain rate.

The observations performed on both specimens after fracture show that strain rate has an influence on the microstructural evolution. For the lowest value of strain rate, the subgrain growth is more pronounced and more heterogeneous than for the highest value of strain rate. Cyclic loading performed at the lowest strain rate induces a significant destabilization of the microstructure, more pronounced than for the highest strain rate, which could explain the higher softening observed at the lowest strain rate (Fig 3.5). However, even if the number of cycle before fracture is lower for the lowest strain rate (see Table 3.2), the difference in microstructural evolution between both tests has no noticeable effect on fatigue lifetime in terms of cumulated visco-plastic strain (see Fig 3.5(b)).

Cyclic loadings lead to significant evolution of the subgrain size of Grade 92 steel, and on the microstructural growth of the tempered martensite seels in general. This study has shown that the strain rate imposed for cyclic loading has an influence on the subgrain growth, without leading to a significant reduction of the fatigue lifetime of the material. The study now focuses on the second main evolution observed in tempered martensite steels: the decrease of dislocation density.

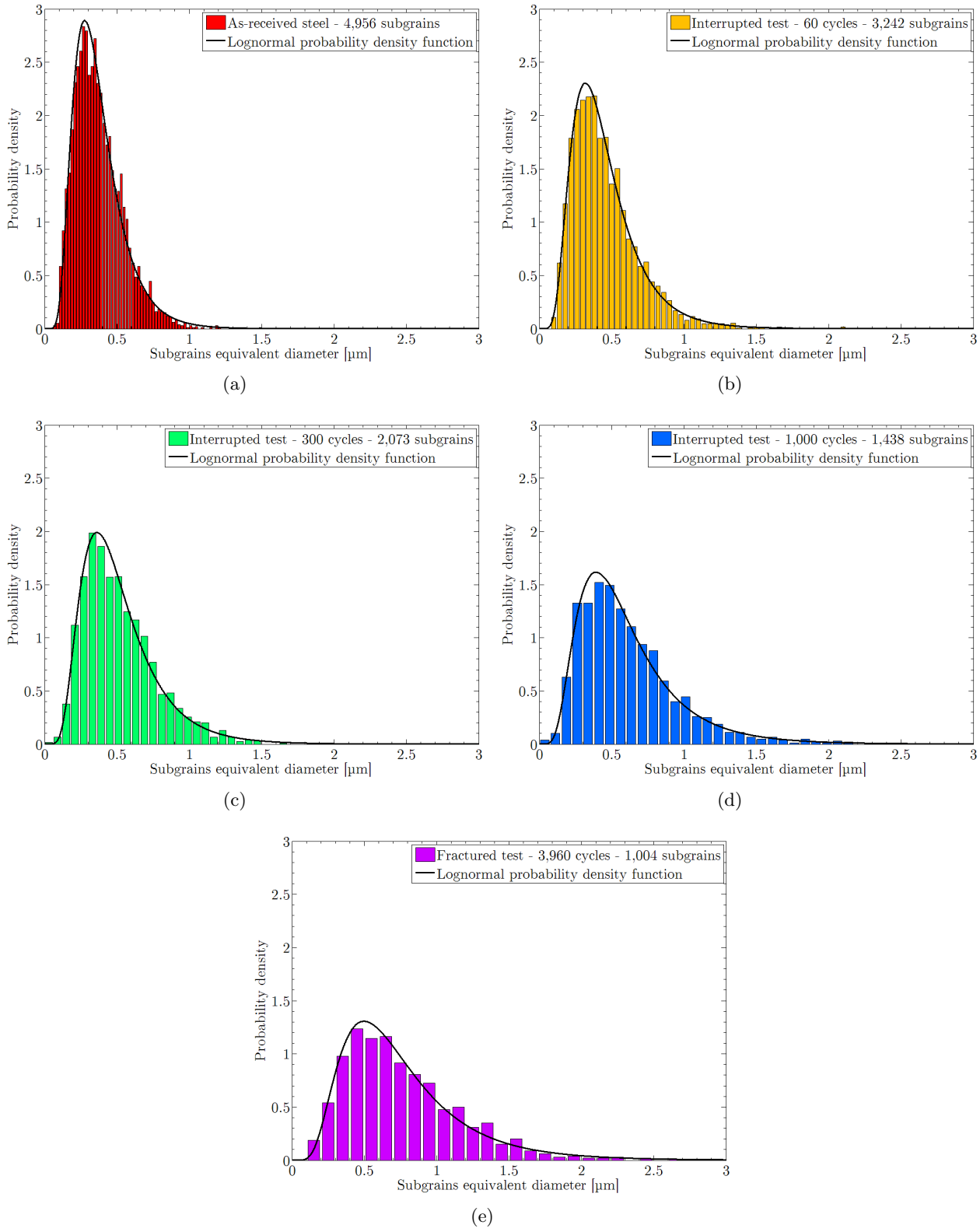

Fig. 3.18. Subgrain size distribution in Grade 92 steel for (a) the as-received sample and after cyclic loading tests at 550 ℃ with a strain amplitude of ± 0.35 % and a strain rate of 1×10^{-5} s^{-1} for (b) the 60 cycles interrupted specimen, (c) the 300 cycles interrupted specimen, (d) the 1,000 cycles interrupted specimen and (e) the 3,960 cycles fractured specimen.

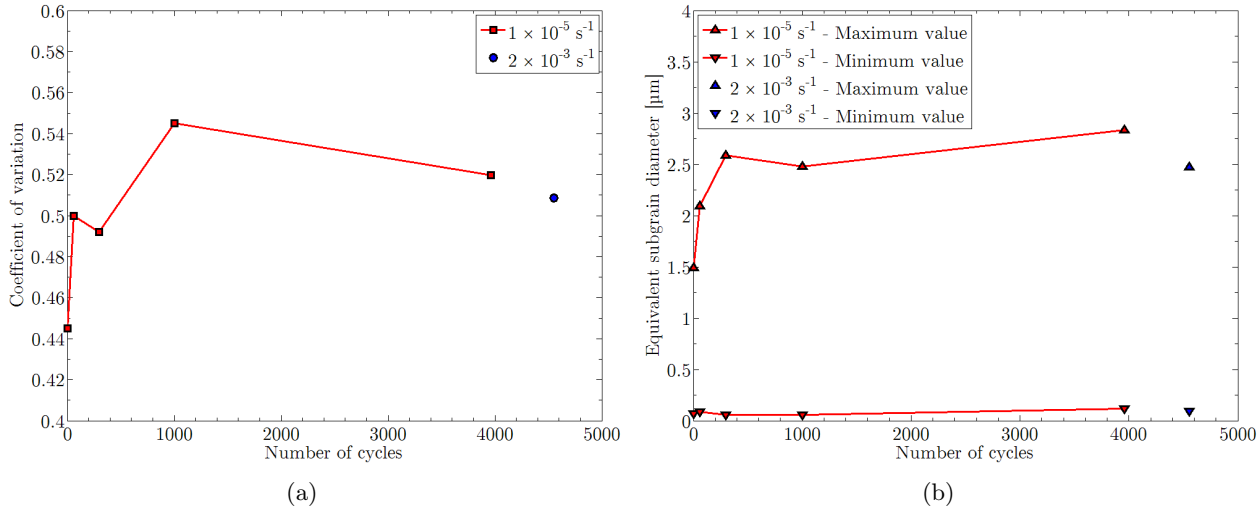

(a) (b)

Fig. 3.19. (a) Evolution of the coefficient of variation defined as the ratio $s/\bar{d}$ with s the standard deviation and $\bar{d}$ the mean subgrain size and (b) evolution of minimum and maximum values of subgrain size during cyclic test at 550 ℃ with a strain amplitude of ± 0.35 % on Grade 92 steel.

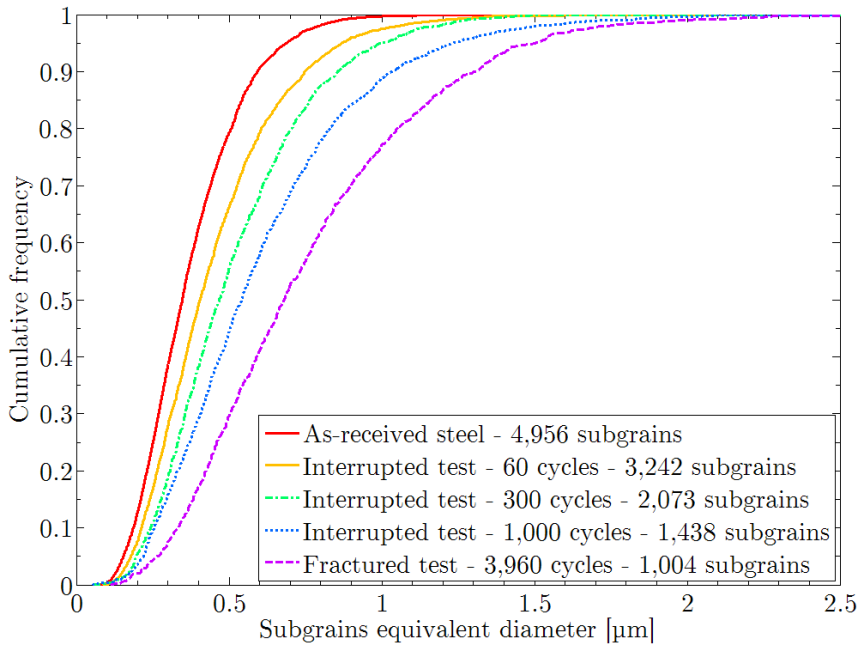

Fig. 3.20. Cumulative distribution functions of subgrain equivalent diameter during cyclic loading tests at 550 ℃ on Grade 92 steel, performed at $\Delta E = \pm$ 0.35 % and 1×10^{-5} s^{-1}.

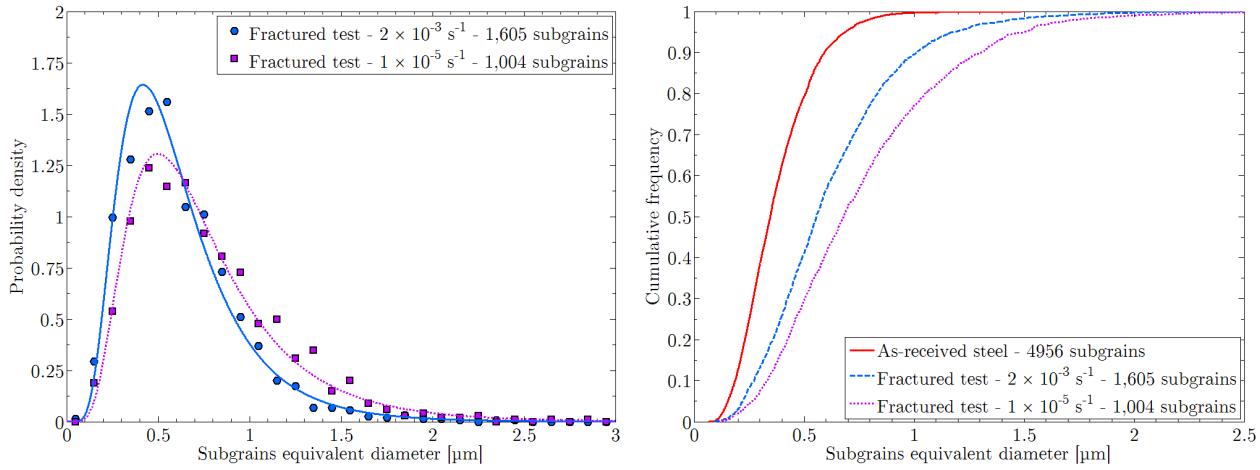

Fig. 3.21. Influence of the strain rate on subgrain evolution during cyclic loading tests performed at 550 ℃ on Grade 92 steel: (a) distribution of subgrain equivalent diameter and (b) corresponding cumulative frequency curves.

3.3.2 Evolution of the dislocation density during high temperature cyclic loading

In tempered martensite steels, the initial thermal heat treatments product a high dislocation density in the as-received material. For the considered Grade 92 steel, we mesured a free dislocation density close to 2×10^{14} m^{-2} (see chapter 2), to be compared to values from 2×10^{14} to 9×10^{14} m^{-2} in literature (these values probably include dislocations which compose the low-angle boundaries), depending on the heat treatment [Ennis and Czyrska-Filemonowicz, 2003]. During high-temperature fatigue testing, the initial high dislocation density decreases significantly leading to a reduction in macroscopic hardness [Kim and Weertman, 1988].

TEM observations performed on as-received material and fractured specimens after cyclic loading at 550 ℃ and 2×10^{-3} s^{-1} and 1×10^{-5} s^{-1} are presented in Fig. 3.22. The dislocation density was measured thanks to linear intercept method, as described in chapter 2. This method permits us to measure an estimation of the free dislocation density within the subgrains. It does not take the heterogeneous distribution of dislocations in the matrix into account: some subgrains have a high dislocation density whereas neighbouring ones seem to be dislocation free (see Fig. 3.23 and [Eggeler, 1989]). In Fig. 3.22, the high dislocation density of the as-received steel decreases significantly, to reach a value close to 1×10^{14} m^{-2} for the high strain rate and a lower value of 3×10^{13} m^{-2} for the low strain rate (Table 3.8).

Specimen	Cyclic strain rate (s^{-1})	Total strain range (%)	Dislocation density (m^{-2})
As-received	-	-	2×10^{14}
Fractured	2×10^{-3}	$\pm$ 0.35	1×10^{14}
Fractured	1×10^{-5}	$\pm$ 0.35	0.3×10^{14}

Tab. 3.8. Estimation of dislocation densities in Grade 92 steel in as-received steel and after cycling.

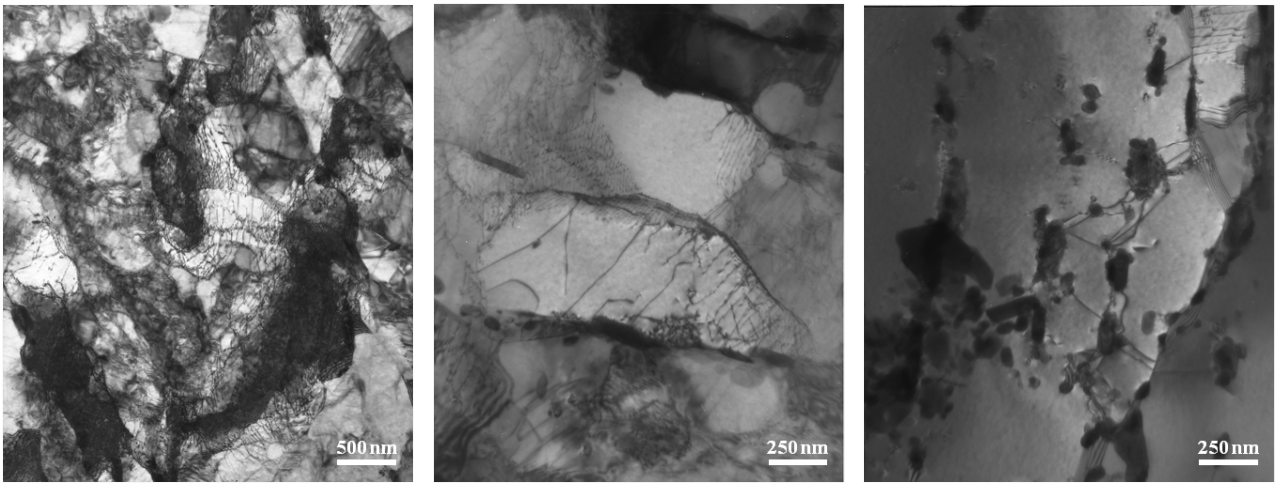

(a) (b) (c)

Fig. 3.22. TEM observations of dislocations within subgrain (a) in the as-received material, (b) in specimen fractured after 4,552 cycles at 2×10^{-3} s^{-1} and strain amplitude of $\pm$ 0.35 % at 550 ℃ and (c) in specimen fractured after 3,960 cycles at 1×10^{-5} s^{-1} and strain amplitude of $\pm$ 0.35 % at 550 ℃ (far away from the fracture surface).

3.3.3 Discussion about deformation and annihilation mechanisms

In the as-received steel, dislocations in the subgrains appear as straight lines, pinned at subgrain boundaries (see Fig. 3.23(a)). On the contrary, Fig. 3.23(b) shows that they are bowed out after cycling (this phenomenon is less pronounced after cycling at high strain rate). This evolution is probably due to the modification of the mobile dislocation character: initially, the main part of dislocations is probably composed by screw dislocations [Wakasa and Wayman, 1981, Guétaz et al., 2003] which are pinned at subgrain boundaries or carbide precipitates localised at boundaries [Mughrabi et al., 1979, Sauzay and Kubin, 2011]. During cycling, these straight screw dislocations bow out and glide in the subgrain. This expansion may lead to the production of mixed dislocations, composed by both screw and edge dislocations.

Fig. 3.24(b) shows the interactions between such dislocations and carbide precipitates. In this picture, the mobile dislocations are pinned between two precipitates. This induces a reduction of their motion and bowing under stress. However, the mechanisms of interaction are not clearly defined. The absence of residual dislocation loops around the precipitates permits us to conclude that Orowan's mechanism does not take place. Other mechanisms of deformation could be considered and studied to explain the crossing of precipitates by dislocations: cross-slip, climb...

The subgrain boundaries were described in chapter 1: their misorientation angle is lower than 5° [Sonderegger et al., 2007, Sonderegger et al., 2008, Tak et al., 2009, Panait et al., 2010a]. Fig. 3.24(a) shows a low-angle boundary observed in Grade 92 steel. It is characterized by a kind of "honeycomb" structure: it is composed by at least two families of dislocations mixed together. Low-angle boundaries can be modelled as arrays of dislocations [Read and Shockley, 1950]. Similar observations carried out for other 9-12%Cr steels have shown the same kind of low-angle boundary structure [Eggeler et al., 1987, Eggeler, 1989, Eggeler et al., 1989, Sauzay, 2009].

The microstructural growth studied in section 3.3.1 is due to the coarsening of the subgrains. This phenomenon can take place if the low-angle subgrain boundaries move or vanish during cycling. After the test, aligned carbides precipitates are observed *within* the larger subgrains (Fig. 3.25). Carbides

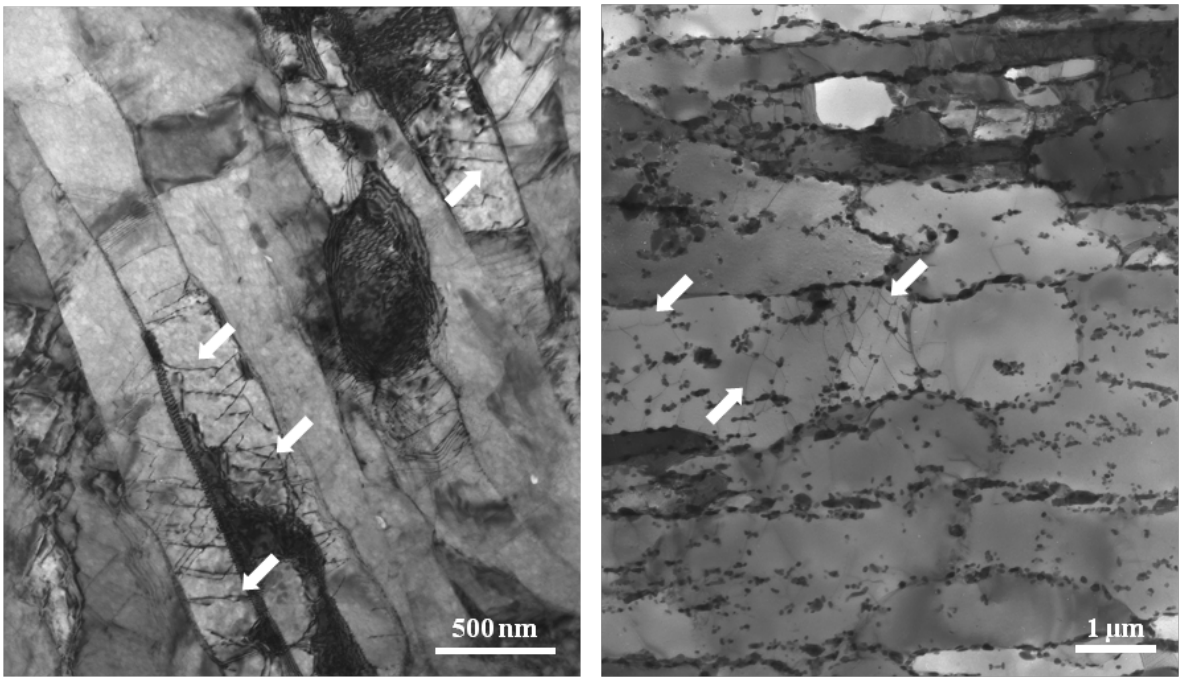

(a) (b)

Fig. 3.23. TEM observations of the dislocations (a) in the as-received material and (b) in fractured specimen after cyclic test at 1×10^{-5} s^{-1} and strain amplitude of $\pm$ 0.35 % at 550 ℃. Mobile dislocations are pointed out by the white arrows.

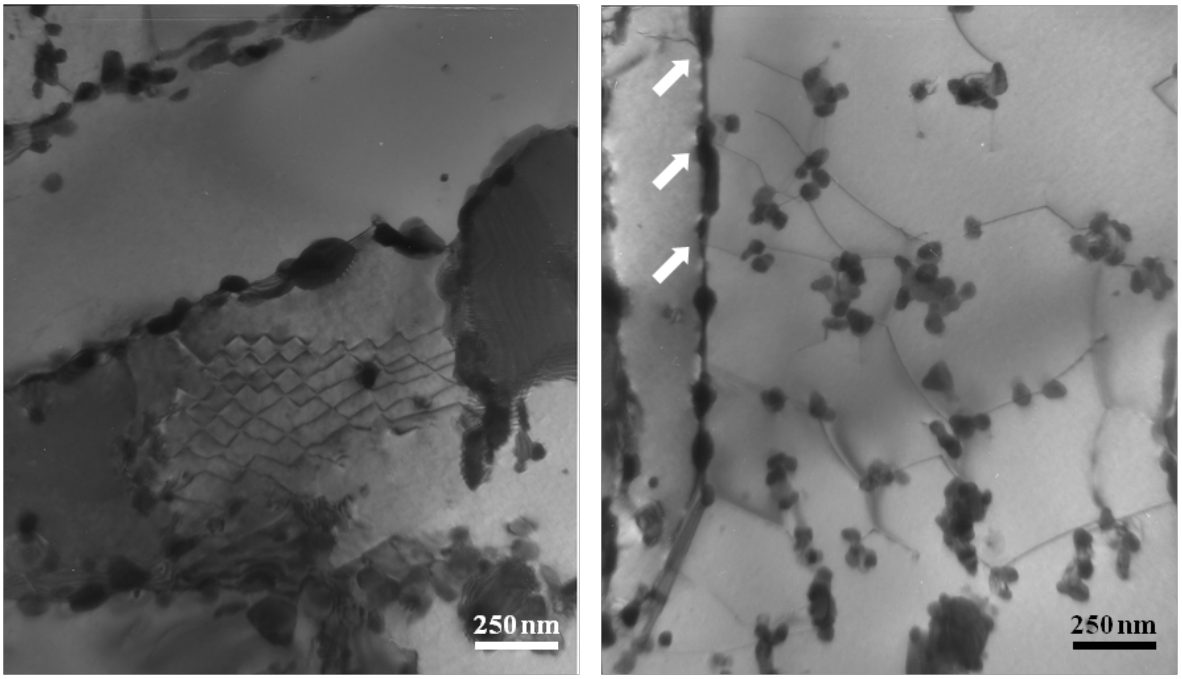

(a) (b)

Fig. 3.24. TEM observations of (a) a low-angle subgrain boundary and (b) the interaction between mobile dislocations and precipitates in the specimen fractured after 3,960 cycles at 1×10^{-5} s^{-1} under a total strain amplitude of $\pm$ 0.35 % at 550 ℃. White arrows point out some dislocations which are pinned on a boundary.

precipitates nucleate during tempering heat treatment at the boundaries [Eggeler et al., 1987, Eggeler and Dlouhý, 2005, Abe et al., 2007] and only MX precipitates are observed in the subgrains [Hättestrand and Andrén, 2001, Abe et al., 2007]. This indicates that the former low-angle boundaries where the carbides precipitates were initially located vanished during cycling (the large number of carbide precipitate prevents the low-angle boundaries from moving). One possible mechanism is proposed: subgrain boundary vanishing during cycling is due to the interaction between the mobile dislocations with the arrays of dislocations which composed the low-angle boundaries [Sauzay, 2009]. Indeed, annihilation can take place between two edge or two screw dislocations with a Burger vector of opposite signs. This phenomenon can occur if their distance is smaller than a critical spontaneous annihilation distance, which is respectively about 2 nm and 50 nm for edge and screw dislocations for copper at room temperature [Essmann and Mughrabi, 1979, Essmann and Differt, 1996] (dislocation climb may be taken into account as well). These mechanisms lead to a decrease in low-angle boundary dislocation density. For a high number of cycles, the vanishing of the low-angle boundary occurs. These hypotheses which permit us to link partially subgrain growth to decrease in free dislocation density are exposed in chapter 4.

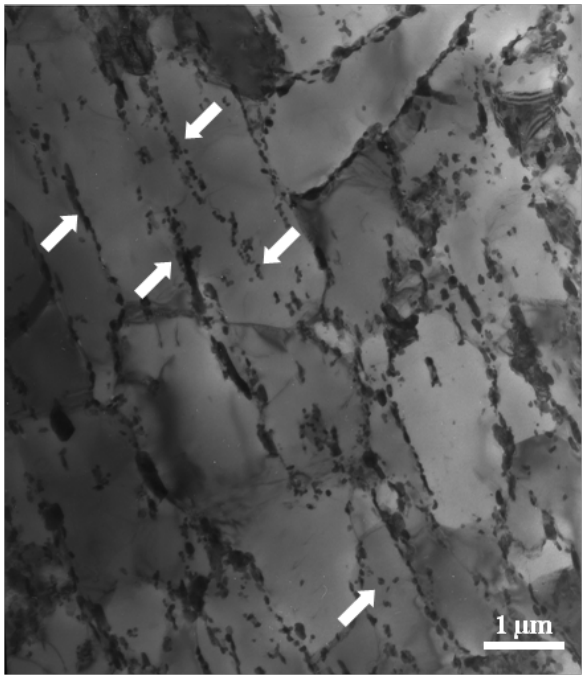

Fig. 3.25. TEM observation carried out after cyclic tests at 550 ℃ on Grade 92 steel, performed at a strain amplitude of $\pm$ 0.35 % and a strain rate of 1×10^{-5} s^{-1}. The white arrows point out aligned carbides precipitates located on former vanished low-angle boundaries.

3.4 Concluding remarks

Cyclic tests, creep tests and cyclic tests including tensile holding periods were carried out at 550 ℃ on a Grade 92 steel. Experimental results lead to the following conclusions:

- According to Manson-Coffin curves, no significant difference between Grade 91 and Grade 92 steels is observed in terms of cyclic lifetime at 550 ℃. Similarly, the parameters of Monkman-Grant equation fitted on Grade 92 steel creep data are close to those established for Grade 91

steel. This suggests that the mecanisms controling cyclic deformation and fatigue lifetime are the same for both steels.

- Grade 92 steel is sensitive to cyclic softening and although it is more pronounced for high values of strain amplitude, this phenomenon is even significant for very low values of visco-plastic strain amplitude (about 10^{-4}).
- Cyclic softening is more pronounced for lower strain rate: the lower the strain rate, the lower the stress amplitude, the higher the visco-plastic strain amplitude per cycle and finally the faster the stress drop. Additionnal effect of time and temperature may play a role. However, the impact of the strain rate on fatigue lifetime is slight.
- Softening behaviour is more pronounced during creep-fatigue than during pure fatigue: it leads to a decrease in fatigue lifetime by about 80 % in terms of number of cycles.
- Similarly to Grade 91 steels, the cyclic softening of the investigated Grade 92 steel at 550 ℃ is mainly due to a decrease in kinematic stress. This indicates a decrease in rather long-range interactions between the mobile dislocations and the dislocation forest or the low-angle subgrain boundaries.
- TEM observations showed that the mean subgrain size increases during cycling. The subgrain size distributions are satisfactory described by log-normal probability density functions. Their evolutions during cycling show that subgrain growth is more pronounced for larger subgrains than for smaller ones, inducing an increase in distribution spread. These phenomena are more pronounced for the lower strain rate.
- A decrease in dislocation density within subgrain is also estimated during cycling from 2×10^{14} m^{-2} down to 0.3×10^{14} m^{-2}. It is more pronounced for low cyclic strain rate.
- The proposed mechanism of interaction between mobile dislocations and low-angle boundaries could account for the TEM observations and partially link decrease in free dislocation density and subgrain growth.

In service conditions, cyclic strain rate and cyclic strain amplitude are expected to be significantly lower than those investigated here. Following the mechanism of deformation described in this chapter, we will now focus on the modelling of the physical mechanisms of deformation, in order to predict both macroscopic mechanical behaviour and microstructural evolution of Grade 92 steel during cycling.

Chapter 4

Modelling of the cyclic behaviour and microstructure evolution during cycling

This fourth chapter focuses on the modelling of the mechanical behaviour of Grade 92 steel during continuous cycling at 550 ℃. The description of the hypotheses of the modelling is divided into two parts: polycrystalline homogeneization (from the block scale to the macroscopic one) and microstructural evolution modelling (subgrain size and dislocation density). Then, the simulations of macroscopic mechanical behaviour and microstructural evolution are presented. Finally, the influence of the values of the parameters on the predictions is studied and discussed.

Ce quatrième chapitre est dédié à la modélisation du comportement mécanique de l'acier Grade 92 lors de sollicitations cycliques continues à 550 ℃. La description du modèle est construite autour de deux axes majeurs : l'homogénéisation polycristalline (du bloc au polycristal) et la modélisation de l'évolution de la microstructure (taille de sous-grain et densité de dislocations). Les résultats des simulations du comportement mécanique macroscopique et de l'évolution microstructurale sont ensuite présentées. Enfin, l'influence des valeurs des paramètres sur les prédictions est étudiée et discutée.

Contents

Abstract (in French) **91**
4.1 Introduction to polycrystalline modelling **93**
4.2 Crystalline constitutive equations **94**
4.2.1 Description and hypotheses of the modelling 94
4.2.2 Isotropic stress 98
4.2.3 Evolution of the kinematic stress 99
4.2.4 Crystal viscoplasticity flow rule 102
4.3 Modelling the microstructural evolutions **103**
4.3.1 Modelling the evolution of dislocation density 103
4.3.2 Modelling of low-angle boundaries misorientation evolution 106
4.3.3 Modelling the subgrain size evolution 108
4.4 Self-consistent homogenization scheme **108**
4.4.1 Thermoelastic modelling proposed by Kröner 108
4.4.2 Molinari's model for viscoplastic material 109
4.5 Choice of the values of the model parameters **110**
4.5.1 Measured, calculated and fixed parameters 110
4.5.2 Identification process 112

4.6 Simulation of cyclic loading 115
4.6.1 Validation of the model on the first macroscopic loop for both strain rates . . . 115
4.6.2 Prediction of cyclic softening for both strain rates 115
4.6.3 Predictions of the macroscopic cyclic softening for different strain amplitudes . 120
4.6.4 Sensitivity of model predictions to the values of model parameters 122
4.7 Concluding remarks 133

Résumé

Ce chapitre est consacré à la modélisation du comportement mécanique et de l'évolution microstructurale de l'acier Grade 92 au cours de sollicitations cycliques à 550 ℃. Dans le cadre de cette étude, un modèle d'homogénéisation polycristalline auto-cohérent est proposé afin de décrire l'adoucissement cyclique des aciers martensitiques revenus à haute température. Ce modèle est capable de prédire le comportement mécanique macroscopique et l'évolution de la microstructure (chute de la densité de dislocations, augmentation de la taille des sous-grains) observée et mesurée au cours du cyclage.

Les équations implémentées dans ce modèle sont fondées sur la description de phénomènes physiques liés à des hypothèses de mécanismes microstructuraux se déroulant lors de la déformation cyclique (interaction entre les dislocations mobiles et les dislocations composant les sous-joints, destruction progressive des sous-joints...). Cette approche permet d'attribuer un sens physique à l'ensemble des paramètres du modèle et de limiter à seulement deux le nombre de variables d'ajustement. Ces derniers (énergie d'activation et volume d'activation) correspondent à l'effet de viscosité et sont ajustés à l'aide des courbes monotones à différentes vitesses de déformation. Ainsi, aucune donnée concernant l'adoucissement cyclique du matériau n'est utilisée pour ajuster ces paramètres. Ce modèle permet donc de prédire l'adoucissement mécanique de l'acier Grade 92 lors d'essais cycliques pour différentes amplitudes de déformation et vitesses de déformation.

L'énergie d'activation et le volume d'activation, seuls paramètres ajustés sur les courbes monotones expérimentales, ont des valeurs de l'ordre de 1,2 eV et 216 b^3 respectivement. Selon des données issues de la littérature [Marmy et al., 1993, Caillard and Martin, 2003], elles correspondent à des mécanismes d'interaction entre les dislocations mobiles et les nuages d'atomes en solution solide, les petits précipités...

Le modèle permet de prédire assez convenablement le comportement mécanique de l'acier Grade 92 durant la première boucle de fatigue, pour deux vitesses de déformation différentes (2×10^{-3} s^{-1} et 1×10^{-5} s^{-1}). Au cours du cyclage, la cinétique d'adoucissement est bien prédite pour l'essai ayant une amplitude de déformation de ±0,35 %. À faible vitesse de déformation, la contrainte maximale en traction prédite est légèrement sous-estimée, alors que, pour une vitesse de déformation élevée, les prédictions sont très proches des valeurs expérimentales. En termes d'évolution microstructurale, le modèle prédit correctement la valeur finale de la densité de dislocations, bien qu'il surestime l'évolution de la taille moyenne de sous-grains au cours de l'essai. L'adoucissement mécanique du matériau est correctement prédit pour des amplitudes de déformation comprises entre ±0,25 et ±0,35 % à vitesse de déformation élevée. En revanche, il est surestimé pour des amplitudes supérieures à ±0,35 %.

Du fait du sens physique attribué aux paramètres du modèle, certaines valeurs ne sont pas connues avec exactitude pour l'acier Grade 92 et sont extrapolées à partir de mesures expérimentales effectuées sur d'autres matériaux et/ou sous différents types de conditions (essais mécaniques, température...). Une étude paramétrique du modèle a donc été menée afin d'étudier la stabilité du modèle vis-à-vis de ces paramètres. Ainsi, cette étude de l'influence de la variation des valeurs des paramètres microstructuraux dans un intervalle physiquement acceptable a montré que les prédictions du comportement mécanique et de l'évolution de la densité de dislocations sont particulièrement stables. Seule la prédiction de l'évolution de la taille moyenne de sous-grains est sensible à ces variations de paramètres.

4.1 Introduction to polycrystalline modelling

A large number of experimental studies of the mechanical behaviour of ferritic-martensite steels (and alloys in general) during cycling is available in literature. At the same time, a significant number of phenomenological models using nonlinear kinematic hardening rule has been proposed in order to reproduce this cyclic behaviour (see [Lemaitre and Chaboche, 1990, Koo and Lee, 2007, Chaboche, 2008] for example). For a modified 9Cr-1Mo steel during cycling at high temperature, Yagushi and Takahashi have developped a model based on the Chaboche model [Chaboche, 1989] to describe cyclic softening behavior by fitting a large number of parameters on the experimental evolution of macroscopic backstress and effective stress [Yaguchi and Takahashi, 2000]. Although their model is able to reproduce experimental macroscopic behaviour during cycling (for example: cyclic hardening, cyclic softening...), it does not focus on the physical phenomena which occur during deformation. In this case, modelling is limited to the loading conditions of the data base used for the identification of the parameters, and predictions and extrapolations of the cyclic behaviour are not much reliable. No guideline for improving material resistance is given either.

Significant efforts were made in order to model the physical mechanisms of deformation and the microstructural changes during cycling or creep deformation. For instance, Blum and coworkers proposed a mechanism of coarsening of subgrains based on the movement of the low-angle boundaries. Using a phenomenological model, they succeed to reproduce the subgrain size evolution during creep [Polcik et al., 1999]. However, no movement of the sugrain boundaries was observed by *in-situ* TEM observations during tensile tests at 550 ℃ in EUROFER [Guétaz et al., 2003]. Dislocation dynamics simulations performed by Holec and Dlouhý showed that symmetric tilt boundaries decorated with precipitates become unstable and move under an applied shear stress only if their misorientation reach a critical value, of the order of a few tenth of degres [Holec and Dlouhý, 2005]. For higher misorientation angle, the pinning effect by precipitates is strong enough to avoid any low-angle boundary climb and/or glide. To describe the dislocation density evolution during cycling or creep, several authors proposed a physical-based modelling which take several observed phenomena into account (production, annihilation, interactions with boundaries...) [Estrin et al., 1998, Blum and Eisenlohr, 2009].

Although they are not so numerous, a few self-consistent homogeneization models are proposed in the literature to simulate the cyclic behavior of polycrystalline metals [Cailletaud, 1992, Pilvin, 1994, Tóth et al., 2000, Fournier et al., 2011b]. However, even if they are able to reproduce the macroscopic mechanical behaviour during cycling, they can not predict accurately the microstructure evolution and mechanical behaviour without fitting parameters using the cyclic softening curves. The aim of this study is to predict the cyclic behaviour of tempered ferritic-martensite steels by fitting a very limited number of physically-based viscoplasticity parameters. Only experimental monotonic tensile curves are used in the identification process but no cyclic data. As the physical mechanisms of deformation are modelled at the dislocation scale, this model may display more relevant predictions and extrapolations for both microstructure evolution and mechanical behaviour during long-term sollicitations (low strain, long hold time...).

In the following part, the physical bases of the model are presented and hypotheses stemming either from experimental observations or from previous numerical simulations are presented.

4.2 Crystalline constitutive equations

4.2.1 Description and hypotheses of the modelling

The as-received material presented in chapter 1 displays several microstructural scales: prior austenitic grains, packets, blocks, laths and subgrains. Martensite packets and blocks are characterized by specific misorientations between neighbours, induced by the martensitic transformation [Kurdjumov and Sachs, 1930, Nishiyama, 1934, Wakasa and Wayman, 1981, Gourgues et al., 2000]. Here, we will consider that there are two kinds of boundaries:

1. The prior austenitic grain boundaries, the packet boundaries and the block boundaries which have misorientation angle higher than 5 ° [Barcelo et al., 2009, Barcelo et al., 2010].
2. Some of laths and subgrain boundaries which have misorientation angle lower than 5 °. They are considered to be low-angle boundaries [Tak et al., 2009]. These ones are located within blocks only.

Both kinds of boundaries are significantly different in terms of stability during mechanical tests at high temperature. EBSD measurements showed that prior austenitic grain boundaries, packet boundaries and block boundaries remain unchanged during mechanical tests [Kimura et al., 2006, Fournier et al., 2009a]. This result is confirmed by TEM observations and subgrain size measurements presented in section 3.3.1: the maximum subgrain size measured in the sample after cycling is lower than $2.5 - 3$ µm, which corresponds to the mean block size [Fournier, 2007]. Moreover, Dronhofer et al. showed that the evolution of the distribution of misorientation angle during creep was mainly limited to the low values of misorientation angle (lower than 5 °) [Dronhofer et al., 2003]. These observations lead us to conclude that the coarsening is confined to subgrains and that blocks are stable during high-temperature mechanical loading. Thus, the microstructural growth is linked to the vanishing of the low-angle subgrain boundaries within the blocks.

The coarsening mechanism proposed by Abe is based on the recombination of two low-angle boundaries [Abe, 2004]. The progressive coalescence of subgrains low-angle boundaries is supposed to be localised near triple points of boundaries, called "Y-junctions". This mechanism was proposed more than fifty years ago for polygonized silicon iron crystals and for zinc single crystal [Dunn and Daniels, 1951, Gilman, 1955]. In these materials, the boundaries, free from precipitates, are highly mobile. In tempered martensite steels, a small number of "Y-junctions" is observed after tempering (see Fig. 3.16 and [Guttmann, 1974] for example). Carbide precipitates stabilize the subgrain boundaries and drastically reduce their mobility. Abe suggests that dissolution and re-precipitation of carbide precipitates take place repeatedly during moving of boundaries and lead to progressive recombination of low-angle boundaries. However, no significant modification of precipitates during cycling at high temperature has been reported in literature, and as mentionned above, in situ TEM observations do not mention any low-angle boundary displacement.

Considering these observations, the mechanism described by Abe is not suitable for cyclic deformation of tempered ferritic-martensite steels. Some other mechanisms were proposed and based on annihilation of dislocations dipoles in subgrain and of dipolar configurations at dislocation boundaries, followed by a mechanism of annihilation and/or recombination of subgrain boundaries [Blum, 2001]. A mechanism based on the interaction between low-angle boundaries and mobile dislocations has been also proposed [Sauzay et al., 2005] based on the knitting-in (free dislocations are absorbed into the low-angle boundaries) and knitting-out (free dislocations are released from the low-angle boundaries) mechanisms, initially highlighted by Eggeler in tempered ferritic-martensite steels [Eggeler, 1989]

and Caillard and Martin in aluminium [Caillard and Martin, 1982b]. The corresponding analytical model is described in section 2.6.2 and in [Sauzay et al., 2005], [Sauzay et al., 2008] for cyclic loading and [Sauzay, 2009] for creep loading. In the following, the microstructural hypothesis adapted to polycrystalline homogenization modelling are presented.

4.2.1.1 Dislocations types considered in the model

For the sake of simplicity, only two types of dislocations are considered in the following:

- Pure edge dislocations characterized by a Bürgers vector perpendicular to the line direction.
- Pure screw dislocations characterized by a Bürgers vector parallel to their line direction.

Following this hypothesis, the well-known dislocations loops generated from Frank-Read sources in a slip plane under shear stress [Frank, 1980] are only described by a succession of edge and screw parts (see Fig. 4.1).

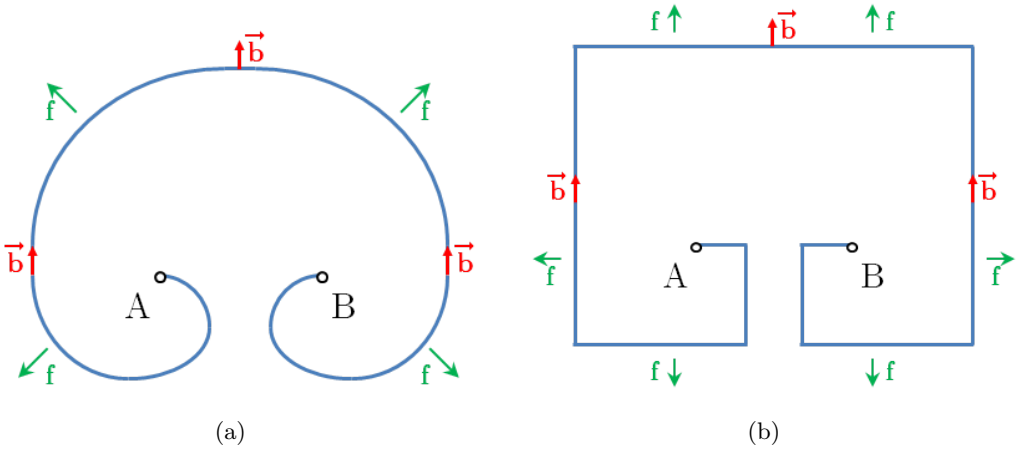

Fig. 4.1. Scheme of (a) a typical Frank-Read source and (b) a modelled Frank-Read source with pure edge and screw parts.

This hypothesis leads to a significant simplification by considering mixed dislocations as pure edge or pure screw dislocations. However, it allows taking dislocation properties which depend on their type (movement, interactions... see section 4.2.1.3) into account. As we focus on the interaction between mobile dislocations and low-angle boundaries, this approach is more realistic than only considering a global dislocation density without distinction between edge and screw part.

In this model, we divide dislocations into two kind of populations: mobile dislocations, which are located within the subgrains and glide during viscoplastic deformation and dislocations composing low-angle boundaries.

4.2.1.2 Low-angle boundaries structures

In the following, low-angle boundaries are considered as interfaces defined by a misorientation angle θ between two subgrains [Sutton and Balluffi, 1995]. They are considered as a periodic network of boundary dislocations [Priester, 2001]. This hypothesis is based on the description proposed by Read

and Shockley which consider low-angle boundaries as planar arrangements of dislocations [Read and Shockley, 1950]. This scheme leads to model two kinds of boundaries:

- Pure tilt boundaries made by a alignment of edge dislocations of the same Bürgers vector (see Fig 4.2).
- Pure twist bondaries made by a arrangement of two families* of screw dislocations. This hypothesis is based on the microstructural observations of subgrain boundaries (see Fig. 3.24(a) and [Guttmann, 1974]).

More generally, all low-angle boundaries can be built using one family of edge dislocations and two families of screw ones.

The proposed mechanism partially links the decrease in the mobile dislocation density to the vanishing of some low-angle boundaries. We consider that mobile dislocations can annihilate with the dislocations composing the low-angle boundaries. During cycling, some slip systems are activated and the mobile dislocations contained in these planes move towards the low-angle boundaries. Annihilation of mobile dislocations with dislocations at the low-angle boundaries leads to a decrease in the lineic dislocation density at the low-angle boundaries. It induces a decrease in the misorientation angle θ of the boundary under interest [Read and Shockley, 1950]:

$$\theta = b\Lambda \tag{4.1}$$

In Eq. 4.1, Λ is the edge dislocation density in the low-angle boundary and b is the Bürgers vector magnitude. Annihilation takes place between two edge (or two screw) dislocations of opposite Bürgers vector and parallel line vectors if their distance is smaller than a critical value, denoted as y_e for edge dislocations and as y_s for screw dislocations [Essmann and Mughrabi, 1979, Differt and Essmann, 1993, Essmann and Differt, 1996, Sauzay et al., 2005]. The annihilation mechanism during cycling is illustrated for a pure tilt boundary in Fig. 4.2. Interactions between two edge (or two screw) dislocations of same Bürgers vector and parallel line vectors are not taken into account because of the local stress field effect close to the finite subgrain boundary [Li, 1960].

The activated slip systems are considered to be the same in both subgrains (this hypothesis is discussed in section 4.2.1.3). In Fig. 4.2, during the first half-cycle, mobile dislocations glide towards the boundary dislocation in subgrain A and annihilation can occur if their distance is smaller than y_e. In subgrain B, mobile dislocations of the same sign glide towards the boundary [Sauzay et al., 2005]. The deformation fields induced by the dislocations of the same sign lead to the creation of a dislocation pile-up on this side of the low-angle boundary [Priester, 2001]. During the second half-cycle, the opposite mechanism happens at this interface. Successive annihilations lead to a decrease in dislocation density within the low-angle boundary and thus in its corresponding misorientation angle. After numerous annihilation events, the low-angle boundary dislocation density may be low enough to induce its complete annihilation. This hypothesis is discussed later.

Interaction between mobile screw dislocations and twist boundaries is similar to interaction described for mobile edge dislocations and tilt boundaries. However, as a simple alignment of screw dislocations is unstable, we assume that twist low-angle boundaries are composed by two families of screw dislocations, as described in [Sutton and Balluffi, 1995]. Thus, the annihilation mechanism between twist boundaries and mobile screw dislocations takes place only when the two families of screw dislocations of opposite signs are activated in the neighboring subgrains.

*A family of dislocation is a set of dislocations with the same Bürgers vector.

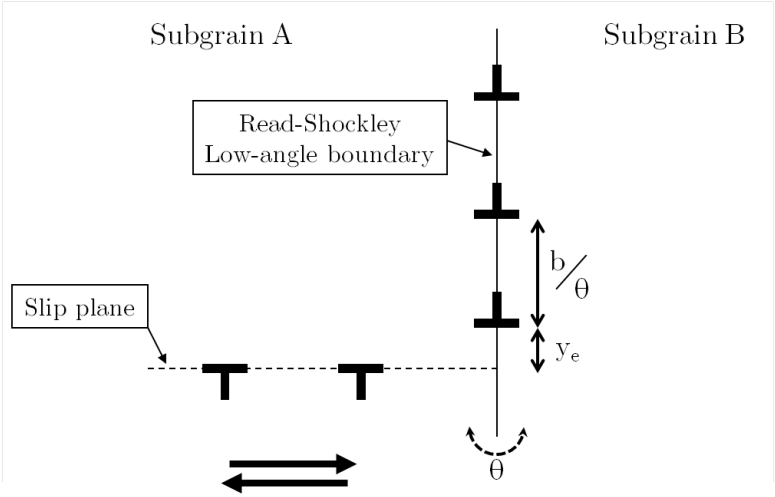

Fig. 4.2. Schematic drawing of the interactions between mobile edge dislocations (moving along the dotted line) and parallel edge dislocations composing a symmetric tilt low-angle boundary (aligned along the continuous line) during cycling.

In order to model these microstructural interactions, we focus on the crystallographic features used in the model.

4.2.1.3 Crystallographic features at the block scale

The tempered martensite structure is almost body-centered cubic because of $M_{23}C_6$ precipitate formation during tempering. For the tempered ferritic-martensite steels, we observed that the smallest imbricated microstructural scale which is stable during cycling is the block of laths (see subsection 3.3.1.3). Blocks of laths are considered as a phase with a almost homogeneous crystallographic orientation. The model predicts the mechanical behaviour of a block of laths in the matrix composed by a large number of other blocks. Although specific misorientations between blocks of laths were described in the literature [Kurdjumov and Sachs, 1930, Wassermann, 1933, Nishiyama, 1934, Wakasa and Wayman, 1981, Gourgues et al., 2000], the crystallographic structure of the as-received material modelled as a large aggregate of blocks is considered here as textureless for the sake of simplicity even concerning their local texture. We thus assume that the crystal orientation of each block of laths is randomly distributed ans does not depend on the neighbour block orientations. Neglecting such local texture should not affect macroscopic predictions strongly.

The body-centered cubic structure requires taking the two families of slip systems {110} and {112} planes which are the easiest to activate and ⟨111⟩ slip directions into account ({123} slip planes are not considered) [Franciosi, 1983, Hoc and Forest, 2001, Caillard and Martin, 2003]. In a given slip system, the structure of dislocation loops, generated from Frank-Read sources, permit us to considered that the number of dislocations of opposite Bürgers vector are the same (see Fig. 4.1(b)). Moreover, low-angle boundary dislocations can interact with mobile dislocations of both subgrain A and subgrain B (Fig. 4.2). The misorientation between these neighbouring subgrains is low enough to considered that their activated slip systems during viscoplastic deformation are the same in all subgrain located in the same block. Consequently, the annihilation mechanism takes place during plastic deformation, independently of the dislocation glide direction, on either the subgrain A side or B one.

This hypothesis allows us to assume that two opposite slip systems are equivalent, leading to divide by 2 the total number of slip systems considered in the model. It means that 24 slip systems

are considered. For a given slip system, the following hypothesis on dislocation structure are:

- One mobile edge dislocation can be activated by only one slip system. No other one has similar parallel dislocations. Therefore, edge dislocations are divided into 24 families.
- Six different slip systems have similar parallel mobile screw dislocations. So screw dislocations are divided into 4 families, coresponding to the four $\langle 111 \rangle$ Bürgers vectors.

These slip properties valid for mobile dislocations are also true for dislocations within low-angle boundaries:

- Pure tilt boundaries are made of parallel edge dislocations, so they are divided into 24 families.
- Pure twist boundaries are made of two families of screw dislocations, so they are divided into 6 families, *i.e.* the number of distinct groups of two families of screw dislocations taken out of 4.

In the model, we assume that dislocations can only glide on their slip system. Although we are concerned by high temperature viscoplasticity, dislocation climb is not taken into account during cycling at least at this stage. Indeed, in a first approximation, we assume that this phenomenon occurs less significantly during cycling at 10^{-5} s^{-1} than during creep or relaxation test with strain rate which can reach $10^{-9} - 10^{-10}$ s^{-1}. Dislocation climb may be taken into account later, increasing softening rate [Sauzay et al., 2008].

These microstructural hypothesis are necessary to propose a set of equations to model the physical mechanisms happening during cycling.

4.2.2 Isotropic stress

Considering one block and one slip system i, the resolved shear stress τ^i is expressed in Eq. 4.2, resulting from the projection of the local stress tensor $\underline{\underline{\sigma}}$ on the i^{th} slip system.

$$\tau^i = \underline{\underline{\sigma}} : \left(\underline{m}^i \otimes \underline{n}^i\right) \tag{4.2}$$

In Eq. 4.2, $\underline{m}^i$ is the slip vector and $\underline{n}^i$ is the normal to the slip plane.

The critical resolved shear stress τ_c required to activate viscoplastic slip is supposed to be the same for all slip systems i. According to the forest model analysis [Kocks and Mecking, 2003], it is expressed as:

$$\tau_c = \tau_0 + \alpha\mu b\sqrt{\rho_e + \rho_s} \tag{4.3}$$

The value of critical resolved shear stress τ_c depends on the interactions due to forest dislocations. It is linked to the total free dislocation density (total free edge dislocation density ρ_e and total free screw dislocation density ρ_s) in the considered block. It is here considered as athermal. This term weakly depends on the temperature, because of the dependance to the shear modulus μ which is influenced by the temperature.

In Eq. 4.3, τ_0 is linked to the energy necessary for the dislocations to move to the next Peierls' valley [Sommer et al., 1998]. This thermally activated process mainly depends on temperature and on viscoplastic strain rate. Sommer and coworkers showed that temperature is high enough to neglect this term for temperatures higher than 150 ℃ in alpha-iron polycrystals, regardless the viscoplastic strain rate [Sommer et al., 1998]. Consequently, the temperature applied during cycling (550 ℃) permits us to take τ_0 equal to zero.

While the effect of Peierls' stress is neglected in the model, solid solution strengthening, which also corresponds to thermally activable obstacles, is taken into account in the model. This effect is linked to the viscoplastic deformation mechanisms and is discussed later in section 4.2.4.

In the well-known Taylor's relationship presented in Eq. 4.3, the average strength of dislocation interactions is defined by the coefficient α, with a value in the range 0.35 ± 0.15 in f.c.c. crystals [Devincre et al., 2005]. This approach was improved by considering the contribution of individual slip systems [Franciosi et al., 1980]. This approach leads to define a cross-hardening matrix composed by the interaction coefficients a^{ij} which correspond to the average strength of the interactions between pairs of slip systems i and j.

Experimental measurements of these coefficients are hardly available and, in b.c.c. crystals, only estimations based on latent hardening tests are available in literature [Takeuchi and Mano, 1972, Franciosi, 1983]. On the other hand, dislocation dynamics simulations were performed to calculate the five interaction coefficients in f.c.c. crystals. But, from our knowledge, only a part of the much more numerous coefficients were calculated in α-iron [Madec and Kubin, 2004, Queyreau et al., 2009]. Consequently, this partial information on the cross-hardening matrix for the b.c.c. structure leads us to approximate the values of the coefficients a^{ij}. For the $\{1\bar{1}0\}\langle 111\rangle$ slip systems in alpha-iron with a threshold friction stress of 30 MPa and a forest density of 2×10^{13} m^{-2}, the interaction coefficients a^{ij} of the four types of reactions between slip systems classically defined in b.c.c. crystals (collinear, symmetrical junction, asymmetrical junction and edge junction) were calculated by dislocation dynamics simulations [Queyreau et al., 2009]. Consequently, the average value of the Taylor coefficient α obtained is close to 0.3 [Queyreau et al., 2009, Naamane, 2008].

4.2.3 Evolution of the kinematic stress

The study of the mechanical behaviour during cycling at high temperature of Grade 92 steel, and more generally of 9%Cr steels, shows that cyclic softening is mainly due to a decrease in the kinematic stress (see section 3.2 and [Fournier et al., 2006b] for Grade 91 steel). Consequently, the model should take this evolution of the kinematic stress into account, here at the crystal scale.

A large number of equations modelling the evolution of kinematic stress are available in literature [Armstrong and Frederick, 1966, Lemaitre and Chaboche, 1990, Steckmeyer et al., 2011]. However, most of them are characterized by phenomenological formula and requires the adjustement of physical baseless parameters. In order to drastically reduce the number of adjustable parameters, the evolution law of the kinematic stress was based in the present model on the slip mechanisms. Consequently, the highest number of parameters correspond to values measured from microstructural observations or at least have a physical meaning.

In the as-received material, we observed that mobile dislocations seem to be straight lines, pinned at subgrain boundaries (see Fig. 3.23(a), [Wakasa and Wayman, 1981] and [Guétaz et al., 2003]). During viscoplastic glide, the resolved shear stress applied on a given slip system i induces a bowing out of these dislocations [Essmann and Differt, 1996] even in the EUROFER 97 steel at 550 ℃ [Guétaz et al., 2003]. Consequently, they move over a mean distance l. During the bowing-out, the Orowan

formula permits us to express the viscoplastic slip as a function of l and of the mobile dislocation density $\rho_e^i + \rho_s^i$ on the slip system i:

$$\gamma^{p,i} = \left(\rho_e^i + \rho_s^i\right) lb \tag{4.4}$$

Considering the low values of viscoplastic slip amplitude during cycling, we assume that mobile dislocations only bow-out and stay pinned at subgrain boundaries (by carbide precipitates or dislocations belonging to the low-angle boundaries). They could not go through the low-angle boundaries [Guétaz et al., 2003]. The average distance h covered by a given dislocation can be expressed as a function of the area swept by this dislocation A and the subgrain diameter d:

$$h = \frac{A}{d} \tag{4.5}$$

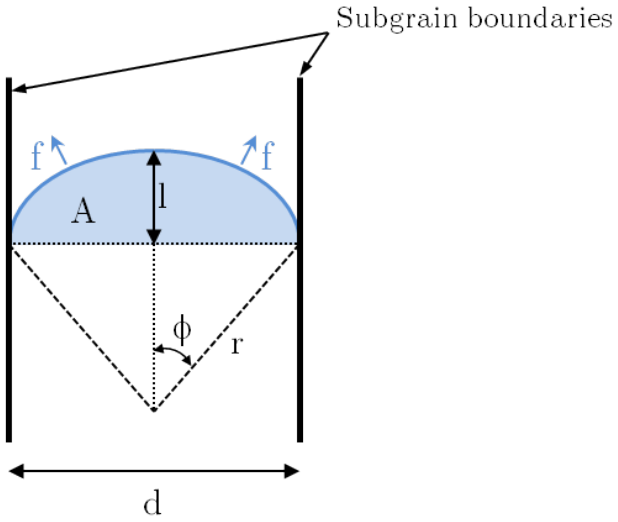

Fig. 4.3. Scheme of a mobile dislocations pinned at subgrain boundaries and bowing-out under shear stress τ. For sake of understanding, the mobile dislocation drawn on the figure is not only composed by pure edge or pure screw parts.

Based on Fig. 4.3, a simple geometrical consideration leads us to link the area swept by the dislocation A, the radius of curvature r, the slip lenght l and the angle ϕ by:

$$\begin{aligned} &A = \phi r^2 - \frac{d}{2}(r - l) \\ &\text{with } \phi = \arctan\left(\frac{d}{2(r-l)}\right) \end{aligned} \tag{4.6}$$

Eqs. 4.4, 4.5 and 4.6 lead to:

$$\gamma^{p,i} = \frac{\rho b}{d}\left[r^2 \arctan\left(\frac{d}{2(r-l)}\right) - \frac{d}{2}(r-l)\right] \tag{4.7}$$

Each element of the curved free dislocation is under equilibrium between the force resulting from the shear stress $F^i = \tau^i b$ and the tension line T which is different for edge and screw dislocations [Brown, 2006]. Dupuy and Fivel have shown that the critical shear stress required to bow-out a dislocation segment of a Frank-Read source weakly vary between a pure edge segment and a pure screw one, in the case of an isotropic linear elastic f.c.c. crystal with a Poisson ratio close to 0.35 [Dupuy and Fivel, 2002]. For the sake of simplicity, this result permits us to use an average value of the tension line for edge and screw dislocations ($T = \mu b^2/2$). For $r \in [\ \frac{d}{2}\ ;\ +\infty\ [$, the radius of curvature r is calculed by:

$$r = \frac{T}{F^i} = \frac{\mu b}{2\tau^i} \tag{4.8}$$

The maximum value of τ^i allowed by the geometric configuration of Fig. 4.3 is reached for $r = d/2$. The local backstress x^i in a slip system i is defined as the stress induced by tension line. Its maximum value is thus given by:

$$x^i_{max} = \frac{\mu b}{d} \tag{4.9}$$

With the geometry of Fig. 4.3, the radius of curvature r can be expressed as a function of the slip length l:

$$r = \frac{l}{2} + \frac{d^2}{8l} \tag{4.10}$$

Eq. 4.10 gives two solutions for the slip length l:

$$l = \frac{2r + \sqrt{4r^2 - d^2}}{2} \tag{4.11}$$

$$l = \frac{2r - \sqrt{4r^2 - d^2}}{2} \tag{4.12}$$

As the slip length l has to be lower than the radius of curvature R, the only acceptable value is that of Eq. 4.12. The slip length l is thus expressed as :

$$l = \frac{\mu b}{2x^i} - \frac{1}{2}\sqrt{\left(\frac{\mu b}{x^i}\right)^2 - d^2} \tag{4.13}$$

Eqs. 4.7, 4.8, 4.9 and 4.13 lead to the expression of the amount of slip $\gamma^{p,i}$, for $x^i \in\ ]-x^i_{max}\ ;\ 0\,[\cup\ ]\,0\ ;\ x^i_{max}\,[$.

$$\gamma^{p,i} = \frac{\left(\rho^i_e + \rho^i_s\right) bd}{4}\left[\frac{\left(x^i_{max}\right)^2}{\left(x^i\right)^2}\arctan\left(\frac{\left(x^i_{max}\right)^2}{\left(x^i\right)^2} - 1\right)^{-\frac{1}{2}} - \sqrt{\frac{\left(x^i_{max}\right)^2}{\left(x^i\right)^2} - 1}\right] \tag{4.14}$$

We assume that dislocations densities ρ_e^i and ρ_s^i and subgrain diameter d do not change during an infinitesimal change in time dt. The derivation of the function presented in Eq. 4.14 with respect to time leads to the evolutionnary equation of the kinematic stress induced by the tension line:

$$\dot{x^i} = \frac{2d\left|\left(x^i\right)^3\right|\dot{\gamma}^{p,i}}{\left(\rho_e^i+\rho_s^i\right)b^3\mu^2}\left[\left(\frac{\left(x_{max}^i\right)^2}{\left(x^i\right)^2}-1\right)^{-\frac{1}{2}}-\arctan\left(\frac{\left(x_{max}^i\right)^2}{\left(x^i\right)^2}-1\right)^{-\frac{1}{2}}\right]^{-1} \tag{4.15}$$

Eq. 4.15 is defined for $x^i \in \left]-x_{max}^i\ ;\ 0\right[\cup \left]0\ ;\ x_{max}^i\right[$. It admits finite limits as x^i approaches 0 and $\pm x_{max}^i$:

$$\begin{aligned}\lim_{x^i\to x_{max}^i}\dot{x^i} &= \lim_{x^i\to -x_{max}^i}\dot{x^i} = 0\\ \lim_{x^i\to 0}\dot{x^i} &= \frac{6\mu}{\left(\rho_e^i+\rho_s^i\right)d^2}\dot{\gamma}^{p,i}\end{aligned} \tag{4.16}$$

The maximum kinematic stress on a slip system is inversely proportional to the subgrain size (see Eq. 4.9). By this way, this law allows us to link subgrain growth and cyclic softening induced by the decrease in kinematic stress. Let us now focus on the expression of viscoplastic slip rate $\dot{\gamma}^{p,i}$ which will be the driving force of the microstructural evolutions.

4.2.4 Crystal viscoplasticity flow rule

In the model, the total free dislocation density is divided into pure edge and pure screw dislocation densities. Viscoplastic slip rates are expressed therefore separately for edge and screw dislocations. For a given block, viscoplastic slip on slip system i requires the existence of a positive viscous stress A^i, defined as [Cottrell, 1953]:

$$A^i = \left|\tau^i - x^i\right| - \tau_c \tag{4.17}$$

If the viscous stress A^i is negative or equal to zero, viscoplastic flow does not occur, and the cumulated viscoplastic slip rate is expressed as:

$$\dot{\gamma}_{e,cum}^{p,i} = \dot{\gamma}_{s,cum}^{p,i} = 0 \tag{4.18}$$

On the contrary, if the viscous stress A^i is positive, viscoplastic glide $\gamma_{cum}^{p,i} = \gamma_{e,cum}^{p,i} + \gamma_{s,cum}^{p,i}$ occurs:

$$\begin{aligned}\dot{\gamma}_{e,cum}^{p,i} &= \nu_0\ b^2\ \rho_e^i\ \exp\left(-\frac{Q}{kT}\right)\sinh\left(\frac{VA^i}{kT}\right)\\ \dot{\gamma}_{s,cum}^{p,i} &= \nu_0\ b^2\ \rho_s^i\ \exp\left(-\frac{Q}{kT}\right)\sinh\left(\frac{VA^i}{kT}\right)\end{aligned} \tag{4.19}$$

Similar equations can be found in the literature [Van Swygenhoven et al., 1999, Conrad and Narayan, 2000, Wei et al., 2004, Fournier et al., 2011b]. In Eq. 4.19, V and Q are respectively the activation volume and the activation energy of viscoplastic slip. Their values are linked to the interaction mechanism between dislocations and local obstacles to their motion. In a first approximation, the mecanisms of glide over these obstacles are considered to be independant from the dislocation nature: V and Q values are assumed to be the same for edge and screw dislocations.

For the sake of simplicity, the obstacles to dislocation motion are considered to be homogeneously distributed in the matrix, *i.e.* we assume that the spacing between the obstacles is the same for all obstacles in the slip plane. This hypothesis leads to the simplified equations presented in Eq. 4.19 [François et al., 1995b, Caillard and Martin, 2003]. Finally, T is the temperature, k is the Boltzmann constant and ν_0 is the Debye frequency. Pre-exponential factor $\nu_0\ b^2$ corresponds to the thermal vibration and the density of obstacles for dislocations movement [Caillard and Martin, 2003].

The local viscoplastic strain rate tensor $\underline{\underline{\dot{\varepsilon}}}^p$ in the considered block is expressed as:

$$\underline{\underline{\dot{\varepsilon}}}^p = \sum_{i=1}^{24} \left(\dot{\gamma}^{p,i}_{e,cum} + \dot{\gamma}^{p,i}_{s,cum}\right)\ \underline{m}^i \otimes \underline{n}^i\ \text{sign}\left(\tau^i - x^i\right) \tag{4.20}$$

In Eq. 4.20, $\text{sign}\left(\tau^i - x^i\right)$ is equal to 1 if $\left(\tau^i - x^i\right)$ is positive and -1 if $\left(\tau^i - x^i\right)$ is negative. In order to predict the macroscopic mechanical behaviour evolution, the model takes microstructural evolutions into account as well.

4.3 Modelling the microstructural evolutions

In chapter 3, we observed that microstructural evolution during cycling at 550 ℃ mainly consists in a decrease in dislocation density and an increase in subgrain diameter. Although the modelled physical mechanisms are based on strong assumptions, some of the main mecanisms features may have been captured. In this part, we focus on the evolutionnary equations which govern the microstructure evolution: the density of free dislocation, the low-angle boundary misorientation angle and the subgrain size. The modelling aims finally at predicting the evolution of dislocation density and subgrain size.

4.3.1 Modelling the evolution of dislocation density

For a given slip system i, the difference in the behaviour of edge and screw dislocations leads us to express the variation of density of free edge and screw dislocations separatly (respectively $\dot{\rho}^i_e$ and $\dot{\rho}^i_s$). Both evolution rates can be divided into three additive terms which correspond to three different mechanisms:

$$\dot{\rho}^i_e = \dot{\rho}^i_{e,1} + \dot{\rho}^i_{e,2} + \dot{\rho}^i_{e,3} \tag{4.21}$$

$$\dot{\rho}^i_s = \dot{\rho}^i_{s,1} + \dot{\rho}^i_{s,2} + \dot{\rho}^i_{s,3} \tag{4.22}$$

The first terms ($\dot{\rho}^i_{e,1}$ and $\dot{\rho}^i_{s,1}$) are linked to the production of dislocations [Estrin et al., 1998, Tóth et al., 2002, Blum and Eisenlohr, 2009]. The second terms ($\dot{\rho}^i_{e,2}$ and $\dot{\rho}^i_{s,2}$) correspond to the annihilation of parallel mobile dislocations with opposite sign [Essmann and Mughrabi, 1979, Estrin et al., 1998, Hoc and Forest, 2001, Tóth et al., 2002, Kubin et al., 2008]. Finally, the third terms ($\dot{\rho}^i_{e,3}$ and $\dot{\rho}^i_{s,3}$) account for the annihilation of free dislocations and dislocations located within the low-angle boundaries [Sauzay et al., 2005]. Let us focus on the individual expression of each of these three terms.

4.3.1.1 Production of dislocations

The terms of production are based on the bowing-out phenomenon of the pinned mobile dislocations during viscoplastic glide. To produce dislocation length, the well-known Frank-Read sources are considered. The hypothesis which consists in describing the dislocations as pure edge or pure screw segments leads us to model the loops as squares or rectangles, only composed by two parts of screw dislocations and two parts of edge dislocations (see Fig. 4.1(b)). In this case, we consider that when edge (screw) dislocations glide, it increases the length of the screw (edge) dislocations.

The mechanism of production of dislocations is based on the Orowan law presented in Eq. 4.4. If we consider one dislocation (edge or screw), we assume that the mean distance l covered by one of the dislocations created by the Frank-Read source is equal to the half-diameter of a subgrain:

$$l = \frac{d}{2} \tag{4.23}$$

The density of produced dislocation length can thus be linked to the viscoplastic slip and the subgrain diameter (we consider only pure edge and pure screw parts):

$$\rho^i_{e,1} = \frac{2}{bd}\gamma^{p,i}_s \tag{4.24}$$

$$\rho^i_{s,1} = \frac{2}{bd}\gamma^{p,i}_e \tag{4.25}$$

Consequently, for an infinitesimal change in time, the production rate for edge and screw dislocations can be written [Essmann and Mughrabi, 1979, Kubin et al., 2008, Blum and Eisenlohr, 2009]:

$$\dot{\rho}^i_{e,1} = \frac{2}{bd}\dot{\gamma}^{p,i}_s \tag{4.26}$$

$$\dot{\rho}^i_{s,1} = \frac{2}{bd}\dot{\gamma}^{p,i}_e \tag{4.27}$$

One of the characteristic of the previous equations is the coupling edge glide and screw production and vice-versa which is not taking into account usually in literature. The hysteresis loop presented in Fig. 4.4 is divided into six parts: two of them correspond to the elastic part, and no dislocation glide occurs during these periods. Parts 1 and 4 are in tension and parts 2 and 3 are in compression. During one cycle, the sign of the shear stress applied on a given slip system changes, depending on time (tension or compression part). It induces a modification of the sign of glide and thus, a variation of the terms of production of dislocations.

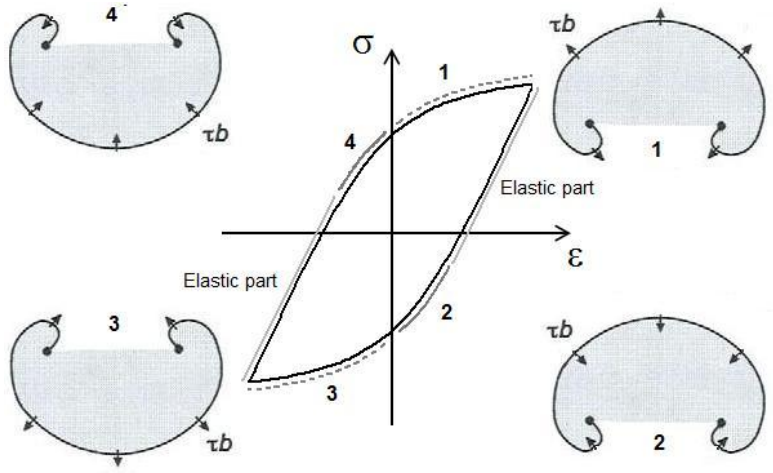

Fig. 4.4. Scheme of a Frank-Read source on an arbitrarily selected slip system during cycling [Giordana et al., 2011]. For the sake of understanding, Frank-Read sources are drawn with mixt dislocations: in the model, only pure edge and screw parts are considered.

4.3.1.2 Inter-annihilation of free dislocations

During viscoplastic slip on an activated given slip system i, two parallel free dislocations can annihilate with each other if their Bürgers vectors are opposite and if their inter-spacing distance is lower than the critical spontaneous annihilation distance y_e for edge dislocations and y_s for screw dislocations. This phenomenon was introduced in detail by Essmann and Mughrabi [Essmann and Mughrabi, 1979]. If we consider an edge dislocation d^+, it can annihilate with another mobile opposite edge dislocation d^- during the time increment if both are located within an area S_a [Essmann and Differt, 1996]:

$$S_a = 2y_e \left(v_{d^+} + v_{d^-}\right) \Delta t \tag{4.28}$$

In Eq. 4.28, v_{d^+} and v_{d^-} are respectively the velocity of dislocations d^+ and d^-. In this region, the variation of dislocation density of d^+ type over a time increment Δt is given by:

$$\Delta\rho^+ = \rho^+ \times 2y_e \left(v_{d^+} + v_{d^-}\right) \Delta t \rho^- \tag{4.29}$$

Following the hypothesis that the dislocations are equally divided into two sets of opposite sign, we assume that $\rho^+ = \rho^- = \rho/2$. Moreover, as opposite dislocations are on the same slip system and submitted to opposite forces, we assume that $v_{d^+} = v_{d^-}$. Consequently, $\Delta\rho = \Delta\rho^+ + \Delta\rho^- = 2\Delta\rho^+$. Following the Orowan equation, the term $\dot{\rho}^i_{e,2}$ for edge dislocations located on slip system i is expressed as:

$$\dot{\rho}^i_{e,2} = -2\frac{y_e}{b}\rho^i_e \dot{\gamma}^{p,i}_{e,cum} \tag{4.30}$$

For screw dislocations, the formula is more complex, because of the number of slip planes which

have to be taken into account for a given Bürgers vector:

$$\dot{\rho}^i_{s,2} = -\frac{y_s}{b}\left(\dot{\gamma}^{p,i}_{s,cum}\sum_{j\in\Omega}\rho^j_s + \rho^i_s\sum_{j\in\Omega}\dot{\gamma}^{p,j}_{s,cum}\right) \tag{4.31}$$

Dislocation annihilation in a given slip system i leads to the vanishing of two parallel and opposite dislocations, which is modelled by the factor two in Eq. 4.30. For screw dislocations in b.c.c. crystals, considering that their Bürgers vector and slip direction are parallel, they may be located on six possible slip planes. Consequently, the computation takes the six slips systems to which a screw dislocation belongs into account. This set of six slip planes is denoted as Ω. Thus, this method is characterized by a careful treatment of the annihilation of screw dislocations, more evolved than the models usually developped in literature [Blum, 2001, Tóth et al., 2002, Fournier et al., 2011b].

4.3.1.3 Annihilation of free dislocations with low-angle boundary dislocations

The annihilation of free dislocations with low-angle boundaries explained in section 4.2.1.2 is modelled by introducing the misorientation angles θ^i_e and θ^i_s. It is expressed as [Fournier et al., 2011b]:

$$\dot{\rho}^i_{e,3} = -\frac{y_e}{b^2}\frac{\theta^i_e}{d}\dot{\gamma}^{p,i}_{e,cum} \tag{4.32}$$

$$\dot{\rho}^i_{s,3} = -\frac{y_s}{b^2}\frac{\dot{\gamma}^{p,i}_{s,cum}}{d}\sum_{j\in\Omega}\theta^j_s \tag{4.33}$$

These equations are deduced from the evolution of misorientation presented in the following section 4.3.2. The evolutionnary equations of free edge and screw dislocation densities on the i^{th} slip system are the following:

$$\dot{\rho}^i_e = \frac{2}{bd}\dot{\gamma}^{p,i}_s - \frac{y_e}{b}\dot{\gamma}^{p,i}_{e,cum}\left(2\rho^i_e + \frac{\theta^i_e}{bd}\right) \tag{4.34}$$

$$\dot{\rho}^i_s = \frac{2}{bd}\dot{\gamma}^{p,i}_e - \frac{y_s}{b}\left[\dot{\gamma}^{p,i}_{s,cum}\left(\sum_{j\in\Omega}\rho^j_s + \frac{1}{bd}\sum_{j\in\Omega}\theta^j_s\right) + \rho^i_s\sum_{j\in\Omega}\dot{\gamma}^{p,j}_{s,cum}\right] \tag{4.35}$$

In the following part, we focus on the modelling of the decrease in low-angle boundary misorientation induced by dislocation annihilation during cycling.

4.3.2 Modelling of low-angle boundaries misorientation evolution

During cycling, we assume that the lineic dislocation density along the low-angle boundaries only decreases because of interactions with free dislocations (knitting reactions) [Eggeler, 1989, Caillard and Martin, 2003]. This phenomenon is illustrated in Fig. 4.5 for a tilt boundary.

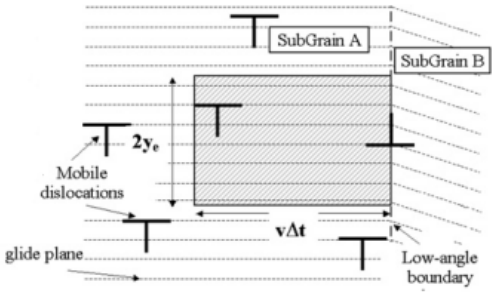

Fig. 4.5. Scheme of the annihilation mechanism of symmetric tilt low-angle boundary dislocations with mobile edge dislocations [Fournier et al., 2011b].

For a given slip system, annihilation takes place if the mobile edge dislocations are located in the region of size A_{box} plotted in Fig. 4.5, expressed as:

$$A_{box} = 2y_e v \frac{\Delta t}{2} \tag{4.36}$$

In Eq. 4.36, v is the velocity of mobile edge dislocations, $\frac{\Delta t}{2}$ is the time necessary to pratice a half-cycle. During the second half-cycle, the same mechanism takes place in subgrain B. Consequently, the variation of linear edge dislocation density in the tilt boundary, $\Delta\Lambda^i$, is given by:

$$\Delta\Lambda^i = -2y_e v \Delta t \frac{\rho_e^i}{2}\Lambda^i \tag{4.37}$$

In Eq. 4.37, only the mobile edge dislocations of opposite Bürgers vector are taken into account, which is expressed by the factor $\frac{1}{2}$. The Orowan equation (Eq. 4.4) leads to the variation of cumulated slip $\Delta\gamma_e^{p,i}$:

$$\Delta\Lambda^i = -\frac{y_e}{b}\Lambda^i \Delta\gamma_{e,cum}^{p,i} \tag{4.38}$$

This equation which models the evolution of dislocation density within the symmetric tilt low-angle boundary allows us to deduce evolution of the misorientation θ_e^i using Eq. 4.1:

$$\dot{\theta}_e^i = -\theta_e^i \frac{y_e}{b}\dot{\gamma}_{e,cum}^{p,i} \tag{4.39}$$

For twist boundaries, we take the other slip systems of the set Ω into account:

$$\dot{\theta}_s^i = -\theta_s^i \frac{y_s}{b}\sum_{j\in\Omega}\dot{\gamma}_{s,cum}^{p,j} \tag{4.40}$$

Two sets Ω_I and Ω_{II} without any interaction are in fact involved for a given twist boundary. Finally, the evolution of the misorientation angles of the low-angle boundaries permits us to deduce the evolution of the subgrain size. These equations allow us to describe the mechanisms of knitting-in/knitting-out highlited by Eggeler [Eggeler et al., 1987] and Caillard and Martin [Caillard and Martin, 1982a, Caillard and Martin, 1982b, Caillard and Martin, 2003]

4.3.3 Modelling the subgrain size evolution

The computation of subgrain size is presented in section 2.6.2 and leads to:

$$d = \frac{d_0}{1-\kappa} \tag{4.41}$$

In Eq. 4.41, the sugrain size d is expressed as a function of the initial subgrain size d_0 and the fraction of vanished low-angle boundaries, κ.

For a given activated slip system, we assume that the interactions between mobile edge dislocations and corresponding symmetric tilt boundary dislocations lead to the vanishing of the corresponding family of tilt low-angle boundary if the misorientation is lower that a critical angle $\theta_{e,crit}$. This criterion was proposed by Holec and Dlouhý [Holec and Dlouhý, 2005] and is based on the fact that the distance between edge dislocations along low-angle boundary is too high to garantee the stability of the array of dislocations when the lineic dislocation density of a tilt boundary reachs a critical value under a given applied shear stress. In this case, the dislocations of the tilt boundary become mobile and the low-angle boundary vanishes.

Let us assume that one-half of the low-angle boundaries is symmetric tilt boundaries and one-half is twist boundaries. In a block, 24 families of low-angle tilt boundaries may be considered (see section 4.2.1.3). Consequently, the vanishing of a family of tilt low-angle boundaries leads to an increase in the value of the fraction κ by $\frac{1}{48}$ if twist low-angle boundaries are taken into account.

For twist boundaries, two families of dislocations are considered. In this case, we consider that a family of twist low-angle boundary vanishes if the two families of screw dislocations which compose them both reach a critical value of misorientation $\theta_{s,crit}$.

As the screw dislocations are divided into 4 families, the different possibilities of arrangements permits us to assume the existence of 6 families of low-angle twist boundaries. The vanishing of a family of low-angle twist boundaries leads to increase the value of the fraction κ by $\frac{1}{12}$ if symmetric low-angle tilt boundaries are taken into account.

The different equations presented in this part model the evolution of the microstructure during cycling. In the following part, we focus on the localisation rule, which links the macroscopic stress tensor to the mean block stress tensor.

4.4 Self-consistent homogenization scheme

4.4.1 Thermoelastic modelling proposed by Kröner

The interaction law proposed by Kröner [Kröner, 1961] is based on thermoelasticity. Using the self-consistent scheme, the interaction law is derived from the solution of Eshelby's inclusion problem [Eshelby, 1957]. Kröner considers each crystal (here, block) as an inclusion, and the deformed matrix as an equivalent homogeneous medium. Thus, for a block with a plastic strain ε^p embedded in the polycrystal deformed with a plastic strain E^p, Kröner solves the localization problem considering an inclusion with a "free" deformation ε^p in the infinite matrix with a uniform "free" deformation. Several assumptions are made to solve and simplify the Eshelby's problem:

- Elasticity is considered as isotropic and homogeneous

- Plastic deformation is isovolumic
- Inclusions (blocks) are considered as spherical

Considering these assumptions, the solution of the Eshelby problem leads to the Kröner interaction law:

$$\begin{aligned} &\underline{\underline{\sigma}} = \underline{\underline{\Sigma}} + 2\mu\,(1-\beta)\left(\underline{\underline{E}}^{p} - \underline{\underline{\varepsilon}}^{p}\right) \\ &\text{with } \beta = \frac{2\,(4-5\nu)}{15\,(1-\nu)} \end{aligned} \tag{4.42}$$

The Kröner model is based on the elastic interaction between the crystals (here, blocks) and the matrix. Consequently, the Kröner model gives us a good approximation of elastic behaviour and plastic behaviour only at low plastic strain. Indeed, at high plastic strains, the Kröner model gives too hard predictions close to those obtained using the Taylor assumption [Taylor, 1938, Berveiller and Zaoui, 1978]. Thus, the Kröner model is expected to give good predictions for low-cycle fatigue tests because of the low values of strain amplitude. But, in the framework of viscoplasticity, the model proposed by Molinari is more suitable [Molinari et al., 1987].

4.4.2 Molinari's model for viscoplastic material

Molinari's model aims at predicting the mechanical behaviour of heterogeneous viscoplastic material still using a self-consistent scheme [Molinari et al., 1987, Molinari and Tóth, 1994, Molinari, 1999]. Considering large deformations, Molinari solves the nonlinear Eshelby problem and obtains an approximate solution calculating the ellipsoide behaviour with uniform nonlinear properties embedded in an infinite homogeneous matrix. In order to simplify the problem, the matrix behaviour is approximated by using a first order expansion of the strain rate based on a tangent approximation and elasticity is neglected. The proposed homogeneization scheme is derived from the use of the Green functions. Introducing a uniform reference medium, the properties of the heterogeneous material are supposed to be carried by the homogeneous equivalent medium.

The interaction law is expressed as follows:

$$\underline{\underline{s}} = \underline{\underline{S}} + \left[\underline{\underline{\underline{\underline{A}}}}^{tg} - \left(\underline{\underline{\underline{\underline{P}}}}^{tg}\right)^{-1}\right] : \left(\dot{\underline{\underline{\varepsilon}}}^{vp} - \dot{\underline{\underline{E}}}^{vp}\right) \tag{4.43}$$

In Eq. 4.43, $\underline{\underline{S}}$ and $\underline{\underline{s}}$ are respectively the macroscopic and local deviatoric stress tensors, $\underline{\underline{\underline{\underline{A}}}}^{tg}$ is a fourth-order macroscopic tangent stiffness modulus tensor and $\underline{\underline{\underline{\underline{P}}}}^{tg}$ is a fourth-order tensor depending on $\underline{\underline{\underline{\underline{A}}}}^{tg}$ and on the shape of the inclusion (block).

Fig.4.6 shows that the tensile stress-plastic strain curve predicted by the Kröner model used in the present study is in accordance with the results available in literature [Hutchinson, 1964] and the Molinari's model seems to tend to the Reuss bound [Reuss, 1929], as expected for f.c.c. polycrystal in literature [Liu and Castañeda, 2004]. To predict the mechanical behaviour of Grade 92 steel

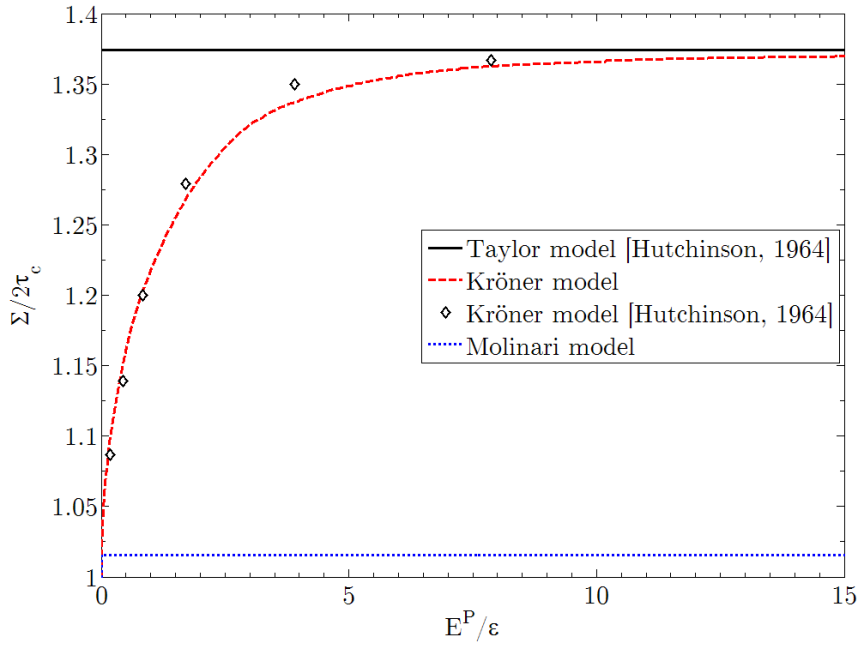

Fig. 4.6. Tensile stress-plastic strain curves of a b.c.c. polycrystal predicted by the models proposed by Kröner (red dashed line) and Molinari (blue dotted line) respectively. The results of Taylor's model (black continuous line) and Kröner's model (empty diamond symbols) available in literature are also plotted [Hutchinson, 1964]. ε is the strain at the initial elastic limit.

during cycling at high temperature, the interaction law of Kröner was chosen in the present study. Indeed, considering the low values of viscoplastic strain amplitudes during the differents tests (lower than a few 10^{-3}), the Kröner's model should be able to give reliable predictions of the mechanical behaviour [Berveiller and Zaoui, 1978, Sauzay, 2000, Rachdi and Sauzay, 2011] and the Molinari's viscoplasticity model will be used as well for comparison. In the following part, we focus on the parameters used in the model, and their physical values, measured or taken from literature.

4.5 Choice of the values of the model parameters

4.5.1 Measured, calculated and fixed parameters

In the presented model, all parameters have a physical meaning. Table 4.1 shows the values of parameters corresponding to constants and intrinsic material parameters.

Parameter	Value	Unit	Reference
ν	0.3		[François et al., 1995b]
μ	68	GPa	
ν_0	10^{13}	s^{-1}	[Caillard and Martin, 2003]
b	2.54×10^{-10}	m	[François et al., 1995b]
k	1.38×10^{-23}	$J.K^{-1}$	

Tab. 4.1. Universal constants and intrinsic material parameters of the model.

The shear stress modulus μ was measured on the Grade 92 steel during cyclic test with a capacitive extensometer. The Poisson ratio ν and the magnitude of the Bürgers vector b were measured on b.c.c.

steels and were taken from literature [François et al., 1995b]. Other parameters such as the Boltzmann's constant k and the Debye frequency ν_0, linked to the thermal vibration of dislocations were taken from literature [Caillard and Martin, 2003].

The microstructural parameters, experimentally measured, calculated or fixed, are presented in Table 4.2.

Measured parameters	Value	Unit	Reference
ρ_e	1×10^{14}	m^{-2}	
ρ_s	1×10^{14}	m^{-2}	
θ_0	1.7	°	[Tak et al., 2009]
d_0	370	nm	
d_{block}	2.3	µm	[Fournier, 2007]
Calculated parameters	**Value**	**Unit**	**Reference**
y_e	4	nm	[Catalao et al., 2005]
y_s	50	nm	[Essmann and Mughrabi, 1979]
α	0.3		[Queyreau et al., 2009]
θ_{crit}	0.4	°	[Holec and Dlouhý, 2005]
τ_0	0	MPa	[Sommer et al., 1998]

Tab. 4.2. Microstructural model parameters. Corresponding values were either experimentally measured, calculated or fixed based on literature data.

The values of the critical annihilation distances y_e and y_s depend on the crystal structure and on temperature. Concerning these parameters, a limited number of studies is available in literature and no measurement was performed on 9%Cr tempered martensitic steels. Consequently, we assume the slip mechanisms of dislocations in b.c.c. structure at high temperature are similar to those in f.c.c. structure (the cross-slip mechanism is easy in b.c.c at high temperature) [Caillard and Martin, 2003]. Value of the critical distance y_e for edge dislocations measured in f.c.c. crystals was estimated from about 1.6 nm to 4 nm (depending on temperature, materials. . .) [Essmann and Mughrabi, 1979, Hähner et al., 1998, Kassner et al., 2000, Gaudin, 2002, Catalao et al., 2005]. The critical distance y_s for screw dislocations measured in f.c.c. crystals was estimated from about 10 nm to 100 nm [Takeuchi, 1975, Essmann and Mughrabi, 1979, Essmann and Differt, 1996, Brown, 2002, Devincre et al., 2008, Mughrabi and Höppel, 2010]. These values are used in the following as indicative bounds for y_e and y_s respectively.

The total free dislocation density was measured on as-received Grade 92 steel and set to about 2×10^{14} m^{-2}. Few data concerning the ratio of screw and edge dislocations in the as-received material are available in the literature and leads us to assume in a first approximation that the total density is equaly divided into edge and screw dislocations. However, experimental observations have shown that mobile dislocations are mainly composed by screw part ([Guétaz et al., 2003] in EUROFER, [Wakasa and Wayman, 1981] in a martensite Fe-20%Ni-5%Mn steel). This hypothesis is discussed later in this chapter (see section 4.6.4).

The initial mean misorientation angle θ_0 carried out by low-angle boundaries was calculed from the measured misorientation angle distribution on as-received X20 steel [Tak et al., 2009]. This value corresponds to the arithmetic mean misorientation angles lower than 5 °. The initial subgrain diameter d_0 was measured in the as-received Grade 92 steel. The block diameter was measured by EBSD investigations on Grade 91 steel [Fournier, 2007]. This parameter is not used explicitly in the modelling but, for the sake of consistency, the mean subgrain size should be lower than the block size, even after cycling.

The critical value of misorientation θ_{crit} was calculed by Holec and Dlouhý and set to 0.4 ° in the conditions of temperature, stress and precipitation close to those of the Grade 92 steel during cycling [Holec and Dlouhý, 2005].

Most parameters values were either experimentaly measured or calculated. However, some parameter values are not exactly known and little information is available in literature concerning their values for Grade 92 steel or more generally for the 9%Cr steel family. Consequently, a parametric study is presented in section 4.6.4 in order to study the impact of each value on the model predictions.

This model uses a low number of ajustable parameters : only the values of the activation volume, V, and the activation energy, Q, are fitted using the first experimental quarters of cycles (monotonic loading). As these physical parameters correspond to the mechanisms of dislocation glide, their order of magnitude is known and consequently, they are not totally let free during the identification process presented in the following section.

4.5.2 Identification process

In order to predict the cyclic behaviour of the material at high temperature, the identification process aims to fit the two ajustable parameters of the model : the activation volume V and the activation energy Q. This low number of ajustable parameters permits us to reduce the identification process to a very limited number of experimental data, excluding all data in relationship to the cyclic softening behaviour. They are ajusted on:

- a monotonic tensile test up to 0.35 % with a strain rate of 2×10^{-3} s^{-1}
- a monotonic tensile test up to 0.35 % with a strain rate of 1×10^{-5} s^{-1}

Only two monotonic tests at different strain rates are used to adjust the two remaining parameters. Thus, all cyclic tests available at different strain amplitudes and strain rates (see Tables 3.1 and 3.2) are kept for the validation process. Moreover, the limited number of adjustable parameters and experimental data used to fit them induces a reduction of the parameter identification time. Finally, it should be noticed that tests using various strain rates are indeed required for adjusting these values of the viscoplasticity parameters.

Numerical simulations, performed with the SiDoLo software [Pilvin, 2003], were carried out on a polycrystalline aggregate (each crystal representing, here, a block of laths) with 100 random crystallographic orientations. The influence of the number of blocks and the set of random orientations on the predicted macroscopic behaviour is presented in Fig. 4.7.

The results presented in Fig. 4.7(a) show that the model gives a similar response for aggregates composed of more than 100 blocks. Consequently, in order to reduce the computation time[†], simulations are carried out using an aggregate of 100 blocks. Fig. 4.7(b) shows that the set of random crystallographic orientations of the 100 blocks has no significant impact on the predicted macroscopic response and it permits us to neglect its influence on the model predictions. This confirms that the number of blocks is high enough to get a representative elementary volume.

The results of the adjustement process are presented in Fig. 4.8. The values of the fitted parameters, the activation volume V and the activation energy Q are reported in Table 4.3.

[†]The computation time is 10 times higher to predict the mechanical behaviour of an aggregate of 500 blocks than of an aggregate of 100 blocks.

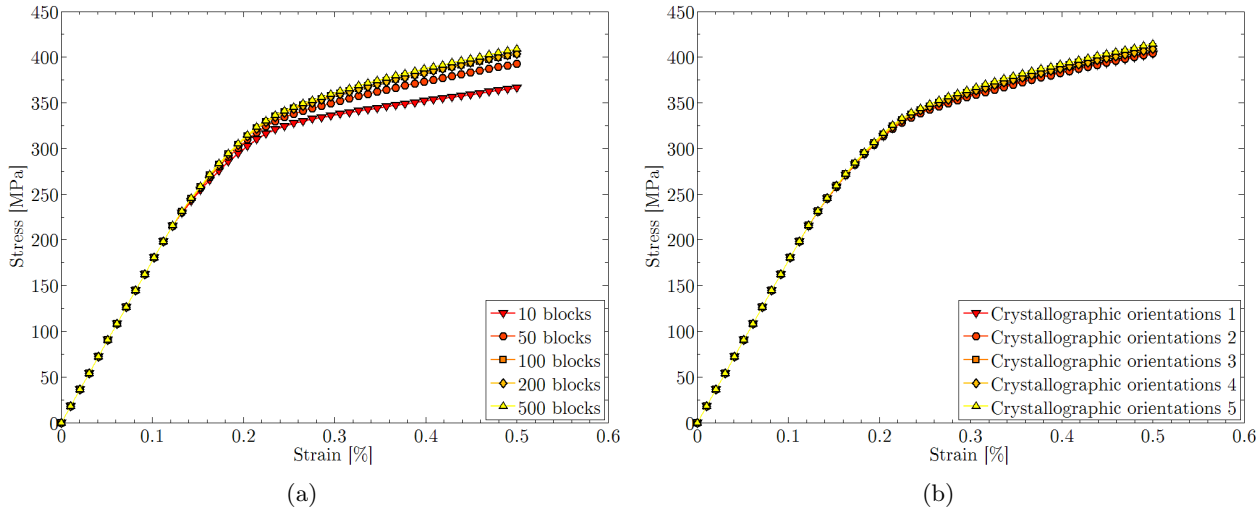

Fig. 4.7. Influence of (a) the number of blocks and (b) different sets of crystallographic orientations of 100 blocks on the simulated monotonic tensile curves up to 0.5% at 2×10^{-3} s^{-1}. For Fig (b), each randomly selected set of 100 crystallographic orientations is different from the others.

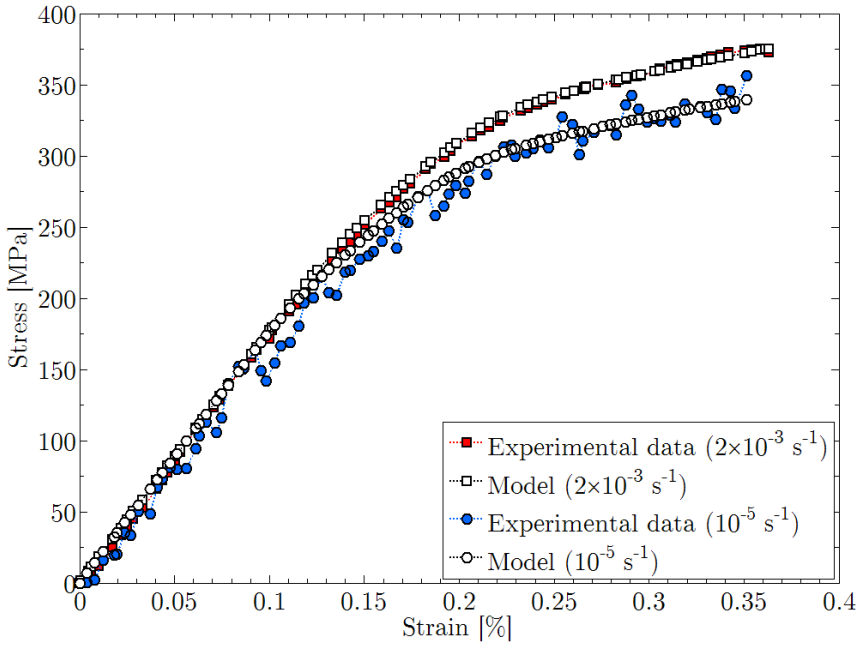

Fig. 4.8. Comparison between the experimental and simulated monotonic curves up to 0.35 %, at two different strain rates.

Parameter	Value	Unit
Q	1.2	eV
V	216	b^3

Tab. 4.3. Values of the parameters fitted on monotonic tensile curves up to 0.35 %, with a strain rate of 2×10^{-3} s^{-1} and 1×10^{-5} s^{-1}.

The study of the hysteresis loops of the Grade 91 steel at 550 ℃ permits Fournier et al. to measure an activation volume close to 60 b^3 [Fournier et al., 2006a]. In a 12%Cr ferritic-martensitic steel containing different alloying elements (C, N, Ni, Mo, V, Nb, Si, Mn and B), Marmy et al. measured a value equal to 45 b^3 during tensile test at 600 ℃ [Marmy et al., 1993]. The b.c.c. materials are known to have low activation volumes (from about 15 to 300 b^3 depending on the temperature) compared to f.c.c. materials which have values 10 to 100 times larger at low temperature [Voyiadjis and Abed, 2005]. The fitted value of the activation volume in the current model is slightly larger than measured values in other steels, but we have to consider this comparison cautiously: the value of the activation volume widely depends on the microstructure of the considered material, and particularly on precipitates and chemical elements which compose the solid solution. Consequently, we can carefully conclude that the fitted value of the activation volume is in accordance with the order of magnitude measured in b.c.c. materials and remains significanly lower than the f.c.c. materials one.

The fitted value of activation volume is low compared to the subgrain size. This indicates that the mechanisms which govern the viscoplastic glide take place at a smaller scale than the subgrain structure in this steel. The fitted value is too high to correspond to interactions with individual solute atom in the matrix (atomic volum is close to 1 b^3) [Conrad and Narayan, 2000, Wei et al., 2004] and seems rather low for corresponding to interactions with small precipitates like MX-types (several thousands of b^3) [Caillard and Martin, 2003]. Several studies on Ni(Al) and Al(Mg) alloys proposed that solid solution hardening is not simply the result of a direct dislocation / solute atoms interaction, but the result of close solute-solute atoms repulsion [Rodary et al., 2004, Proville et al., 2006, Proville and Patinet, 2010]. This repulsion force is considered to be an obstacle to dislocation glide [Rodary et al., 2004]. Thus, the interaction between dislocations and solid solution is not only describe with isolated solute atoms but also with clusters of solute atoms. We can assume that similar mechanisms may occur in ferritic-martensite steels strengthened by Mo and/or W solute atoms. In this case, the fitted value of the activation volume may correspond to the volume of (Mo,W) clusters.

As for the activation volume, experimental values of the activation energy published in literature widely vary and depend on the considered deformation mechanism, the experimental technique used, temperature and material under consideration [Spigarelli et al., 1997, Fournier et al., 2006a]. The fitted value of the activation energy is significantly lower than the bulk diffusion one which is measured to 2.5 eV [François et al., 1995b]. In 12%Cr-Mo-VNb ferritic-martensitic steel, Marmy and coworkers have measured a value of the activation energy of about 1.2 eV during tensile test at 600 ℃ [Marmy et al., 1993]. The fitted value of activation energy in the current model is equal to this experimental value. According to Marmy et al., this energy barrier corresponds to mechanims of deformation which need low activation energy and we can assume that it corresponds to the energy required for dislocations glide through solid solution and small carbo-nitride obstacles [Marmy et al., 1993], assumed to be composed of small clusters of solute atoms. Following the experimental study of Abe using various amounts of W and C elements, both W solid solution and MX precipitates lead to decrease in creep strain rates [Abe, 2001]. This means that both are obstacles to dislocation glide. The activation volume and energy adjusted previously may be effective values corresponding to several kinds of obstacles.

Values of the parameters used during the identification process remain the same for all the presented simulation results in the following sections, unless it is explicitely expressed in the parametric study. Because of the few experimental data that are necessary to fit the two adjustable parameters, a large number of independant tests are available to validate the model. In the following section, the experimental hysteresis loops at the first cycle of fatigue test and the corresponding predicted ones are compared for both strain rates.

4.6 Simulation of cyclic loading

4.6.1 Validation of the model on the first macroscopic loop for both strain rates

The first step of the validation concerns the prediction of the first loop. As the identification process requires two monotonic tests at different strain rates, their corresponding first cycles are compared to the model predictions. Results are presented in Fig. 4.9.

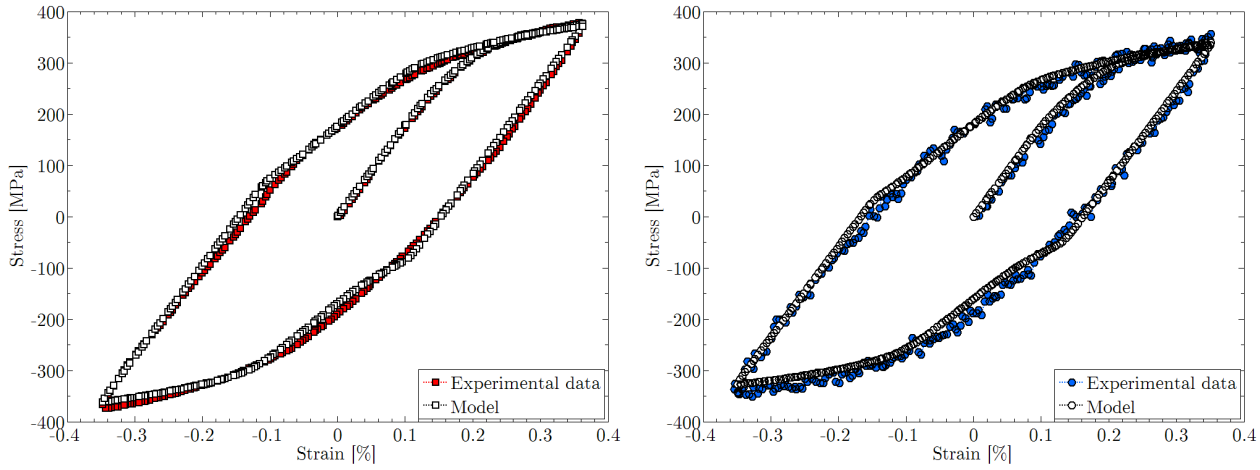

Fig. 4.9. Comparison between experimental and predicted macroscopic cycles for a strain amplitude of ± 0.35% (a) with a strain rate of 2×10^{-3} s^{-1} and (b) with a strain rate of 1×10^{-5} s^{-1}.

The model predicts the mechanical behaviour of the Grade 92 steel during the first hysteresis loop quite accurately for both strain rates. A slight difference between the model and the experimental data is observed for the minimum stress in compression: for both tests, the predicted minimum stress is slightly overestimated, whereas the predicted maximum stresses are very close to the experimental data. This phenomenon is probably due to, on the one hand, experimental scatter or, on the other hand, to a too fast softening rate.

Although maximum and minimum stresses are rather accurately predicted, the shape of the predicted hysteresis loop is characterized by a change in curvature both in compression and tension, but not during the first quarter of cycle. This unexpected behaviour is due to the expression of the kinematic stress evolution. However, the reasons which induce this problem are not clearly established and complementary studies are necessary to understand this phenomenon exactly. This unaccuracy takes place only during a short part of each cycle and it probably has no significant influence on the prediction of the softening behaviour of the material.

4.6.2 Prediction of cyclic softening for both strain rates

4.6.2.1 Predicted macroscopic behaviour

The main objective of the model is to predict the softening behaviour, which characterizes the tempered martensite steels during cycling. In order to clarify the presentation of the results, only the experimental and predicted data corresponding to the maximum tensile stress are compared. It is very close to the amplitude. Fig. 4.10 shows the cyclic softening predicted by the modelling at ± 0.35% and two

different strain rates. The computation time is approximatly equal to 25 - 30 hours to obtain these results.

According to Fig. 4.10, the model predicts a cyclic softening for both strain rates: it reproduces the stress drop of 70 MPa measured experimentally during the test. Moreover, the cyclic evolution is correctly predicted by the model. The difference between the predicted and experimental curves is lower than 10 MPa for the higher strain rate and 20 MPa for the lower one (in both case, these differences are lower than 5 % of the corresponding initial stress). Thus, the model is able to predict reasonably the overall softening observed during cycling at intermediate strain amplitude.

However, although the softening rate is well predicted (predicted slopes are almost parallel to the experimental ones), the predicted and experimental curves are not superimposed for the lower strain rate. This leads to an underestimation of the maximum tensile stress during all the test whereas for high strain rate, this phenomenon is limited to the beginning of the tests, up to 500 cycles, and the model accurately predicts the mechanical behaviour after 900 cycles. This difference may be explained by the experimental scatter (which can reach ± 15 MPa) of the data measured during cycling at low strain rate (see Fig. 4.8 for example). Scatter is lower at higher strain rate (see Fig. 4.9).

4.6.2.2 Predicted microstructural evolution

The mean subgrain size evolution is presented in Fig. 4.11. Although the model reproduces the experimentally observed tendency of the subgrain size evolution (fast growth followed by a reduction of evolution rate), this figure shows that the subgrain growth rate is overestimated. Indeed, the modelling predicts a too fast evolution of the subgrain growth up to 400 cycles, which might induce at least partially the high softening rate observed on the predicted macroscopic behaviour. Moreover, predicted final subgrain sizes for both strain rate are overestimated (see Table 4.4): for high strain rate, the growth factor is equal to about 2.2 (experimental data gives about 1.7) and for low strain rate, it is equal to about 3.1 (experimental data gives about 2.0). These results can be explained by the strong assumptions made to describe the low-angle boundary structure (pure symmetric tilt boundary with only one family of edge dislocations, pure twist boundaries...): these simplifications probably lead to an overestimation of the number of vanished low-angle boundaries.

Strain rate	Final experimental mean subgrain size	Final predicted mean subgrain size
2×10^{-3} s^{-1}	0.62 ± 0.12 µm	0.84 µm
1×10^{-5} s^{-1}	0.78 ± 0.08 µm	1.16 µm

Tab. 4.4. Values of the measured and predicted mean subgrain size in a sample of fractured specimen after fatigue test of a strain amplitude of ± 0.35 %, for different strain rates.

The effect of strain rate on the subgrain growth is clearly observable. For the lower strain rate, the predicted subgrain growth rate is significantly higher than for the higher strain rate, even after 1,000 cycles. This difference might be explained by the plastic strain amplitude applied on the material during fatigue cycles. Indeed, Fig. 4.8 shows that for imposed total strain amplitude, the model predicts a higher plastic strain amplitude for the low strain rate than for the high strain rate, as experimentally observed (see Table 3.1 and 3.2). Thus, the amount of cumulated viscoplastic strain is higher in the material deformed at low strain rate. In addition, Fig. 4.12 shows the predicted evolution of the mean number of activated slip system per block during a monotonic tensile test up to 0.5 % and for the two different strain rates. We observe that a decrease in strain rate leads to a significant increase in the mean number of activated slip system per block. Thus, the annihilation terms and annihilation probabilities between the free dislocations and the low-angle boundaries are

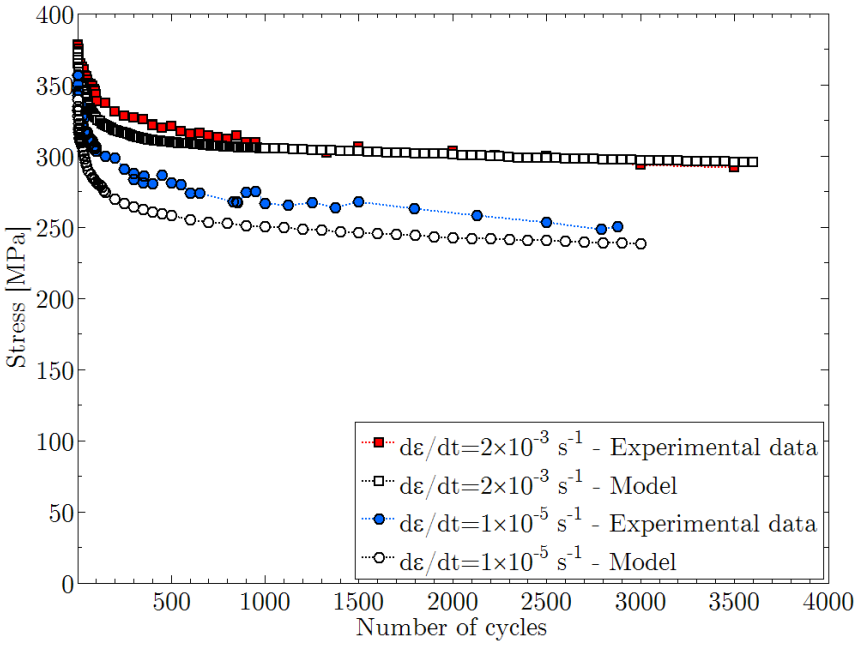

(a)

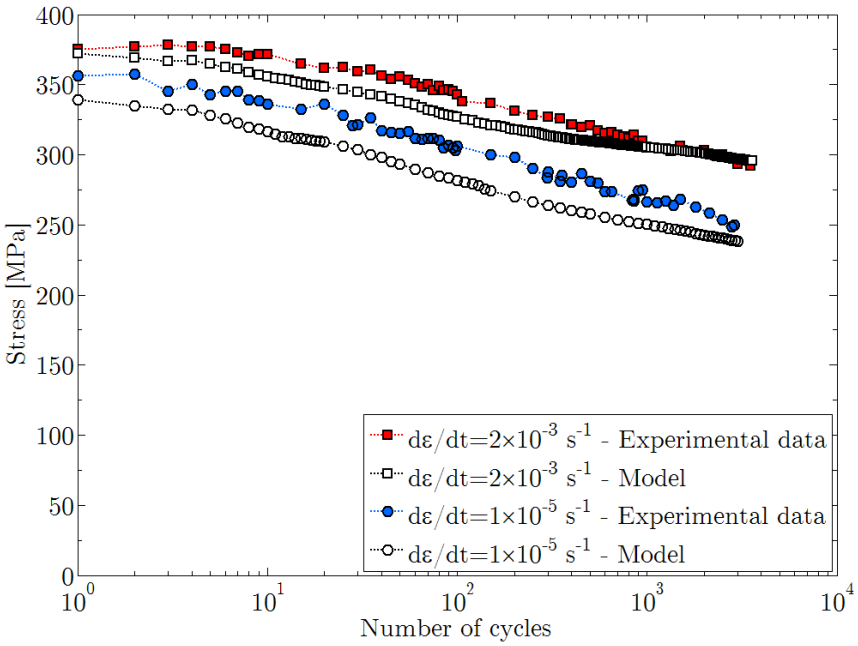

(b)

Fig. 4.10. Comparison between experimental and predicted cyclic softening curves for a strain amplitude of ± 0.35% for two different strain rates (a) in linear scale and (b) in logarithmic scale. Maximum stress is computed or measured at different cycles.

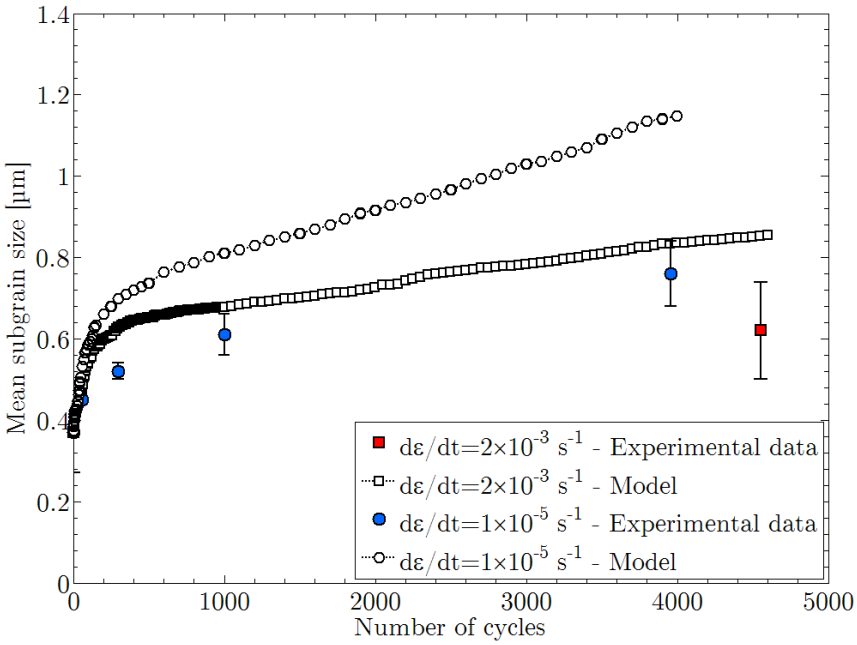

Fig. 4.11. Comparison between experimental and predicted mean subgrain size evolutions during fatigue tests with a strain amplitude of ± 0.35% for two different strain rates.

higher in material during cycling at the lower strain rate than during cycling at the higher strain rate. Consequently, the decrease in strain rate leads to an enhancement of the annihilation phenomena between mobile dislocations and low-angle boundaries in the aggregate and finally, to a faster growth of subgrains.

Fig. 4.13 presents the predictions of the mobile edge and screw dislocation density evolutions. The local variations of the curves are due to the term of production of dislocations introduced in the dislocation density evolutionnary equations (see Eqs. 4.34 and 4.35). Fig. 4.13(a) shows that the model predicts a fast evolution of the mobile dislocation density: the main variations occur before 1,000 cycles and they remain approximatly stable. As expected, mobile screw dislocations annihilate faster than mobile edge dislocations, due to their geometrical properties (higher probability of annihilation [Sauzay et al., 2005]) and higher critical annihilation distance with respect to the edge ones.

The model predicts a very fast evolution of the mobile dislocation densities: the main variations occur during the 100 first cycles. The strain rate has an influence on the predicted dislocations densities. Although this effect is slight on the mobile screw dislocation density evolution, it is clearly visible on the mobile edge dislocation density evolution. Up to 20 cycles, no significant difference between both curves is observed, but after the 20^{th} cycle, the mobile edge dislocation density decreases faster in the case of the lower strain rate than in the case of the higher strain rate. As for subgrain growth, that is the consequence of the plastic strain amplitude per cycle, higher for the lower strain rate, which leads to a higher number of actived slip systems in blocks too and finally, promotes the annihilation phenomena.

No experimental value of dislocation density evolution is available for this material. Only the total dislocation density were measured at the end of the test and can be compared to the predicted values. Experimental and predicted values are presented in Table 4.5. Although the predicted value for the low strain rate is overestimated, the model correctly predicts the final value measured in the foils extracted from the specimens fractured at high strain rate.

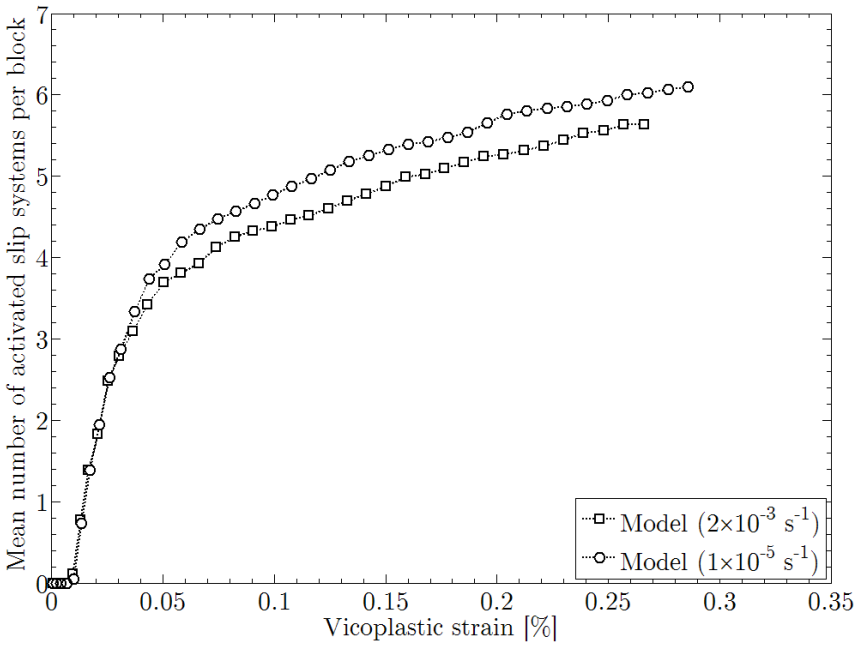

Fig. 4.12. Comparison between the predicted mean number of activated slip systems per blocks for two different strain rates during a monotonic tensile test up to a total strain of 0.5 %. A slip system is considered to be activated if the plastic glide is higher than 10^{-4}.

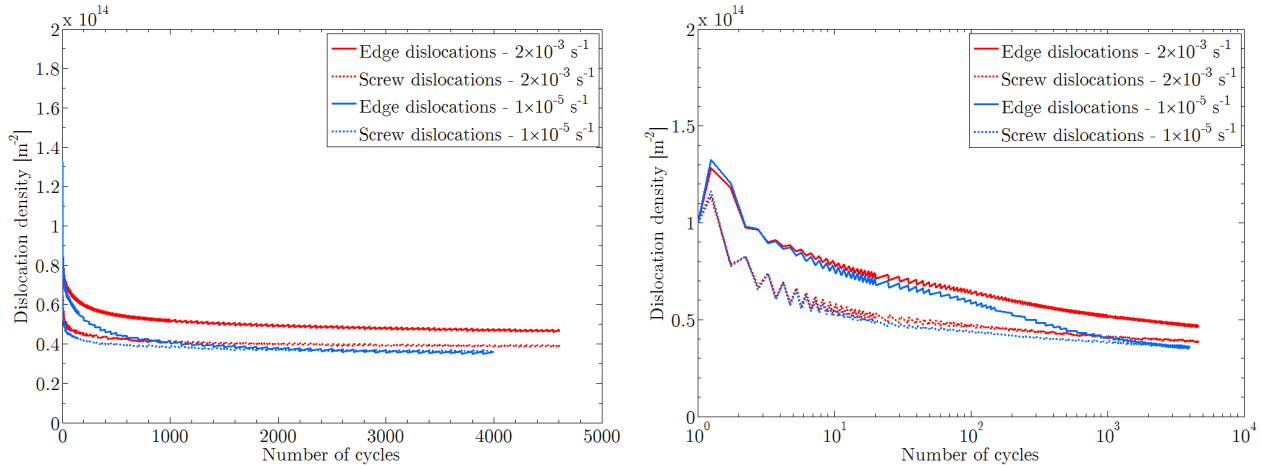

Fig. 4.13. Predicted edge and screw dislocation densities during fatigue test simulations using a strain amplitude of ± 0.35% for two different strain rates (a) in linear scale and (b) in logarithmic scale.

Strain rate	Experimental average dislocation density	Predicted mean dislocation density
2×10^{-3} s^{-1}	$\approx 1 \times 10^{14}$ m^{-2}	$\approx 0.9 \times 10^{14}$ m^{-2}
1×10^{-5} s^{-1}	$\approx 0.3 \times 10^{14}$ m^{-2}	$\approx 0.7 \times 10^{14}$ m^{-2}

Tab. 4.5. Values of the measured and predicted dislocation densities in a foils extracted from fractured specimens after fatigue tests at strain amplitude of ± 0.35 %, for different strain rates.

The model predicts the microstructural evolution during cycling rather well. Although the mean subgrain size evolution is overestimated, the model is able to reproduce the influence of the strain rate on the softening behaviour and microstructural evolution, which are experimentally observed. In the following part, we focus on the influence of strain amplitude on the prediction of the mechanical behaviour for a wider set of experimental conditions.

4.6.3 Predictions of the macroscopic cyclic softening for different strain amplitudes

In this section, the influence of the cyclic strain amplitude on the prediction of mechanical softening is studied. Model predictions are compared to the cyclic test results performed on Grade 92, presented in chapter 3.

For all simulations, the parameters of the model have the same values as those presented in Tables 4.2 and 4.3. Figs. 4.14 to 4.17 present the evolutions of the maximum stress recorded during the experimental tests and predicted by the model.

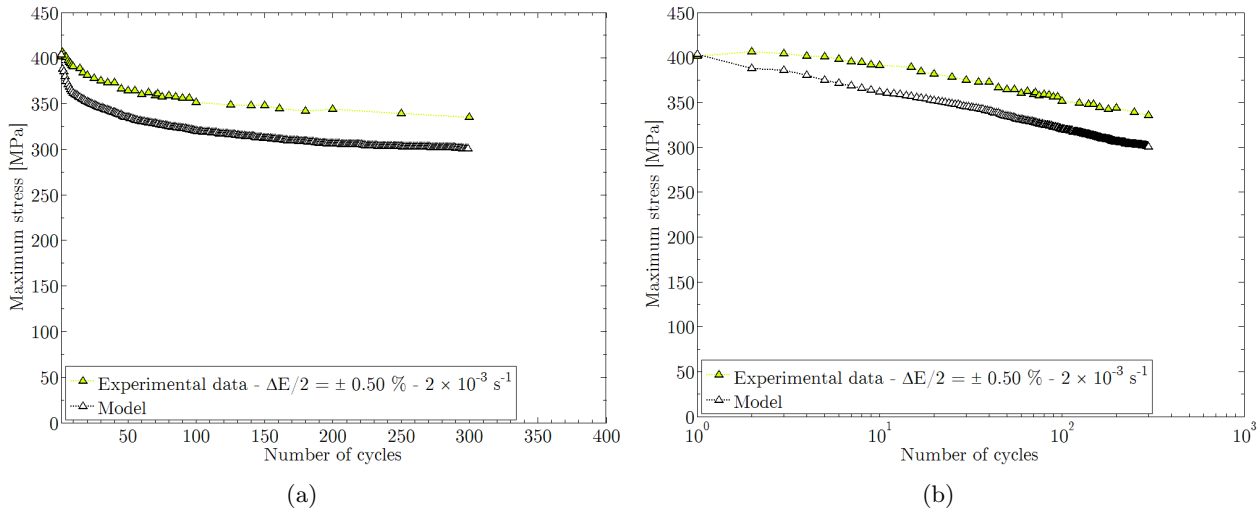

Fig. 4.14. Comparison between experimental and predicted cyclic softening curves for $\Delta E/2 = \pm$ 0.50 % in (a) in linear and (b) logarithmic scale. Maximum stress is computed or measured at different cycles.

These results show that for all tests, the model predicts a cyclic softening behaviour. For the tests performed at $\Delta E/2 = \pm$ 0.30 % and $\Delta E/2 = \pm$ 0.25 % (Figs. 4.15 and 4.16), both the amplitudes of the cyclic softening effect (which are equal to about 60 and 50 MPa respectively) and the stationary softening rate are correctly predicted by the model.

For the highest value of strain amplitude $\Delta E/2 = \pm$ 0.50 %, the predicted softening is clearly higher than the experimental one during the first ten cycles (see Fig. 4.14). Consequently, the predicted maximum tensile stress is widely underestimated, by 25 to 40 MPa depending on the number of cycles. As shown in Fig. 4.14(b), the difference between predicted and experimental curves increases up to 10 cycles and remains them stable until the end of test. This indicates that the predicted softening rate, higher than experimental one for the first ten cycles, is approximately the same than experimental one from the 20^{th} to the end of the test: this is clear when comparing the softening slopes in Fig. 4.14(b). This phenomenon is probably due to the sensitivity of the model to the plastic strain amplitude. As this test is characterized by a high viscoplastic strain amplitude, we assume that it leads to an overestimation of the predicted microstructural evolution, which fastly occurs from the second cycle.

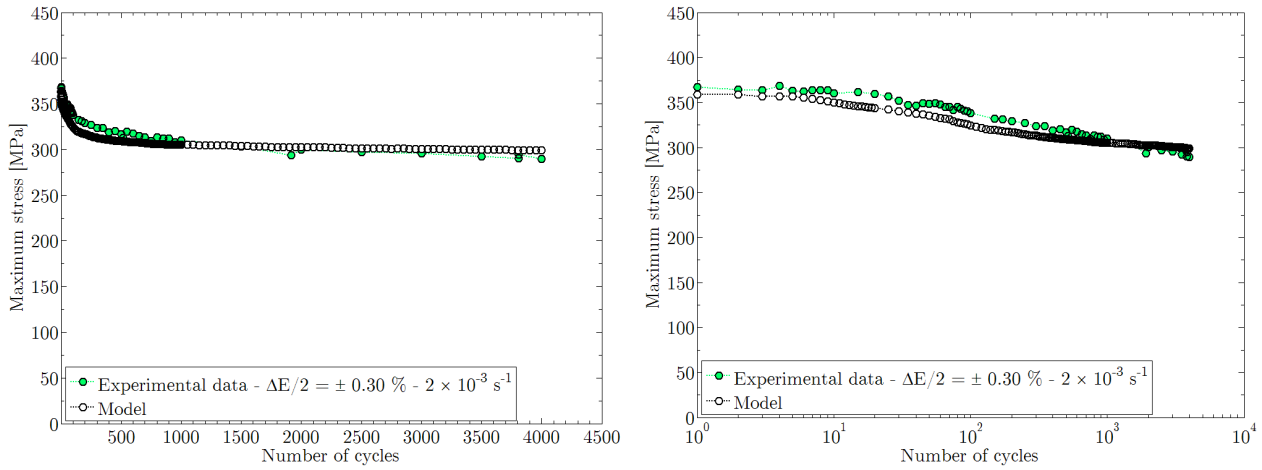

Fig. 4.15. Comparison between experimental and predicted cyclic softening curves for $\Delta E/2 = \pm$ 0.30 % in (a) in linear and (b) logarithmic scale. Maximum stress is computed or measured at different cycles.

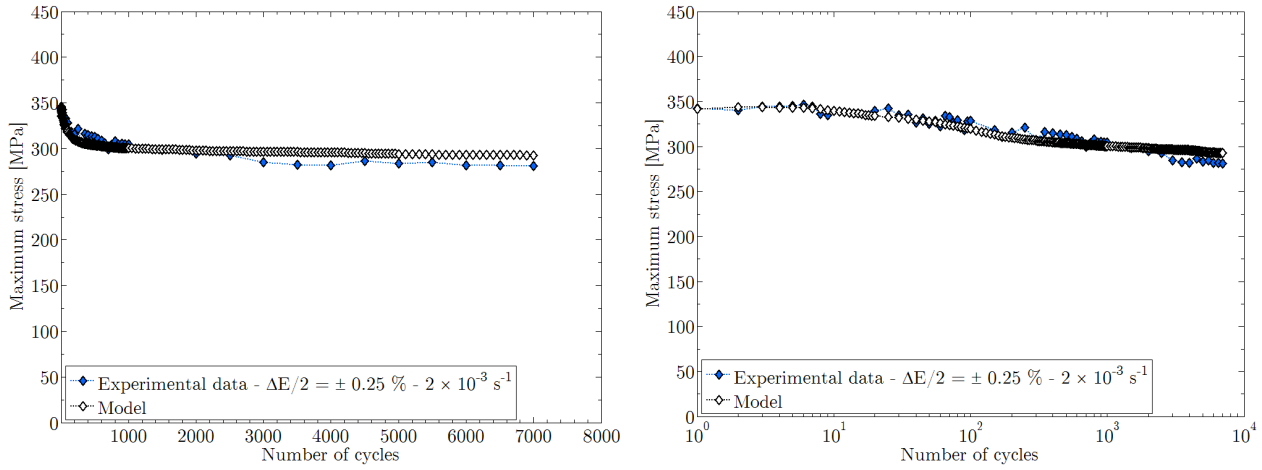

Fig. 4.16. Comparison between experimental and predicted cyclic softening curves for $\Delta E/2 = \pm$ 0.25 % in (a) in linear and (b) logarithmic scale. Maximum stress is computed or measured at different cycles.

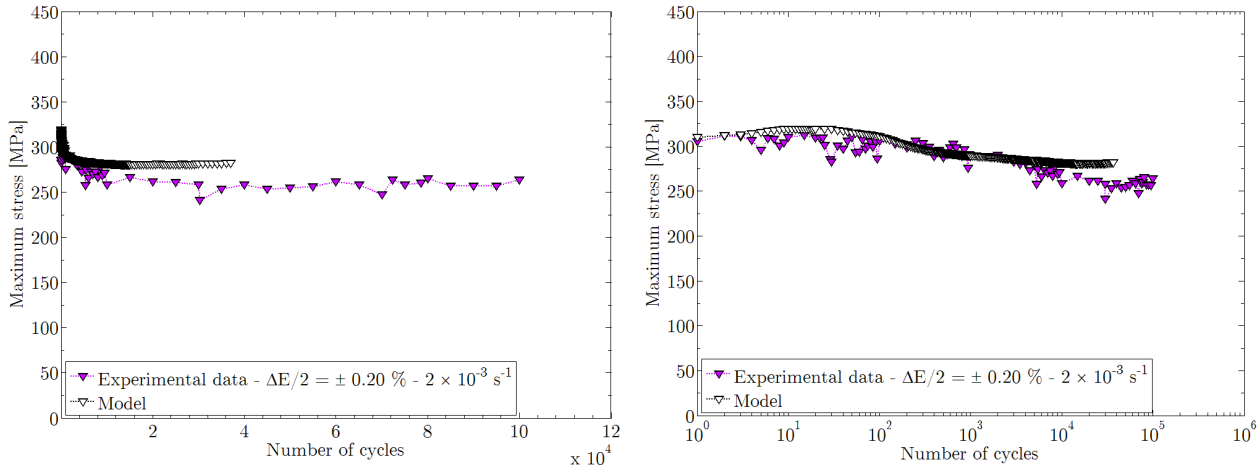

Fig. 4.17. Comparison between experimental and predicted cyclic softening curves for $\Delta E/2 = \pm$ 0.20 % in (a) in linear and (b) logarithmic scale. Maximum stress is computed or measured at different cycles.

This hypothesis is discussed in chapter 5.

The opposite case can be described with the test performed using $\Delta E/2 = \pm$ 0.20 % presented in Fig. 4.17. In this case, the viscoplastic strain amplitude is very low at the first cycle. Instead of cyclic softening, the model predicts a slight hardening up to about 40 cycles. After this stage, a slight decrease in the maximum stress is predicted, but neither its amplitude nor its kinetics are in a correct agreement with the experimental data. Thus, the predicted softening amplitude is underestimated by about 20 - 25 MPa.

Because of its sensitivity to the viscoplastic strain amplitude during cycling, the model is not able to predict the mechanical behaviour of the material for low strain amplitudes ($\Delta E/2 \leq \pm$ 0.20 %) and for high strain amplitudes ($\Delta E/2 \geq \pm$ 0.50 %) very accurately.

4.6.4 Sensitivity of model predictions to the values of model parameters

All the parameters used in the model have a physical meaning. However, most of them were not experimentally determined in the conditions under interest and only very limited amount of information is available in literature concerning annihilation distances, initial and critical misorientations angle and the ratio between the free edge or screw dislocations densities and the total free dislocation densities. Consequently, in a first approximation, their assigned parameter values corresponded to measurements or computation carried out for a different material, in different conditions of environment, temperature or mechanical loadings. The involved parameters are presented in the following list:

- The critical annihilation distance of edge dislocations y_e
- The critical annihilation distance of screw dislocations y_s
- The initial mean low-angle boundary misorientation θ_0
- The critical value of low-angle boundary misorientation θ_{crit}
- The ratio between the mobile edge and screw dislocations densities and the total mobile dislocation density

To analyse the sensitivity of the model to each parameter, all the values of the other parameters are kept the same as those used for the identification process (Tables 4.2 and 4.3). A upper and a lower bound values are defined for the studied parameters, based on information available in literature. Using both values, two predictions of the mechanical behaviour and microstructure evolution during cyclic test at a strain amplitude of $\pm$ 0.35 % and a strain rate of 1×10^{-5} s^{-1} are then calculed using the model. Then, they are compared to the reference curves obtained in the previous section and the influence of parameter values on the prediction is discussed.

4.6.4.1 Influence of the critical annihilation distance for edge dislocations on model predictions

As it has been described in section 4.5, little information about the value of the critical annihilation distance at high temperature for edge dislocations y_e is available in the literature and no measurement was performed in 9%Cr steels at 550 ℃. Considering the different values published in the literature, the upper and lower bounds are fixed to 2 nm and 4 nm respectively. The impact of this parameter change on the macroscopic mechanical behaviour is presented in Fig. 4.18.

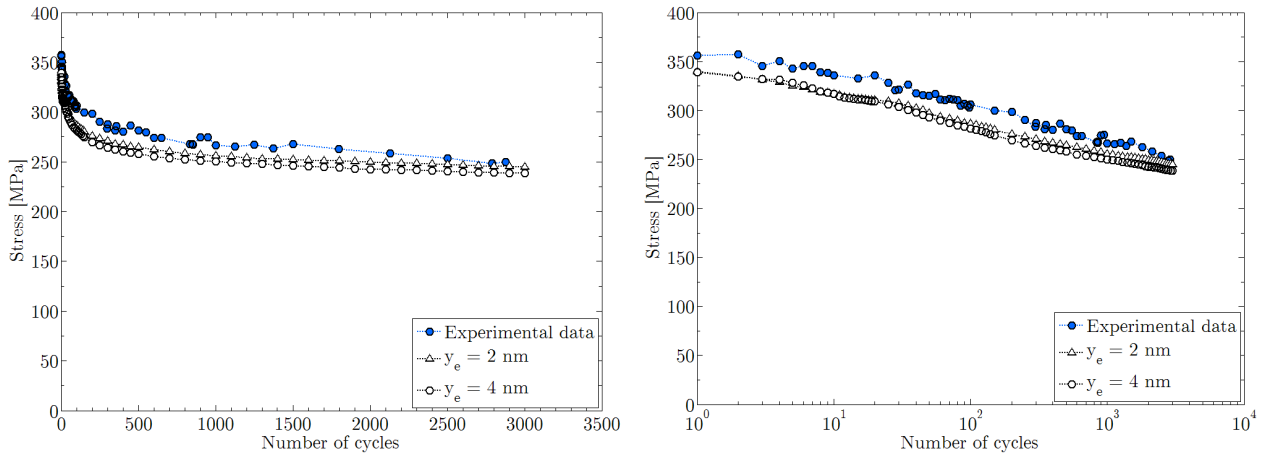

Fig. 4.18. Influence of the value of y_e on the predicted macroscopic mechanical behaviour.

Up to 10 cycles, the value of y_e has no influence on the predicted mechanical behaviour. Then, up to about 200 cycles, the softening rate slightly increases with the value of y_e: as expected, the higher the annihilation distance, the higher the softening rate. Finally, at the end of the test, the parameter change induces a difference of about 10 MPa for the maximum tensile stress (which is less than 5 % of the current value).

The influence of the value of y_e on the predicted mean subgrain size evolution is presented in Fig. 4.19. As expected, the subgrain growth rate is higher when y_e increases. Consequently, the predicted final subgrain size varies by about 17 % between both calculations. The impact of y_e on the predicted average dislocation density evolution is presented in Fig 4.20. As expected, no impact on the screw dislocation density evolution is observed. But an effect is visible for edge dislocation density evolution rate: as expected, the higher the value of y_e, the faster the free edge dislocation density decreases. However, y_e does not impact the prediction of the final dislocation density.

The sensitivity of the model to the value of y_e is limited to the predicted subgrain size evolution. Its impact on the macroscopic mechanical behaviour is slight. This indicates that, except for subgrain

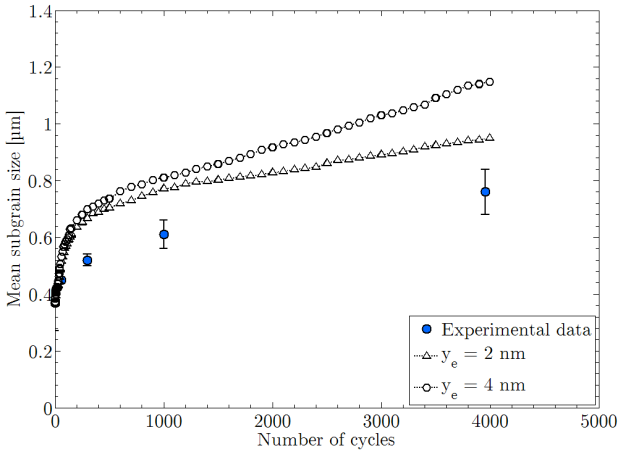

Fig. 4.19. Influence of the value y_e on the predicted mean subgrain size evolution.

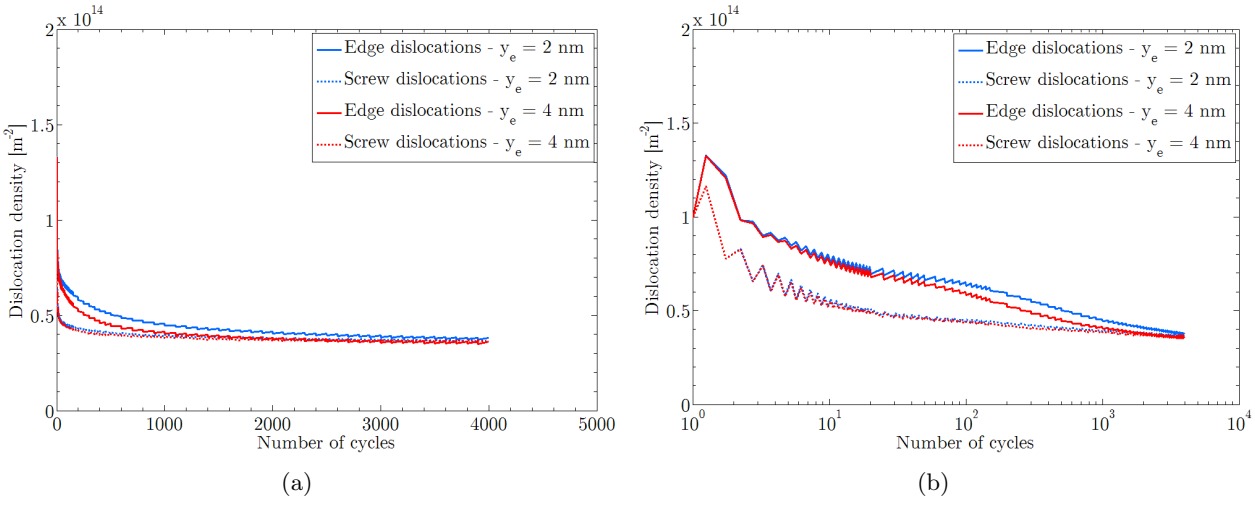

Fig. 4.20. Influence of the value y_e on the predicted mean dislocation density evolution.

size, the predictions are relatively stable with respect to the variation of this parameter.

4.6.4.2 Influence of the critical annihilation distance for screw dislocations on model predictions

As for parameter y_e, little information about the critical annihilation distance for screw dislocations y_s is available in the literature at high temperature and no measurement was performed in 9%Cr steels. By considering the values presented in section 4.5, the upper and lower bound values are fixed to 25 nm and 100 nm respectively, which include almost all values available in literature. The influence of this parameter on the macroscopic mechanical behaviour is presented in Fig. 4.21.

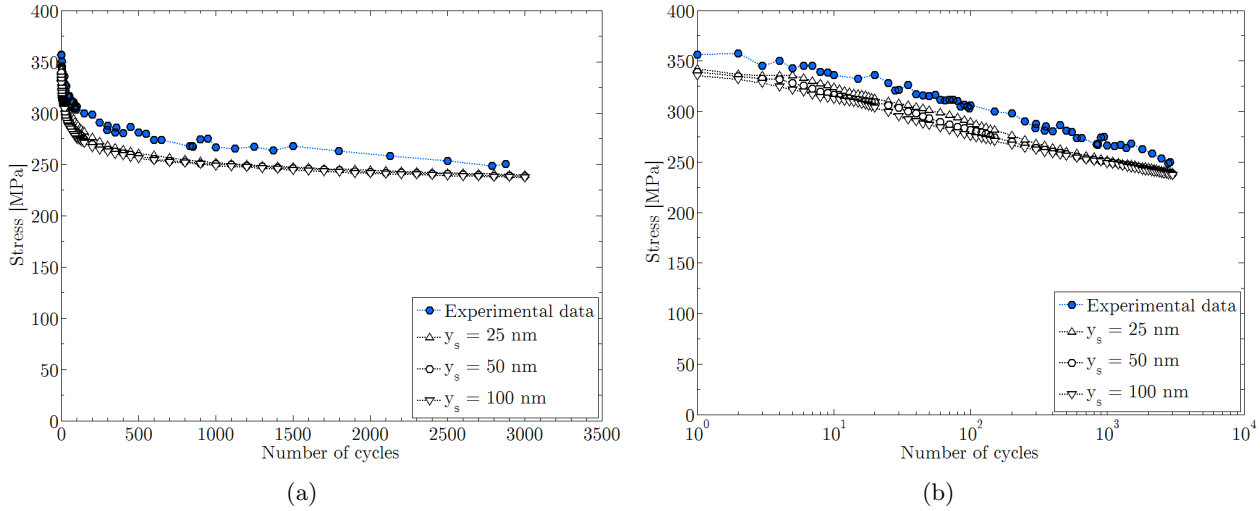

Fig. 4.21. Influence of the value of y_s on the predicted macroscopic mechanical behaviour. 50 nm is the value used in the previous section.

The influence of y_s on the predicted mechanical behaviour is noticeable up to about 300 cycles. During this short first stage, the parameter change induces a variation of about $\pm$ 10 MPa of the maximum tensile stress (which is lower than 4 % of the current value). After this transient stage, the predicted mechanical behaviour is no longer influenced by the value of y_s.

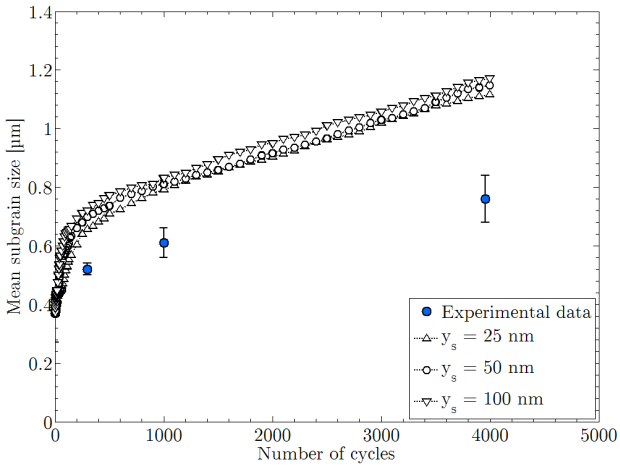

Fig. 4.22. Influence of the value of y_s on the predicted mean subgrain size evolution.

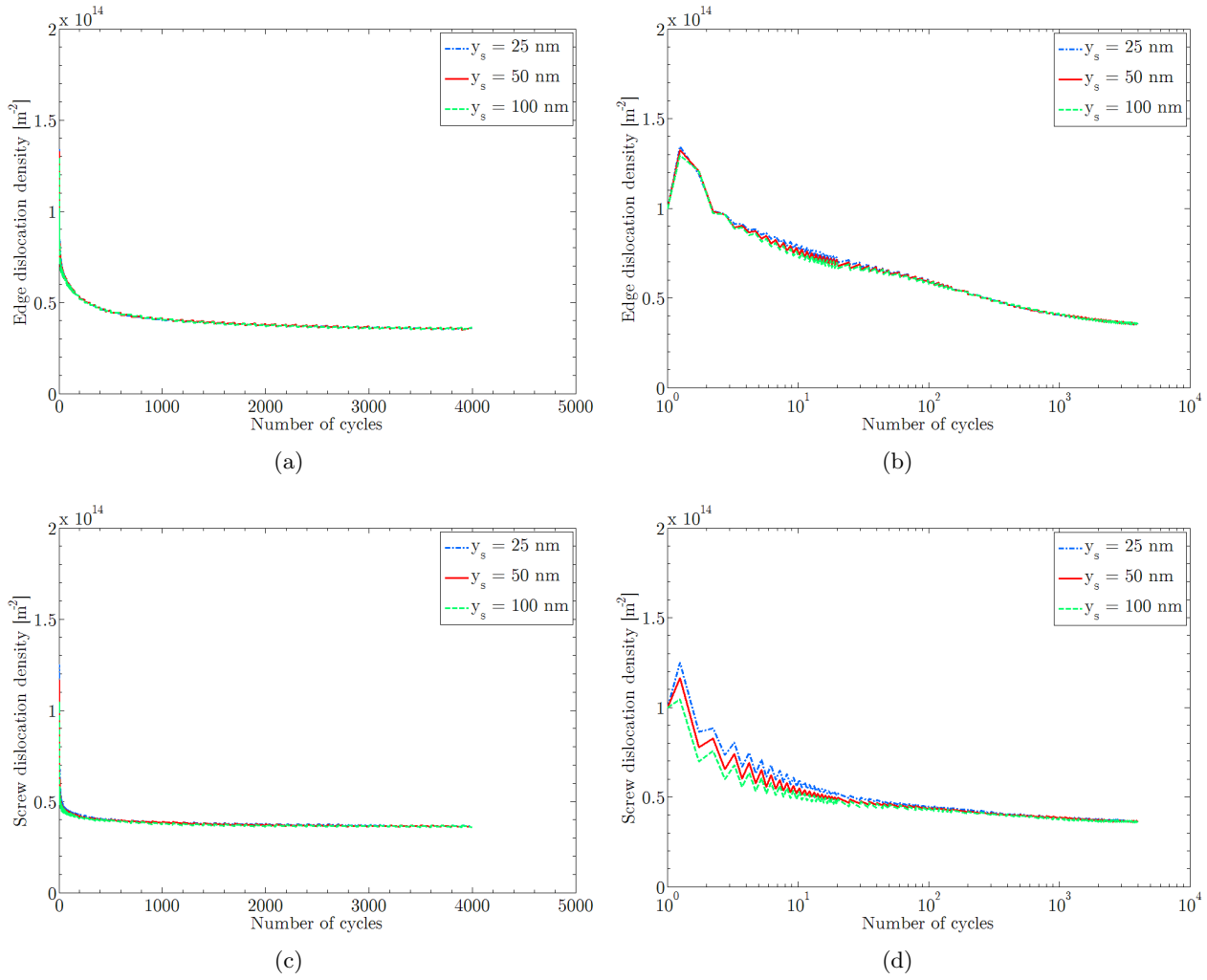

Fig. 4.23. Influence of the value of y_s on the predicted mean dislocation density evolution for free edge dislocations ((a) and (b)) and free screw dislocations ((c) and (d)).

The influence of the value of y_s on the predicted mean subgrain size evolution is presented in Fig. 4.22. The predicted final subgrain size varies by about ± 2.5 %. The impact of the value of y_s on the predicted dislocation density evolution is presented in Fig 4.23. Only a slight influence is observed on the screw dislocation density evolution up to 50 cycles: as expected, the higher the value of y_s, the faster the free screw dislocation density decreases. Moreover, the evolution is so fast that the influence of the value of y_s is limited to the first fifty cycles. No effect is visible on the edge dislocation density evolution and the predicted final free dislocation densities are not impacted.

Contrary to that of y_e, the influence of y_s on the model predictions is significant neither on the mechanical behaviour nor on the microstructural evolution. These results are probably due to the hypothesis which considers the low-angle twist boundaries as an array of *two* families of screw dislocations. Thus, the vanishing phenomenon of this kind of boundary occurs if two dislocations corresponding to different families are activated. This hypothesis induces a stabilization of the predictions and widely reduce the sensitivity to the y_s value.

4.6.4.3 Influence of the initial mean low-angle boundary misorientation on model predictions

Several measurements were carried on different materials to estimate the initial mean low-angle boundary misorientation θ_0 [Dronhofer et al., 2003,Tak et al., 2009,Panait et al., 2010a]. These misorientation angles are very small (lower than 5 °) and the accuracy of measurements performed with EBSD-FEG is appromatively equal to ± 1 °. The upper and lower bounds are fixed to 1.4 ° and 2.0 ° respectively, which correspond to a variation of ± 0.3 ° of the mean subgrain misorientations measured by Tak et al. on as-received X20 steel [Tak et al., 2009]. The influence of this parameter on the macroscopic mechanical behaviour is presented in Fig. 4.24.

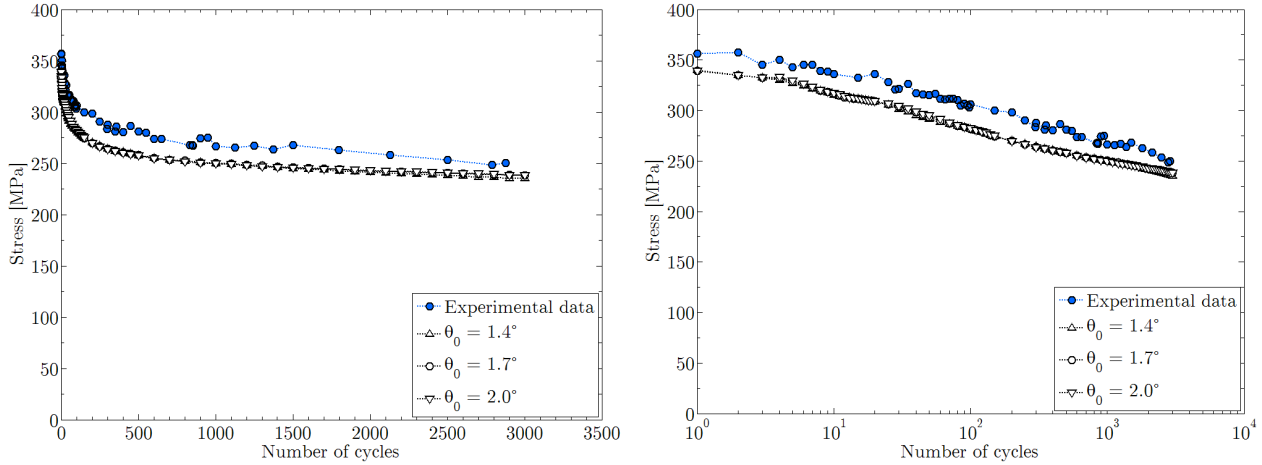

Fig. 4.24. Influence of the value of θ_0 on the predicted macroscopic mechanical behaviour. 1.7 ° is the value used in the previous section.

The variation of θ_0 has no impact on the mechanical behaviour predicted by the model.

The influence of θ_0 on the predicted mean subgrain size evolution is presented in Fig. 4.25. No significant difference is observed on the predicted subgrain size evolution up to 600 cycles. Then, the subgrain growth rate increases with decreasing θ_0. This leads to a variation of the predicted final subgrain size, from about 1.1 µm up to about 1.3 µm, which is equal to ± 8 %. No impact is observed

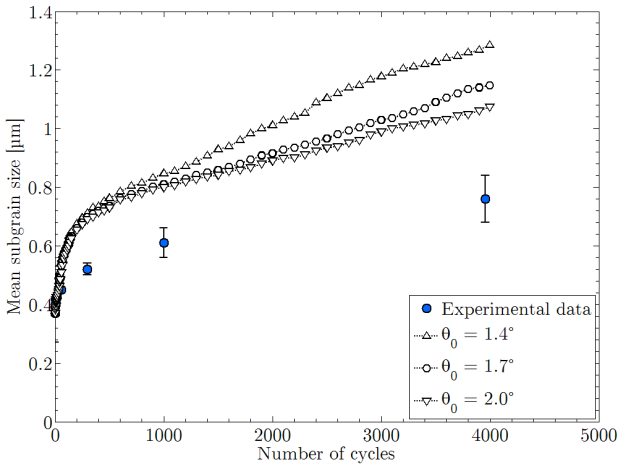

Fig. 4.25. Influence of the value of θ_0 on the predicted mean subgrain size evolution.

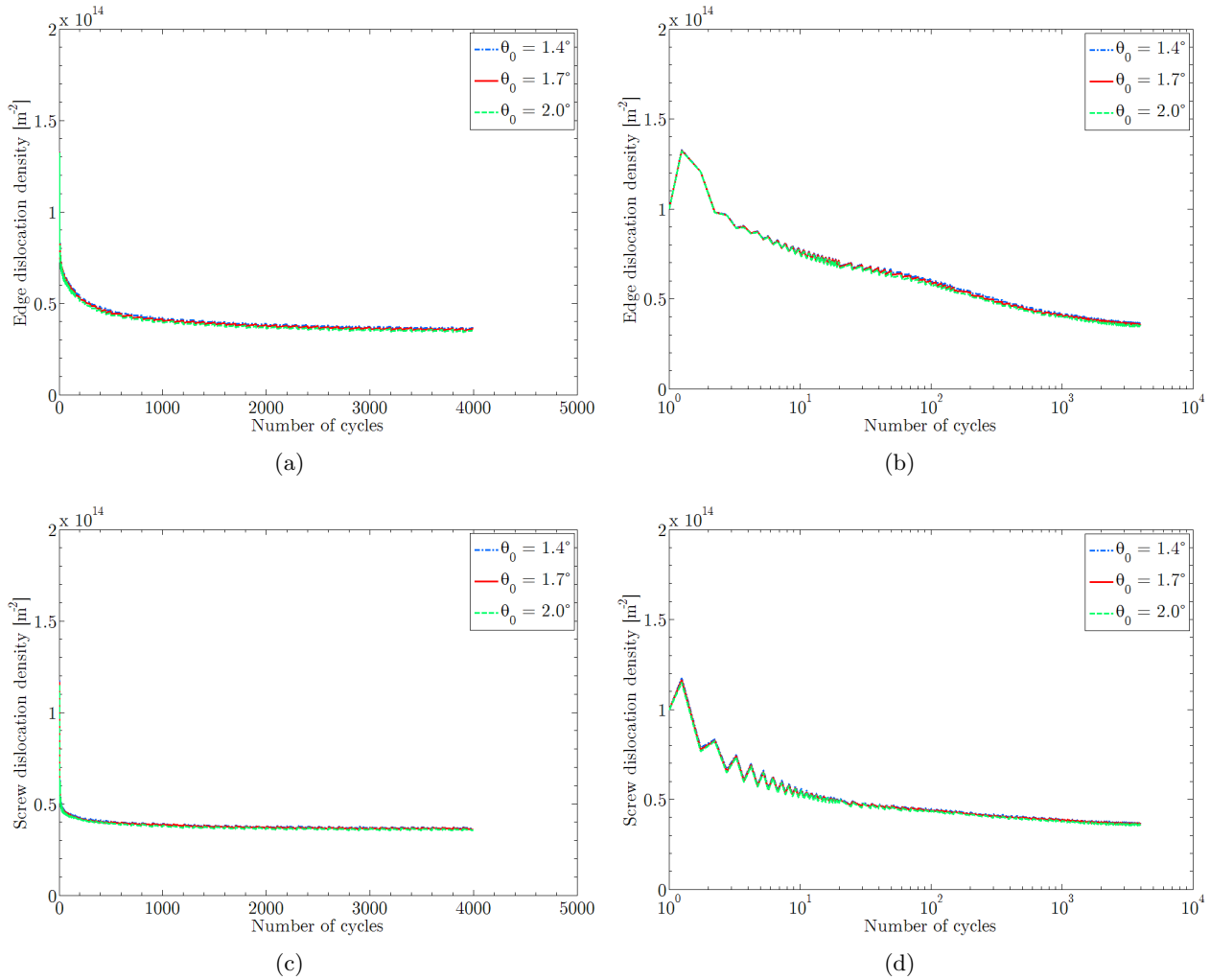

Fig. 4.26. Influence of the value of θ_0 on the predicted mean dislocation density evolution for free edge dislocations ((a) and (b)) and free screw dislocations ((c) and (d)).

on the dislocation density evolution predicted by the model.

The influence of the parameter θ_0 is limited to the predicted subgrain size evolution. The prediction of the macroscopic mechanical behaviour is not influenced by its variations provided it belongs to a reasonable physical range. Consequently, even if the misorientation of the low-angle boundaries in the material is not accurately measured, the stability of the model permits us to predict its mechanical behaviour during cycling satisfactorily.

4.6.4.4 Influence of the value of the critical misorientation on model predictions

The value of the critical misorientation was estimated based on a numerical study [Holec and Dlouhý, 2005]. Due to the small value of this parameter, no experimental measurements can be performed easily. Moreover, the model proposed by Holec and Dlouhý is based on the study of a low-angle tilt boundary and no information is available for twist boundaries. In our model, we assume that this critical value is the same for both kinds of boundaries. All these hypotheses would lead us to consider a wide variation of the value of this parameter. On the other hand, to keep a physical meaning, θ_{crit} has to be significantly higher than 0 ° (the distance between dislocations in the low-angle boundary cannot be infinite) and significantly lower than the initial misorientation of subgrains. Moreover, the numerical study performed by Holec and Dlouhý shows that this parameter is weakly impacted by the variation of the microstructural parameters (precipitate size and precipitate inter-spacing) provided they belong to values close to those measured in Grade 92 steel [Holec and Dlouhý, 2005]. In these conditions, the upper and lower bound values are fixed to 0.3 ° and 0.5 ° respectively. The influence of θ_{crit} on the predicted macroscopic mechanical behaviour is presented in Fig. 4.27.

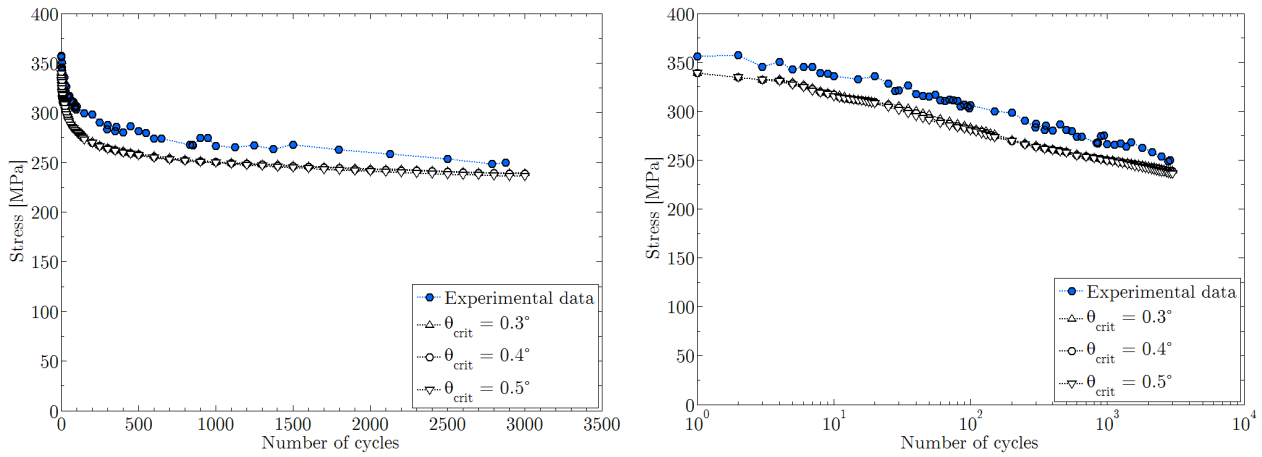

Fig. 4.27. Influence of the value of θ_{crit} on the predicted macroscopic mechanical behaviour. 0.4 °is the value used in the previous section.

As for parameter θ_0, θ_{crit} has almost no influence on the predicted mechanical behaviour.

The influence of θ_{crit} on the predicted mean subgrain size evolution is presented in Fig. 4.25. Its effect is very close to the effect of θ_0 on the model predictions. As expected, the subgrain growth rate increases with the increase of θ_{crit}. This leads to a variation of the predicted final subgrain size, from about 1.1 µm to about 1.3 µm, which corresponds to a variation of ± 8 %. The dislocation densities evolutions predicted by the model are not influenced by the value of θ_{crit} provided it belongs to the previous range.

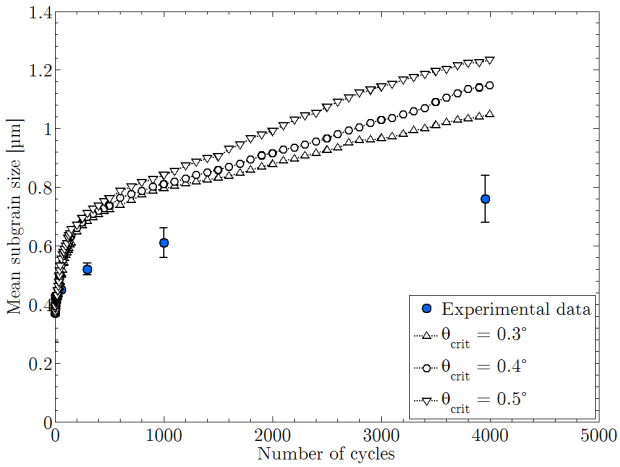

Fig. 4.28. Influence of the value of θ_{crit} on the predicted mean subgrain size evolution.

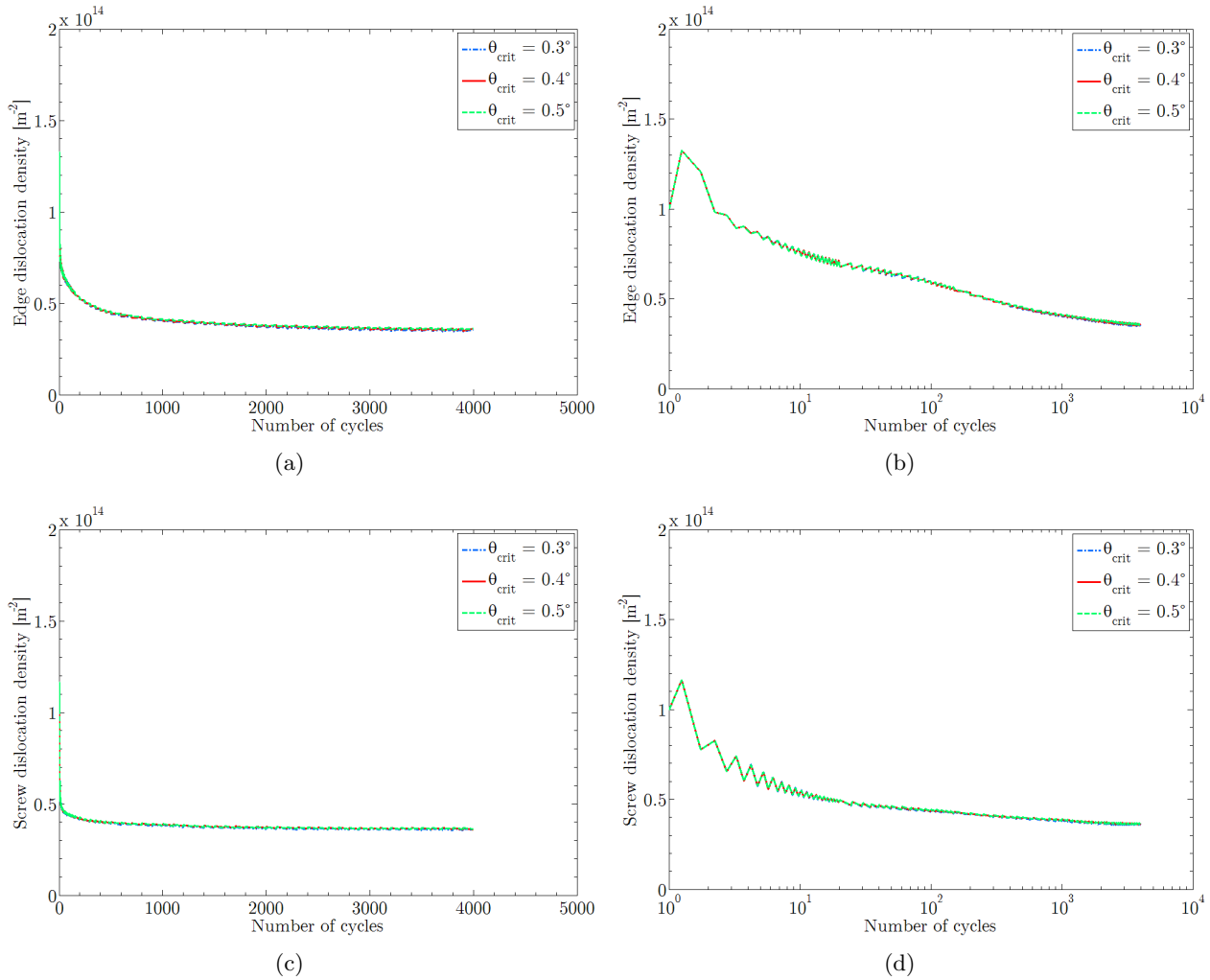

Fig. 4.29. Influence of the value of θ_{crit} on the predicted mean dislocation density evolution for free edge dislocations ((a) and (b)) and free screw dislocations ((c) and (d)).

As for parameter θ_0, the influence of the parameter θ_{crit} is limited to the predicted subgrain size evolution. The prediction of the macroscopic mechanical behaviour is not influenced by its value. Consequently, the stability of the model permits us to predict correctly the mechanical behaviour of the material during cycling, knowing of the range of the value of θ_{crit}.

4.6.4.5 Influence of the respective fractions of mobile edge / screw dislocation densities on model predictions

In the model, mobile dislocations are divided into pure edge and pure screw dislocations. This simple assumption leads to set an initial value of the fraction of these both populations in the total dislocation density. Experimental observations in different materials show that the number of screw dislocations is probably higher than the number of edge dislocations [Mughrabi et al., 1979, Sauzay and Kubin, 2011]. As no measurement is available in the literature, the chosen ratios vary from 50 % screw / 50 % edge to 100 % screw / 0 % edge. Their influence on the predicted macroscopic mechanical behaviour is presented in Fig. 4.30.

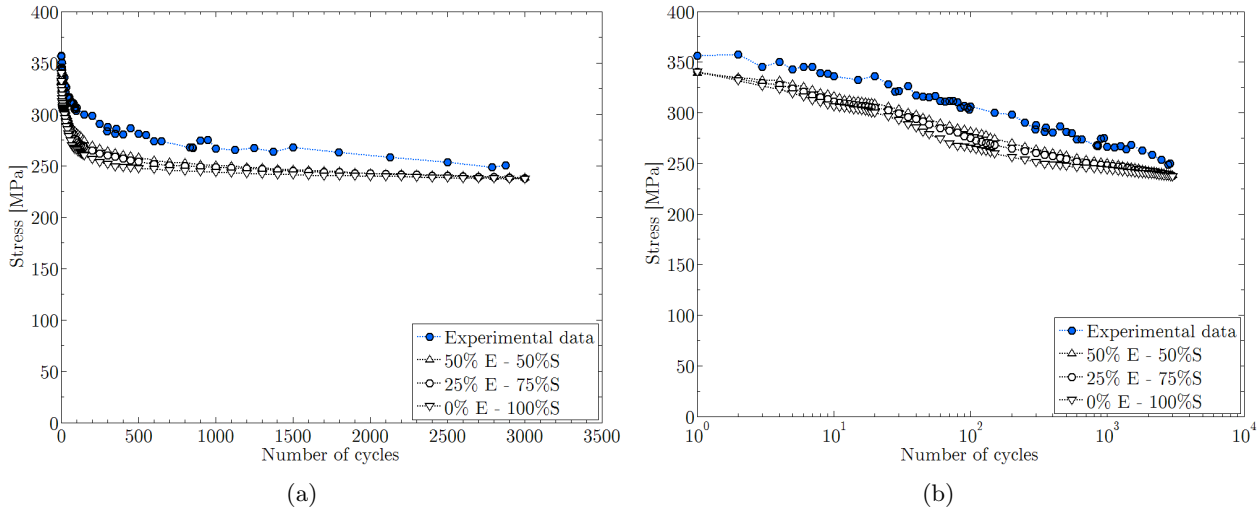

Fig. 4.30. Influence of the value of the fraction of mobile edge / screw dislocation densities on the predicted macroscopic mechanical behaviour.

The impact of fraction of mobile edge / screw dislocation densities on the mechanical behaviour is visible up to 500 cycles. As expected, the softening rate slightly increases with the proportion of mobile screw dislocations. This results can be easily explained by the properties of screw dislocations (higher critical annihilation distance, geometrical properties of the slip systems). For higher number of cycles, no influence of the fraction on the predicted mechanical behaviour is observed.

Concerning the subgrain size evolution presented in Fig. 4.31, a slight difference between the three curves is observed but no signicant influence on the final subgrain size is found. Between 3,000 and 3,500 cycles, the three curves cross each other but stay close to one another.

The evolution of dislocation densities presented in Fig. 4.32 is significantly impacted by the fraction value. However, this effect is limited to a transient stage: indeed, the final predicted total mobile dislocation densities are approximatively the same for the three curves, and the final proportions are identical to the initial ones. These results show that the model is sensitive to the fraction value up to 500 cycles and this sensitivity becomes negligeable for the final predictions. The effect of the terms of production of dislocation length is clearly observed in Fig. 4.32(b): even if ρ_e is equal to zero in the

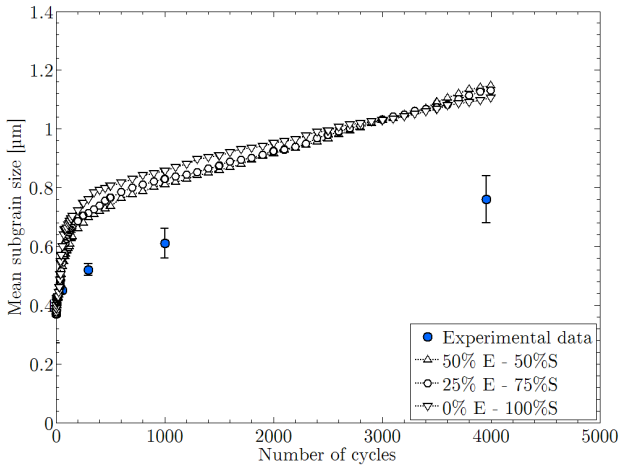

Fig. 4.31. Influence of the value of the fraction of mobile edge / screw dislocations densities on the predicted mean subgrain size evolution.

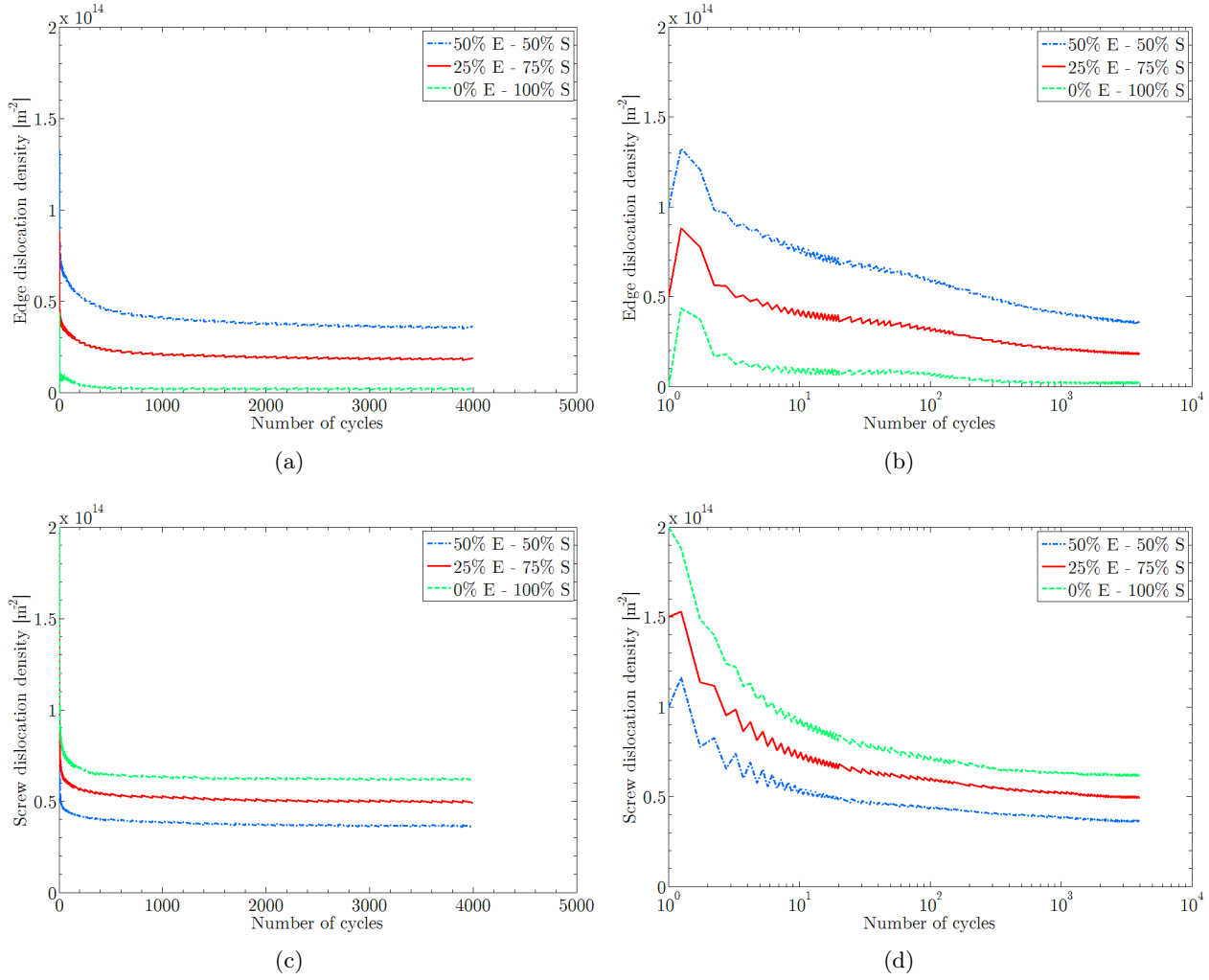

Fig. 4.32. Influence of the value of the fraction of mobile edge / screw dislocations densities on the predicted mean dislocation density evolution for free edge dislocations ((a) and (b)) and free screw dislocations ((c) and (d)).

initial state, a significant increase in free edge dislocation density occurs during the first cycle and the value then decreases until the end of the test.

4.6.4.6 Concluding remarks from the parametric study

The accurate values of the five parameters considered in this section are not exactly known but their range can be defined. The study of the influence of the variation of their values on model predictions leads to the following conclusions:

- Except for the critical annihilation distance of edge dislocations, the studied parameters have no influence on the predicted long-term macroscopic behaviour.
- Most of these parameters lead to significant differences of the predicted final subgrain size (about 20 %).
- The predicted final dislocation density is not significantly influenced by the variation of the considered parameters.

The proposed model is relatively stable with respect to the variation of the physically-based parameters, which values are not accurately known. Only the prediction of the main subgrain size evolution is sensitive to the variation of these parameters. It could probably be improved by a better description of the low-angle boundary structure taking into account three kinds of dislocations in each low-angle boundaries (one edge and two screw dislocations) [Sutton and Balluffi, 1995].

4.7 Concluding remarks

In order to described the cyclic softening effect measured at high temperature on tempered ferritic-martensite steels and particularly on a Grade 92 steel, a self-consistent homogeneisation model is proposed. This modelling is able to predict the softening behaviour and the microstructure evolution (decrease of dislocation density and coarsening of subgrains) measured during cycling. Constitutive equations of the model are based on physical phenomena occuring during deformation. Thus, all the parameters used in this model have a physical meaning, and only two of them corresponding to the viscosity effect are adjusted in order to predict well monotonic curves. No experimental data concerning the softening behaviour is used to adjust the model parameters. Predictions of the mechanical behaviour are performed for all amplitudes used in the cyclic tests presented in chapter 3. The main results lead to the following conclusions:

- The activation volume and the activation energy, fitted on experimental monotonic curves correspond to the mechanisms of interaction of dislocations with clusters of solute atoms, small precipitates...
- The model predicts quite accurately the mechanical behaviour of the Grade 92 steel during the first hysteresis loop at different strain rates (2×10^{-3} and 1×10^{-5} s^{-1}). Although the predicted subgrain size evolution is overestimated, the predictions of the final dislocation density are correct.
- During cycling at $\Delta E/2 = 0.35$ %, the softening rate is well predicted. However, at low strain rate, the maximum tensile stress is slightly underestimated whereas predictions agree rather well with experimental data for high strain rate.

- The cyclic softening effect is correctly predicted for tests performed at high strain rate with total strain amplitude from 0.25 to 0.35 %.
- The proposed model is relatively stable with respect to the variation of the physically-based parameters which values are not accurately known. Only the prediction of the mean subgrain size evolution is sensitive to the variation of these parameters.

As it was discussed in the previous section, some hypothesis of the model can be improved to lead to better predictions of the cyclic behaviour (better description of the subgrain boundary structure...). In the following chapter, some elements contributing to improve the predictions of the modelling are presented, mainly taking into account initial distributions of mean block subgrain size and dislocation density. Other loading conditions and material are considered as well.

Chapitre 5

Effet de l'hétérogénéité initiale de la microstructure, de la multiaxialité, de la température et du matériau sur les prédictions du modèle

This fifth chapter focuses on two important improvements of the model presented in chapter 4: an initial mean subgrain size distribution per block and an initial mean block dislocation density distribution are taken into account. The influence of these refinement on the predictions of the macroscopic mechanical behaviour and of the microstructural evolution is presented and discussed. Then, predictions of the softening under cyclic torsion are studied and discussed with respect to experimental data concerning the Grade 91 steel. Finally, the predictions of the microstructural evolution of the EUROFER 97 steel during cycling at room temperature are presented. These results were recently presented at the EUROMAT conference [Giordana et al., 2011].

Ce cinquème chapitre présente deux améliorations apportées au modèle décrit dans le chapitre 4 : la prise en compte d'une distribution de taille moyenne initiale de sous-grains par bloc et d'une distribution de densité de dislocations initiale. L'impact de ces deux modifications sur les prédictions du comportement mécanique macroscopique et sur l'évolution microstructurale est présenté et discuté. Dans un second temps, le modèle est appliqué à des chargements cycliques de torsion et les prédictions obtenues sont étudiées qualitativement au regard de résultats d'essai sur l'acier Grade 91. Enfin, ce chapitre se clôt sur une présentation des prédictions du modèle lors d'une sollicitation cyclique à température ambiante sur l'acier EUROFER 97, dont les résultats ont été récemment présentés à la conférence EUROMAT [Giordana et al., 2011].

Contents

5.1 Use of the measured initial distributions of subgrain sizes and dislocation densities . . . 136
5.1.1 Initial subgrain size distribution . . . 136
5.1.2 Initial mobile dislocation density distribution . . . 142
5.2 Simulations of cyclic torsion . . . 148
5.3 Modelling of the cyclic behaviour of the EUROFER 97 steel at room temperature . . . 149
5.4 Conclusions . . . 151

5.1 Prise en compte de la distribution initiale des tailles de sous-grains et des densités de dislocations bloc par bloc

Dans le chapitre 4, nous avons vu que le modèle, tel que nous l'avons implémenté, est capable de prédire assez précisément l'adoucissement cyclique du matériau. De plus, l'étude paramétrique présentée dans la sous-partie 4.6.4 nous a montré que le comportement mécanique macroscopique prédit est assez peu influencé par les variations des valeurs des paramètres testées (distances critiques d'annihilation des dislocations coin et vis, désorientations initiale et critique portées par les sous-grains, proportion des densités de dislocations coin et vis par rapport à la densité totale de dislocations), lorsque ces dernières appartiennent à un intervalle de valeurs physiquement acceptables d'après les mesures expérimentales ou estimées comme réalistes par le calcul. En revanche, si la valeur de la densité finale de dislocations est correctement prédite par le modèle, la prédiction de l'évolution de la taille moyenne des sous-grains au cours du cyclage met en évidence une surestimation de la taille moyenne par rapport aux valeurs mesurées expérimentalement. Comme nous l'avons vu dans la conclusion de l'étude paramétrique (voir sous-partie 4.6.4.6), cette prédiction peut probablement être améliorée en utilisant un jeu de paramètres adéquats, tout en restant dans un intervalle de valeurs physiquement acceptables.

Cette approche permet d'obtenir une prédiction assez raisonable de l'évolution de la microstructure. Cependant, pour des raisons de simplicité, nous avons fait le choix dans le chapitre 4 de considérer uniquement l'évolution de la taille moyenne des sous-grains dans la matrice. Ainsi, nous avons pris comme hypothèse de départ que le matériau à l'état de réception présentait une taille de sous-grains homogène. Or cette hypothèse est restrictive puisqu'elle est très simplificatrice vis-à-vis du caractère hétérogène de la microstructure initiale. Comme nous l'avons vu dans le chapitre 3, le matériau de réception se caractérise par une distribution de la taille des sous-grains d'allure log-normale. Les objectifs de cette amélioration du modèle sont donc de :

1. Permettre une approche plus physique et complète de la microstructure du matériau.
2. Intégrer aux prédictions du modèle une information supplémentaire : une distribution statistique à partir de laquelle on peut calculer une dispersion autour de la valeur moyenne.
3. Permettre une comparaison plus pertinente avec les distributions mesurées après essai cyclique (par exemple pour les densités de dislocations [Pešička et al., 2003, Pešička et al., 2004], les angles de désorientation entre sous-grains [Tak et al., 2009] ou encore les tailles de sous-grains [Eggeler et al., 1987, Dronhofer et al., 2003]).

En effet, nous avons vu dans le chapitre 3 que la dispersion de la taille des sous-grains autour de leur moyenne augmente au cours du cyclage (voir Fig. 3.18). Dans la sous-partie suivante, nous allons donc étudier l'influence de la prise en compte de la distribution de la taille initiale de sous-grains sur les prédictions du modèle. Pour mesurer au mieux les changements apportés par cette nouvelle hypothèse, nous utiliserons les valeurs "de référence" des paramètres présentées dans les Tableaux 4.1, 4.2 et 4.3.

5.1.1 Distribution initiale de la taille de sous-grain bloc par bloc

Concernant les tailles de sous-grains, le modèle présenté dans le chapitre 4 ne nous permet pas de considérer dans chaque bloc la taille de chaque sous-grain individuellement. En effet, pour raisons des simplicité liées à la vitesse de calcul, la taille des sous-grains est considérée comme homogène au sein d'un même bloc. Ainsi, en ce qui concerne les prédictions, nous préfèrerons utiliser ici le terme de

"taille moyenne de sous-grains par bloc", plus juste dans ce cas que le terme "taille de sous-grains" qui renvoie aux mesures expérimentales présentées dans le chapitre 3.

Dans ce modèle, la taille moyenne de sous-grains est définie pour chaque bloc, et celle-ci varie suivant l'Eq. 4.41 en fonction de la taille initiale, de l'angle de désorientation initiale θ_0 et de la proportion κ de sous-joints ayant disparu au cours de l'essai*. Ainsi, le modèle est capable de prédire une dispersion de la taille moyenne de sous-grains par bloc après cyclage. Cependant, l'hypothèse consistant à définir une taille de sous-grains initiale homogène au sein de la matrice (*i.e.* la même dans tous les blocs) conduit à des résultats très différents de ceux mesurés expérimentalement, comme le montre la Fig. 5.1.

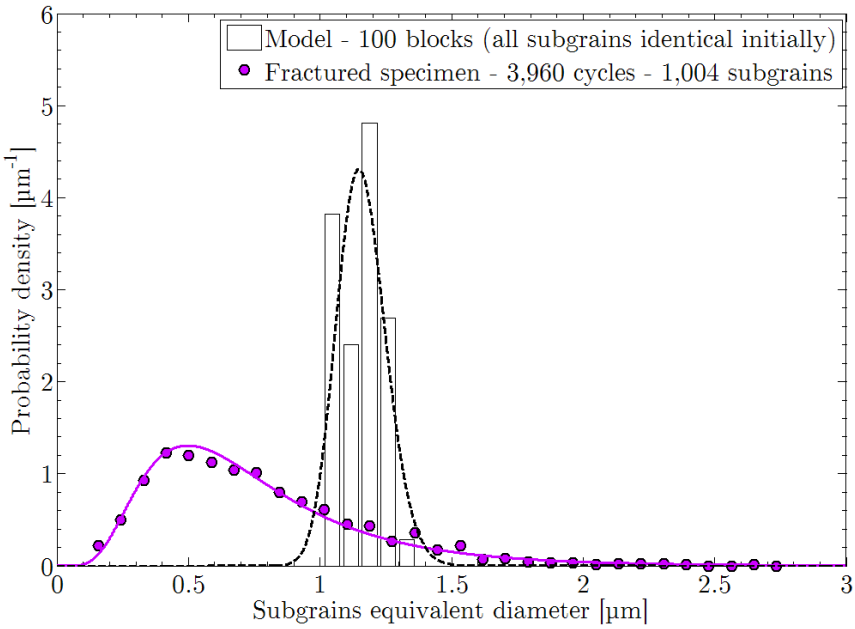

Fig. 5.1. Comparaison de la distribution de la taille de sous-grains mesurée expérimentalement et de la distribution de la taille de sous-grains par bloc prédite par le modèle présenté dans le chapitre 4, après 3 960 cycles à 1×10^{-5} s^{-1} et amplitude de déformation $\Delta E/2 = \pm 0.35\%$ à 550 ℃.

Comme nous l'avions remarqué lors de l'analyse des résultats de la modélisation (voir partie 4.6.2.2), la taille moyenne de sous-grains par bloc finale prédite (1.16 µm) est supérieure à la taille moyenne de sous-grain finale mesurée dans le matériau (0.78 µm). De plus, il est intéressant de remarquer que le modèle prédit une croissance assez homogène : l'ensemble des tailles moyennes de sous-grain par bloc prédites sont très proches de la valeur moyenne calculée sur l'ensemble du polycristal de 100 blocs. La dispersion de la distribution prédite est donc beaucoup plus faible que celle mesurée expérimentalement.

Dans l'optique d'améliorer la prediction de la taille moyenne des sous-grains dans le matériau et leur dispersion, nous avons choisi de prendre en compte une taille moyenne initiale de sous-grains par bloc différente d'un bloc à l'autre. Ainsi, à l'aide du logiciel Matlab, nous avons tiré aléatoirement 100 valeurs parmi la population composée de 4 956 valeurs de taille de sous-grains mesurée expérimentalement à l'état initial. Le résultat de ce tirage est présenté sur la Fig. 5.2.

Les fonctions cumulées des deux distributions présentées sur la Fig. 5.2 sont très proches l'une de l'autre, ce qui indique que le tirage des 100 valeurs de taille de sous-grain représente d'une manière satisfaisante la distribution des tailles de sous-grains mesurée dans le matériau de réception.

*voir page 108

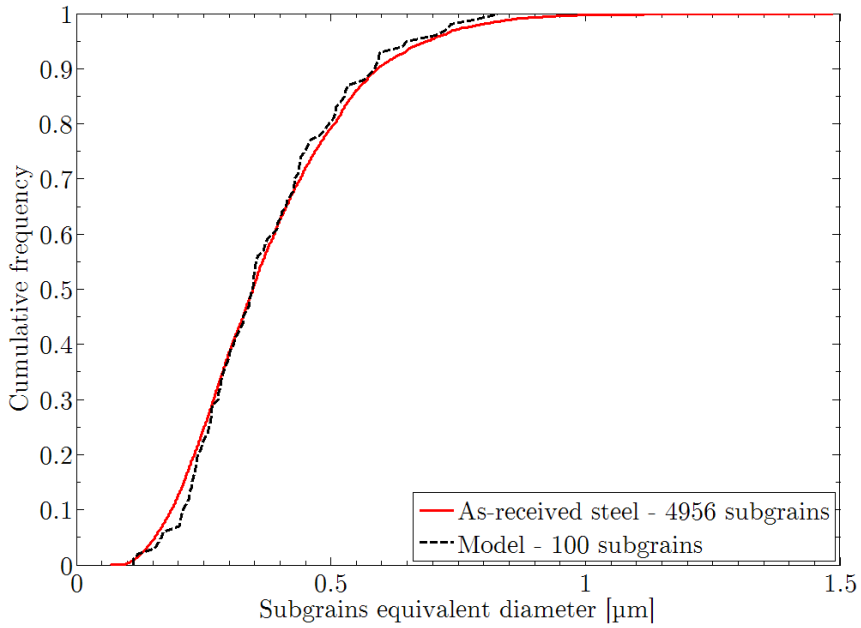

Fig. 5.2. Comparaison des fréquences cumulées des tailles de sous-grains mesurées expérimentalement dans le matériau de réception et des tailles de sous-grains choisies aléatoirement parmi la population de tailles initiales de sous-grains mesurées expérimentalement au MET (chapitre 3).

La prise en compte de ce nouveau paramètre ne nécessite pas de nouvelle identification de la valeur de l'énergie d'activation Q et du volume d'activation V comme le montre la Fig. 5.3. Ainsi, les valeurs des deux paramètres liés aux mécanismes de déformation viscoplastique utilisés pour la prédiction du comportement mécanique du matériau sont identiques à celles du Tableau 4.3. Dans la suite, nous comparerons les courbes tracées à partir des prédictions du modèle raffiné aux courbes présentées dans la partie 4.6 du chapitre 4.

La Fig. 5.3 nous montre donc que la prise en compte d'une distribution de la taille moyenne de sous-grains par bloc n'a pas d'influence significative sur la prédiction du comportement monotone du matériau, au moins jusqu'à 0,35 % de déformation. Les courbes d'adoucissement cyclique simulées pour deux vitesses de déformation sont présentées en Fig. 5.4.

Bien qu'aucune influence significative ne soit détectée en comportement monotone, les prédictions du comportement mécanique du matériau lors du cyclage montrent que la prise en compte d'une distribution de taille moyenne initiale de sous-grains par bloc conduit à une surestimation de l'adoucissement mécanique prédit par le modèle présenté dans le chapitre 4. Cette surestimation est à corréler avec l'évolution de la taille moyenne de sous-grains prédite présentée sur la Fig. 5.5.

Si aucune influence sur la prédiction de l'évolution de la densité de dislocation n'est observée sur la Fig. 5.6 (à comparer avec la Fig. 4.13), l'évolution de la taille moyenne des sous-grains est toujours clairement surestimée par rapport aux données expérimentales. Si nous comparons ces courbes avec la prédiction présentée sur la Fig. 4.11, il apparaît que la prise en compte de la ditribution initiale de taille moyenne de sous-grains par bloc conduit à une prédiction de la croissance des sous-grains plus élevée : les tailles moyennes de sous-grain prédites en fin de cyclage sont supérieures de 5 et 20 % pour respectivement la faible vitesse de déformation et la vitesse de déformation élevée, en comparaison des courbes de la Fig. 4.11. Afin de discuter plus en détail la prédiction de l'évolution de la taille des sous-grains au cours du cyclage, la Fig. 5.7 illustre les comparaisons des distributions des tailles de sous-grains mesurées expérimentalement et prédites par le modèle raffiné.

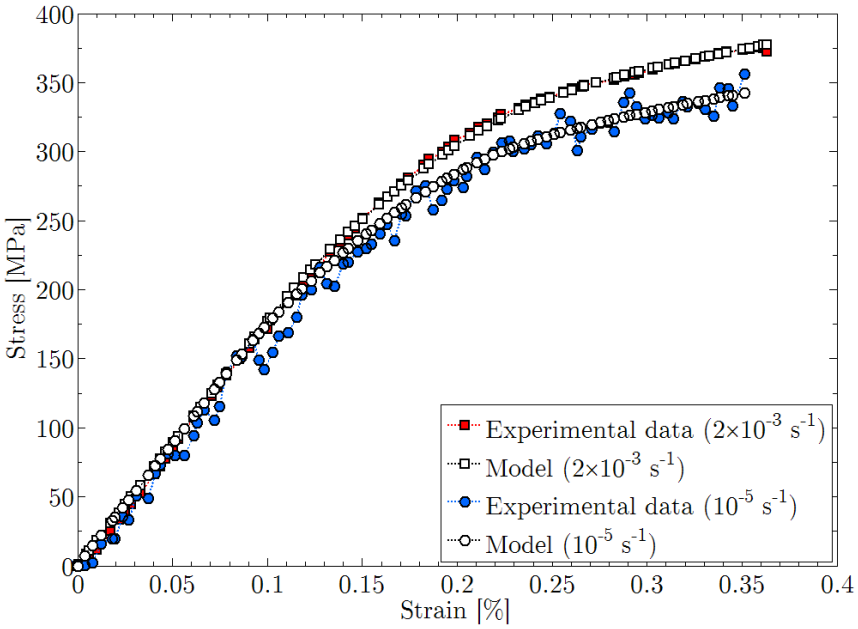

Fig. 5.3. Comparaison entre les courbes monotones expérimentales et simulées avec le modèle tenant compte de la distribution initiale de taille de sous-grains, jusqu'à 0,35 % à deux vitesses de déformation différentes (Q = 1.2 eV et V = 216 b^3).

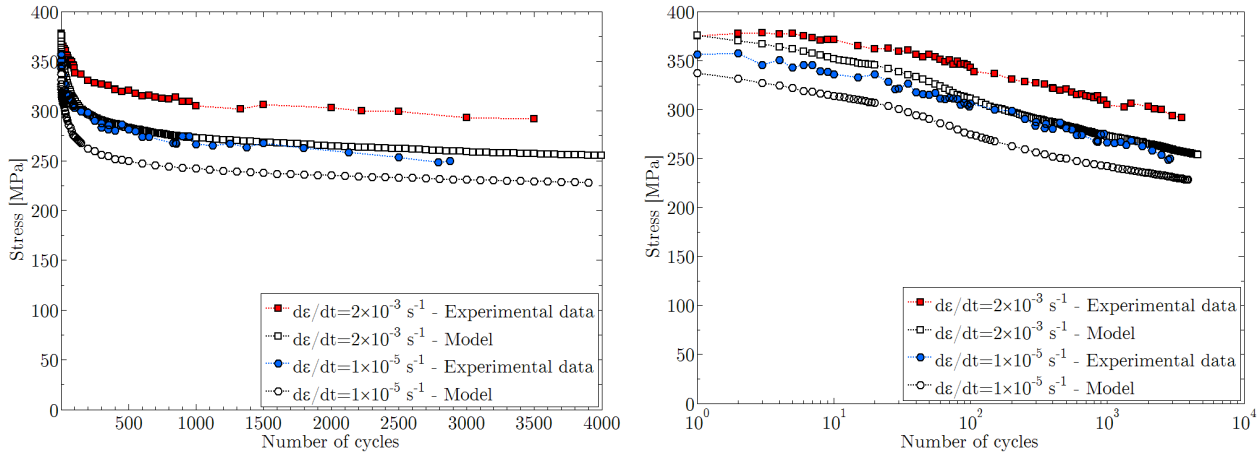

(a) (b)

Fig. 5.4. Comparaison entre les courbes d'adoucissement cyclique expérimentales et prédites avec le modèle tenant compte de la distribution initiale de taille de sous-grains pour une amplitude de déformation de $\pm\, 0,35\%$ et deux vitesses de déformation (a) en échelle linéaire et (b) en échelle logarithmique. La contrainte maximale est calculée ou mesurée en fonction du nombre de cycles.

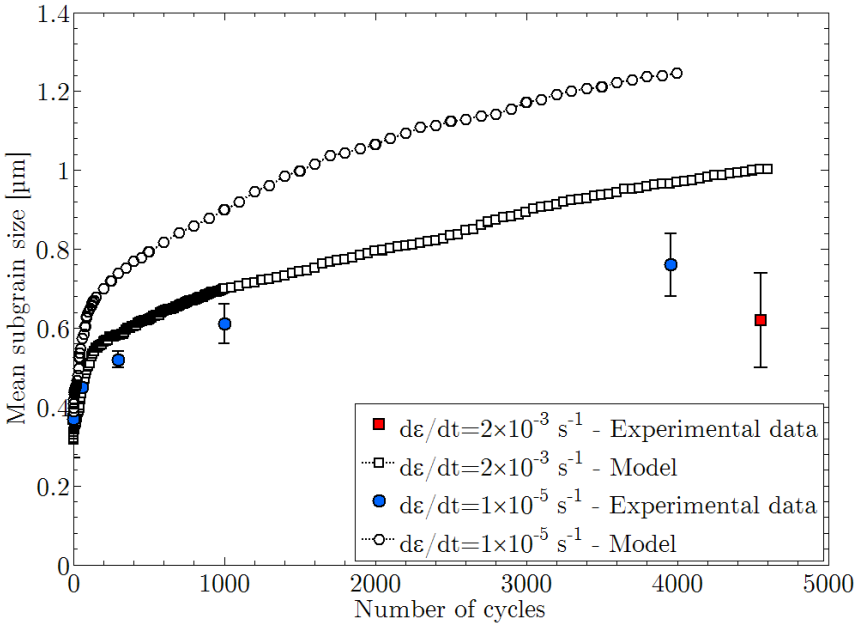

Fig. 5.5. Comparaison entre la taille moyenne de sous-grains prédite par le modèle tenant compte de la distribution initiale de taille de sous-grains et expérimentale au cours du cyclage pour une amplitude de déformation de ± 0.35% et deux vitesses de déformation.

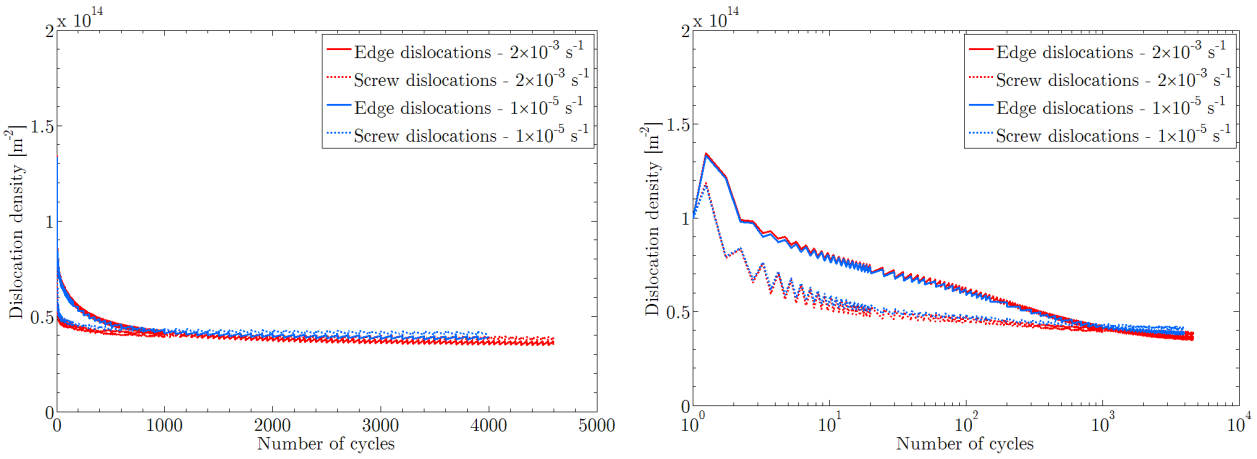

Fig. 5.6. Prédictions des évolutions des densités de dislocations mobiles coin et vis au cours du chargement cyclique pour une amplitude de déformation de ± 0.35% et deux vitesses de déformation (a) en échelle linéaire et (b) en échelle logarithmique. Modèle tenant compte de la distribution initiale de taille de sous-grains.

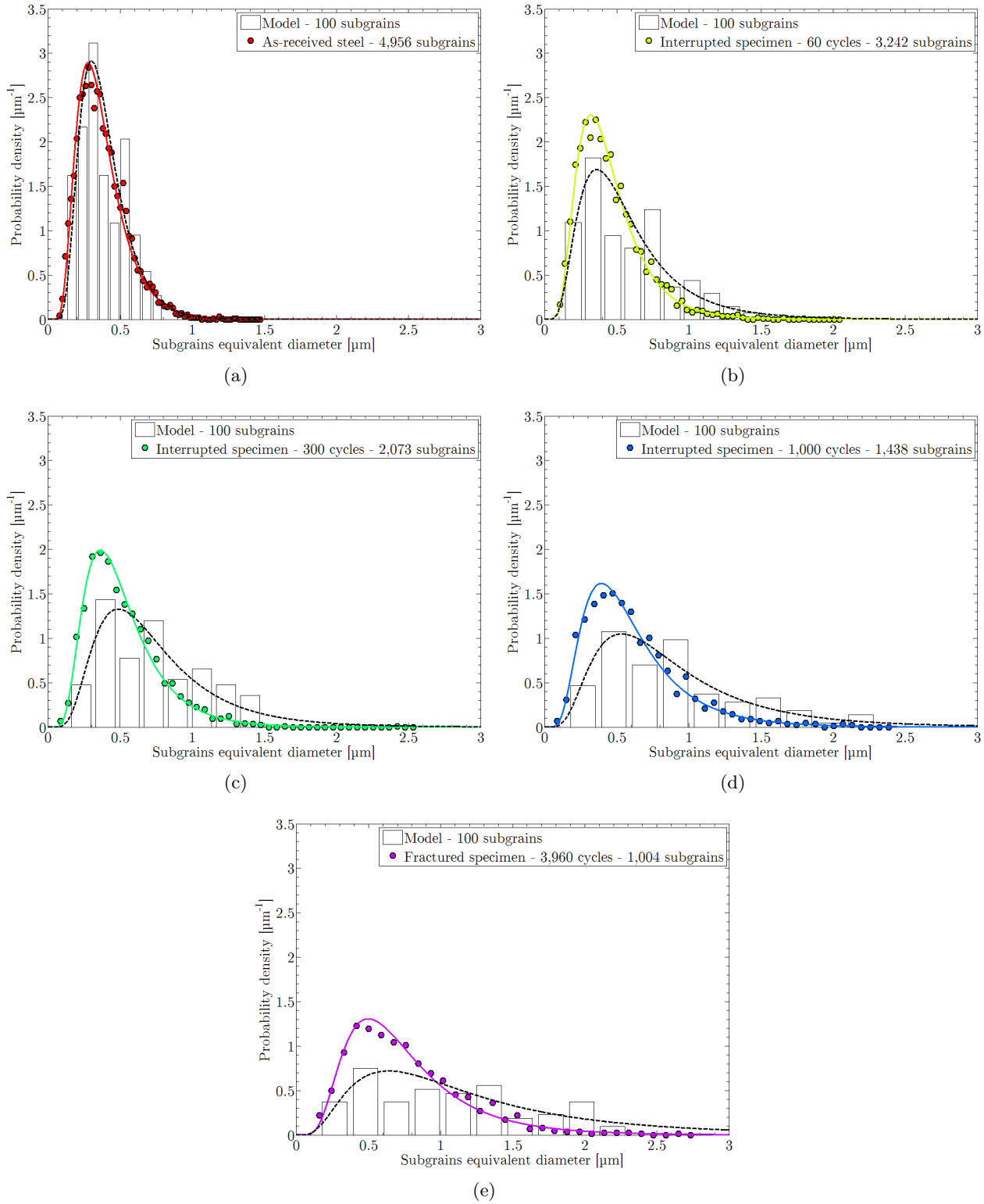

Fig. 5.7. Comparaison de la distribution de la taille de sous-grain mesurée expérimentalement et prédite par le modèle tenant compte de la distribution initiale de taille de sous-grains (a) initialement et après (b) 60 cycles, (c) 300 cycles, (d) 1 000 cycles et (e) 3 960 cycles. Cas de l'essai à 1×10^{-5} s^{-1} avec une amplitude de déformation $\Delta E/2 = \pm 0.35\%$.

La Fig. 5.7 montre que la taille moyenne prédite des sous-grains est surestimée par rapport aux mesures expérimentales. Cependant, la prise en compte de la dispersion de la taille moyenne initiale de sous-grains par bloc permet une meilleure prédiction de la dispersion des valeurs autour de la moyenne, plus conforme aux mesures expérimentales que la dispersion issue de la prédiction présentée sur la Fig. 5.1. Ceci tend à montrer que la dispersion de taille de sous-grains en fin d'essai est en grande partie conditionnée par la distribution de taille de sous-grains à l'état initial.

La prise en compte de la distribution initiale de la taille moyenne de sous-grains bloc par bloc n'apporte donc pas de réelle amélioration au modèle présentée dans le chapitre 4. En effet, cette hypothèse induit une surestimation de l'adoucissement mécanique et de la croissance de la taille moyenne des sous-grains. En revanche, elle permet de prédire une dispersion des valeurs de taille de sous-grains, plus proche de celle observée expérimentalement. Dans la partie suivante, nous allons coupler cette hypothèse avec la prise en compte d'une distribution initiale de densités de dislocations mobiles bloc par bloc.

5.1.2 Distribution initiale des densités de dislocations mobiles bloc par bloc

Tout comme la taille initiale de sous-grains par bloc, le modèle raffiné peut tenir compte d'une distribution initiale de densité de dislocations mobiles par système de glissement de chaque bloc considéré. Dans le modèle initial présenté dans le chapitre 4, de la même manière que la taille initiale de sous-grains par bloc, la densité initiale de dislocations est supposée homogène pour des raisons de simplicité. Or, bien qu'il soit long et fastidieux de mesurer une distribution expérimentale des densités de dislocations par système de glissement, il apparaît toutefois possible d'estimer la distribution de la densité de dislocations par bloc au sein du matériau.

Le nombre de mesures de densités de dislocations effectuées sur le Grade 92 étudié ne nous permet pas d'établir une distribution statistique satisfaisante. En revanche, des mesures, en beaucoup plus grand nombre, ont été effectuées par Giordana sur un acier EUROFER 97 à l'état de réception [Giordana et al., 2011]. Vingt-cinq mesures de densités de dislocations ont été effectuées dans 25 blocs différents de façon à établir une représentation statistique considérée comme plus significative de la distribution des densités. En prenant toutes les précautions nécessaires à l'utilisation de ces valeurs, nous avons fait l'hypothèse que la dispersion des densités était similaires dans l'acier EUROFER 97 et l'acier de Grade 92. La densité de dislocations moyenne mesurée dans l'EUROFER 97 à l'état de réception (environ $2,3 \times 10^{14}$ m^{-2}) étant très proche de celle mesurée dans le Grade 92 (environ 2×10^{14} m^{-2}), nous avons donc construit un ensemble de 100 valeurs de densités de dislocations moyenne par bloc en effectuant un tirage aléatoire parmi les 25 mesures disponibles sur l'acier EUROFER 97. Cet ensemble a ensuite été pris en compte dans le modèle. Ainsi, à l'état initial, à chaque bloc du polycristal de la section précédente est associé une valeur de densité de dislocations et une valeur de taille de sous-grains, toutes deux issues de nombreuses mesures expérimentales.

La prise en compte additionnelle de la distribution initiale de densités initiale de dislocations par bloc n'a pas nécessité un nouvel ajustement des valeurs de l'énergie d'activation Q et du volume d'activation V, qui restent identiques à celles du Tableau 4.3. Les courbes monotones expérimentales et simulées jusqu'à 0.35 % pour deux vitesses de déformation différentes sont présentées sur la Fig. 5.8.

Si les courbes simulées du comportement monotone jusqu'à 0.35 % de déformation ne présentent pas de différence notable par rapport aux courbes présentées sur les Figs. 4.8 et 5.3, une amélioration de la prédiction de l'adoucissement mécanique est observée, comme le montre la Fig. 5.9.

Comme le montre la Fig. 5.9, les prédictions de l'adoucissement cyclique sont proches du comportement expérimental mesuré. Bien que la cinétique d'adoucissement prédite soit un peu plus rapide que

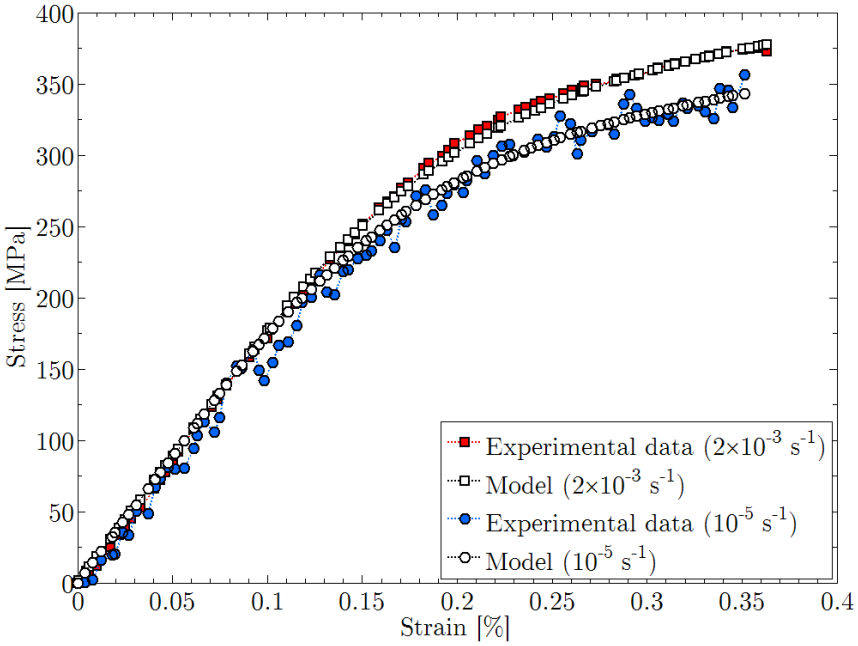

Fig. 5.8. Comparaison entre les courbes monotones expérimentales et simulées jusqu'à 0.35 % à deux vitesses de déformation différentes. Modèle tenant compte de la distribution initiale de taille de sous-grains et de la distribution initiale de densités de dislocations moyenne bloc par bloc.

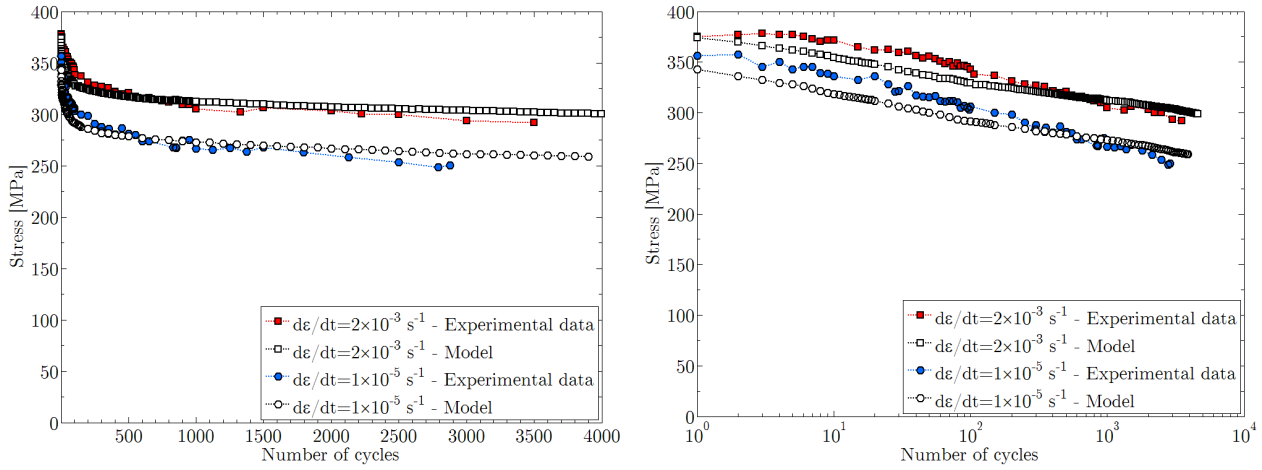

Fig. 5.9. Comparaison entre les courbes d'adoucissement cycliques expérimentales et prédites par le modèle tenant compte de la distribution initiale de taille de sous-grains et de la distribution initiale de densités de dislocations moyenne bloc par bloc pour une amplitude de déformation de ± 0.35% et deux vitesses de déformation (a) en échelle linéaire et (b) en échelle logarithmique. La contrainte maximale est calculée ou mesurée en fonction du nombre de cycles.

celle mesurée expérimentalement pour les 10 premiers cycles, puis plus lente à partir du 100$^{\text{ème}}$ cycle, les valeurs finales de la contrainte maximale prédite et mesurée diffèrent de moins de 5 % pour les deux vitesses de déformation. Cette évolution de la contrainte peut être reliée à la prédiction de l'évolution de la taille moyenne de sous-grains, représentée sur la Fig. 5.10.

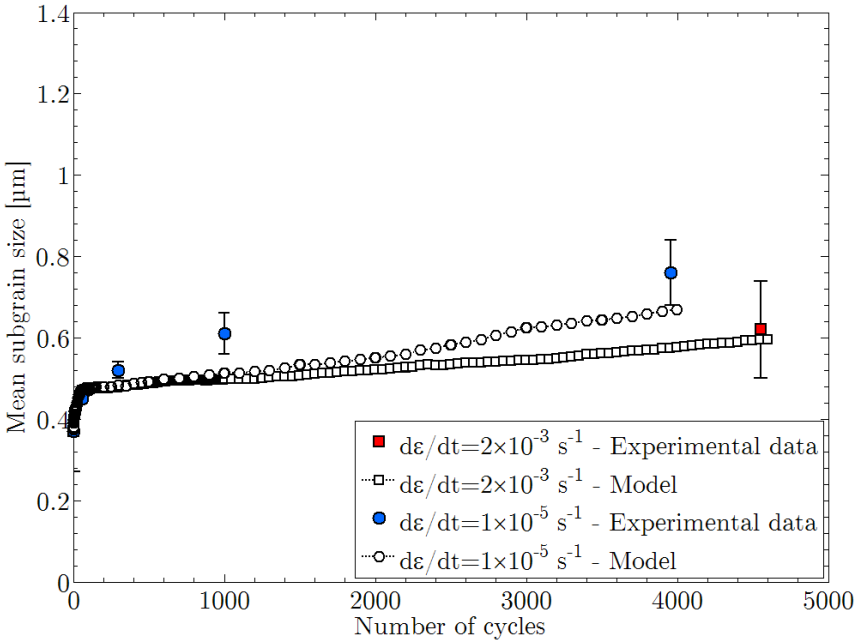

Fig. 5.10. Comparaison entre la taille moyenne de sous-grains prédite avec le modèle utilisant la distribution initiale de taille de sous-grains et la distribution initiale de densités de dislocations bloc par bloc et expérimentale au cours du cyclage pour une amplitude de déformation de ± 0.35% et deux vitesses de déformation.

La prise en compte d'une distribution initiale de densités de dislocations bloc par bloc dans les simulations conduit donc à une modification non négligeable de la prédiction de l'évolution de la taille moyenne des sous-grains. Ainsi, le modèle prédit une forte croissance de la taille moyenne de sous-grains au cours des premiers cycles, telle qu'elle est observée expérimentalement. Ce phénomène entraîne une cinétique d'adoucissement élevée, observée sur la Fig. 5.9. Au bout de quelques dizaines de cycles, cette croissance ralentit fortement. Cette simulation plus précise prédit une vitesse de croissance de la taille des sous-grains plus lente, expliquant ainsi la réduction de la cinétique d'adoucissement observée à partir du 100$^{\text{ème}}$ cycle environ sur la Fig. 5.9. Les tailles moyennes finales sont convenablement prédites pour les deux essais cycliques à différentes vitesses de déformation.

La Fig. 5.11 présente l'évolution de la densité moyenne de dislocations au cours du cyclage. Aucune différence significative n'est observée par rapport aux courbes prédites par les deux autres versions du modèle, Figs. 5.6 (distribution initiale de taille de sous-grains et densité de dislocations homogène initialement) et 4.13 (taille de sous-grains et densité de dislocations homogènes initialement). Ainsi, la prise en compte d'une distribution de la densité de dislocations bloc par bloc n'a pas d'impact sur l'évolution de la densité moyenne de dislocations au cours du cyclage.

La Fig. 5.12 présente une comparaison des distributions des tailles de sous-grains mesurées expérimentalement et des distributions des tailles de sous-grains par bloc prédites par le modèle à l'état initial et après 60, 300, 1 000 cycles et à l'état final. Ces courbes montrent que le modèle prédit cette fois-ci convenablement l'ensemble de la distribution des tailles de sous-grains et non plus seulement la dispersion des valeurs de tailles de sous-grains autour de la moyenne.

La prise en compte d'une distribution des densités initiales de dislocations bloc par bloc induit

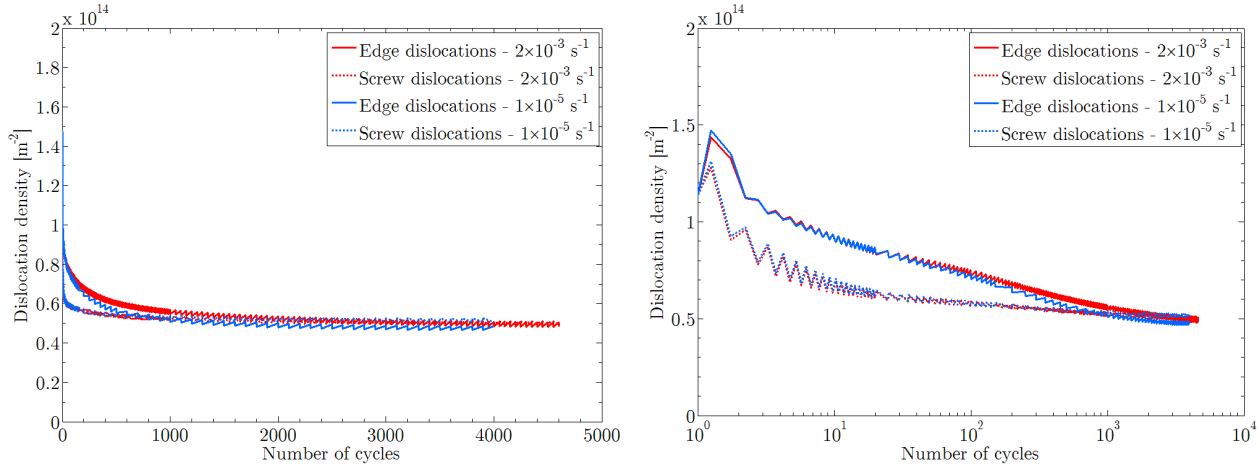

Fig. 5.11. Prédictions des évolutions des densités de dislocations mobiles coin et vis au cours du cyclage pour une amplitude de déformation de ± 0.35% et deux vitesses de déformation (a) en échelle linéaire et (b) en échelle logarithmique. Modèle utilisant la distribution initiale de taille de sous-grains et la distribution initiale de densités de dislocations bloc par bloc .

donc une amélioration de la prédiction de l'évolution de la microstructure, tout en menant à une prédiction de l'adoucissement macroscopique en accord avec les mesures expérimentales. Cependant, comment la prise en compte de l'hétérogénéité des densités de dislocations initiales influence-t-elle les prédictions des évolutions microstructurales ? La Fig. 5.13 nous apporte un élément de réponse.

Sur la Fig. 5.13, nous avons reporté pour chaque bloc considéré dans le modèle sa densité de dislocations (en ordonnée) et sa taille moyenne de sous-grains (en abscisse). Initialement, les blocs ont une densité de dislocations élevée et une taille moyenne de sous-grain faible : ils sont représentés par les symboles circulaires rouges. A l'état final, après 3 960 cycles simulés, les blocs correspondent au nuage de symboles carrés bleus. Cette figure nous permet de constater trois phénomènes :

1. Le modèle prédit bien une baisse globale de la densité de dislocations bloc par bloc. Il faut noter qu'un petit nombre de blocs ont une densité de dislocations et une taille moyenne de sous-grains qui évoluent peu au cours du cyclage.

2. À l'inverse, certains blocs connaissent une forte transformation de leur microstructure : leur densité de dislocations diminue (moins de 5×10^{13} m^{-2}) et leur taille moyenne de sous-grain croît fortement (supérieure à 1 µm en fin d'essai). Ce phénomène est en accord avec les observations expérimentales (voir Fig. 3.16(c)).

3. Enfin, le dernier cas regroupe un grand nombre de blocs qui ont vu leur densité de dislocations diminuer alors que leur taille moyenne de sous-grains n'a pas autant évoluée. Ce phénomène est aussi observé expérimentalement (voir Fig. 3.16(c)).

En l'état actuel des investigations, il est hasardeux de proposer directement une interprétation des mécanismes qui pourrait expliquer ces résultats. Il est en effet préférable d'étudier au préalable l'évolution individuelle de chaque bloc au cours de l'essai. Cependant, quelques hypothèses pourraient servir de pistes de travail afin d'interpréter ces résultats :

- Le premier groupe est composé de blocs qui se déforment probablement peu au cours du cyclage,

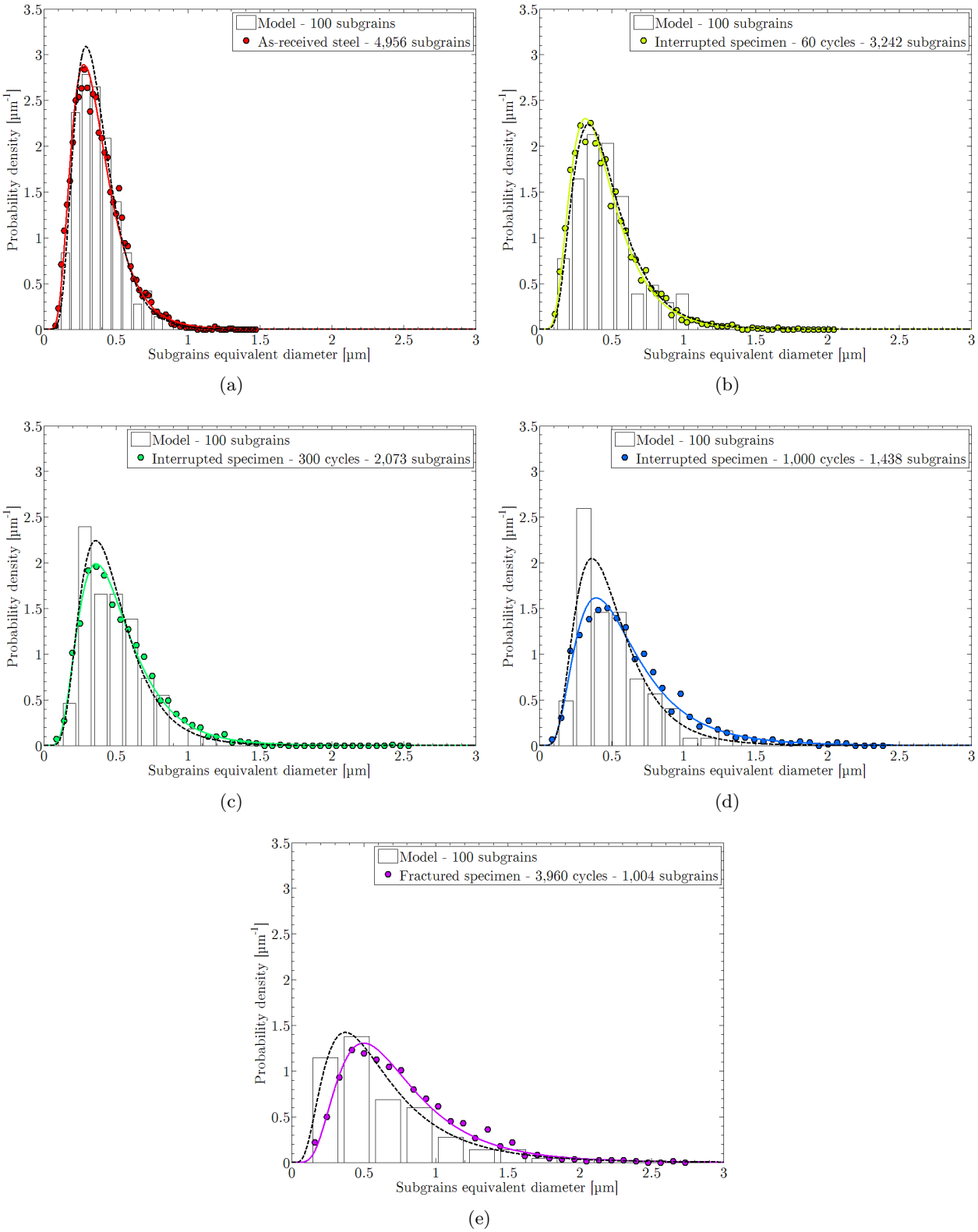

Fig. 5.12. Comparaison de la distribution de la taille de sous-grains par bloc mesurée expérimentalement et de la distribution de la taille de sous-grains par bloc prédite par le modèle tenant compte de la distribution initiale de taille de sous-grains et la distribution initiale de densités de dislocations bloc par bloc (a) initialement et après (b) 60 cycles, (c) 300 cycles, (d) 1 000 cycles et (e) 3 960 cycles. Cas de l'essai à 1×10^{-5} s^{-1} avec une amplitude de déformation $\Delta E/2 = \pm 0.35\%$.

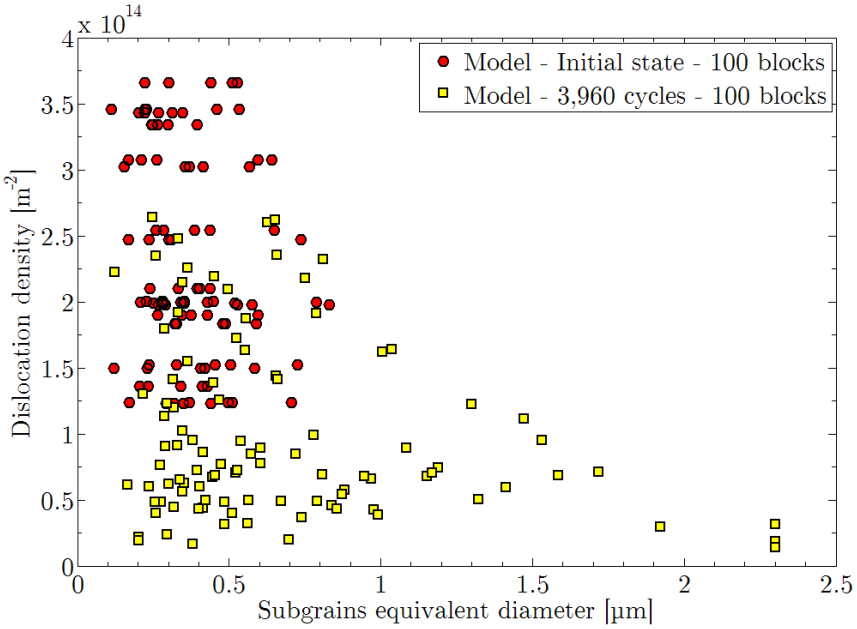

Fig. 5.13. Corrélation entre la taille de sous-grains moyenne par bloc et la densité de dislocations par bloc à l'état initial et après cyclage à 1×10^{-5} s^{-1} pour une amplitude de déformation $\Delta E/2 = \pm 0.35\%$ avec le modèle utilisant la distribution initiale de taille de sous-grains et la distribution initiale de densités de dislocations bloc par bloc.

du fait de leur orientation cristalline (faible facteur de Schmid). Ainsi, le nombre d'annihilations entre dislocations de signes opposés (mobile/mobile et mobile/dislocations de sous-joint) est faible. Peu de transformations microstructurales sont observées. C'est le fait d'un pilotage de ces évolutions par les glissements viscoplastiques en accord avec les observations.

- Le second groupe pourrait à l'inverse correspondre à des sous-grains très déformés plastiquement durant le cyclage. Leur nombre de système de glissement activés est donc sans doute élevé. Initialement, ils ont probablement une forte densité de dislocations mobiles, ce qui entraîne un grand nombre de phénomènes d'annihilation et donc des transformations microstructurales majeures.

- Enfin, le dernier groupe se compose probablement de blocs qui sont moins déformés que les précédents ou qui ont une faible densité initiale de dislocations mobiles. La majorité des annihilations doit se produire entre dislocations mobiles, les annihilations dislocations mobiles / dislocations des sous-joints étant trop peu nombreuses pour permettre la destruction complète des sous-joints de faible désorientation. Ainsi, ces blocs sont "nettoyés" de leurs dislocations mobiles mais ne subissent pas pour autant une modification de leur taille moyenne de sous-grains.

Il convient toutefois de rester prudent vis-à-vis de ces interprétations. En effet, elles nécessitent une étude complémentaire des résultats, en suivant l'évolution individuelle de chaque bloc.

Les résultats de la figure 5.13 sont particulèrement intéressants du point de vue des perspectives de travail. Outre l'interprétation des mécanismes mis en œuvre, il serait en effet possible de mesurer les tailles de sous-grains dans lequels la densité de dislocation est aussi mesurée. Des graphiques d'origine expérimentale similaires à ceux prédits pourraient être tracés et comparés (Fig. 5.13). Bien que cette étude puisse être fastidieuse vu le grand nombre de mesures à effectuer pour obtenir une distribution statistiquement représentative (et les difficultés expérimentales liées à la précision des

mesures elles-mêmes et à la complexité de la structure des aciers martensitiques revenus – comme le soulignent [Pešička et al., 2004]), elle pourrait apporter des éléments de comparaison intéressants afin de discuter les prédictions du modèle.

Cette partie nous a montré que la prise en compte simultanée des distributions initiales de taille moyenne de sous-grains par blocs et de densité de dislocations dans les blocs permettait d'améliorer les prédictions du modèle tant à l'échelle macroscopique que microscopique. Bien qu'un certain nombre de paramètres dont les variations pourraient avoir un impact sur les prédictions du modèle restent à étudier (l'influence du tirage aléatoire, du nombre de bloc considéré. . . sur les prédictions du comportement mécanique et de l'évolution microstructurale), ces améliorations donnent quelques perspectives de travail, tant sur le plan de la modélisation que sur le plan expérimental.

Dans la partie suivante, nous étudions les prédictions du modèle pour d'autres sollicitations cycliques de type torsion. Dans ce cadre, nous utiliserons le modèle tel qu'il est implémenté dans le chapitre 4.

5.2 Simulation de la torsion cyclique

Le modèle présenté dans le chapitre 4 a été identifié sur des essais cycliques de traction / compression. Ce mode de sollicitation uniaxiale est fréquemment utilisé pour caractériser les propriétés mécaniques des matériaux, ce qui permet de disposer d'une base de données expérimentales conséquente pour établir des comparaisons avec les prédictions du modèle. Cependant, dans l'optique d'une application à l'échelle industrielle, les sollicitations mécaniques appliquées au matériau ne se limitent pas à des chargements uniaxiaux et il convient donc d'étudier les propriétés pour des sollicitations plus complexes, telles que des chargements multiaxiaux par exemple.

Dans ce cadre, nous avons choisi d'étudier les prédictions du modèle pour un chargement cyclique de type torsion. Dans la base de données expérimentales, nous ne disposons pas de résultats du comportement mécanique de l'acier Grade 92 sous ce type de sollicitation. Cependant, de nombreux essais ont été effectués sur un acier de Grade 91 [Sauzay et al., 2006]. Ces deux nuances d'aciers étant assez proches en termes de comportement à haute température (ils présentent tous les deux un adoucissement cyclique à 550 ℃), la comparaison des courbes d'adoucissement cyclique expérimentales en traction / compression et en torsion de l'acier de Grade 91 peuvent nous renseigner sur la tendance qui pourrait être observée sur l'acier de Grade 92 dans les mêmes conditions d'essais. Ainsi, nous nous bornerons à une étude qualitative des prédictions du modèle. La courbe de torsion cyclique de l'acier Grade 91 à 550 ℃ pour une amplitude de déformation $\Delta\gamma/2 = \pm 0.52\%$ et une vitesse de déformation de 2×10^{-3} s^{-1} est présentée sur la Fig. 5.14(a). Afin de comparer l'adoucissement cyclique en traction / compression à l'adoucissement cyclique en torsion, un essai de traction / compression soumis à une déformation viscoplastique équivalente est aussi présenté.

En tenant compte des orientations cristallographiques des blocs, la formulation des équations du modèle permet de simuler des chargements multiaxiaux. La courbe de prédiction du comportement mécanique pour un essai de torsion cyclique appliquée à l'acier de Grade 92 est présentée sur la Fig. 5.14(b). La courbe de prédiction du comportement en traction / compression pour une déformation viscoplastique équivalente est aussi présentée en Fig. 5.14(b).

En torsion, le modèle est capable de prédire un adoucissement cyclique, observé expérimentalement sur l'acier de Grade 91. Des études complémentaires sont à mener pour caractériser de manière quantitative les prédictions du modèle pour ce type de sollicitation. En l'absence de données expérimentales sur l'acier Grade 92, une identification des paramètres de la viscoplasticité cristalline pour l'acier Grade 91 est à envisager. Ce travail a déjà été mis en place dans le cadre de l'étude du

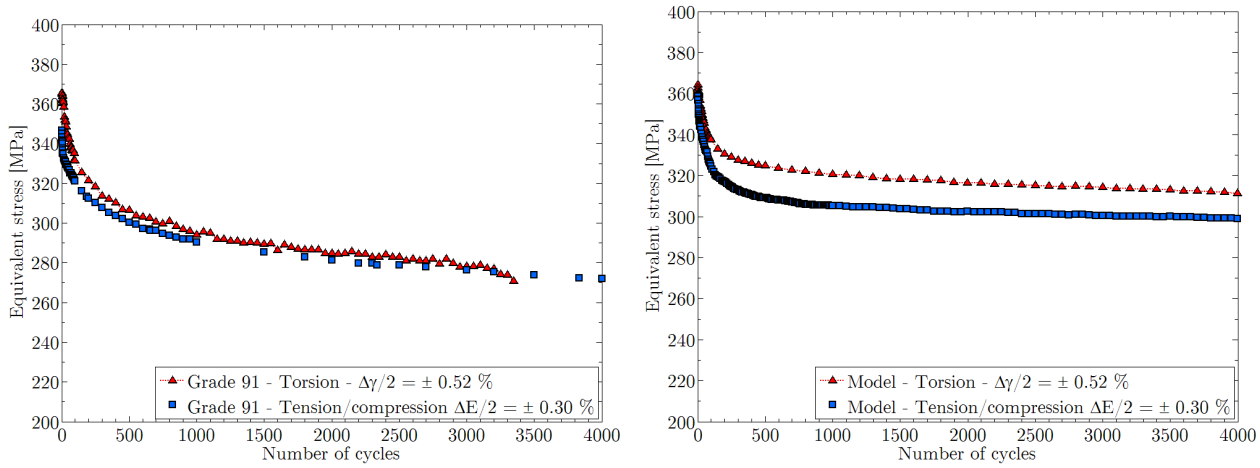

Fig. 5.14. (a) Courbes expérimentales en torsion et traction / compression d'un acier Grade 91 à 550 ℃ avec une vitesse de déformation de 2×10^{-3} s^{-1} et deux amplitudes de déformation équivalentes identiques pour les deux essais et (b) courbes prédictives du comportement d'un acier Grade 92 dans les mêmes conditions.

comportement cyclique de l'acier EUROFER 97 à température ambiante, dans le cadre d'une collaboration avec M. F. Giordana, étudiante en doctorat à l'Université de Rosario (Argentine). Son sujet de thèse porte sur l'étude expérimentale de l'adoucissement cyclique de l'acier EUROFER 97 à différentes températures et sur la simulation grâce à une modélisation similaire à la nôtre.

5.3 Application du modèle à l'acier EUROFER 97

Dans cette partie, nous aborderons succinctement les résultats des prédictions du modèle issus du travail de M. F. Giordana sur les propriétés mécaniques de l'acier EUROFER 97 sous sollicitation cyclique uniaxiale à température ambiante [Giordana et al., 2011].

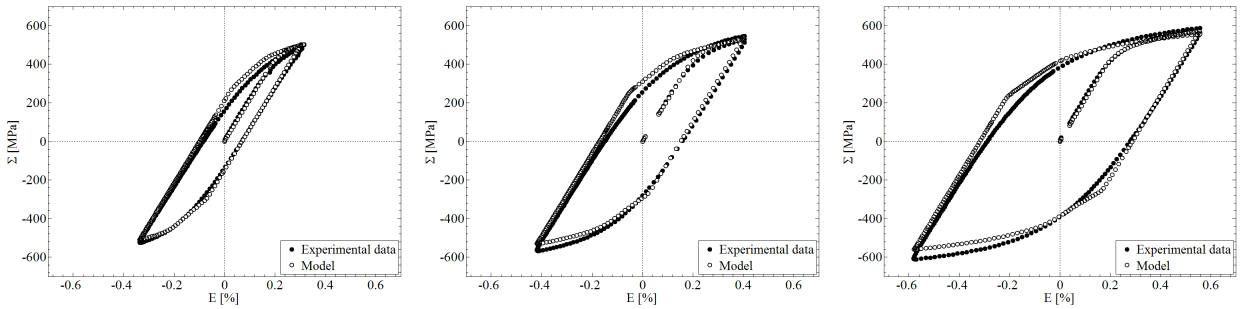

Fig. 5.15. Comparaison entre les données expérimentales et les prédictions de la première boucle d'un essai cyclique sur l'acier EUROFER 97 à température ambiante pour une variation de déformation plastique de (a) 0,2 %, (b) 0,3 % et (c) 0,6 %.

La Fig. 5.15 présente une comparaison entre les boucles expérimentales d'un acier EUROFER 97 à température ambiante sous sollicitations cycliques pour plusieurs amplitudes de déformation plastique et les prédictions correspondantes. Bien que de légères imperfections soient visibles sur le cycle prédit

(tout comme sur les courbes présentées au chapitre 4 dans le cas du Grade 92 sous chargement cyclique à haute température), le modèle prédit assez correctement le comportement mécanique de l'acier EUROFER 97 à température ambiante durant le premier cycle de fatigue. Seule la courbe expérimentale de la Fig. 5.15(a) a été utilisée pour l'identification, en imposant de plus un effet de vitesse négligeable.

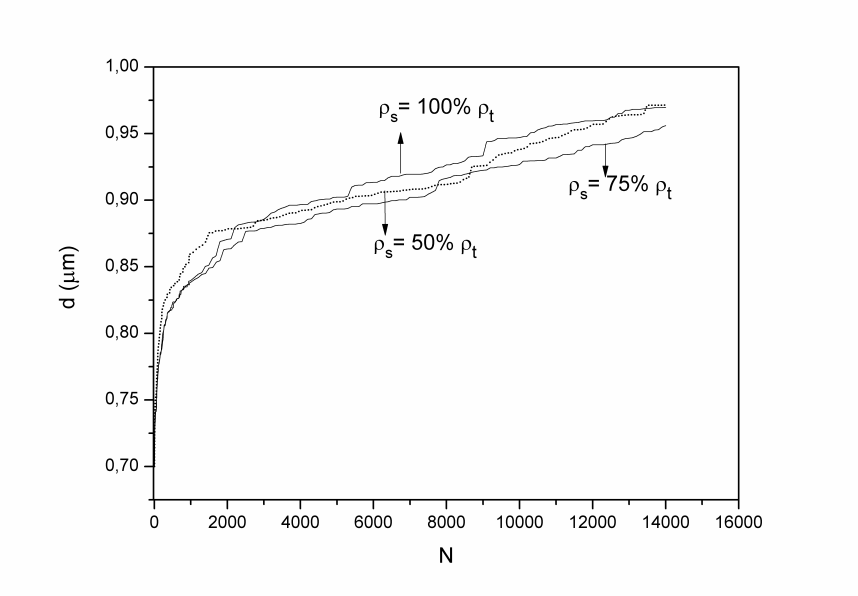

Fig. 5.16. Stabilité des prédictions du modèle vis-à-vis de la valeur de la proportion de densité de dislocations vis mobiles dans le matériau (essai de déformation cyclique sur acier EUROFER 97 à température ambiante pour une variation de déformation plastique de 0,2 %).

La Fig. 5.16 démontre que les prédictions sont stables vis-à-vis de la proportion de dislocations vis mobiles parmi la population totale de dislocations mobiles. En effet, dans ce cas, l'évolution de la taille moyenne de sous-grain varie très peu (moins de 3 %) par rapport à la valeur de ce paramètre. Cette étude de la stabilité des prédictions du modèle menée par M. F. Giordana (et dont nous présentons ici le résultat pour un paramètre seulement) aboutit aux mêmes conclusions que celles observées à haute température, abordées dans la partie 4.6.4 : les prédictions varient très faiblement lorsque les paramètres évoluent dans un intervalle de valeurs physiquement acceptables.

La Fig. 5.17 représente les évolutions expérimentales et prédites de la taille moyenne de sous-grains et de la densité de dislocations moyenne au cours d'un essai cyclique avec une variation de déformation plastique de 0,2 % sur un acier EUROFER 97 à température ambiante. Dans le cas de l'évolution de la taille moyenne des sous-grains, bien que le modèle prédise une valeur finale légèrement sous-estimée, l'évolution prédite au cours du cyclage est assez proche des observations expérimentales. La densité de dislocations finale prédite est clairement surestimée. Cependant, le modèle reproduit correctement la chute très rapide de la densité de dislocations constatée dès les premiers cycles. Pour le moment, des études complémentaires sont en cours afin de proposer une prédiction convenable du comportement mécanique macroscopique de l'acier EUROFER 97 sous sollicitation cyclique à température ambiante.

Ces résultats montrent que le modèle peut être appliqué à la fois à des aciers de la famille des 9 %Cr autres que l'acier Grade 92 et à des températures différentes de 550 ℃.

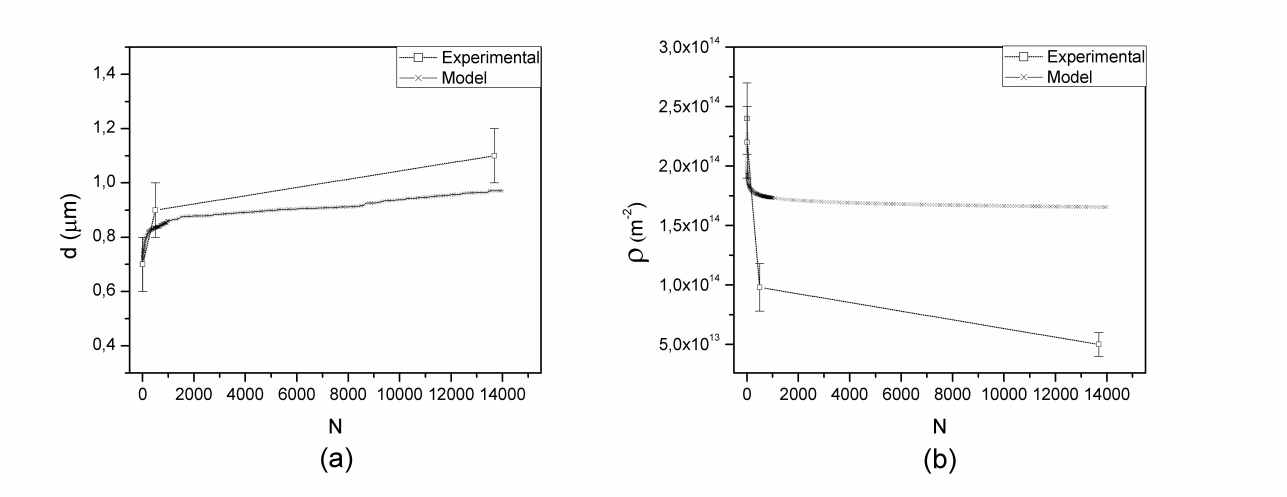

Fig. 5.17. Comparaison entre les données expérimentales et les prédictions des évolutions microstructurales au cours d'un essai de cyclique sur l'acier EUROFER 97 à température ambiante pour une variation de déformation plastique de 0,2 % : (a) évolution de la taille moyenne de sous-grains et (b) évolution de la densité totale de dislocations mobiles.

5.4 Conclusions

Dans ce cinquième chapitre, nous avons abordé trois aspects nouveaux liés au modèle : son amélioration avec la prise en compte de la distribution initiale de la taille des sous-grains et la distribution initiale de la densité de dislocations, sa capacité à prédire le comportement mécanique du matériau pour d'autres sollicitations et son adaptation à d'autres types de matériaux et conditions de températures.

En conclusion, il convient de retenir les points suivants :

- La prise en compte de la distribution de la taille initiale de sous-grain conduit à une surestimation de l'adoucissement cyclique prédit par le modèle. Celle-ci s'explique par une évolution très rapide de la taille moyenne de sous-grain prédite.
- La prise en compte de la distribution initiale de la densité de dislocations, et de la distribution initiale de la taille des sous-grains permet d'améliorer les prédictions microstructurales. Le comportement mécanique macroscopique prédit est assez proche des données expérimentales et les prédictions des évolutions microstructurales sont en accord avec les évolutions de la taille de sous-grains et de la densité finale de dislocations mesurées expérimentalement.
- La prise en compte des hétérogénités de la microstructure initiale (taille de sous-grains et densité de dislocations) permet d'établir une corrélation entre l'état initial des blocs dans le matériau et leur évolution au sein de la matrice au cours du cyclage. Ainsi, dans le cas d'un chargement cyclique à $1 \times 10^{-5}\ \mathrm{s}^{-1}$ et une amplitude de déformation de $\Delta E/2 = \pm 0,35$ % à 550 ℃, le modèle prédit la coexistence d'un petit nombre de blocs ayant peu évolué au niveau de leur microstructure, d'un petit nombre de blocs ayant une taille moyenne de sous-grains élevée et une densité de dislocations faible, et enfin d'un nombre assez important de blocs ayant peu évolué en termes de taille moyenne de sous-grain mais dont la densité de dislocations est faible, en accord avec les observations microstructurales.
- Le modèle appliqué à une sollicitation de torsion cyclique donne une première tendance de l'évolution du comportement macroscopique et prédit un adoucissement mécanique comme cela

est observé pour l'acier Grade 91.

- L'application du modèle à des chargements de traction / compression sur l'acier EUROFER 97 à température ambiante, un autre acier de la famille des 9 %Cr, permet de prédire correctement l'évolution de la taille de sous-grains au cours du cyclage, mais seulement qualitativement celle de la densité de dislocations.

Chapter 6

General conclusions and recommendations for further work

6.1 Conclusions

The present work was concerned with the high temperature mechanical behaviour of tempered ferritic-martensite steel Grade 92 (9%Cr-0.5%Mo-1.8%W-NbV), considered as potential candidate for structural components in Generation IV nuclear power plants. Already used for energy production in fossil power plants, tempered martensitic are subjected to strong softening during high-temperature cycling.

This study focused on the following two main points:

- The experimental study of macroscopic mechanical behaviour and microstructural evolution during monotonic tensile tests and cyclic loading at 550 ℃.
- The modelling of some of the most relevant deformation and recovery mechanisms in order to predict both macroscopic mechanical behaviour and microstructural evolution during monotonic and cyclic loading.

The first objective of this work was addressed using an approach based on the coupling of mechanical test results and microstructural observations (mainly TEM observations). In the second chapter, the mechanical behaviour and microstructural evolution during monotonic tensile tests at 550 ℃ and various strain rates were studied. Two simple analytical models were proposed in order to predict respectively the beginning of the mechanical instability (necking) and the subgrain growth. The following conclusions can be drawn:

1. For strain rates lower than $2.5 \times 10^{-4}\ s^{-1}$, engineering stress-strain curves show a first softening stage well before the onset of macroscopic visible necking. This stage is characterised by constantly decreasing load.
2. True stress-strain curves show this softening stage which depends on the strain rate: the lower the strain rate, the more pronounced the softening stage.
3. Modelling of mechanical instability using the Hart criterion predicts its onset for a low elongation close to the elongation at maximum load. In fact, diffuse necking occurs after a few percents of elongation. Macroscopic necking, in turn, induces a second softening stage with a stronger decreasing slope, leading to fracture.
4. The first softening stage is not due to ductile cavity nucleation and growth in the specimens.
5. Subgrain size increases by about 21%, contributing to the material softening behaviour. This growth is overestimated by the simple model founded on a basic mechanism of low-angle boundaries vanishing by interactions with mobile dislocations.

In the third chapter, the mechanical behaviour of the Grade 92 steel during continuous cyclic loading and creep at 550 ℃ is studied experimentally. It was shown that:

1. No significant difference appears between the Grade 91 and Grade 92 steels in terms of cyclic lifetime, according to Manson-Coffin curves. The Monkman-Grant equation fitted on the Grade 92 steel creep data is close to that etablished for the Grade 91 steel. This indicates that the mechanisms controling cyclic deformation and creep lifetime are the same for both steels.

2. Grade 92 steel is subjected to cyclic softening. This phenomenon is more pronounced for high values of strain amplitude in agreement with literature results. However, it is still significant for very low values of viscoplastic strain amplitude.

3. Cyclic softening is more pronounced for lower strain rate. However, the impact of strain rate on fatigue lifetime is slight.

4. Cyclic softening is mainly due to a decrease in kinematic stress, as it was measured in Grade 91 steels. This indicates a decrease in rather long-range interactions between the mobile dislocations and the dislocation forest or the low-angle subgrain boundaries.

5. The subgrain size distributions (at initial state and during cycling) are satisfactorily described by log-normal probability density functions.

6. During cycling, mean subgrain size increases and a decrease in dislocation density within subgrains is observed. Corresponding evolutions are faster and more pronounced for low cyclic strain rate.

The second objective consisted in proposing a model able to predict both macroscopic mechanical behaviour and microstructural evolution during cycling. This self-consistent homogeneisation model aimed at taking into account the deformation and recovering mechanisms observed in agreement with our TEM observations and already described in literature. It is based on experimentally measured, calculated or fixed parameters which have a physical meaning. Only two of them (activation volume and activation energy) corresponding to the viscosity effect are adjusted using experimental monotonic tensile curves at two strain rates only. The identification process is reduced to a very limited number of experimental data, excluding all data in relationship to the softening behaviour. The activation volume and activation energy may correspond to the mechanisms of interaction of dislocations with clusters of solute atoms or small carbo-nitride precipitates. Due to the various obstacles existing in tempered martensite ferritic steels (solid solution, MX particles...), only such inverse adjustement is possible. Simulation results lead to the following conclusions:

1. The mechanical behaviour of the Grade 92 steel during the first hysteresis loop at different strain rates (2×10^{-3} and 1×10^{-5} s^{-1}) is rather accuratly predicted.

2. Cyclic softening effect is correctly predicted for tests performed at high strain rate with total strain amplitude from 0.25 to 0.35 %.

3. At low strain rate, the maximum tensile stress is slightly underestimated whereas predictions are rather accurate for high strain rate.

4. Although the predicted subgrain size evolution is overestimated, the predictions of the final dislocation density are in agreement with measured one.

5. The proposed model is relatively stable with respect to the variation of the physically-based parameters which values are only known to belong to specific range. Only the prediction of the main subgrain size evolution is sensitive to the variation of these parameters.

Two main improvements of the modelling are presented in chapter 5: initial mean subgrain size distribution per block and initial dislocation density distribution are taken into account based on measured distributions. Following conclusions can be drawn:

1. When only the initial mean subgrain size distribution per block is taken into account, the subgrain size growth and the cyclic softening are both overestimated.

2. To improve the accuracy of the prediction, it is necessary to take into account the initial mean subgrain size distribution per block and the initial dislocation density distribution. By this way, the cyclic softening is rather well predicted and predictions of the microstructural evolution give a fair estimation of subgrain size evolution and final dislocation density whatever the applied strain rate.

3. At the block scale, the modelling is able to predict the microstructural heterogeneities concerning the subgrain size and dislocation density in the material, in agreement with distributions measured during interrupted tests and after failure whatever the conditions.

Although this model was identified using uniaxial tensile curves on a Grade 92 steel, a torsion test was simulated and showed that modelling is able to predict a cyclic softening during torsion test, as it is experimentally observed in the Grade 91 steel. The same modelling was applied to the prediction of the microstructural evolution during cycling at room temperature in EUROFER 97 steel. Results showed that subgrain growth is rather well predicted but dislocation density decrease is underestimated.

The experimental study permits us to observe and quantify the two main evolutions in the tempered martensite steels during tensile tests and cycle fatigue tests at 550 ℃: subgrain growth and decrease in dislocation density. A deformation and recovery mechanism based on the knitting-in / kitting-out [Eggeler et al., 1987, Eggeler, 1989] and low-angle boundary vanishing [Holec and Dlouhý, 2005, Sauzay et al., 2005] was proposed to link the microstructural evolution to the cyclic softening measured at high temperature. These experimental hypothesis permitted us to propose a model which enables to give rather fair predictions of the microstructural evolution and cyclic softening behaviour at high temperature.

Although the proposed model is able to predict macroscopic mechanical softening and microstructural evolution during cycling (tension / compression, torsion), some improvements are necessary to predict the mechanical behaviour during loading conditions like creep, creep-fatigue and relaxation loading. Several ideas are proposed and discussed in the following part.

6.2 Some recommendations for future work

Constant applied stress

At this stage, the proposed modelling is not able to reproduce correctly the influence of constant applied stress on material. Even if the viscoplastic model of Molinari is used, the model predicts an increase in dislocation density during creep, which is not observed experimentally. Consequently, this phenomenon lead to the impossibility to reproduce the macroscopic mechanical behaviour during creep or cyclic loading with constant applied stress (creep-fatigue, torsion).

A possible way to partially solve this problem is to take dislocation climb mechanism into account. This mechanism, observed during long-term exposure at high temperature, should induce a decrease in dislocation density experimentally observed in tempered martensite steels during creep tests. This improvement is already implemented in a model, and it would permit us to describe the diffusion mechanisms, important during creep and relaxation tests.

Precipitate state

In this study, we assumed that no evolution of the precipitate state takes place during low-cycle fatigue test at 550 ℃. Indeed, TEM observations performed on thin foils taken from both as-received material and specimens after cycling at high strain rate did not show a significant difference in terms of precipitate size. However, during cycling at low strain rate, high-temperature time exposure is approximatly equal to two months for test performed at $1 \times 10^{-5}\,\mathrm{s}^{-1}$ with a strain amplitude of ± 0.35 % and TEM observations on thin foils taken from corresponding specimens showed large aligned precipitates on existing and former boundaries. It should be important to investigate the nature and chemical composition of these precipitates and a complementary study of their size evolution should be necessary in order to describe the influence of this phenomenon on the mechanical behaviour.

In the present model, the influence of the precipitate state is indirectly taken into account by the criterion allowing the destruction of low-angle boundaries proposed by Holec and Dlouhý [Holec and Dlouhý, 2005]. However, it should be important to take the influence of other particles whithin the subgrain (like MX precipitates for example) into account because of their beneficial influence on the mechanical properties in V-Nb optimised steels. Indeed, a correlation between secondary creep rate and low-angle boundary interparticle distance was highlighted [Kuchařová et al., 1997]. Modelling the influence of these particules is necessary to predict correctly the macrocopic mechanical behaviour during creep. More generally, the simulation of long-term sollicitations at high temperature leads to extend the microstructural evolution to particule size evolution.

Prediction of the mechanical properties over a larger temperature range

The prediction of the microstructural evolution in EUROFER 97 steel showed that the model is able to predict qualitatively the mechanical behaviour at room temperature. However, it would interesting to study the predictions of the mechanical behaviour for different temperatures and compare them to experimental data. This study would permit us to charactize the influence of temperature on the predictions of the model and to know if it is able to reproduce the temperature effect on the mechanical behaviour which is experimentally observed.

References

[Abe, 2001] Abe, F. (2001). Creep rates and strengthening mechanisms in tungsten-trengthened 9Cr steels. *Materials Science and Engineering A - Structural Materials Properties Microstructure and Processing*, 319:770–773.

[Abe, 2004] Abe, F. (2004). Coarsening behavior of lath and its effect on creep rates in tempered martensitic 9Cr-W steels. *Materials Science and Engineering A - Structural Materials Properties Microstructure and Processing*, 387:565–569.

[Abe, 2011] Abe, F. (2011). Creep life estimation of Gr.91 based on creep strain analysis. *Materials at High Temperatures*, 28(2):75–84.

[Abe et al., 2004] Abe, F., Horiuchi, T., Taneike, M., and Sawada, K. (2004). Stabilization of martensitic microstructure in advanced 9Cr steel during creep at high temperature. *Materials Science and Engineering A - Structural Materials Properties Microstructure and Processingl*, 378(1-2):299–303.

[Abe et al., 2007] Abe, F., Taneike, M., and Sawada, K. (2007). Alloy design of creep resistant 9Cr steel using a dispersion of nano-sized carbonitrides. *International Journal of Pressure Vessels and Piping*, 84(1-2):3–12.

[Aghajani et al., 2009] Aghajani, A., Somsen, C., and Eggeler, G. (2009). On the effect of long-term creep on the microstructure of a 12% chromium tempered martensite ferritic steel. *Acta Materialia*, 57(17):5093–5106.

[Armas et al., 2004] Armas, A. F., Petersen, C., Schmitt, R., Avalos, M., and Alvarez, I. (2004). Cyclic instability of martensite laths in reduced activation ferritic/martensitic steels. *Journal of Nuclear Materials*, 329:252–256.

[Armas et al., 2002] Armas, A. F., Petersen, C., Schmitt, R., Avalos, M., and Alvarez-Armas, I. (2002). Mechanical and microstructural behaviour of isothermally and thermally fatigued ferritic/martensitic steels. *Journal of Nuclear Materials*, 307:509–513.

[Armstrong and Frederick, 1966] Armstrong, P. J. and Frederick, C. O. (1966). A mathematical representation of the multiaxial bauschinger effect. Technical Report RD/B/N731, C.E.G.B., Berkeley Nuclear Laboratories, Berkeley, U.K.

[Barcelo et al., 2010] Barcelo, F., Béchade, J. L., and Fournier, B. (2010). Orientation relationship in various 9%Cr ferritic/martensitic steels - EBSD comparison between Nishiyama-Wassermann, Kurdjumov-Sachs and Greninger-Troiano. *Phase Transitions*, 83(8):601–614.

[Barcelo et al., 2009] Barcelo, F., De Carlan, Y., Béchade, J. L., and Fournier, B. (2009). Orientation relationship in Eurofer martensitic steels. *Phase Transitions*, 82(11):808–820.

[Berveiller and Zaoui, 1978] Berveiller, M. and Zaoui, A. (1978). Extension of the self-consistent scheme to plastically-flowing polycrystals. *Journal of the Mechanics and Physics of Solids*, 26(5):325–344.

[Bhadeshia, 2001] Bhadeshia, H. K. D. H. (2001). *Bainite in steels - 2nd Edition*. Institute of Materials.

[Blum, 2001] Blum, W. (2001). Creep of crystalline materials: experimental basis, mechanisms and models. *Materials Science and Engineering A - Structural Materials Properties Microstructure and Processing*, 319:8–15.

[Blum and Eisenlohr, 2009] Blum, W. and Eisenlohr, P. (2009). Dislocation mechanics of creep. *Materials Science And Engineering A - Structural Materials Properties Microstructure and Processing*, 510-11:7–13.

[Brachet, 1991] Brachet, J.-C. (1991). *Alliages martensitiques 9Cr-1Mo : effets de l'addition de l'azote, du niobium et du vanadium sur la microstructure, les transformations de phase et les propriétés mécaniques*. PhD thesis, Université de Paris-Sud, Orsay.

[Béranger et al., 1994] Béranger, G., Henry, G., and Sanz, G. (1994). *Le livre de l'acier*. Lavoisier, Paris.

[Brown, 2002] Brown, L. M. (2002). A dipole model for the cross-slip of screw dislocations in fcc metals. *Philosophical Magazine A*, 82:1691–1711.

[Brown, 2006] Brown, L. M. (2006). Dislocation bowing and passing in persistent slip bands. *Philosophical Magazine*, 86(25–26):4055–4068.

[Caillard and Martin, 1982a] Caillard, D. and Martin, J. L. (1982a). Microstructure of alumninum during creep at intermediate temperature. I. Dislocation networks after creep. *Acta Metallurgica*, 30(2):437–445.

[Caillard and Martin, 1982b] Caillard, D. and Martin, J. L. (1982b). Microstructure of alumninum during creep at intermediate temperature. II. In situ study of subboundary properties. *Acta Metallurgica*, 30(4):791–798.

[Caillard and Martin, 2003] Caillard, D. and Martin, J. L. (2003). *Thermally activated mechanisms in crystal plasticity*, volume 8. Pergamon Materials Series.

[Cailletaud, 1992] Cailletaud, G. (1992). A micromechanical approach to inelastic behavior of metals. *International Journal of Plasticity*, 8(1):55–73.

[Catalao et al., 2005] Catalao, S., Feaugas, X., Pilvin, P., and Cabrillat, M. T. (2005). Dipole heights in cyclically deformed polycrystalline AISI 316L stainless steel. *Materials Science and Engineering A - Structural Materials Properties Microstructure and Processing*, 400:349–352.

[Cerri et al., 1998] Cerri, E., Evangelista, E., Spigarelli, S., and Bianchi, P. (1998). Evolution of microstructure in a modified 9Cr-1Mo steel during short term creep. *Materials Science and Engineering A - Structural Materials Properties Microstructure and Processing*, 245(2):285–292.

[Chaboche, 1989] Chaboche, J. L. (1989). Constitutive equations for cyclic plasticity and cyclic viscoplasticity. *International Journal of Plasticity*, 5:247–302.

[Chaboche, 2008] Chaboche, J. L. (2008). A review of some plasticity and viscoplasticity constitutive theories. *International Journal of Plasticity*, 24:1642–1693.

[Choudhary et al., 1991] Choudhary, B. K., Rao, K. B. S., and Mannan, S. L. (1991). High temperature low cycle fatigue properties of a thick-section 9wt.%Cr-1wt.%Mo ferritic steel forging. *Materials Science and Engineering A - Structural Materials Properties Microstructure and Processing*, 148(2):267–278.

[Conrad and Narayan, 2000] Conrad, H. and Narayan, J. (2000). On the grain size softening in nanocrystalline materials. *Scripta Materialia*, 42(11):1025–1030.

[Cottrell, 1953] Cottrell, A. H. (1953). *Dislocations and plastic flow in crystals*. Oxford University Press.

[Devincre et al., 2005] Devincre, B., Hoc, T., and Kubin, L. P. (2005). Collinear interactions of dislocations and slip systems. *Materials Science and Engineering A - Structural Materials Properties Microstructure and Processing*, 400-401:182–185.

[Devincre et al., 2008] Devincre, B., Hoc, T., and Kubin, L. P. (2008). Dislocation mean free paths and strain hardening of crystals. *Science*, 320:1745–1748.

[Differt and Essmann, 1993] Differt, K. and Essmann, U. (1993). Dynamic model of the wall structure in persistent slip bands of fatigued metals. I. Dynamical model of edge dislocation walls. *Materials Science and Engineering A - Structural Materials Properties Microstructure and Processing*, 164(1-2):295–299.

[Dlouhý et al., 2009] Dlouhý, A., Kuchařová, K., and Orlová, A. (2009). Long-term creep and creep rupture characteristics of TiAl-base intermetallics. *Materials Science and Engineering A - Structural Materials Properties Microstructure and Processing*, 510-511:350–355.

[Dronhofer et al., 2003] Dronhofer, A., Pešička, J., Dlouhý, A., and Eggeler, G. (2003). On the nature of internal interfaces in tempered martensite ferritic steels. *Zeitschrift fur Metallkunde*, 94(5):511–520.

[Dubey et al., 2005] Dubey, J. S., Chilukuru, H., Chakravartty, J. K., Schwienheer, M., Scholz, A., and Blum, W. (2005). Effects of cyclic deformation on subgrain evolution and creep in 9-12 % Cr-steels. *Materials Science and Engineering A - Structural Materials Properties Microstructure and Processing*, 406(1-2):152–159.

[Dumoulin et al., 2003] Dumoulin, S., Tabourot, L., Chappuis, C., Vacher, P., and Arrieux, R. (2003). Determination of the equivalent stress-equivalent strain relationship of a copper sample under tensile loading. *Journal of Materials Processing Technology*, 133(1-2):79–83.

[Dunn and Daniels, 1951] Dunn, C. G. and Daniels, F. W. (1951). Formation and behavior of subboundaries in silicon iron crystals. *Transactions of the American Institute of Mining and Metallurgical Engineers*, 191(2):147–154.

[Dupuy and Fivel, 2002] Dupuy, L. and Fivel, M. C. (2002). A study of dislocation junctions in FCC metals by an orientation dependent line tension model. *Acta Materialia*, 50(19):4873–4885.

[Earthman et al., 1989] Earthman, J. C., Eggeler, G., and Ilschner, B. (1989). Deformation and damage processes in a 12%Cr-Mo-V steel under high temperature low cycle fatigue conditions in air and vacuum. *Materials Science and Engineering A - Structural Materials Properties Microstructure and Processing*, 110:103–114.

[Eggeler, 1989] Eggeler, G. (1989). The effect of long-term creep on particle coarsening in tempered martensite ferritic steels. *Acta Metallurgica*, 37(12):3225–3234.

[Eggeler and Dlouhý, 2005] Eggeler, G. and Dlouhý, A. (2005). Boron segregation and creep in ultra-fine grained tempered martensite ferritic steels. *Zeitschrift fur Metallkunde*, 96(7):743–748.

[Eggeler et al., 1989] Eggeler, G., Earthman, J. C., Nilsvang, N., and Ilschner, B. (1989). Microstructural study of creep rupture in a 12% chromium ferritic steel. *Acta Metallurgica*, 37(1):49–60.

[Eggeler et al., 1987] Eggeler, G., Nilsvang, N., and Ilschner, B. (1987). Microstructural changes in a 12-percent chromium steel during creep. *Steel Research*, 58(2):97–103.

[Ennis and Czyrska-Filemonowicz, 2003] Ennis, P. J. and Czyrska-Filemonowicz, A. (2003). Recent advances in creep-resistant steels for power plant applications. *Sadhana - Academy Proceedings in Engineering Sciences*, 28(Part 3-4):709–730.

[Ennis et al., 2000] Ennis, P. J., Zielinska-Lipiec, A., and Czyrska-Filemonowicz, A. (2000). Influence of heat treatments on microstructural parameters and mechanical properties of P92 steel. *Materials Science and Technology*, 16(10):1226–1232.

[Ennis et al., 1997] Ennis, P. J., Zielinska-Lipiec, A., Wachter, O., and Czyrska-Filemonowicz, A. (1997). Microstructural stability and creep rupture strength of the martensitic steel P92 for advanced power plant. *Acta Materialia*, 45(12):4901–4907.

[Eshelby, 1957] Eshelby, J. D. (1957). The determination of the elastic field of an ellipsoidal inclusion, and related problems. *Proceedings of the Royal Society*, 241:376–396.

[Essmann and Differt, 1996] Essmann, U. and Differt, K. (1996). Dynamic model of the wall structure in persistent slip bands of fatigued metals. II. The wall spacing and the temperature dependence of the yield stress in saturation. *Materials Science and Engineering A - Structural Materials Properties Microstructure and Processing*, 208(1):56–68.

[Essmann and Mughrabi, 1979] Essmann, U. and Mughrabi, H. (1979). Annihilation of dislocations during tensile and cyclic deformation and limits of dislocation densities. *Philosophical Magazine A - Physics of Condensed Matter Structure Defects and Mechanical Properties*, 40(6):731–756.

[Estrin et al., 1998] Estrin, Y., Tóth, L. S., Molinari, A., and Bréchet, Y. (1998). A dislocation-based model for all hardening stages in large strain deformation. *Acta Materialia*, 46(15):5509–5522.

[Fardoun et al., 1997] Fardoun, F., Polák, J., and Degallaix, S. (1997). Internal and effective stress analysis in stainless steels using the statistical approach method. *Materials Science and Engineering A - Structural Materials Properties Microstructure and Processing*, 234:456–458.

[Feaugas and Gaudin, 2001] Feaugas, X. and Gaudin, C. (2001). Different levels of plastic strain incompatibility during cyclic loading: in terms of dislocation density and distribution. *Materials Science and Engineering A - Structural Materials Properties Microstructure and Processing*, 309:382–385.

[Feaugas and Haddou, 2003] Feaugas, X. and Haddou, H. (2003). Grain-size effects on tensile behavior of nickel and AISI 316L stainless steel. *Metallurgical and Materials Transactions A - Physical Metallurgy and Materials Science*, 34A(10):2329–2340.

[Fournier, 2007] Fournier, B. (2007). *Fatigue-fluage des aciers martensitiques à 9-12%Cr : comportement et endommagement*. PhD thesis, École Nationale Supérieure des Mines de Paris.

[Fournier et al., 2011a] Fournier, B., Dalle, F., Sauzay, M., Longour, J., Salvi, M., Caës, C., Tournié, I., Giroux, P. F., and Kim, S. H. (2011a). Comparison of various 9-12%Cr steels under fatigue and creep-fatigue loadings at high temperature. *Materials Science and Engineering A - Structural Materials Properties Microstructure and Processing*, 528(22-23):6934–6945.

[Fournier et al., 2010] Fournier, B., Salvi, M., Dalle, F., De Carlan, Y., Caës, C., Sauzay, M., and Pineau, A. (2010). Lifetime prediction of 9-12%Cr martensitic steels subjected to creep-fatigue at high temperature. *International Journal of Fatigue*, 32(6):971–978.

[Fournier et al., 2006a] Fournier, B., Sauzay, M., Caës, C., Mottot, M., Noblecourt, A., and Pineau, A. (2006a). Analysis of the hysteresis loops of a martensitic steel - Part II: Study of the influence of creep and stress relaxation holding times on cyclic behaviour. *Materials Science and Engineering A - Structural Materials Properties Microstructure and Processing*, 437(2):197–211.

[Fournier et al., 2006b] Fournier, B., Sauzay, M., Caës, C., Noblecourt, M., and Mottot, M. (2006b). Analysis of the hysteresis loops of a martensitic steel - Part I: Study of the influence of strain amplitude and temperature under pure fatigue loadings using an enhanced stress partitioning method. *Materials Science and Engineering A - Structural Materials Properties Microstructure and Processing*, 437(2):183–196.

[Fournier et al., 2009a] Fournier, B., Sauzay, M., Caës, C., Noblecourt, M., Mottot, M., Allais, L., Tournié, I., and Pineau, A. (2009a). Creep-fatigue interactions in a 9 pct Cr-1 pct Mo martensitic steel: Part I. Mechanical test results. *Metallurgical and Materials Transactions A - Physical Metallurgy and Materials Science*, 40A(2):321–329.

[Fournier et al., 2008] Fournier, B., Sauzay, M., Caës, C., Noblecourt, M., Mottot, M., Bougault, A., Rabeau, V., and Pineau, A. (2008). Creep-fatigue-oxidation interactions in a 9Cr-1Mo martensitic steel. Part I: effect of tensile holding period on fatigue lifetime. *International Journal of Fatigue*, 30(4):649–662.

[Fournier et al., 2011b] Fournier, B., Sauzay, M., and Pineau, A. (2011b). Micromechanical model of the high temperature cyclic behavior of 9-12%Cr martensitic steels. *International Journal of Plasticity*, 27(11):1803–1816.

[Fournier et al., 2009b] Fournier, B., Sauzay, M., Renault, A., F., B., and Pineau, A. (2009b). Microstructural evolutions and cyclic softening of 9%Cr martensitic steels. *Journal of Nuclear Materials*, 386:71–74.

[Franciosi, 1983] Franciosi, P. (1983). Glide mechanisms in bcc crystals: an investigation of the case of α-iron through multislip and latent hardening tests. *Acta Metallurgica*, 31:1331–1341.

[Franciosi et al., 1980] Franciosi, P., Berveiller, M., and Zaoui, A. (1980). Latent hardening in copper and aluminium single crystals. *Acta Metallurgica*, 28:273–283.

[Frank, 1980] Frank, F. C. (1980). The Frank-Read source. *Proceedings of the Royal Society of London Series A - Mathematical Physical and Engineering Sciences*, 371(1744):136–138.

[François et al., 1995a] François, D., Pineau, A., and Zaoui, A. (1995a). *Comportement mécanique des matériaux - élasticité et plasticité.* Hermès, Paris.

[François et al., 1995b] François, D., Pineau, A., and Zaoui, A. (1995b). *Comportement mécanique des matériaux - viscoplasticité, endommagement, mécanique de la rupture, mécanique du contact.* Hermès, Paris.

[Gaudin, 2002] Gaudin, C. (2002). *Étude des mécanismes associés au rochet cyclique d'un acier austénitique AISI 316L.* PhD thesis, Université de Technologie de Compiègne.

[Ghassemi-Armaki et al., 2009] Ghassemi-Armaki, H., Chen, R. P., Maruyama, K., Yoshizawa, M., and Igarashi, M. (2009). Static recovery of tempered lath martensite microstructures during long-term aging in 9-12% Cr heat resistant steels. *Materials Letters*, 63(28):2423–2425.

[Gieseke et al., 1993] Gieseke, B. G., Brinkman, C. R., and Maziasz, P. J. (1993). The influence of thermal aging on the microstructure and fatigue properties of modified 9Cr-1Mo steel. In *First International Conference on Microstructure and Mechanical Properties of Aging Materials*, pages 197–205. Minerals, Metals & Materials Society.

[Gilman, 1955] Gilman, J. J. (1955). Structure and polygonization of bent zinc monocrystals. *Acta Metallurgica*, 3(3):277–288.

[Giordana et al., 2011] Giordana, M. F., Giroux, P. F., Alvarez-Armas, I., Sauzay, M., and Armas, A. (2011). Microstructural evolution during cyclic loading of ferritic/martensitic steels at room temperature. In *European Congress and Exhibition on Advanced Materials and Processes, EUROMAT 2011, 12-15 september 2011, Montpellier, France.*

[Giroux et al., 2009] Giroux, P. F., Dalle, F., Sauzay, M., Bougault, A., Fournier, B., Malaplate, J., Pérez, G., Rabeau, V., Tancray, A., Tournié, I., Van Den Berghe, T., and Gourgues-Lorenzon, A. F. (2009). Étude des propriétés de restauration dynamique en traction de l'acier P92. Technical report, DEN/DANS/DMN/SRMA/LC2M-09-2997.

[Giroux et al., 2010] Giroux, P. F., Dalle, F., Sauzay, M., Malaplate, J., Fournier, B., and Gourgues-Lorenzon, A. F. (2010). Mechanical and microstructural stability of P92 steel under uniaxial tension at high temperature. *Materials Science and Engineering A - Structural Materials Properties Microstructure and Processing*, 527(16-17):3984–3993.

[Götz and Blum, 2003] Götz, G. and Blum, W. (2003). Influence of thermal history on precipitation of hardening phases in tempered martensite 10%Cr-steel X12CrMoWVNbN 10-1-1. *Materials Science and Engineering A - Structural Materials Properties Microstructure and Processing*, 348(1-2):201–207.

[Gourgues et al., 2000] Gourgues, A. F., Flower, H. M., and Lindley, T. C. (2000). Electron backscattering diffraction study of acicular ferrite, bainite, and martensite steel microstructures. *Materials Science and Technology*, 16(1):26–40.

[Greeff et al., 2000] Greeff, A. P., Louw, C. W., and Swart, H. C. (2000). The oxidation of industrial FeCrMo steel. *Corrosion Science*, 42(10):1725–1740.

[Gustafson and Hättestrand, 2002] Gustafson, A. and Hättestrand, M. (2002). Coarsening of precipitates in an advanced creep resistant 9% chromium steel - quantitative microscopy and simulations. *Materials Science and Engineering A - Structural Materials Properties Microstructure and Processing*, 333(1-2):279–286.

[Guétaz et al., 2003] Guétaz, L., Millier, J.-P., and Urvoy, S. (2003). Mécanisme de déformation de l'acier martensitique Eurofer. Technical report, CEA/DTEN/SMP/LSMM 2002-128.

[Guttmann, 1974] Guttmann, D. (1974). *Étude du revenu de la martensite dans les aciers faiblement alliés à 2 % de manganèse. Influence de l'antimoine.* PhD thesis, Université de Nancy.

[Haddou et al., 2001] Haddou, H., Gaudin, C., and Feaugas, X. (2001). Stacking fault energy (s.f.e.) and grain size effects (d) on the tensile behaviour of f.c.c. polycrystalline alloys at 300 K: Back stress and effective stress evolutions. *Journal de Physique IV*, 11(PR4):283–291.

[Haddou et al., 2004] Haddou, H., Risbet, M., Marichal, G., and Feaugas, X. (2004). The effects of grain size on the cyclic deformation behaviour of polycrystalline nickel. *Materials Science and Engineering A - Structural Materials Properties Microstructure and Processing*, 379(1-2):102–111.

[Hähner et al., 1998] Hähner, P., Tippelt, B., and Holste, C. (1998). On the dislocation dynamics of persistent slip bands in cyclically deformed fcc metals. *Acta Materialia*, 46(14):5073–5084.

[Hald, 2008] Hald, J. (2008). Microstructure and long-term creep properties of 9-12%Cr steels. *International Journal of Pressure Vessels and Piping*, 85(1-2):30–37.

[Haney et al., 2009] Haney, E. M., Dalle, F., Sauzay, M., Vincent, L., Tournié, I., Allais, L., and Fournier, B. (2009). Macroscopic results of long-term creep on a modified 9Cr-1Mo steel (T91). *Materials Science and Engineering A - Structural Materials Properties Microstructure and Processing*, 510-11:99–103.

[Hart, 1967] Hart, E. W. (1967). Theory of the tensile test. *Acta Metallurgica*, 15:351–355.

[Hättestrand and Andrén, 1999] Hättestrand, M. and Andrén, H. O. (1999). Boron distribution in 9-12% chromium steels. *Materials Science and Engineering A - Structural Materials Properties Microstructure and Processing*, 270(1):33–37.

[Hättestrand and Andrén, 2001] Hättestrand, M. and Andrén, H. O. (2001). Evaluation of particle size distributions of precipitates in a 9% chromium steel using energy filtered transmission electron microscopy. *Micron*, 32(8):789–797.

[Hättestrand et al., 1998] Hättestrand, M., Schwind, M., and Andrén, H. O. (1998). Microanalysis of two creep resistant 9-12% chromium steels. *Materials Science and Engineering A - Structural Materials Properties Microstructure and Processing*, 250(1):27–36.

[Henry et al., 2003] Henry, J., Averty, X., Dai, Y., Lamagnere, P., Pizzanelli, J. P., Espinas, J. J., and Wident, P. (2003). Tensile properties of 9Cr-1Mo martensitic steel irradiated with high energy protons and neutrons. *Journal of Nuclear Materials*, 318:215–227.

[Hoc and Forest, 2001] Hoc, T. and Forest, S. (2001). Polycrystal modelling of IF-Ti steel under complex loading path. *International Journal of Plasticity*, 17(1):65–85.

[Holec and Dlouhý, 2005] Holec, D. and Dlouhý, A. (2005). Interactions between particles and low-angle dislocation boundaries during high-temperature deformation. *Zeitschrift fur Metallkunde*, 96(6):558–565.

[Hutchinson, 1964] Hutchinson, J. W. (1964). Plastic deformation of b.c.c polycrystals. *Journal of the Mechanics and Physics of Solids*, 12(1):25–33.

[Kannan et al., 2009] Kannan, R., Sandhya, R., Ganesan, V., Valsan, M., and Rao, K. B. S. (2009). Effect of sodium environment on the low cycle fatigue properties of modified 9Cr-1Mo ferritic martensitic steel. *Journal of Nuclear Materials*, 384(3):286–291.

[Kannan et al., 2010] Kannan, R., Srinivasan, V. S., Valsan, M., and Rao, K. B. S. (2010). High temperature low cycle fatigue behaviour of P92 tungsten added 9Cr steel. *Transactions of the Indian Institute of Metals*, 63(2-3):571–574.

[Kassner et al., 2000] Kassner, M. E., Pérez-Prado, M. T., Vecchio, K. S., and Wall, M. A. (2000). Determination of internal stresses in cyclically deformed copper single crystals using convergent-beam electron diffraction and dislocation dipole separation measurements. *Acta Materialia*, 48:4247–4254.

[Kim and Weertman, 1988] Kim, S. and Weertman, J. R. (1988). Investigation of microstructural changes in a ferritic steel caused by high temperature fatigue. *Metallurgical Transactions A - Physical Metallurgy and Materials Science*, 19(4):999–1007.

[Kimura et al., 2006] Kimura, M., Yamaguchi, K., Hayakawa, M., Kobayashi, K., and Kanazawa, K. (2006). Microstructures of creep-fatigued 9-12% Cr ferritic heat-resisting steels. *International Journal of Fatigue*, 28(3):300–308.

[Kishore and Sinha, 1996] Kishore, R. and Sinha, T. K. (1996). Analysis of the stress-strain curves of a modified 9Cr-1Mo steel by the Voce equation. *Metallurgical and Materials Transactions A - Physical Metallurgy and Materials Science*, 27(10):3340–3343.

[Kitahara et al., 2006] Kitahara, H., Ueji, R., Tsuji, N., and Minamino, Y. (2006). Crystallographic features of lath martensite in low-carbon steel. *Acta Materialia*, 54(5):1279–1288.

[Klaar et al., 1992] Klaar, H., Schwaab, P., and Österle, W. (1992). Round robin investigation into the quantitative measurement of dislocation density in the electron microscope. *Praktische Metallographie*, 29:1–24.

[Kocks and Mecking, 2003] Kocks, U. F. and Mecking, H. (2003). Physics and phenomenology of strain hardening: the FCC case. *Progress in Materials Science*, 48:171–273.

[Koo and Lee, 2007] Koo, G. and Lee, J. (2007). Investigation of ratcheting characteristics of modified 9Cr-1Mo steel by using the Chaboche constitutive model. *International Journal of Pressure Vessels and Piping*, 84:284–292.

[Korcakova et al., 2001] Korcakova, L., Hald, J., and Somers, M. A. J. (2001). Quantification of Laves phase particle size in 9CrW steel. *Materials Characterization*, 47(2):111–117.

[Kostka et al., 2007] Kostka, A., Tak, K. G., Hellmig, R. J., Estrin, Y., and Eggeler, G. (2007). On the contribution of carbides and micrograin boundaries to the creep strength of tempered martensite ferritic steels. *Acta Materialia*, 55(2):539–550.

[Kröner, 1961] Kröner, E. (1961). Zur plastischen verformung des vielkristalls. *Acta Metallurgica*, 9:155–161.

[Kubin et al., 2008] Kubin, L. P., Devincre, B., and Hoc, T. (2008). Toward a physical model for strain hardening in fcc crystals. *Materials Science and Engineering A - Structural Materials Properties Microstructure and Processing*, 483-484:19–24.

[Kuchařová et al., 1997] Kuchařová, K., Němec, J., and Dlouhý, A. (1997). Microstructure and creep strength of tempered martensite ferritic steels. In *Creep and Fracture of Engineering Materials and Structure*, pages 79–88.

[Kunz and Lukáš, 2001] Kunz, L. and Lukáš, P. (2001). Cyclic stress-strain behavior of 9Cr1Mo steel at positive mean stress. *Materials Science and Engineering A - Structural Materials Properties Microstructure and Processing*, 319:555–558.

[Kurdjumov and Sachs, 1930] Kurdjumov, G. V. and Sachs, G. (1930). Über den mechanismus der stahlhärtung. *Zietschrift für Physik A - Hadrons and Nuclei*, 64:325–343.

[Lemaitre and Chaboche, 1990] Lemaitre, J. and Chaboche, J. L. (1990). *Mechanics of solid materials*. Cambridge University Press.

[Li, 1960] Li, J. (1960). The interaction of parallel edge dislocations with a simple tilt dislocation wall. *Acta Metallurgica*, 8:296–311.

[Lim et al., 2011] Lim, R., Sauzay, M., Dalle, F., Tournié, I., Bonnaillie, P., and Gourgues-Lorenzon, A. F. (2011). Modelling and experimental study of the tertiary creep stage of Grade 91 steel. *International Journal of Fracture*, 169(2):213–228.

[Lindau et al., 2002] Lindau, R., Möslang, A., and Schirra, M. (2002). Thermal and mechanical behaviour of the reduced-activation-ferritic-martensitic steel EUROFER. *Fusion Engineering and Design*, 61-62:659–664.

[Liu and Castañeda, 2004] Liu, Y. and Castañeda, P. P. (2004). Homogenization estimates for the average behavior and field fluctuations in cubic and hexagonal viscoplastic polycrystals. *Journal of the Mechanics and Physics of Solids*, 52(5):1175–1211.

[Madec and Kubin, 2004] Madec, R. and Kubin, L. P. (2004). Dislocation interactions and symmetries in bcc crystals. In *Kitagawa, H., Shibutani, Y. (Eds.), IUTAM Symposium on Mesoscopic Dynamics of Fracture Process and Materials Strength*, volume 115, pages 69–78. Kluwer Academic Publishers, Dordrecht, The Netherlands.

[Marder and Marder, 1969] Marder, J. M. and Marder, A. R. (1969). Morphology of iron-nickel massive martensite. *Transactions of the ASM*, 62(1):1–10.

[Marmy and Kruml, 2008] Marmy, P. and Kruml, T. (2008). Low cycle fatigue of Eurofer 97. *Journal of Nuclear Materials*, 377(1):52–58.

[Marmy et al., 1993] Marmy, P., Martin, J. L., and Victoria, M. (1993). Deformation mechanisms of a ferritic-martensitic steel between 290 K and 870 K. *Materials Science and Engineering A - Structural Materials Properties Microstructure and Processing*, 164(1-2):159–163.

[Milititsky et al., 2008] Milititsky, M., De Wispelaere, N., Petrov, R., Ramos, J. E., Reguly, A., and Hänninen, H. (2008). Characterization of the mechanical properties of low-nickel austenitic stainless steels. *Materials Science and Engineering A - Structural Materials Properties Microstructure and Processing*, 498(1-2):289–295.

[Milička and Dobeš, 2006] Milička, K. and Dobeš, F. (2006). Small punch testing of P91 steel. *International Journal of Pressure Vessels and Piping*, 83(9):625–634.

[Molinari, 1999] Molinari, A. (1999). Extensions of the self-consistent tangent model. *Modelling and Simulation in Materials Science and Engineering*, 7(5):683–697.

[Molinari et al., 1987] Molinari, A., Canova, G. R., and Ahzi, S. (1987). A self-consistent approach of the large deformation polycrystal plasticity. *Acta Metallurgica*, 35(12):2983–2994.

[Molinari and Tóth, 1994] Molinari, A. and Tóth, L. S. (1994). Tuning a self-consistent viscoplastic model by finite element results. Part I: Modelling. *Acta Metallurgica et Materialia*, 42(7):2453–2458.

[Monkman and Grant, 1956] Monkman, F. C. and Grant, N. J. (1956). An empirical relationship between rupture life and minimum creep rate in creep-rupture tests. *Proceedings of the ASTM*, 56:593–620.

[Moosbrugger et al., 2000] Moosbrugger, J. C., Morrison, D. J., and Jia, Y. (2000). Nonlinear kinematic hardening rule parameters - relationship to substructure evolution in polycrystalline nickel. *International Journal of Plasticity*, 16(3-4):439–467.

[Morrison and Moosbrugger, 1997] Morrison, D. J. and Moosbrugger, J. C. (1997). Effects of grain size on cyclic plasticity and fatigue crack initiation in nickel. *International Journal of Fatigue*, 19(1):S51–S59.

[Mughrabi et al., 1979] Mughrabi, H., Ackermann, F., and Herz, K. (1979). Persistent slipbands in fatigued face-centered and body-centered cubic metals. In Fong., J. T., editor, *Fatigue Mechanisms: a symposium*, pages 69–105, Kansas City, Missouri, U.S.A. American Society for Testing and Materials, Proceedings of an ASTM-NBS-NSF symposium.

[Mughrabi and Höppel, 2010] Mughrabi, H. and Höppel, H. W. (2010). Cyclic deformation and fatigue properties of very fine-grained metals and alloys. *International Journal of Fatigue*, 32:1413–1427.

[Naamane, 2008] Naamane, S. (2008). *Étude de la déformation plastique de la ferrite à basse température : simulations de dynamique des dislocations*. PhD thesis, Université Pierre et Marie Curie Paris VI.

[Nagesha et al., 2002] Nagesha, A., Valsan, M., Kannan, R., Rao, K. B. S., and Mannan, S. L. (2002). Influence of temperature on the low cycle fatigue behaviour of a modified 9Cr-1Mo ferritic steel. *International Journal of Fatigue*, 24(12):1285–1293.

[Nishiyama, 1934] Nishiyama, Z. (1934). Science report. Technical Report 23, Tohoku University.

[Orlová et al., 1998] Orlová, A., Buršik, J., Kuchařová, K., and Sklenička, V. (1998). Microstructural development during high temperature creep of 9% Cr steel. *Materials Science and Engineering A - Structural Materials Properties Microstructure and Processing*, 245(1):39–48.

[Panait, 2010] Panait, C. G. (2010). *Metallurgical evolution and creep strength of 9-12%Cr heat resistant steels at 600 ℃ and 650 ℃*. PhD thesis, École Nationale Supérieure des Mines de Paris.

[Panait et al., 2010a] Panait, C. G., Bendick, W., Fuchsmann, A., Gourgues-Lorenzon, A. F., and Besson, J. (2010a). Study of the microstructure of the Grade 91 steel after more than 100,000 h of creep exposure at 600 ℃. *International Journal of Pressure Vessels and Piping*, 87(6):326–335.

[Panait et al., 2010b] Panait, C. G., Zielińska-Lipiec, A., Koziel, T., Czyrska-Filemonowicz, A., Gourgues-Lorenzon, A. F., and Bendick, W. (2010b). Evolution of dislocation density, size of subgrains and MX-type precipitates in a P91 steel during creep and during thermal ageing at 600 ℃ for more than 100,000 h. *Materials Science and Engineering A - Structural Materials Properties Microstructure and Processing*, 527(16-17):4062–4069.

[Park et al., 2001] Park, J. S., Kim, S. J., and Lee, C. S. (2001). Effect of W addition on the low cycle fatigue behavior of high Cr ferritic steels. *Materials Science and Engineering A - Structural Materials Properties Microstructure and Processing*, 298(1-2):127–136.

[Paul et al., 2008] Paul, V. T., Saroja, S., and Vijayalakshmi, M. (2008). Microstructural stability of modified 9Cr-1Mo steel during long term exposures at elevated temperatures. *Journal of Nuclear Materials*, 378(3):273–281.

[Petersmeier et al., 1998] Petersmeier, T., Martin, U., Eifler, D., and Oettel, H. (1998). Cyclic fatigue loading and characterization of dislocation evolution in the ferritic steel X22CrMoV121. *International Journal of Fatigue*, 20(3):251–255.

[Pešička et al., 2004] Pešička, J., Dronhofer, A., and Eggeler, G. (2004). Free dislocations and boundary dislocations in tempered martensite ferritic steels. *Materials Science and Engineering A - Structural Materials Properties Microstructure and Processing*, 387-89:176–180.

[Pešička et al., 2003] Pešička, J., Kužel, R., Dronhofer, A., and Eggeler, G. (2003). The evolution of dislocation density during heat treatment and creep of tempered martensite ferritic steels. *Acta Materialia*, 51(16):4847–4862.

[Pilvin, 1994] Pilvin, P. (1994). The contribution of micromechanical approaches to the modelling of inelastic behaviour of polycrystals. In *Proceeding of the Fourth International Conference on Biaxial/Multiaxial Fatigue and Fracture*, volume 1, pages 31–46. SF2M, ESIS, Paris.

[Pilvin, 2003] Pilvin, P. (2003). *Notice d'utilisation de SiDoLo version 2.4495*. Laboratoire de Génie Mécanique des Matériaux, 56321 Lorient, France.

[Polák et al., 2001a] Polák, J., Fardoun, F., and Degallaix, S. (2001a). Analysis of the hysteresis loop in stainless steels I. Austenitic and ferritic steels. *Materials Science and Engineering A - Structural Materials Properties Microstructure and Processing*, 297(1-2):144–153.

[Polák et al., 2001b] Polák, J., Fardoun, F., and Degallaix, S. (2001b). Analysis of the hysteresis loop in stainless steels II. Austenitic-ferritic duplex steel and the effect of nitrogen. *Materials Science and Engineering A - Structural Materials Properties Microstructure and Processing*, 297(1-2):154–161.

[Polcik et al., 1999] Polcik, P., Sailer, T., Blum, W., Straub, S., Buršik, J., and Orlová, A. (1999). On the microstructural development of the tempered martensitic Cr-steel P91 during long-term creep - a comparison of data. *Materials Science and Engineering A - Structural Materials Properties Microstructure and Processing*, 260(1-2):252–259.

[Povolo, 1985] Povolo, F. (1985). Comments on the Monkman-Grant and the modified Monkman-Grant relationships. *Journal of the Materials Science*, 20:2005–2010.

[Priester, 2001] Priester, L. (2001). "Dislocation-interface" interaction - stress accomodation processes at interfaces. *Materials Science and Engineering A - Structural Materials Properties Microstructure and Processing*, 309-310:430–439.

[Proville and Patinet, 2010] Proville, L. and Patinet, S. (2010). Atomic-scale models for hardening in fcc solid solutions. *Physical Review B*, 82(5):054115.

[Proville et al., 2006] Proville, L., Rodney, D., Bréchet, Y., and Martin, G. (2006). Atomic-scale study of dislocation glide in a model solid solution. *Philosophical Magazine*, 86(25-26):3893–3920.

[Qin et al., 2003] Qin, Y., Götz, G., and Blum, W. (2003). Subgrain structure during annealing and creep of the cast martensitic Cr-steel G-X12CrMoWVNbN 10-1-1. *Materials Science and Engineering A - Structural Materials Properties Microstructure and Processing*, 341(1-2):211–215.

[Queyreau et al., 2009] Queyreau, S., Monnet, G., and Devincre, B. (2009). Slip systems interactions in α-iron determined by dislocation dynamics simulations. *International Journal of Plasticity*, 25:361–377.

[Rachdi and Sauzay, 2011] Rachdi, F. and Sauzay, M. (2011). Modélisation du comportement cyclique des polycristaux métalliques. In *Congrès Français de Mécanique 2011, Besançon*.

[Read and Shockley, 1950] Read, W. T. and Shockley, W. (1950). Dislocation models of crystal grain boundaries. *Physical Review*, 78(3):275–289.

[Reuss, 1929] Reuss, A. (1929). Berechnung der fließgrenze von mischkristallen auf grund der plastizitätsbedingung für einkristalle. *Journal of Applied Mathematics and Mechanics*, 9:49–58.

[Rodary et al., 2004] Rodary, E., Rodney, D., Proville, L., Bréchet, Y., and Martin, G. (2004). Dislocation glide in model Ni(Al) solid solutions by molecular dynamics. *Physical Review B*, 70(5):054111.

[Sanchez-Hanton and Thomson, 2007] Sanchez-Hanton, J. J. and Thomson, R. C. (2007). Characterization of isothermally aged Grade 91 (9Cr-1Mo-Nb-V) steel by electron backscatter diffraction. *Materials Science and Engineering A - Structural Materials Properties Microstructure and Processing*, 460:261–267.

[Sauzay, 2000] Sauzay, M. (2000). *Effets de surface et d'anisotropie en fatigue multiaxiale*. PhD thesis, Université Pierre et Marie Curie Paris VI.

[Sauzay, 2009] Sauzay, M. (2009). Modelling of the evolution of micro-grain misorientations during creep of tempered martensite ferritic steels. *Materials Science and Engineering A - Structural Materials Properties Microstructure and Processing*, 510-511:74–80.

[Sauzay et al., 2005] Sauzay, M., Brillet, H., Monnet, I., Mottot, M., Barcelo, F., Fournier, B., and Pineau, A. (2005). Cyclically induced softening due to low-angle boundary annihilation in a martensitic steel. *Materials Science and Engineering A - Structural Materials Properties Microstructure and Processing*, 400:241–244.

[Sauzay et al., 2006] Sauzay, M., Caës, C., Noblecourt, M., Allais, L., Bougault, A., and Fournier, B. (2006). Bilan des essais de torsion cyclique avec et sans contrainte moyenne réalisés sur acier 9Cr à 550 ℃. Technical report, CEA/DEN/DANS/DMN/SRMA/LC2M/NT/2006-2757/A.

[Sauzay et al., 2008] Sauzay, M., Fournier, B., Mottot, M., Pineau, A., and Monnet, I. (2008). Cyclic softening of martensitic steels at high temperature - Experiments and physically based modelling. *Materials Science and Engineering A - Structural Materials Properties Microstructure and Processing*, 483-484:410–414.

[Sauzay and Kubin, 2011] Sauzay, M. and Kubin, L. P. (2011). Scaling laws for dislocation microstructures in monotonic and cyclic deformation of fcc metals. *Progress in Materials Science*, 56(6):725–784.

[Sawada et al., 2001] Sawada, K., Kubo, K., and Abe, F. (2001). Creep behavior and stability of MX precipitates at high temperature in 9Cr-0.5Mo-1.8W-VNb steel. *Materials Science and Engineering A - Structural Materials Properties Microstructure and Processing*, 319:784–787.

[Sawada et al., 2006] Sawada, K., Kushima, H., and Kimura, K. (2006). Z-phase formation during creep and aging in 9-12% Cr heat resistant steels. *The Iron and Steel Institute of Japan International*, 46(5):769–775.

[Sawada et al., 2007] Sawada, K., Kushima, H., Kimura, K., and Tabuchi, M. (2007). TTP diagrams of Z phase in 9-12% Cr heat-resistant steels. *The Iron and Steel Institute of Japan International*, 47(5):733–739.

[Sawada et al., 1999] Sawada, K., Takeda, M., Maruyama, K., Ishii, R., Yamada, M., Nagae, Y., and Komine, R. (1999). Effect of W on recovery of lath structure during creep of high chromium martensitic steels. *Materials Science and Engineering A - Structural Materials Properties Microstructure and Processing*, 267(1):19–25.

[Senior et al., 1986] Senior, B. A., Noble, F. W., and Eyre, B. L. (1986). The nucleation and growth of voids at carbides in 9Cr-1Mo steel. *Acta Metallurgica*, 34(7):1321–1327.

[Shamardin et al., 1999] Shamardin, V. K., Golovanov, V. N., Bulanova, T. M., Povstianko, A. V., Fedoseev, A. E., Goncharenko, Y. D., and Ostrovsky, Z. E. (1999). Mechanical properties and microstructure of advanced ferritic-martensitic steels used under high dose neutron irradiation. *Journal of Nuclear Materials*, 271:155–161.

[Shankar et al., 2006] Shankar, V., Valsan, M., Rao, K. B. S., Kannan, R., Mannan, S. L., and Pathak, S. D. (2006). Low cycle fatigue behavior and microstructural evolution of modified 9Cr-1Mo ferritic steel. *Materials Science and Engineering A - Structural Materials Properties Microstructure and Processing*, 437(2):413–422.

[Sommer et al., 1998] Sommer, C., Mughrabi, H., and Lochner, D. (1998). Influence of temperature and carbon content on the cyclic deformation and fatigue behaviour α-iron. Part I. Cyclic deformation and stress-behaviour. *Acta Materialia*, 46(5):1527–1536.

[Sonderegger et al., 2007] Sonderegger, B., Mitsche, S., and Cerjak, H. (2007). Martensite laths in creep resistant martensitic 9-12% Cr steels - Calculation and measurement of misorientations. *Materials Characterization*, 58(10):874–882.

[Sonderegger et al., 2008] Sonderegger, B., Mitsche, S., and Cerjak, H. (2008). Microstructural analysis on a creep resistant martensitic 9-12% Cr steel using the EBSD method. *Materials Science and Engineering A - Structural Materials Properties Microstructure and Processing*, 481:466–470.

[Spigarelli et al., 1997] Spigarelli, S., Kloc, L., and Bontempi, P. (1997). Analysis of creep curves in a 9Cr-1Mo modified steel by means of simple constitutive equations. *Scripta Materialia*, 37(4):399–404.

[Steckmeyer et al., 2011] Steckmeyer, A., Sauzay, M., Weidner, A., and Hieckmann, E. (2011). Micromechanical modelling of the cyclic stress-strain behaviour of nickel polycrystals. *International Journal of Fatigue*, In Press.

[Stratil et al., 2011] Stratil, L., Hadraba, H., Buršík, J., and Dlouhý, I. (2011). Comparison of microstructural properties and Charpy impact behaviour between different plates of the Eurofer97 steel and effect of isothermal ageing. *Journal of Nuclear Materials*, 416:311–317.

[Sutton and Balluffi, 1995] Sutton, A. P. and Balluffi, R. W. (1995). *Interfaces in crystalline materials*. Clarendon Press, Oxford.

[Tak et al., 2009] Tak, K. G., Schulz, U., and Eggeler, G. (2009). On the effect of micrograin crystallography on creep of FeCr alloys. *Materials Science and Engineering A - Structural Materials Properties Microstructure and Processing*, 510-511:121–129.

[Takeuchi, 1975] Takeuchi, T. (1975). Work hardening of copper single crystals with multiple glide orientations. *Transactions of the Japan Institute of Metals*, 16(10):629–640.

[Takeuchi and Mano, 1972] Takeuchi, T. and Mano, J. (1972). Latent hardening in Fe single-crystals with 1 1 0 extension axis. *Acta Metallurgica*, 20:809–817.

[Taylor, 1938] Taylor, G. I. (1938). Plastic strain in metals. *Journal of the Institute of Metals*, 62:307–324.

[Toloczko et al., 2003] Toloczko, M. B., Hamilton, M. L., and Maloy, S. A. (2003). High temperature tensile testing of modified 9Cr-1Mo after irradiation with high energy protons. *Journal of Nuclear Materials*, 318:200–206.

[Tomkins, 1968] Tomkins, B. (1968). Fatigue crack propagation - an analysis. *Philosophical Magazine*, 18(155):1041–1066.

[Tóth et al., 2002] Tóth, L. S., Molinari, A., and Estrin, Y. (2002). Strain hardening at large strains as predicted by dislocation based polycrystal plasticity model. *Journal of Engineering Materials and Technology*, 124:71–77.

[Tóth et al., 2000] Tóth, L. S., Molinari, A., and Zouhal, N. (2000). Cyclic plasticity phenomena as predicted by polycrystal plasticity. *Mechanics of Materials*, 32:99–113.

[Vaillant et al., 2008] Vaillant, J. C., Vandenberghe, B., Hahn, B., Heuser, H., and Jochum, C. (2008). T/P23, 24, 911 and 92: New grades for advanced coal-fired power plants – Properties and experience. *International Journal of Pressure Vessels and Piping*, 85(1-2):38–46.

[Van Swygenhoven et al., 1999] Van Swygenhoven, H., Spaczer, M., Caro, A., and Farkas, D. (1999). Competing plastic deformation mechanisms in nanophase metals. *Physical Review B*, 60(1):22–25.

[Voyiadjis and Abed, 2005] Voyiadjis, G. Z. and Abed, F. H. (2005). Microstructural based models for bcc and fcc metals with temperature and strain rate dependency. *Mechanics of Materials*, 37(2-3):355–378.

[Wakasa and Wayman, 1981] Wakasa, K. and Wayman, C. M. (1981). The morphology and crystallography of ferrous lath martensite. Studies of Fe-20%Ni-5%Mn - II. Transmission electron microscopy. *Acta Metallurgica*, 29:991–1011.

[Wassermann, 1933] Wassermann, G. (1933). Einfluß der α–γ–umwandlung eines irreversiblen nickelstahls auf kristallorientierung und zugfestigkeit. *Arch. Eisenhüttenwes*, 6:347–351.

[Wei et al., 2004] Wei, Q., Cheng, S., Ramesh, K. T., and Ma, E. (2004). Effect of nanocrystalline and ultrafine grain sizes on the strain rate sensitivity and activation volume: fcc versus bcc metals. *Materials Science and Engineering A - Structural Materials Properties Microstructure and Processing*, 381(1-2):71–79.

[Yaguchi and Takahashi, 2000] Yaguchi, M. and Takahashi, Y. (2000). A viscoplastic constitutive model incorporating dynamic strain aging effect during cyclic deformation conditions. *International Journal of Plasticity*, 16(3-4):241–262.

[Yi et al., 2006] Yi, Y., Lee, B., Kim, S., and Jang, J. (2006). Corrosion and corrosion fatigue behaviors of 9Cr steel in a supercritical water condition. *Materials Science and Engineering A - Structural Materials Properties Microstructure and Processing*, 429(1-2):161–168.

[Zhang et al., 1991] Zhang, J. G., Noble, F. W., and Eyre, B. L. (1991). Comparison of effects of aging on fracture of 9Cr-1Mo and 2.25Cr-1Mo steel. 1. Quenched and tempered material. *Materials Science and Technology*, 7(3):218–223.

[Zhang et al., 2011] Zhang, N., Xu, H., Mao, X., and Wang, G. (2011). Study on high temperature creep behaviors of P92 steel. *Key Engineering Materials*, 452-453:521–524.

Étude expérimentale et modélisation de l'adoucissement cyclique des aciers ferritiques-martensitiques revenus

Résumé : Inscrit au sein d'un grand projet aboutissant à la mise en œuvre des réacteurs nucléaires de génération IV, ce travail de thèse porte sur l'étude des aciers martensitiques revenus à 9 % de chrome. Actuellement utilisés pour des applications à haute température, notamment dans les centrales thermiques, ils présentent en fatigue et en fatigue-fluage un phénomène d'adoucissement mécanique et des évolutions microstructurales particulièrement prononcées : disparition de nombreux joints de sous-grains, baisse de la densité de dislocations, apparition et/ou grossissement de précipités et de nouvelles phases. Les objectifs principaux de cette thèse sont (i) d'établir expérimentalement une corrélation entre l'adoucissement mécanique des aciers à 9 % de chrome constaté en fatigue à 550 °C et l'évolution de leur microstructure au cours de ce type de sollicitation et (ii) de modéliser les mécanismes physiques de déformation afin de prédire le comportement mécanique de ces aciers sous chargement cyclique.

Une étude des propriétés mécaniques en traction monotone et sous sollicitations cycliques à 550 °C a été conduite sur un acier de Grade 92 (9Cr-0,5Mo-1,8W-V-Nb). L'expertise des éprouvettes de traction suggère que l'adoucissement du matériau est principalement lié à une augmentation de la taille moyenne des sous-grains de plus de 15 % par rapport à l'état initial. L'étude de l'évolution de la contrainte macroscopique durant les essais cycliques montre que l'adoucissement du matériau est dû à la diminution de l'écrouissage cinématique. Les observations effectuées au MET montrent une augmentation de la taille moyenne des sous-grains comprise entre 65 et 95 % et une diminution de la densité de dislocations de plus de 50 % dans le matériau après les essais de fatigue, par rapport à l'état initial.

Un modèle auto-cohérent à champs moyens fondé sur l'élastoviscoplasticité polycristalline, prédisant le comportement mécanique macroscopique du matériau et l'évolution microstructurale au cours de la déformation est proposé. En décrivant les mécanismes de déformation à partir d'observations microstructurales, le modèle utilise seulement deux paramètres ajustables (énergie et volume d'activation) liés aux mécanismes de déformation viscoplastique. Les valeurs de l'ensemble des autres paramètres sont fixées grâce à des mesures expérimentales ou des calculs issus de la littérature. Le modèle prédit correctement l'adoucissement macroscopique et donne une bonne tendance des évolutions microstructurales au cours de la déformation. L'étude paramétrique montre une bonne stabilité des prédictions dès lors que les paramètres expérimentaux varient dans un intervalle de mesure physiquement acceptable. Enfin, quelques perspectives d'amélioration du modèle sont testées et des essais de torsion cyclique avec et sans contrainte moyenne sont simulés.

Mots-clés : Adoucissement cyclique à haute température ; Aciers martensitiques revenus ; Évolution microstructurale ; Modélisation polycristalline.

Experimental study and simulation of the cyclic softening of tempered martensite ferritic steels

Abstract: The present work focuses on the high temperature mechanical behaviour of 9%Cr tempered martensite steels, considered as potential candidates for structural components in future Generation IV nuclear power plants. Already used for energy production in fossil power plants, they are sensitive to softening during high-temperature cycling and creep-fatigue. This phenomenon is coupled to a pronounced microstructural degradation: vanishing of subgrain boundaries, decrease in dislocation density, nucleation and/or growth of precipitates and new phases. This study aims at (i) linking the macroscopic cyclic softening of 9%Cr steels and their microstructural evolution during cycling and (ii) proposing a physically-based modelling of deformation mechanisms in order to predict the macroscopic mechanical behaviour of these steels during cycling.

Mechanical study including uniaxial tensile tests and cycling at 550 °C was performed on a Grade 92 steel (9Cr-0,5Mo-1,8W-V-Nb). Examination of tensile specimens suggested that the physical mechanism responsible for softening is mainly the evolution of mean subgrain size, which increases by more than 15 % compared to the as-received state. The evolution of macroscopic stress during cycling shows that cyclic softening is due to the decrease in kinematic hardening. TEM observations highlighted that the mean subgrain size increases by 65 to 95 % while the dislocation density decreases by more than 50 % during cycling, compared to the as-received state.

A self-consistent homogenization model based on polycrystalline elastoviscoplasticity, predicting the mechanical behaviour of the material and its microstructural evolution during deformation is proposed. This model takes the physical deformation mechanisms into account and only two adjustable parameters (activation energy and activation volume) linked to the viscoplastic deformation mechanisms are used. The value of other parameters were either experimentally measured or deduced from computations available in literature. The model correctly predicts the macroscopic softening behaviour and gives a good trend of the microstructural evolution during cycling. The parametrical study shows that the predictions of the model are rather stable with respect to the variation of the physically-based parameters. Finally, some hypotheses which permit us to improve the model are presented and torsion tests (with or without constant superimposed tensile stress) are modeled.

Keywords: High-temperature cyclic softening; Tempered martensite steels; Polycrystalline model; Microstructural evolution.

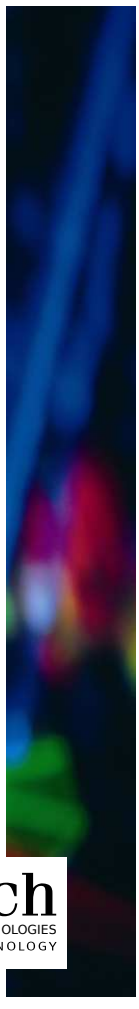

MINES ParisTech

ParisTech
INSTITUT DES SCIENCES ET TECHNOLOGIES
PARIS INSTITUTE OF TECHNOLOGY